THE UNIVERSITY *of* EDINBURGH

Advancing a Methodology for Implant-Triggered Cancer Treatment with Bioorthogonal Palladium-Labile Prodrugs

Thomas L. Bray

PhD in Molecular Medicine

University of Edinburgh

2017

DECLARATION

This thesis has been entirely composed by the author Thomas Bray. I have carried out all experiments except where otherwise stated. This work herein has not been submitted for any other degree or professional qualification. Some of this work has been published in the scientific literature and most of it is protected under patent. Printed versions of the primary research resulting from this thesis are included in the appendix.

Patent:

Palladium Activated Prodrugs PCT/GB2017/051379. Priority Date: 29.04.2016. Inventors: Belén Rubio-Ruiz, Thomas L. Bray, Ana M Pérez-López, Asier Unciti-Broceta.

Article:

Pérez-López AM, Rubio-Ruiz B, Sebastián V, Hamilton L, Adam C, Bray TL, Irusta S, Brennan PM, Lloyd-Jones GC, Sieger D, Santamaría J, Unciti-Broceta A, et al. *Gold-Triggered Uncaging Chemistry in Living Systems*. Angewandte Chemie - International Edition. 2017; 56(41): 12548 - 12552. DOI 10.1002/anie.201705609

Book chapter:

Rubio-Ruiz B, Bray TL, Pérez-López AM, *Masking Strategies for the Bioorthogonal Release of Anticancer Glycosides.* Z.J. Witczak and R. Bielski (eds.), Coupling and Decoupling of Diverse Molecular Units in Glycosciences (Springer) 2017.

ABSTRACT

Chemotherapeutics are potent molecules capable of systematically treating cancer. As healthy tissues contain features also inherent to cancer cells, treatment often results in unwanted side-effect. As chemotherapeutic side-effect produces significant harm and often limits optimal drug dosing, new strategies must be developed to improve treatment selectivity. A prodrug strategy provides one option to improve the selectivity of an established chemotherapeutic. By modifying a pharmaceutically active drug, interaction with biology may be functionally masked. Subsequent 'un-masking' the prodrug exclusively at the intended treatment site may direct treatment only to where the anticancer effect is required.

This thesis progresses the novel approach of bioorthogonal organometallic (BOOM) prodrug activation. A metal catalyst and masked chemotherapeutic constitute reaction partners to provide a new strategy for intratumoural prodrug activation. Whereby the prodrug and metal catalyst are independently non-cytotoxic, in combination the prodrug undergoes catalytic activation to deliver an anticancer affect. By positioning the metal catalyst within a tumour (i.e. by microsurgery), an administered masked prodrug sensitive to catalyst-mediated activation could allow for 'targeted' chemotherapy localised to the tumour site.

The design, synthesis and study of new BOOM prodrug candidates are reported herein. Novel protecting groups are developed to enhance drug masking to biology and subsequent catalyst-mediated activation. Prodrug screening studies are carried out in cancer cell culture models, with zebrafish and in *ex vivo* rodent model tumour explants. The catalyst, a palladium (Pd^0) functionalised bead system, is optimised for enhanced activation, drug release and *in vivo* implantation. The potentially infinite generation of active chemotherapeutics exclusively in tumour would increase the efficacy of treatment whilst reducing harmful effect on healthy tissue.

ACKNOWLEDGEMENTS

I first acknowledge the significant resources that the University of Edinburgh, Cancer Research UK and the Medical Research Council have developed for the benefit of cancer research within the city. This collective ecosystem offers the potential to pursue inventive science without the constraints of cost, access or delay. I am thankful of that.

My life and study here has been most enriched by Asier Unciti-Broceta. Your careful guidance allowed us to conduct some good studies and explore new realms of science I had not thought possible. My colleagues in the lab especially Samuel Myers, Belen Rubio-Ruiz, Ana Perez-Lopez, Catherine Adam and Carolin Temps have been important contributors to this body of work. In turn they have each advised and solved challenges I was faced with and could not overcome alone. Many of the experiments herein were conducted with the support of technical staff, collaborators and PI's - in Edinburgh at the IGMM, Kings Buildings and QMRI and at the Beatson in Glasgow, reflective of the communal nature of science in Scotland.

Scott Warchal and I made spheroids for a few months and in the meantime spent some cold weekend mornings riding along the coast. Alessandro Brombin displayed great resolve in developing and then fine-tuning the zebrafish assay. Mark Salji and Laura Galbraith believed in this technology enough to receive me numerous times in Glasgow and labour late into the evening on our *in vivo* studies. The IGMM is a vibrant place for the life of a researcher. I have been supported by the institute on an ambitious project or two, and received training through internships within the College – a testament to the support offered to students. The IGMM has also provided a place to build friendships, many of whom shall carry on. My friends know to come and stay with me in Oxford when they are passing by.

The spiral molecules
Of desoxyribonucleic acid
Form a brave ladder
To that lofty outlook
From where the present
Watches the past,
And vice versa.

✦✦✦

CONTENTS

p.

DECLARATION 2

ABSTRACT 3

ACKNOWLEDGEMENTS 4

CONTENTS 5

LIST OF FIGURES AND TABLES 8

ABBREVIATIONS 11

CHAPTER 1

Introduction 13
1.1 The Bioorthogonal Chemistry Horizon 13
1.2 Bioorthogonal Cleavage Reactions in Biological Systems 18
1.3 Cancer Therapy 24
1.4 Small Molecule Kinase Inhibitors 27
1.5 Immunotherapy 30
1.6 Prodrugs 32
1.7 BOOM Chemistry; Development and Current Advances 33
1.8 Design of Bioorthogonal Pd^0 labile prodrugs 35
1.9 Aims: to advance BOOM chemotherapeutic approaches 37

CHAPTER 2

Introduction 38
2.1 5-fluorouracil Overview 38
2.2 Current Progress with N-alkylated 5FU prodrugs 41
2.3 Design and Synthesis of a Novel O-propargylated 5FU prodrug 43
2.4 5FU prodrug biocompatibility assays 47
2.5 Pd-mediated 5FU prodrug *in vitro* conversion study 48
2.6 5FU Prodrug Biological Conversion Assay in Combination with Pd^0 50
2.7 Investigating Analytical Modalities to Study 5FU Prodrug Deprotection: NMR 52
2.8 Investigating Analytical Modalities to Study 5FU Prodrug Deprotection: Raman Spectroscopy 56
2.9 Conclusions 59

CHAPTER 3

Introduction 63

3.1 Gemcitabine Overview 63
3.2 Current Progress with Gemcitabine Prodrugs 67
3.3 Rational Design and Incorporation of a Novel Protecting Group for Gemcitabine Prodrugs 69
3.4 Gemcitabine Prodrug Biocompatibility Assays 73
3.5 Pd-mediated Gemcitabine Prodrug *in vitro* Conversion Study 74
3.6 Conclusions 76

CHAPTER 4

Introduction 78
4.1 Doxorubicin Overview 78
4.2 The Rational Design Basis for Masking the C3' Amino Group of Doxorubicin 80
4.3 Synthesis of Novel Doxorubicin Prodrugs 83
4.4 Doxorubicin Prodrug Biocompatibility Assays 85
4.5 Design of the *bis*-o-Pobc Protecting Group 87
4.6 Reviewing the Pd^0 device 90
4.7 Design, Synthesis and Characterization of Pd^0 Functionalized beads 90
4.8 Non-biological Pd-mediated Dox Prodrug Conversion Study 92
4.9 Pd-mediated Doxorubicin Prodrug *in vitro* Conversion study 96
4.10 The Sequestration Effect of Doxorubicin and Prodrugs on Activation 100
4.11 Design and Synthesis of Novel Pd^0 Beads for Enhanced Activation 100
4.12 Testing the Catalytic Properties of 30 μm Pd^0 Beads in a Biological System 103
4.13 Biocompatibility of 30 μm Pd^0 Beads *in vitro* 105
4.14 Non-biological Pd-mediated Doxorubicin Prodrug Conversion Study with 30 μm Pd^0 Beads 106
4.15 Pd-mediated conversion of Doxorubicin prodrugs with 30 μm Pd^0 beads in cancer cell culture 107
4.16 Conclusions 111

CHAPTER 5

Introduction 114
5.1 Spheroid Cell Culture Study
5.1.1 Three-dimensional cell culture overview 114
5.1.2 MCTS Assay Optimization 116
5.1.3 MCTS BOOM Activation Assay 118
5.2 Zebrafish Study
5.2.1 Zebrafish as a model animal for doxorubicin induced cardiomyopathy 121
5.2.2 Zebrafish doxorubicin induced cardiac oedema assay 122
5.3 *in vivo* / *ex vivo* prodrug activation assay
5.3.1 *n vivo* / *ex vivo* prodrug activation assay overview 126
5.3.2 Pilot study of intratumoural Pd-mediated floxuridine prodrug activation 126
5.3.3 Optimising an intratumoural *in vivo* Pd^0 bead implantation / *ex vivo* activation assay 133
5.3.4 Development of an ultrasound guided in-vivo Pd^0 bead injection protocol 134
5.3.5 *ex vivo* Pd-mediated probe activation 136
5.3.6 *ex vivo* tumour explant drug/prodrug biocompatibility study 138

5.3.7 Intratumoural *in vivo* Pd^0 bead implantation / *ex vivo* prodrug activation assay 142
5.3.8 Conclusions 145

CHAPTER 6

Conclusions and Future Work 148

CHAPTER 7

7.1 Chemistry
7.1.1 Chemicals 158
7.1.2 Chromatography 158
7.1.3 Nuclear Magnetic Resonance 158
7.1.4 Mass Spectrometry 159
7.1.5 Scanning Electron Microscopy Imaging 159
7.1.6 Synthesis and Characterisation of Pd^0 Beads 159
7.1.7 Synthesis and Characterisation of 5-fluorouracil prodrugs 161
7.1.8 Synthesis and Characterisation of Pd^0 labile moieties 164
7.1.9 Synthesis and Characterisation of gemcitabine prodrugs 169
7.1.10 Synthesis and Characterisation of doxorubicin prodrugs 177
7.2 Biology
7.2.1 Cell culture 183
7.2.2 Non Biological Pd^0 mediated Conversion Study 183
7.2.3 Bioorthogonal Comparative Study of Prodrug to Parental Drug 183
7.2.4 Pd^0-Mediated Dealkylation of Prodrugs in Cell Culture 184
7.2.5 Spontaneous Raman Spectroscopy of Drug, Prodrug and Cell Pellet 185
7.2.6 Spheroid Assay 185
7.2.7 Zebrafish Assay 186
7.2.8 *In vivo* / *ex vivo* Mouse Assays 187

CHAPTER 8

Bibliography 190

APPENDIX 204

LIST OF FIGURES, SCHEMES AND TABLES

p.

CHAPTER 1

Figure 1.1 Conventional methods for studying biomolecules in native environments…… 14
Figure 1.2 Fluorescent labelling of a specific recombinant protein molecule in live cells..... 15
Figure 1.3 Staudinger Azide Ligation on cell surface…….. 16
Figure 1.4 Bioorthogonal ligation reactions..... 18
Figure 1.5 Prototype bioorthogonal cleavage: photolytic release of ATP in a human red blood cell..…… 19
Figure 1.6 Synthesis of Pd^0 microspheres..…….. 21
Figure 1.7 Tetrazine ligation to release drugs in living systems..…….. 22
Figure 1.8 Bioorthogonal cleavage reactions to release amines..…..... 23
Figure 1.9 Schematic of DNA alkylating agents..……..…… 25
Figure 1.10 Dihydrofolate Reductase (DHFR) complexed with Methotrexate..……..…….. 26
Figure 1.11 Effect of Gefitinib on the epidermal growth factor receptor (EGFR) signalling pathway..…… …… 29
Figure 1.12 Treatment of patients with B-cell malignancies using anti-CD19 CAR-T cells..…… 31
Figure 1.13 Overview of Directed Enzyme Prodrug Therapy (DEPT)..…….. 33
Figure 1.14 BOOM Chemotherapeutic Concept..…….. 34

CHAPTER 2

Figure 2.1 Structure of 5-fluorouracil……. 39
Figure 2.2 5-fluorouracil binds to Dihydropyrimidine Dehydrogenase via interaction with multiple amino acid residues..…….. 40
Figure 2.3 5-fluorouracil mechanism of action..…… 41
Scheme 2.4 5-fluorouracil conjugate bases……...…… 42

Scheme 2.5 Synthesis of N1 alkylated 5-fluorouracil prodrugs…….. 42
Figure 2.6 Development of a trapped di-lactim analogue of 5FU..…… 44
Figure 2.7 Experimental clogP of 5FU and 5FU prodrugs..…… 44
Scheme 2.8 Synthesis of 5FU prodrug 2..…… 45
Scheme 2.9 1st Attempted synthesis of O-monoalkylated propargyloxy-5-fluorouracil prodrug 7……..... 46
Scheme 2.10 2nd Attempted synthesis: O-monoalkylated propargyloxy-5-fluorouracil prodrugs: O vs N Alkylation of 5FU derivatives…… …… 47
Figure 2.11 Study of 5-fluorouracil cytotoxic reduction produced by prodrug 2 in cell culture..…… 48
Figure 2.12 Non-biological stability assay of 5FU prodrug 2..…… 49
Figure 2.13 Non-biological Pd^0 conversion assay with 5FU prodrug 2. …….. 50
Figure 2.14 Preliminary Pd-mediated activation assay to compare activity of 5FU prodrug 2 against drug..…… 51
Figure 2.15 Pd-mediated activation of 5FU prodrug 2 in BxPC3 and HCT116 cell culture…….. 52

Figure 2.16 Overlaid ^{19}F NMR spectra of 5FU and prodrugs..... 54
Figure 2.17 ^{19}F NMR reaction product of 5FU prodrug 5 with Pd^0 beads..... 55
Figure 2.18 Raman Spectroscopy of 5FU and 5FU prodrug 2 as powder samples..... 58
Figure 2.19 i*n vitro* Raman study of 2 prodrug in cell pellet..... 59

CHAPTER 3

Figure 3.1 Structure of Gemcitabine..... 63
Figure 3.2 Deoxycytidine Kinase (dCK) in complex with gemcitabine..... 65
Figure 3.3 Cellular metabolism of gemcitabine..... 66
Scheme 3.4 Synthesis of reported gemcitabine prodrugs..... 68
Figure 3.5 The propargyloxybenzyl carbonyl (Pobc) group..... 69
Scheme 3.6 Proposed mechanism for the Pd^0 catalysed cleavage of Pobc groups in water..... 70
Scheme 3.7 Synthesis of novel gemcitabine prodrugs..... 71
Figure 3.8 Study of hydroxybenzyl alcohol byproduct cytotoxicity..... 72
Figure 3.9 Study of acetol byproduct cytotoxicity..... 72
Figure 3.10 Study of gemcitabine cytotoxic reduction produced by prodrugs 25, 26 and 33 – 36 in cell culture..... 73
Figure 3.11 Preliminary Pd-mediated activation assay to compare activity of gemcitabine prodrugs 25, 26, 33 and 36 against drug in MiaPaCa-2 cells..... 75
Figure 3.12 Pd-mediated activation of gemcitabine prodrugs in MiaPaCa-2 cell culture..... 76

CHAPTER 4

Figure 4.1 Structure of Doxorubicin..... 78
Figure 4.2 Doxorubicin mechanism of action..... 79
Figure 4.3 C3' amino-protected prodrugs of doxorubicin..... 83
Scheme 4.4 Synthesis of doxorubicin prodrugs 42, 43, 44 and 45..... 85
Figure 4.5 Study of doxorubicin cytotoxic reduction produced by 42-45 prodrugs in cell culture..... 86
Scheme 4.6 The *bis*-2,6-propargyloxybenzylcarbonyl (*bis*-o-Pobc) group..... 87
Scheme 4.7 Synthesis of doxorubicin prodrug 50..... 88
Figure 4.8 Study of doxorubicin cytotoxic reduction produced by prodrug 50 in cell culture..... 89
Figure 4.9 Assessment of 130 µm diameter Pd^0 beads for coupling and size homogeneity..... 92
Figure 4.10 Non-biological stability assay of doxorubicin prodrugs 42 – 45 and 50..... 93
Figure 4.11 Non-biological conversion assay of doxorubicin prodrugs 42 – 45 and 50 in combination with 130 µm Pd^0 beads..... 94-96
Figure 4.12 Preliminary Pd-mediated activation assay to compare activity of doxorubicin prodrugs 42-45 and 50 against drug in DU145 cell culture..... 97
Figure 4.13 Pd-mediated activation of doxorubicin prodrugs in DU145 cell culture..... 98
Figure 4.14 Pd-mediated activation of doxorubicin prodrugs in U87 cell culture..... 99
Figure 4.15 Sequestration of doxorubicin prodrugs by 130 µm Pd^0 beads..... 100
Figure 4.16 Scanning Electron Microscopy (SEM) images of variable sized Pd^0 beads..... 102
Table 4.17 Pd loading in variable sized beads..... 103
Figure 4.18 Fluorescent analysis of Pd-mediated Poc-Rho activation assay in PBS..... 104

Figure 4.19	Fluorescent analysis of Pd-mediated Poc-Rho activation in PBS with FBS serum added……	104
Figure 4.20	Biocompatibility of 30 μm vs 130 μm Pd^0 beads in cell culture……..	105 - 106
Figure 4.21	Non-biological conversion assay of doxorubicin prodrugs 42, 43 and 50 in combination with 30 μm Pd^0 beads……..	107
Figure 4.22	Comparative Pd-mediated activation of doxorubicin prodrugs 42 and 43 with 30 μm vs 130 μm Pd^0 beads in DU145 cell culture……	108
Figure 4.23	Comparative Pd-mediated activation of doxorubicin prodrugs 42 and 43 with 30 μm vs 130 μm Pd^0 beads in U87 cell culture……..	109
Figure 4.24	Pd-mediated activation of 42 with 30 μm Pd^0 beads……	110
Figure 4.25	Pd-mediated activation of 43 with 30 μm Pd^0 beads……	111

CHAPTER 5

Figure 5.1.1	Illustrative example of a two dimensional (2D) vs three dimensional (3D) *in vitro* BOOM assay……	116
Figure 5.1.2	MCTS single Pd^0 bead incubation model……	117
Figure 5.1.3	MCTS Pd^0 bead incubation model with increased catalyst loading……	118
Figure 5.1.4	MCTS prodrug activation using 43 + Pd^0 beads……	119
Figure 5.1.5	MCTS prodrug activation using pre-incubated 43 + 30 μm Pd^0 beads……..	120
Figure 5.2.1	Phases of heart formation in the zebrafish embryo……..	121
Figure 5.2.2	Initial study of doxorubicin induced cardiac oedema on the zebrafish embryonic heart……..	122
Figure 5.2.3	Study on the potential cardioprotective properties of 43 on embryonic zebrafish cardiac tissue……..	123
Figure 5.2.4	Dose-dependent viability effects of exposure to dox or 43 between 24 - 120 hpf…	124
Figure 5.2.5	Fluorescence study of prodrug and drug uptake into zebrafish……..	125
Figure 5.3.1	Design and assessment of a biocompatible N3 alkylated Floxuridine prodrug *in vitro*……	127
Figure 5.3.2	Representative High Dose Rate (HDR) Brachytherapy treatment protocol for prostate cancer……	128
Figure 5.3.3	Observing the outcome of Pd^0 bead injections on tumour tissue samples……	129
Figure 5.3.4	Immunohistochemistry staining of an intratumoural Pro-FUdR Pd-mediated activation assay……..	130
Figure 5.3.5	Proposed site of Pd^0 beads within a caspase 3 stained CWR22 prostate tumour tissue slice……	131
Figure 5.3.6	Xylene free histology for Pd^0 bead visualisation……	132
Figure 5.3.7	Schematic representation of *in vivo* Pd^0 implantation / *ex vivo* activation assay…..	134
Figure 5.3.8	Subcutaneous ultrasound guided intratumoural prostate injection of 30 μm Pd^0 beads into anaesthetized mouse……..	135
Figure 5.3.9	Resected tumor halved to visualise intratumoral Pd-implant distribution……..	136
Figure 5.3.10	Conversion schematic of non-fluorscent bis-N,N'-propargyloxycarbonylrhodamine 110 (Poc-Rho) into fluorescent hydrophilic rhodamine 110 (Rho) by Pd-mediated carbamate cleavage……	136
Figure 5.3.11	*ex vivo* Pd-mediated carbamate cleavage of *bis*-N,N'-Poc-Rhodamine 110 incubated with *in vivo* Pd^0 bead injected prostate tumour samples……	137
Figure 5.3.12	Fluorescence spectra of dox and prodrugs……	139
Figure 5.3.13	*ex vivo* biocompatibility study of dox in prostate tumour samples……..	140
Figure 5.3.14	*ex vivo* biocompatibility study of 42 in prostate tumour samples……	140
Figure 5.3.15	*ex vivo* biocompatibility study of 43 in prostate tumour samples……	141
Figure 5.3.16	*ex vivo* Pd^0-mediated carbamate cleavage of 43 with shortly administered *in vivo* Pd^0 bead injection into prostate tumour samples……..	143

Figure 5.3.17 *ex vivo* Pd^0-mediated carbamate cleavage of 43 with 3 week incubated *in vivo* Pd^0 bead injections into prostate tumour samples…… 143
Figure 5.3.18 Sequestration effect of Prodrug 43 within + 3 week incubated Pd^0 bead injections into prostate tumour samples…… 144
Figure 5.3.19 Fluorescence signal merge (blue and red channels) corresponding to dox induced cellular cytotoxicity…… 145

ABBREVIATIONS

^{13}C	NMR Carbon-13 Nuclear Magnetic Resonance
^{1}H	NMR Proton Nuclear Magnetic Resonance
A549	Human Adenocarcinomic Alveolar Basal Epithelial Cell Line
Alloc	Allyloxycarbonyl
BxPC3	Human Pancreas Adenocarcinoma Cell Line
Cbz	Carboxybenzyl
d	Doublet
DBU	1,8-Diazabicyclo[5.4.0]undec-7-ene
DCM	Dichloromethane
dd	Double Doublet
DIAD	Diisopropyl Azodicarboxylate
DMEM	Dulbecco's Modified Eagle Media
DMF	*N,N*-Dimethylformamide
DMSO	Dimethyl sulfoxide
dpf	Days Post-fertilisation
dq	Doublet Quartet
dt	Double Triplet
DU145	human prostate cancer cell line
equiv.	Equivalents
ESI	Electrospray Ionisation
EtOAc	Ethyl Acetate
FBS	Fetal Bovine Serum
HCT116	Human Colorectal Carcinoma cell line
hpf	Hours Post-fertilisation
HPLC	High Performance Liquid Chromatography
hr	hour
HRMS	High Resolution Mass Spectrometry
Hz	Hertz
ICP-OES	Inductively Coupled Plasma Optical Emission Spectrometry
J	Coupling Constant
KOH	Potassium Hydroxide
LRMS	Low Resolution Mass Spectrometry
m	multiplet
m/z	Mass-to-charge ratio
MeCN	Acetonitrile
MeOH	Methanol
MHz	Mega Hertz
MiaPaCa2	Human Pancreas Carcinoma Cell Line
MS	mass spectrometry
MW	Molecular Weight
N_2	Nitrogen
Na_2CO_3	Sodium Bicarbonate
NaH	Sodium Hydride
$NaHCO_3$	Sodium Hydrogen Carbonate
NaOH	Sodium Hydroxide

nm	Nanometer
NMR	Nuclear Magnetic Resonance
PBS	Phosphate Buffered Saline
Pd	Palladium
$Pd(OAc)_2$	Palladium(II) Acetate
Pd_0	Palladium with an Oxidation State of 0
Pd^{2+}	Palladium with an Oxidation State of 2
PdNP	Palladium Nanoparticles
PEG	Polyethylene Glycol
Ph_3P	Triphenylphosphine
Pobc	propargyloxybenzyl carbonyl
Poc	Propargyloxycabonyl
PS	Polystyrene
q	Quartet
qt	Quartet of Triplets
Rf	Retention Factor
rpm	Revolutions Per Minute
RPMI	Roswell Park Memorial Institute Medium
rt	Room Temperature
s	Singlet
SEM	Scanning Electron Microscopy
TBAF	Tetra-n-butylammonium fluoride
TBS-Cl	tert-Butyldimethylsilyl chloride
TCO	*trans*-cyclooct-2-ene
TFA	Trifluoroacetic Acid
TG	Tenta Gel
THF	Tetrahydrofuran
TLC	Thin Layer Chromatography
U87	Human bonafide Glioblastom Cell Line
δ	Chemical Shift

CHAPTER 1

Introduction

Improving methods for the study and modification of biomolecules in their native environment is a key frontier in chemical biology. Genetic engineering and bioconjugation has allowed for key advances in the understanding of biology and the development of new medicines. In this introductory chapter the caveats of classical biochemical methodologies will be briefly explored. Bioorthogonal chemistry strategies will be examined that may solve such caveats. New ways to form and break covalent bonds orthogonal to living systems will also be described.

1.1 The Bioorthogonal Chemistry Horizon

By utilising synthetic gene reporting systems that express modified variants of a molecule of interest, the expression and localisation of specific proteins *in vitro*[1] and *in vivo*[2] is now a standard technique in biological sciences. Synthetic gene reporting was established by the discovery and characterisation of green fluorescent protein (GFP), now a commercialised fluorescent probe. GFP is a protein composed of 238 amino acid residues first isolated from the jellyfish *Aequorea victoria*[3], and is recognised as a key reagent for the native study of biomolecules[4]. By attaching a GFP genetic sequence to a regulatory gene of interest, co-expression of GFP bound to a target protein allows for protein tracking and quantitative protein expression in a living system. Significant limitations exist however in utilising GFP proteins to study biomolecules in living systems. As the function of GFP is dependent upon its co-expression with a gene of interest, GFP and variants are unable to study biomolecules not encoded for by DNA. This precludes GFP based studies on lipids, nucleic acids, glycans and metabolites within the cell (fig 1.1).

Although sequence optimisation has expanded the repertoire of fluorescent protein tags to include emission wavelengths across the entire visible spectrum[5], other imaging modalities are still inaccessible. Perhaps most importantly, the structural perturbation imposed by

genetically engineering a large synthetic protein to covalently bond to its target alters the native function of the molecule of interest.

Another established method to study living systems is to covalently couple molecules of interest to target native amino acids through key functional groups. This is a process known as bioconjugation. Unlike GFP based strategies, a diverse range of small molecules may be synthetically coupled to a target, including fluorescent dyes, biotin and polymers, drug conjugates, nanoparticles and surfaces[6,7]. Traditional bioconjugation reactions rely on chemistry specific to functional groups present on native amino acid residues. Frequently, targeted functional groups for bioconjugation include the N- and C- end termini and the R groups of lysine, cysteine, tyrosine and tryptophan. Whilst this methodology expands the position and number of sites available for protein modification, these key functional groups are ubiquitous to biology, and off target modification is inevitable (fig 1.1).

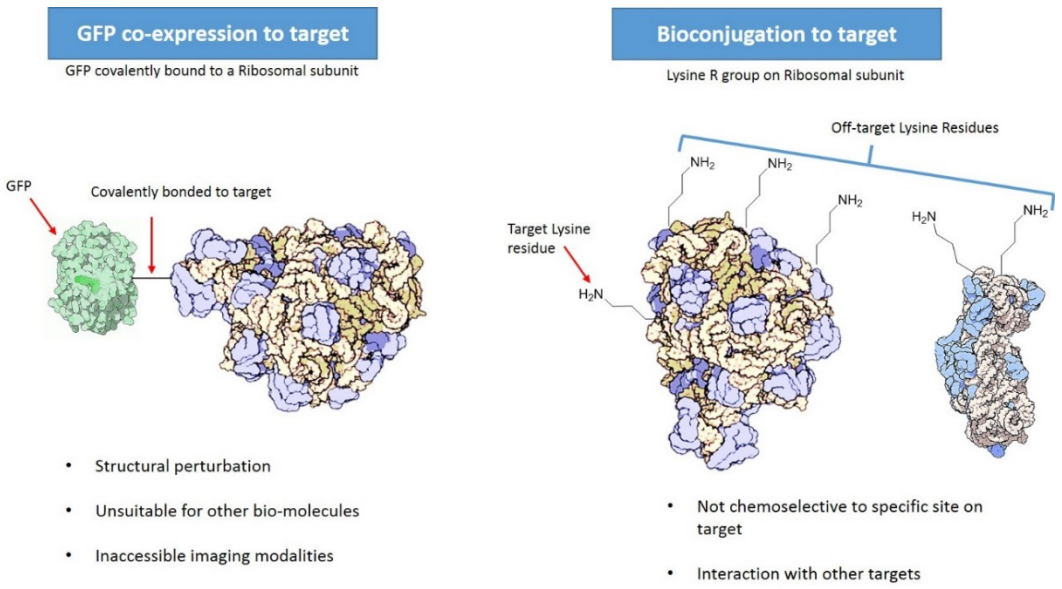

Figure 1.1 Conventional methods for studying biomolecules in native environments. Target proteins may be studied by synthetically modifying the gene sequence of a target protein to include a gene encoding green fluorescent protein (GFP). GFP imposes structural perturbation, is only visualised by fluorescence microscopy and is not applicable to biomolecules that are not genetically encoded for. Target biomolecules (including proteins, lipids, glycans and DNA) may be studied by traditional bioconjugation reactions, where probes are attached to functional groups on native amino acids. Chemoselectivity to the target amino acid hinders the specificity of this approach. Image adapted from open source database Protein Data Bank (2017)[8,9].

Chemoselectivity remains an intractable limitation on the efficiency of native residue based covalent bonding strategies, and biology imposes complex demands on target specificity. Perturbational and chemoselective disadvantages in genetic engineering and bioconjugation have led to new methods that increase the scope of biomolecule investigation with retained control of target specificity and reduced effect on the surrounding environment. Covalent bonding chemistry conducted 'orthogonal' to a living system was initially validated with bespoke chemical strategies capable of bond ligation *in situ*[10–12]. Tsien and colleagues first reported the development of a dye that would fluoresce *in vitro* when attached to cysteine rich positions of a recombinant protein by rapid covalent bond formation between an organoarsenic group and a di-thiol[10]. This strategy was validated in living cells by labelling expressed proteins containing a CCXXCC motif (fig 1.2). For the first time selective reversible fluorescence in a living system was possible with the use of a small molecule reporter. Shortly after, Bertozzi described the use of a biocompatible Staudinger ligation on the surface of live cells[11]. This novel class of chemistry was referred to as 'bioorthogonal chemistry'.

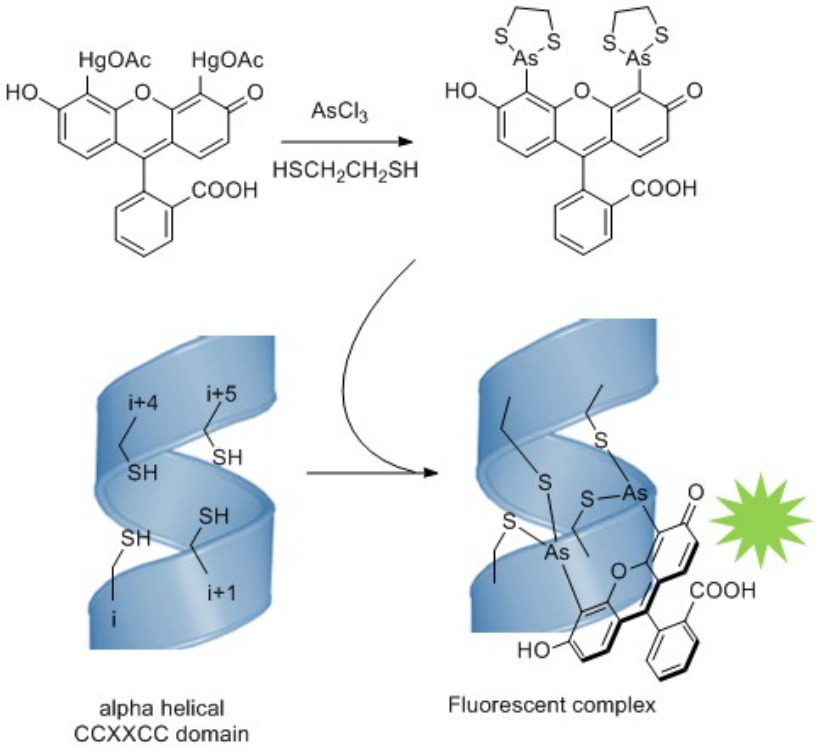

Figure 1.2 Fluorescent labelling of a specific recombinant protein molecule in live cells. One step synthesis of 4',5'-bis(1,3,2-dithioarsolan-2-yl)fluorescein (FLASH) followed by FLASH fluorescent labelling of a recombinant protein containing four cysteines at the i, i+1, i+4, and i+5 positions of an α helix (core motif CCXXCC) in living cells. Image reprinted and adapted with permission from reference[10], copyright (1998), Science.

Formally, bioorthogonal chemistry describes the subset of synthetic chemical reactions between chemospecific partners occurring in a biological environment without perturbation. The reaction must form (ligate) or break (cleave) stable covalent bond(s) between bioinert functional groups at physiological pH and temperature, with sufficient kinetic rate that the product is formed rapidly, even when reactants are present in low concentration.

Although the term for bioorthogonal chemistry was formally coined in 2003[11], the first truly biorthogonal ligation reaction proceeded it's definition. In 1986 Rideout and colleagues demonstrated that two biologically inert molecular building blocks (an aldehyde and a hydrazine) were capable of self-assembling into cytotoxic hydrazones *in vitro* by hydrazone condensation[12]. Later, Bertozzi delivered seminal work on the use of a Staudinger ligation between a biotin conjugated phosphine and a cell surface bound azido sialic acid to produce an aza-ylide biotin tagged cell surface adduct[11,13] (fig 1.3).

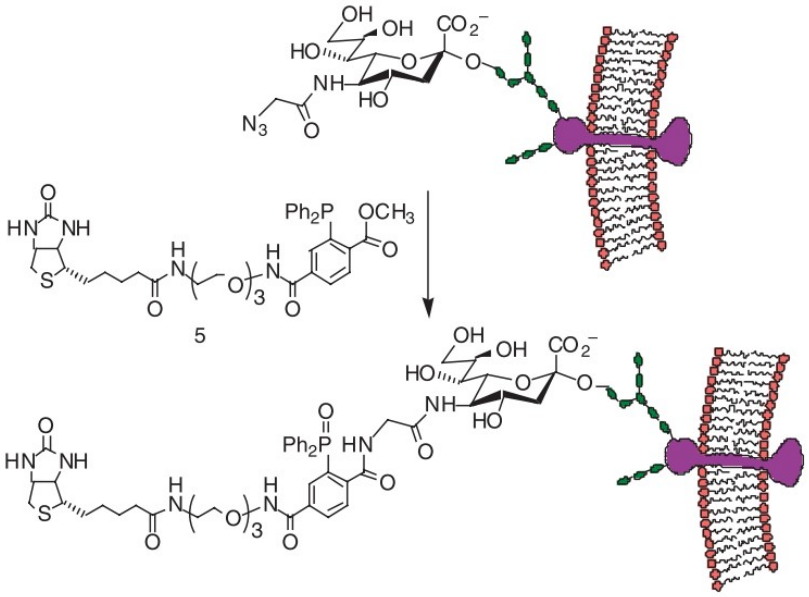

Figure 1.3 Staudinger Azide Ligation on cell surface. Bioorthogonal ligation reaction between a water-soluble biotinylated phosphine and a cell surface covalently bound azido sialic acid. The azido sialic acid was introduced onto a glycosylated protein (purple, green) on cellular surfaces (orange) by incubating Jurkat cells with *N*-azidoacetylmannosamine. Water-soluble biotinylated phosphine was added, and biotinylation was monitored by flow cytometry. Reprinted and adapted with permission from reference[13], copyright (2000) Science.

A range of ligation reactions have since developed to meet the strict definition of bioorthogonal chemistry (fig 1.4). Looking to overcome slow kinetics associated with Staudinger ligation chemistry, a Copper(Cu)(I)-catalyzed azide alkyne cycloaddition (CuAAC) 'click reaction' with fast reaction kinetics and non-toxic reaction partners was reported[14,15]. Cu(I) catalysts are limited however by cytotoxicity, and the reaction rate drops considerably when catalyst concentration is decreased. Three concerted strategies have been able to overcome this. First, libraries of Cu(I) stabilizing ligands have reduced cytotoxicity whilst boosting reactivity in living systems[16]. Second, different metal catalysts such as Palladium (Pd) and Ruthenium (Ru) and their associated ligands have been designed for bioorthogonal cross coupling and olefin metathesis reactions respectively[17]. Third, innovative 'metal-free' versions of click chemistry have made significant progress beyond CuAAC. The strain-promoted azide-alkyne cycloaddition (SPAAC)[18] and inverse electron-demand Diels-Alder (IED-DA)[19] reactions display superior biocompatibility and comparative reaction kinetics to metal catalysed equivalents. The field of bioorthogonal ligation has rapidly grown to include a diverse range of strategies including exotic strained, cyclic and 'traceless' (producing only gaseous by-products such as H_2O, N_2 or CO_2) reaction partners.

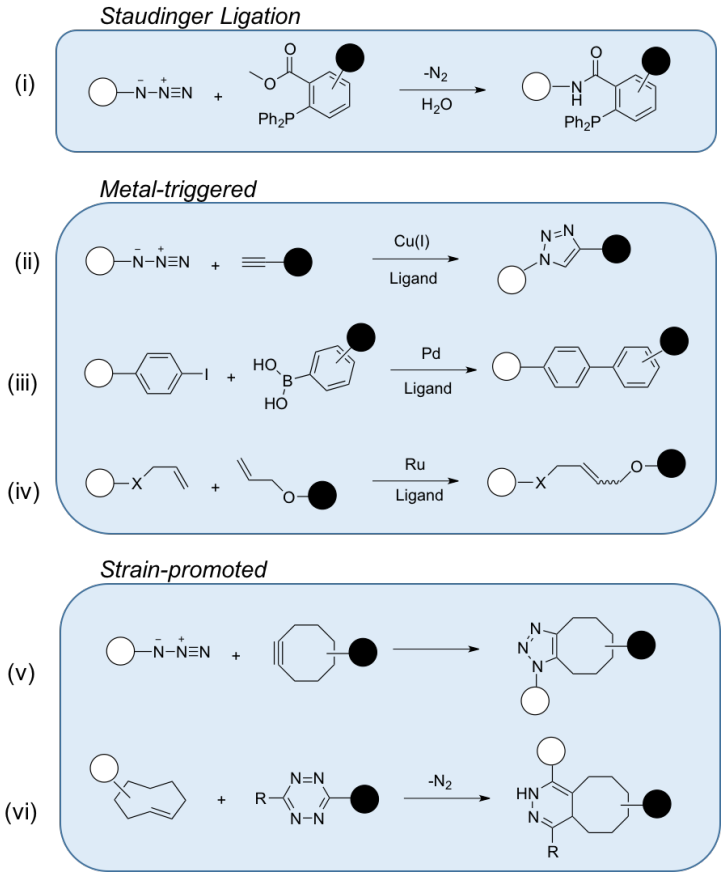

Figure 1.4 Bioorthogonal ligation reactions. A representative collection of three widely used bioorthogonal ligation strategies that have been developed over the last few decades including (i) prototypical **Staudinger ligation**; **Metal-triggered** (ii) copper-mediated azide-alkyne cycloaddition (CuAAC), (iii) palladium-mediated Suzuki cross-coupling, (iv) ruthenium-mediated olefin metathesis; and **Strain promoted** (v) azide-alkyne cycloaddition (SPAAC) and (vi) inverse electron-demand Diels-Alder reaction (IED-DA).

1.2 Bioorthogonal Cleavage Reactions in Biological Systems

Just as biorthogonal ligation was developed to overcome challenges in bioconjugation, biorthogonal cleavage reactions were conceived to improve molecular decaging reactions in living systems. Photo-decaging (or photo-deprotection) describes the selective cleavage of bioinert, Ultra Violet (UV)-sensitive functional groups by UV irradiation in biological systems. The *o*-nitrobenzylic derivative is a widely used photo-decaging group readily cleaved when irradiated by UV light. Time resolved spectroscopy has revealed that upon irradiation, hydrogen transfer from the *o*-alkyl substituent to the nitro group results in an *aci*-nitro tautomer in the ground state[20,21]. If a leaving group is attached at the benzylic position, aci-nitro intermediates will readily release the leaving group during flash photolysis. Originally

developed as a tool for organic synthesis[22], *o*-nitrobenzylic variants were first repurposed to 'cage' and release Adenosine Triphosphate (ATP) selectively in human red blood cells by Kaplan in 1978[23] (fig 1.5). The *o*-nitrobenzylic group remains a popular photo-decaging moiety.

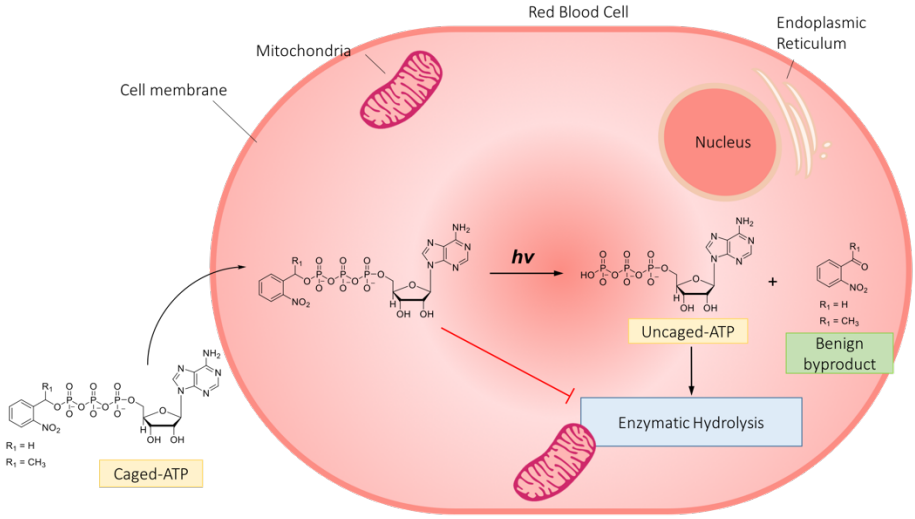

Figure 1.5 Prototype bioorthogonal cleavage: photolytic release of ATP in a human red blood cell. 2-nitrobenzyl phosphate and 1-(2-nitro)phenylethyl phosphate were attached to the terminal phosphate of adenosine 5-triphosphate. The 'caged-ATP' product was incorporated into resealed human red blood cells starved of ATP. Whilst the caged-ATP was unable to activate an ATP dependant Na:K pump, photolysis at 340 nm for 30 s liberated ATP to activate the pump. This figure illustrates the original strategy proposed by Kaplan et al. *Biochemistry* (1978)[23].

As a bond cleavage strategy, photo-decaging has a number of practical limitations for use in living systems. Nitrobenzylic caged compounds are readily metabolized by nitroreductases, an enzyme class conserved across mammalian and bacterial cells[24,25]. Whilst UV-triggered reactions are high yielding and rapid in controlled environments, sophisticated instrumentation limits the ability to develop high throughput or clinically relevant photo-decaging methodologies. Furthermore UV light has low penetrance and both the method of irradiation and the formation of nitrobenzylic by-products is perturbing to biology.

Seeking to overcome these problems, scientists have looked to small molecule reaction partners capable of controlled non-perturbing covalent bond cleavage in the living system. Taking photo-induced decaging as the prototype reaction, a number of small molecule

deprotection strategies have been advanced around freeing hydroxy and amine functional groups (fig 1.8).

As with bioorthogonal ligation chemistry, metal catalysts were first investigated to break chemical bonds in accordance with the stringent requirements imposed by bioorthogonal chemistry. Conceptually, metal based de-caging strategies pair tolerated metal catalyst species with protecting groups that are biologically inert and selectively cleavable with fast kinetics in homeostatic conditions. Allyloxycarbonyl (Alloc) and propargyloxycarbonyl (Poc) are standard protecting groups that are readily cleaved by a range of metal catalysts in peptide synthesis[26–28]. Furthermore, bioorthogonal ligation reactions regularly utilize both Alloc and Poc reaction handles, further evidence of their stability to enzymatic processing.

Encouraged by evidence that a Ru catalyst was capable of catalysing the allylation of thiols[29], a water soluble, cell permeating 'half-sandwich' type chelated Ru complex was reported to release amines from allylcarbamates under biocompatible conditions in cell culture[30]. Later, by modifying ligand design a new Ru catalyst emerged, capable of deprotecting allyloxycarbonyl bearing fluorescent probes and prodrugs with dramatically improved reactivity and reduced toxicity[31]. This proof of concept led to further investigation surrounding ligand design as a key factor for the performance and stability of bioorthogonal metal catalysts.

Shortly after, a Pd^0 catalyst was reported as being capable of deprotecting *O*-allyl carbamate protected fluorescein *in vivo*[32]. A separate heterogeneous Pd^0 catalyst capable of metal catalysed bioorthogonal cleavage was reported in 2011[33] (fig 1.6).

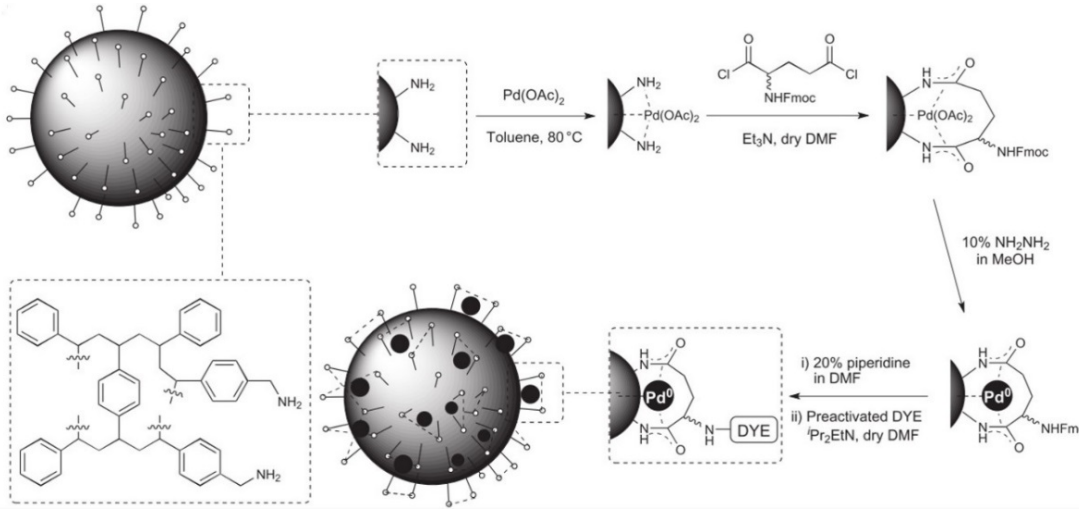

Figure 1.6 Synthesis of Pd^0 microspheres. Amino-functionalized polystyrene resin microspheres were treated with $Pd(Oac)_2$. Coordinated Pd^{2+} was subsequently trapped by crosslinking with the *bis* acid chloride of racemic Fmoc-glutamic acid (generated in situ). Hydrazine was used to reduce Pd^{2+} to Pd^0. Labelling of the Pd^0 microspheres was carried out by deprotection of the Fmoc group and subsequent treatment with an activated dye under basic conditions. Reprinted with permission from reference[33], copyright (2011), Nature Publishing Group.

By internalizing Pd^0 nanoparticles onto a solid support, the investigators reasoned that an 'artificial organelle' type catalyst could permeate target cells and preferentially accumulate a product within the cellular cytoplasm. The solid support would prevent Pd^0 nanoparticles from leaking into the surrounding environment by enhanced Pd^0 ligand stability. Following this, extracellular Pd functionalized devices were developed as implantable devices to deprotect prodrugs and probes in cell culture and *in vivo*[34].

More recently still, 'metal-free' catalysts capable of bioorthogonal cleavage without the presence of a metal have been investigated. Initially utilized for bond ligation, the inverse electron demand – Diels Alder (IED-DA) reaction product between a *trans*-cyclooct-2-ene (TCO) and a tetrazine was observed to readily undergo cycloaddition and tautomerisation to form a 1-4,dihydropyridazine product[19]. Evidence suggests that the 1-4,dihydropyridazine intermediate can further undergo base-promoted deprotonation with subsequent elimination of the carbamate group via pyridazine formation[35]. This observation lead to the development of a modified TCO bearing a carbamate-linked drug at the 2 position of the cyclooctene ring[36] (fig 1.7). When tetrazine is introduced, TCO would rapidly release drug via the IED-DA reaction.

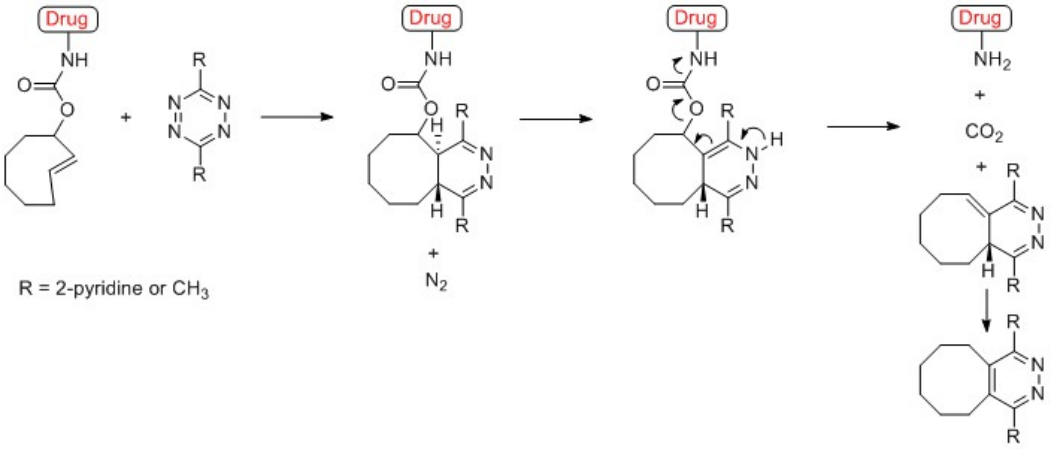

Figure 1.7 Tetrazine ligation to release drugs in living systems. Proposed IED-DA cycloaddition reaction between a strained *trans*-cyclooctene (TCO) and tetrazine releases N_2, resulting in a 4,5-dihydropyridazine intermediate that re-arranges through double bond shift, releases a leaving group at the vinylic position (in this case a carbamate), liberates an NH_2 bearing drug, CO_2 and 3-hydropyridazine which rearranges to the pyridazine byproduct. Reprinted and adapted with permission from reference[36], copyright (2013), Wiley-VCH Verlag GmbH & Co.

This modified IED-DA reaction, termed 'click and release', has been employed to release a TCO carbamate linked drug from an anti-tumour antibody drug conjugate (ADC) *in vitro* by simply adding tetrazine[36]. By replacing tetrazine with an aryl azide, the unstable cycloaddition product formed rapidly breaks down to an imine upon nitrogen release, which then hydrolyses to the aryl amine product. This strategy has selectively released an active compound *in vitro*[37]. As with bioorthogonal ligation partners, a range of cleavage reaction partners now exist. Bond breakage, including with metallic catalysts, non-metallic strained cyclic partners and traceless systems are now routinely utilized for selective chemical cleavage in living systems (fig 1.8).

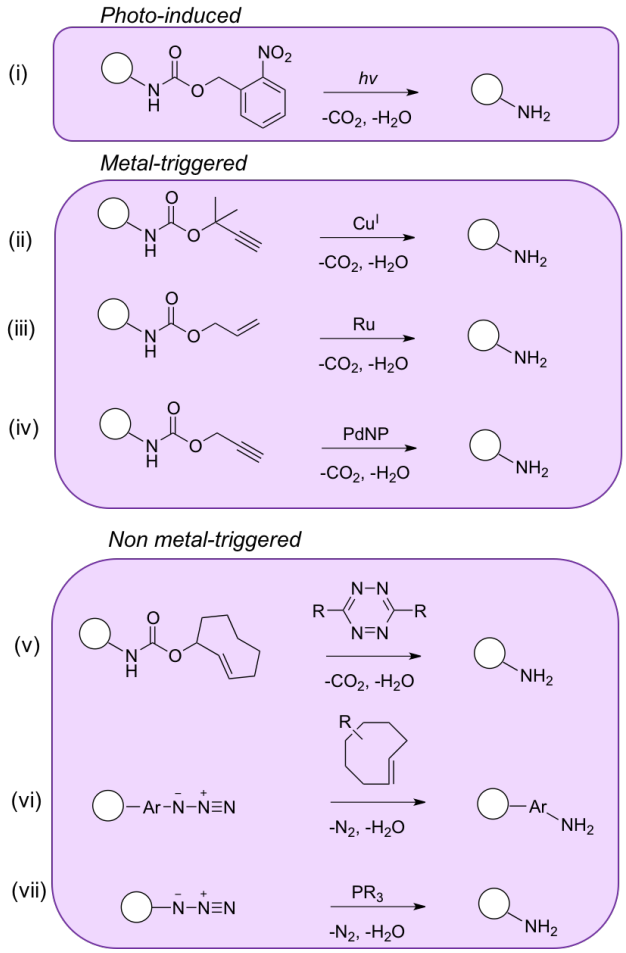

Figure 1.8 Bioorthogonal cleavage reactions to release amines. A representative collection of three widely used bioorthogonal cleavage strategies that have been developed over the last few decades to release amines, including (i) prototypical **Photo-induced** cleavage; **Metal-triggered** (ii) Copper(I)-induced removal of tertiary propargyl group, (iii) Ruthenium-induced deallylation, (iv) Palladium nanoparticle (PdNP)-induced depropargylation; and **Non metal-triggered** (v) IED-DA-induced 'click and release', (vi) strain-promoted trans-cyclooctene (TCO)-azide cycloaddition, also capable of releasing an R-NH_2 group at the TCO vinylic position (see fig 1.7), and (vii) the Staudinger reaction.

Bioorthogonal cleavage reactions are increasingly relevant for new targeting methods in medicine. The development of drugs and their excipient formulations has historically focused on modulating absorption, distribution, metabolism and excretion (ADME) properties to improve efficacy. Bioorthogonal cleavage reactions offer the added potential to modulate the activity of a drug proximal to its intended target by spatio-temporal control of molecule release in living systems. Much research in this field focuses on developing technologies capable of diagnosing, monitoring and treating disease, with a clear basis for use as a potential cancer therapy.

1.3 Cancer Therapy

Cancer is an amalgamation of diseases defined by specific neoplastic properties; namely self-sufficient growth, insensitivity to growth-inhibitory (antigrowth) signals, evasion of programmed cell death (apoptosis), limitless replicative potential, sustained angiogenesis, and tissue invasion and metastasis[38]. Prior to 1950, excision surgery was the only viable method of treatment routinely available to cancer patients. Radiation therapy alone or as an adjuvant became available in the 1960's, however neither surgery nor radiation was capable of treating metastasis, the primary cause of relapse, progression and death.

Since the discovery of nitrogen mustards and antifolate drugs in the 1940's, traditional chemotherapeutic agents have also developed as a mainstay in cancer treatment. Chemotherapy describes the various small molecules, biologics and immune-mediated therapies developed over the last 75 years to systemically treat the disease, where an administered therapeutic is carried by the bloodstream to act on cancer tissue irrespective of its position in the body. Treatments seek to exploit empirical and molecular pathway differences between healthy and malignant tissue to hinder cell neoplasticity; alone or in combination; as the first line of defence or in an adjuvant setting.

The first evidence that systemic drug administration could cause tumour regression was demonstrated by the use of nitrogen mustard on non-Hodgkin's lymphoma in the 1940s[39]. By studying the molecular mechanism of action, the same investigators deduced that nitrogen mustards induced apoptosis by alkylation mediated purine base cross linkage (fig 1.9).

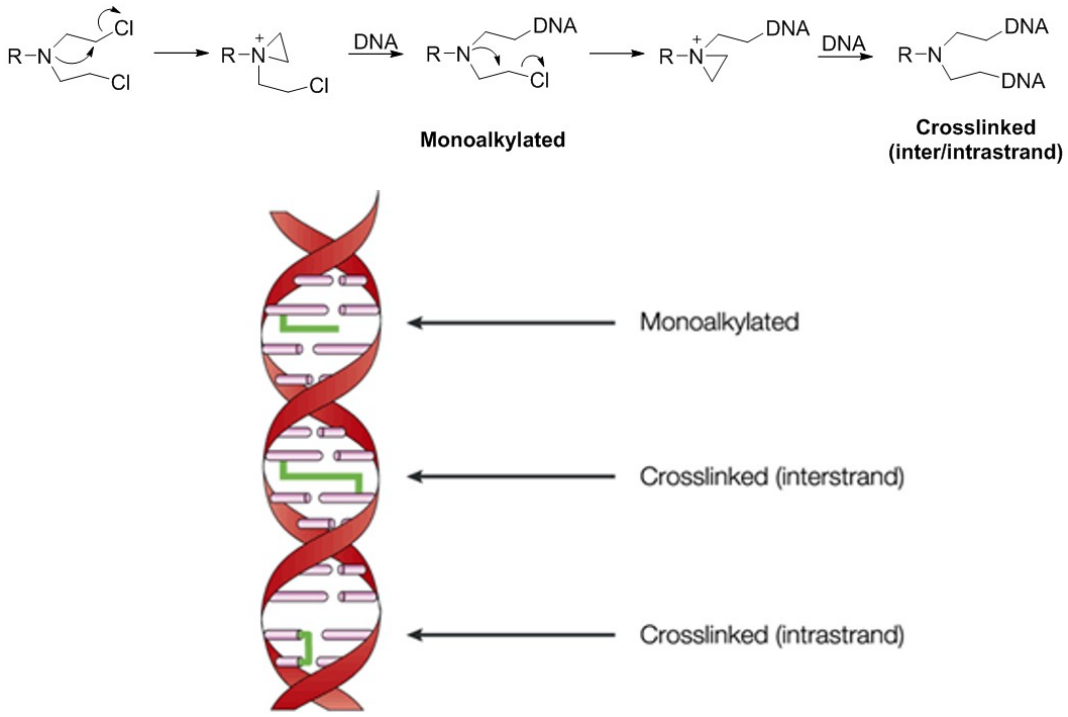

Figure 1.9 Schematic of DNA alkylating agents. Nitrogen mustard agents adduct to DNA through nucleophilic attack of the strained iminium ring system by Guanine. Resulting mono and di-alkylation (crosslinked) adduct to DNA triggers apoptosis. Figure reprinted and adapted with permission from reference[40], copyright (2002) Nature Publishing Group.

For the first time small molecules were shown to preferentially induce apoptosis in cancer cells over healthy cells by leveraging fundamental differences in tumour cell biology. Nitrogen mustards such as cyclophosphamide and chlorambucil are still routinely used to treat various tumours in combination with other therapeutics. Despite widespread use, cyclophosphamide alkylates DNA in healthy tissue, inducing severe side-effect to patients at therapeutically relevant doses. Cyclophosphamide induced side effects significantly increases the risk of treatment attributed patient death, limiting the maximum efficacious dosage[41,42].

A separate study during the same period correlated folic acid administration with cancer cell stimulation in acute lymphoblastic leukaemia (ALL) patients. This led to the development of the 'antifolate' class of chemotherapeutics; folate analogues capable of blocking enzymes that drive ALL proliferation. One such antifolate, methotrexate was observed to induce short periods of remission in patients, a key step that linked cancer progression in patients with the ability to disrupt critical proliferative pathways in cancer cells. Methotrexate reduces the level

of folate available to proliferating cells by competing with dihydrofolate at the active site of Dihydrofolate Reductase (DHFR)[43] (fig 1.10). Competitive inhibition of DHFR prevents the reduction of dihydrofolate to tetrahydrofolate[44]. Tetrahydrofolate is required as a co-factor for the enzyme Thymidine Synthase (TS) to methylate uracil to thymine, a key DNA building block in dividing cells[45]. By disrupting the conversion of uracil to thymine in rapidly dividing cell populations, growing DNA chains fragment after erroneous incorporation of uracil in the absence of thymine. DNA fragmentation then drives cellular apoptosis[46]. Currently, high dose methotrexate regimens in combination with toxicity limiting adjuncts treat a wide range of malignancies. Renal toxicity is a serious side-effect commonly associated with methotrexate treatment[47].

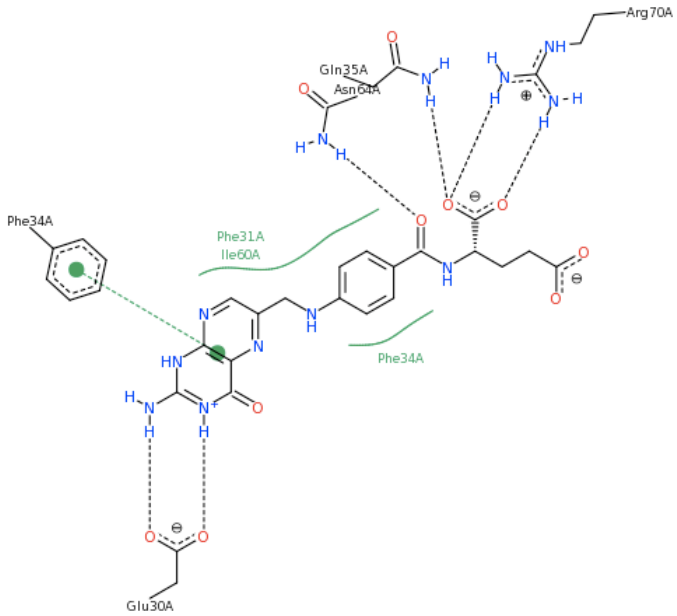

Figure 1.10 Dihydrofolate Reductase (DHFR) complexed with methotrexate. Methotrexate binds tightly to DHFR by mimicking the structure of folate. Key DHFR residues involved include pi-stacking between aromatic rings in methotrexate and Phe 31, Phe 34 as well as hydrogen bonding donation to Glu 30, Ile 60, Asn 64, Gln 35 and Arg 70. Figure reprinted from open source database Proteopedia (2011).

All chemotherapeutic agents exhibit side-effect by virtue of non-tumour specific activity. An entire field of medicine has been developed for treating chemotherapeutic derived toxicity, with many adjuncts administered alongside conventional chemotherapeutics to mitigate toxicity

burden to the patient. Chemotherapeutic side-effect has driven investigation of new classes of molecules capable of specifically targeting tumour cells.

Tumour cell biology understanding has advanced rapidly over the last 30 years. Key developments have elucidated cellular signalling networks underpinned by genetic and molecular differences between healthy and cancerous tissue. Some cancers have been stratified into specific disease subsets based on aberrant signalling pathways[48–51], prompting concerted efforts to develop 'targeted therapies' capable of repairing or blocking specific molecular aberrations. Tractable (treatable) molecular targets now include cell growth and repair factors, proliferation drivers, cell-cycle modulators and cell surface receptors. Key chemotherapeutic targeting therapies approaches include small molecule kinase inhibitors and immunotherapy. Each will be briefly detailed.

1.4 Small Molecule Kinase Inhibitors

The search for small molecule kinase inhibitors began in the early 1990s. Large combinatorial chemistry libraries underwent *in vitro* screens against cancer cell lines with known point mutations. Small molecule kinase inhibitors promised to turn cancer into a treatable chronic condition; eliminating cancer cells by binding with high affinity to aberrant kinases present in cancer tissue only. This would drive cancer cell specific apoptosis whilst reducing the off target toxicity burden associated with chemotherapy. Imatinib and Gefitinb are two landmark examples notable for their success in the clinic.

Imatinib is an inhibitor of BCR-ABL1 kinase. When the two independent genes Breakpoint Cluster Region (BCR) and Abelson murine leukaemia viral oncogene homolog 1 (ABL1) are erroneously fused during chromosomal translocation, the gene forms a protein product, BCR-ABL1 that drives cancer proliferation. As well as inhibiting BCR-ABL1, Imatinib also inhibits platelet-derived growth factor receptors (PDGFRs) and tyrosine-protein kinase Kit (KIT) proteins. PDGFR and KIT are also responsible for driving tumour proliferation in chronic myeloid leukaemia (CML) and gastrointestinal stromal tumour (GIST) patients[52]. Potent, orally

available and metabolically stable, Imatinib has achieved high remission rates amongst subsets of the CML patient population[53,54]. Whereas BCR-ABL1 fusion proteins are expressed uniquely in cancer cells, BCR, ABL, KIT and PDGFR are also independently expressed in normal cells where they modulate vascularization, typical injury and stress response pathways in healthy cardiac tissue[55,56]. As a result, cardiotoxicity is commonly observed in Imatinib treated patients[57]. Furthermore, approximately one in three patients will develop hematologic and cytogenetic resistance, rendering Imatinib ineffective within those patient subsets after initial treatment[58].

Gefitinib is an ATP binding site competitive inhibitor to epidermal growth factor receptor (EGFR). EGFR is a kinase that mediates cancer cell growth, proliferation, apoptosis invasion and metastasis[59]. EGFR over-expression is routinely detected in non-small cell lung cancer (NSCLC) resected primary tumours by immuno-histochemistry[60] and mRNA analysis[61], and a clear correlation exists between overexpression of EGFR and NSCLC progression[62]. By inhibiting EGFR, Gefitinib provides partial remission to roughly 10 % of NSCLC patients, reflecting of the difficulty of treating the disease.

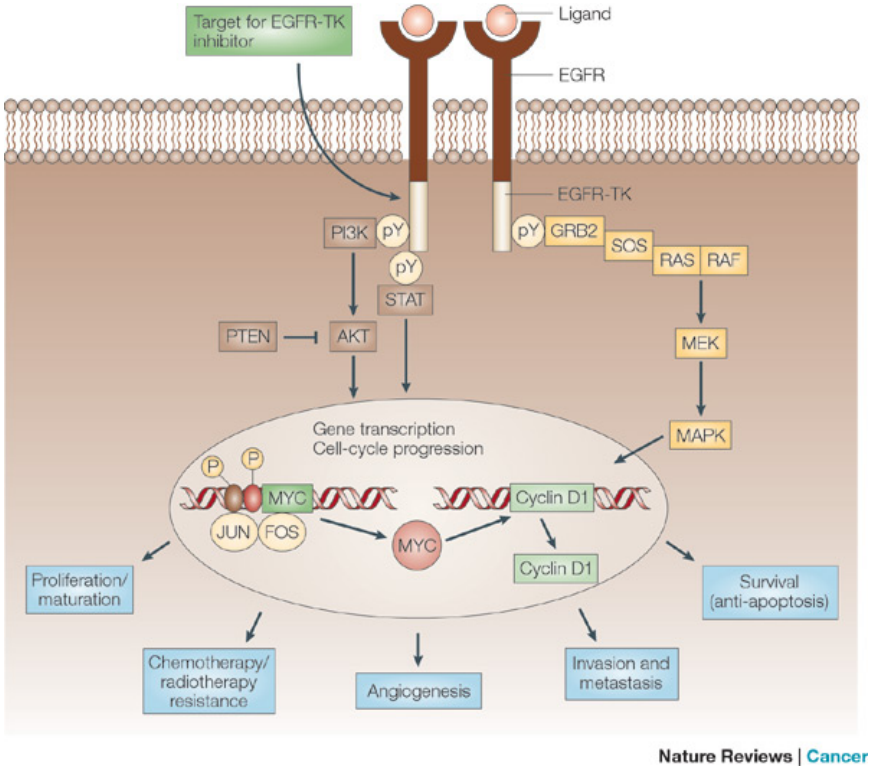

Figure 1.11 Effect of Gefitinib on the epidermal growth factor receptor (EGFR) signalling pathway. Ligand binding to EGFR extracellular domain triggers formation of homo- or heterodimeric complexes with HER family, causing autophosphorylation at the tyrosine (pY) residue. This leads to activation cascades across numerous cell signalling pathways. Two key pathways are shown. (Yellow boxes) GRB2 and SOS recruitment activates small G-proteins RAS and RAF, then MEK and MAPK. (Brown boxes) pY also activates PI3K and AKT which is the signal transducer and activator of STAT. Signal transduction to the nucleus in both pathways activates gene transcription factors MYC, JUN, FOS and Cyclin D1, inducing cancer proliferation pathways (blue boxes). Gefitinib inhibits the interaction between pY and the tyrosine kinase binding domain of EGFR, inhibiting EGFR and signal transduction. Figure reprinted with permission from reference[63], copyright (2004) Nature Publishing Group.

The unique clinical success of Imatinib, Gefitinib and others, coupled with improvements in genetic testing has markedly increased efforts to develop precision medicines over the last 20 years. As a result, a number of targeted therapeutics have been developed over the last decade to match with validated biological targets deemed crucial to tumour growth and metastasis. Despite this, accumulated evidence is beginning to push back on the assumption that targeted medicines will drive remission rates for many other indications as is observed in CML[64]. The survival and growth of heterogeneous cancer cell populations in different tissues may not be wholly contingent on the activity of a single molecular pathway. Targeted therapeutics will conform to the same principals and limitations existent in traditional therapies.

Recent empirical evidence from clinical trials matching precision medicine with traditional therapies has provided data to affirm this. The SHIVA trial[65] found that assigning treatment according to molecular profiling did not improve outcome, and conversely those administered targeting agents recorded more grade three-four adverse events. Another recent trial could only pair 6.4 % of 2,600 patients with a targeted therapy based on identifiable mutations[66]. A third could only pair 2.5 % of relapsed solid tumour and lymphoma patients with a targeted therapy[67]. Incidents of 'super-responders' continue to fuel enthusiasm about the potential of targeted therapeutics, and though individual cases are meaningful, these are rare events typically confined to very small patient subsets. Basic drug resistance pathways and toxicity induced side effects still drive the pursuit of enhanced treatment options.

1.5 Immunotherapy

Immunotherapy describes manipulation of the immune system to favour cell polarization states capable of eliciting a strong anticancer effect. The immune mediated anticancer effect is utilized by targeting specific surface antigens that trigger cancer cell death or killing. This effect was uncovered over a century ago in the 1890s[68]. By injecting patient tumours with dead bacterial cultures, Coley's toxin was capable of triggering a remarkable immune response that drove remission in sarcoma patients. The immunological effect caused by Coley's toxin is now mechanistically well understood.

Tumour-infiltrating leukocytes (including neutrophils, macrophages, T and B cells and Natural Killer (NK) cells) are first recruited to the site of injection. Bacterial cell surface antigens engage with and prime $CD4^+$ and $CD8^+$ T cells within the tumour[69] to drive inflammatory interleukin production[70], induce clonal T cell expansion and activate B cells[71]. This ultimately stimulates leukocyte mediated tumour cell targeting and elimination. This cascade of immune cell recruitment and activation still underpins the function of immuno-oncology drugs that harness

the immune-system to recognise, infiltrate and eliminate tumours. Recent treatment strategies, including the development of Chimeric Antigen Receptor-T cell (CAR-T) therapies and immune checkpoint inhibitors have reported high remission rates in previously relapsed treatment resistant indications[72].

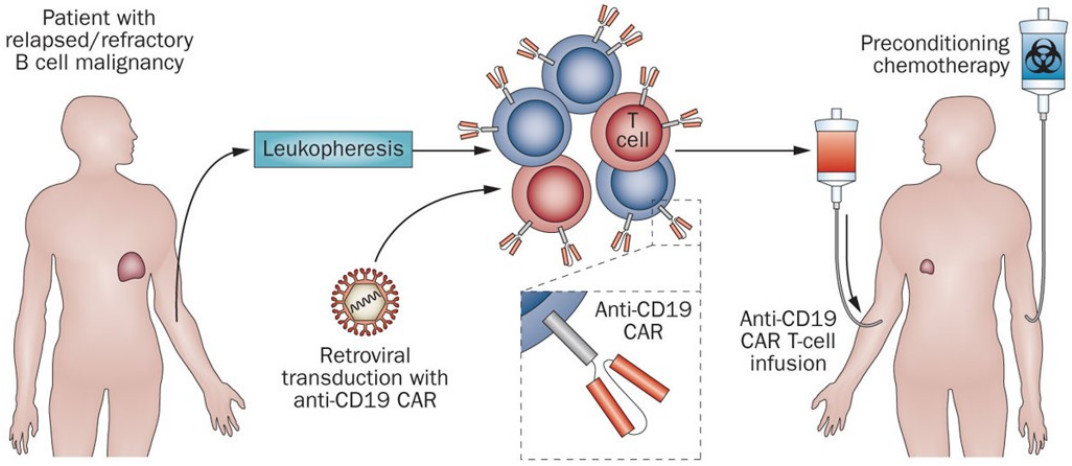

Figure 1.12 Treatment of patients with B-cell malignancies using anti-CD19 CAR-T cells. Patients with relapsed/refractory B-cell malignancies that express the CD19 cell-surface protein may be treated with anti-CD19 CAR-T therapy. Patient derived T cells are isolated to undergo adoptively transferred autologous genetic engineering by a retroviral anti-CD19 CAR vector. Engineered T cells are then infused back into the patient alongside chemotherapy to induce an immune mediated anti-CD19 cellular response. Figure reprinted with permission from reference[73], copyright (2014) Nature Publishing Group.

Now showing efficacy in some solid tumours, immunotherapy is positioned as the preeminent strategy for targeted cancer treatment. Despite new approvals for monoclonal antibodies in 2016, immunotherapy still faces significant hurdles. Reduced efficacy in low-immunogenic cancers[74] and tissues that cannot be targeted by immunotherapy (i.e. the brain), immune dependant side effects[75] and induced autoimmunity[76] restrict the relevance of immunotherapy to certain indications. Coupled with the high costs of manufacture and typically exorbitant prices of treatment, new ground breaking treatments in immunotherapy may only be applicable to small patient groups.

1.6 Prodrugs

Whereby targeted therapeutics are limited to small patient subsets, prodrug therapies leverage the demonstrated efficacy of already established chemotherapeutics. Prodrugs are derivatives of active drugs designed for selective activation. Activation may be via irradiative, enzymatic, or chemical action after prodrug administration, allowing for accumulation of the active drug at the site of interest. By careful selection of the masking group; enhanced adsorption, distribution, metabolism and excretion (ADME) properties of the prodrug may simultaneously improve physiochemical and pharmacokinetic properties of the parent drug alongside improved activity at the site of interest[77]. Thus a clear rationale exists for the use of prodrug therapy in cancer treatment.

Directed enzyme prodrug therapy (DEPT) first localizes an exogenous enzyme to the tumour site. Next a prodrug is administered where it is 'un-masked' in the presence of that exogenous enzyme or its products. Enzymatic prodrug activation requires that the exogenous enzyme is sufficiently accumulated only in tumour tissue to ensure high levels of selective drug activity. Genetic (GDEPT), viral-vector (VDEPT)[78], and antibody (ADEPT)[79] approaches (fig 1.13) have been utilized with varying success in isolated clinical trials.

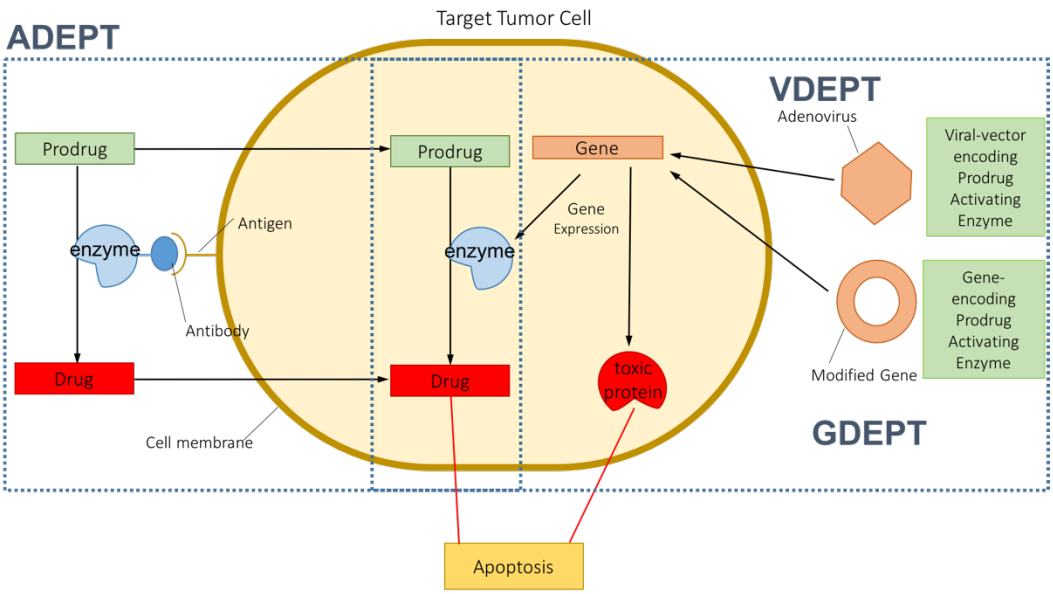

Figure 1.13 Overview of Directed Enzyme Prodrug Therapy (DEPT). ADEPT relies on the introduction and antibody directed localisation of exogenous enzymes to the target tissue to catalyse the activation of prodrugs to drugs in intra- or intercellular space. VDEPT and GDEPT introduces a synthetic gene into the target tissue which may directly encode a toxic protein, or an enzyme capable of activating a prodrug to a drug.

DEPT technology is intrinsically restricted by the effectiveness of exogenous enzymes to activate the prodrug[80]. This is a common limitation encountered by activation strategies that rely on enzymes for efficacy. As therapeutic advances continue to drive the search for safer, more efficacious treatments, new methodologies emerge as promising ways to control the release of cytotoxins in cancerous tissues.

1.7 BOOM Chemistry - Development and Current Advances

In 2011, *Yusop et al* described the development of heterogenous Pd^0 microspheres capable of deprotecting molecular probes in biocompatible conditions by allylcarbamate cleavage[33]. This catalytic system laid the groundwork for the use of Pd^0 beads to conduct inter/extracellular chemical reactions in cell assays[81]. Described as bioorthogonal organometallic (BOOM) chemistry, this cleavage concept is under investigation as a new potential for chemotherapeutic treatment. By postulating that a heterogenous Pd^0 source could affect localised bioorthogonal activation of Pd^0 labile prodrugs, the selective high concentration

release of drugs could be directed into cancer tissue. This approach would confer advantage over DEPT by removing reliance on enzymatic action to drive drug activation. Instead the site of activation would be determined by accurate surgical implantation of the Pd^0 device into a tumour (fig 1.14).

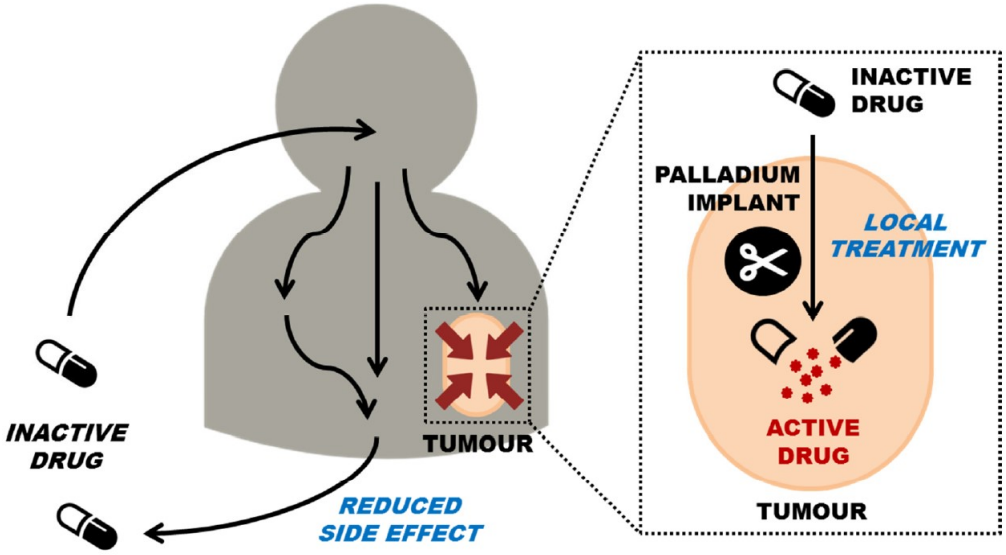

Figure 1.14 BOOM Chemotherapeutic Concept. A heterogeneous catalytic palladium implant is surgically inserted into patient tumour during standard intraoperative tumour resection treatment or during initial biopsy. Implant is benign and does not convey toxicity during essential post-operative wound healing. Pd^0 labile prodrugs would be systematically administered, where they are activated exclusively in the presence of the implant.

Theoretically a Pd^0 functionalised implant inserted into the tumour would activate drug at the site of interest on systemic administration of a Pd^0 labile prodrug. Drug activation in a biocompatible environment is solely dependent on the interaction between a Pd^0 source and the Pd^0 labile functional group masking the prodrug, and does not require further biotic or environmental stimulus to induce cell death. Therefore the BOOM chemotherapeutic concept most closely approximates a focalised chemotherapy and radiotherapy approach. Although a novel strategy, BOOM chemotherapy could be employed using established focal radiotherapy techniques, such as the two described below.

Brachytherapy is a radiotherapy focalised technique used in head and neck, prostate and cervical cancers[82]. Sealed radioisotope 'seeds' (notably including palladium ^{103}Pd) are surgically inserted by an implant gun into the tumour mass, which then induce cell death by emitting high energy short-range radiation to the surrounding tissue. Guided ultrasound allows for accurate positioning of the radioisotope seeds within the body to deliver optimal radiation doses across the entire tumour site whilst reducing damage to nearby healthy tissue and organs[83].

Implantable carmustine wafers (Gliadel®, BCNU) show efficacy as a focal therapy used in glioblastoma multiforme[84]. Wafers soaked in carmustine are placed on the tumour bed during intraoperative tumour resection, where they release carmustine to the surrounding tissue as a single dosed treatment over a five day period[85].

Both brachytherapy and wafer implantation suffer from wound healing complications post implantation. This is due to the uncontrolled 'ON' activation state of implants, inducing cytotoxicity to the surgical wound as well as cancer tissue immediately once inserted. Wound healing complications in both radioactive seed[86] and BCNU implants[87] cause more conservative dosing regiments, resulting in detrimental reduction in tumour ablation efficiency and also subsequent difficulties in reconstructing the excised area.

BOOM chemotherapy may resolve this complication. The Pd^0 implant can be inserted immediately into the tumour excision space after surgical resection. A brief uninterrupted period of essential wound healing takes place, and then the prodrug can be administered to drive a chemotherapeutic response. The catalytic nature of the activating device means that prodrugs can be repeatedly administered as many times as required. In addition, the therapeutic effect may be regulated by altering the type and dosage of BOOM activatable prodrug, a clinically desirable option during treatment.

1.8 Design of Bioorthogonal Pd^0 labile prodrugs

Several important design features are required for the development of palladium activatable cytotoxic prodrugs and the catalysts that activate them.

First, prodrugs should be designed with sufficient information about key functional groups responsible for eliciting biological effect. This information will allow the rational development of chemical 'masking groups' capable of employing a pharmacophoric blockade on the activity of the drug. **Second**, the masking group must be designed to simultaneously impart resistance to biological cleavage and lability in the presence of the palladium device. Improving the masking group by rational design will fine tune the extent of both bioorthogonality and Pd^0 activation. **Third**, whereby the drug itself undergoes metabolic conversion in the body to its active form (such as an antimetabolite), the prodrug must not competitively inhibit the enzymes that manage this conversion process; as this would limit the efficacy of ongoing treatment by saturating enzymes with inactive prodrug, preventing the accumulation of antimetabolites and repressing the cytotoxic effect associated. **Fourth**, the masking strategy should ideally reduce the cytotoxicity of the drug by at least 100 fold. **Fifth**, the conversion process between the Pd^0 device and the prodrug should liberate the active drug alongside non-toxic by-products, and do so in a way that allows for the repeated turnover of prodrug to drug without reducing the catalytic effect of the Pd^0 device. **Sixth**, the Pd^0 catalyst must be biocompatible, capable of repeated prodrug conversion and amenable to incorporation into a medical device capable of being implanted into a tumour. This suggests the use of a heterogeneous catalytic system.

Prior work in the Unciti-Broceta lab has made significant progress in each of these design considerations. Promoieties were developed to chemically mask key functional groups in four established chemotherapeutics (5-fluorouracil, Gemcitabine, FUdR and vorinostat), drastically reducing the cytotoxic effect of each drug in *in vitro* assays. Pd devices that were simple to synthesise, handle and modify were adapted from previous work to mediate deprotection *in vitro*[33]. Each of the chemotherapeutics was subsequently re-activated in the presence of the catalyst[34,88–90]. Preliminary *in vivo* work further validated the ability to selectively mask and

activate a chemotherapeutic drug in zebrafish[34,89]. Importantly this work proposed important considerations to guide the development of subsequent research in this field.

1.9 Aims: to advance BOOM chemotherapeutic approaches

Building on previous work, this thesis will advance the chemistry and biology of a prodrug chemotherapeutic strategy already validated in *in vitro* models for two chemotherapeutics. Exploratory research will improve the effect of the catalyst and develop novel protecting groups capable of improving both the bioorthogonality and Pd lability of the promoiety. These findings will be incorporated into a previously untested chemotherapeutic in order to further expand the applicability of the BOOM prodrug approach in cancer research. Specifically:

1. The lactam/lactim tautomery properties of 5-fluoruracil will be utilised to synthesise and test a novel *O*-alkylated prodrug capable of fast deprotection and tautomerisation to the active antimetabolite in biocompatible conditions.
2. Utilising self-immolative linker chemistry, a new promoiety will be developed and incorporated into gemcitabine as a series of *N*- and *O*- linked prodrugs capable of improved bioorthogonality and activation.
3. Findings from 2. will guide the development of a BOOM prodrug strategy in doxorubicin.
4. New Pd^0 devices will be investigated to improve aspects of BOOM activation *in vitro*.
5. A 3D cell culture assay will be designed and tested to validate the efficacy of doxorubicin prodrugs in a representative *in vivo* setting.
6. A zebrafish cardiac toxicity assay will be developed to study the effect of masking doxorubicin on cardiac tissue.
7. *in vivo* / *ex vivo* BOOM mouse models will be designed and tested using the best prodrugs developed in this thesis.

CHAPTER 2

A Prodrug of 5-Fluorouracil

The antimetabolite 5-fluoruracil will be investigated to develop optimised candidates of previously reported prodrugs sensitive to Pd-mediated activation. Prodrug design will focus on improving the physicochemical properties of the prodrug based on lactam/lactim tautomeric forms of the active drug. Analytical modalities will be investigated for their potential utility in future *in vivo* ADME studies.

2.1 5-fluorouracil Overview

5-fluorouracil (5FU) **1** is a fluorinated pyrimidine analogue of uracil, designed in the 1950's as one of the earliest antimetabolite anticancer compounds (fig. 2.1). Early studies in rat hepatomas suggested that the endogenous pyrimidine uracil was metabolised at a higher rate in cancer cells than in healthy tissue[91]. By chemically replacing the C5 hydrogen atom of uracil with a fluorine atom, 5FU was capable of eliciting selective cancer cell cytotoxicity via disruption of the upregulated anabolic uracil pathway; by conversion of 5FU into active metabolites capable of inhibiting biosynthesis and incorporating into essential macromolecules[92].

Initial tests demonstrated that 5FU was cytotoxic against numerous cancer cell lines *in vitro*[93], predicting broad efficacy in the treatment of cancer due to the increased demand for uracil in the macromolecule synthesis of all rapidly proliferating cells. 5FU is now routinely administered as a monotherapy or in combination across a range of cancers including pancreatic[94], stomach[95], breast[96] and head and neck[97]. The indication for which 5FU has had the greatest impact however is colorectal cancer, where 5FU is used as a frontline treatment in patients with stage III resected disease[98], a diagnosis that previously had no chemotherapeutic option.

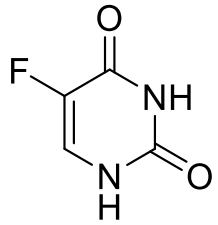

5-fluorouracil (5FU)
(1)

Figure 2.1. Structure of 5-fluorouracil.

5FU is administered by bolus injection, continuous infusion or oral administration during a dosing cycle with typical concentrations not exceeding 1000 mg/m^2 [99,100]. In addition, 5FU is administered as a topical treatment for eye[101] and skin[102] cancers. 5FU rapidly enters into the cell using the same facilitated transport mechanism as uracil[103]. 5FU simultaneously undergoes anabolic activation to its cytotoxic products and catabolic deactivation to inactive by-products via the same pathways as uracil. Accordingly, much of the study pertaining to the understanding of 5FU has focused on metabolic pathways that activate, deactivate or clear the drug from the body upon administration.

The availability of 5FU active metabolites to the tumour is dependent on the rate of drug catabolism. Early studies demonstrated that 5FU is catabolised, primarily in the liver, by dihydropyrimidine dehydrogenase (DPD) into 5,6-dihydrofluoruracil, and subsequently α-fluoro-β-ureido-propionic acid (FUPA) and α-fluoro-β-alanine (FBAL)[104]. This pathway rapidly removes 5FU, with the majority (~80 %) of the administered drug excreted as FBAL in urine within 24 hr[105]. An additional ~10 % of 5FU is directly excreted in urine as non-metabolised drug[106], leaving ~10 % of administered 5FU available to exert an antitumour effect.

Studies with a halogen analogue of 5FU, 5-Iodouracil (5IU) suggest that 5FU binds to the active site of DPD via numerous hydrogen bonding interactions. Coordination likely occurs between 5FU's C4-O atom and Asp 668/Asp 736, the N3 atom and Asp 736, the C2-O atom and Thr 737/Asp 609 and the N1 atom and Asp 609 within the active pocket of DPD[107] **(**fig

2.2**)**. This coordination complex then allows for the reduction of 5FU to 5,6-dihydrofluorouracil by a closely bound NADPH molecule in a catalytic fashion[108,109].

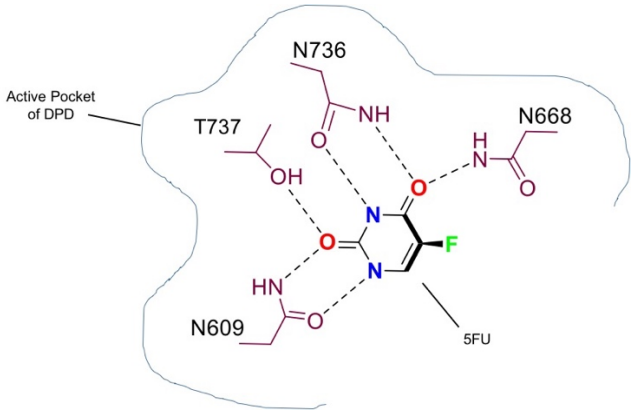

Figure 2.2 5-fluorouracil binds to Dihydropyrimidine Dehydrogenase via interaction with multiple amino acid residues. Proposed molecular interactions between 5FU and DPD amino acid residues within the active pocket of DPD based on 5-iodouracil crystal structure[110]. Predicted coordination occurs between active site amino acid residues Asp 668, Asp 736, Thr 737, Asp 609 and 5FU.

After catabolism and excretion, remaining bioavailable 5FU is preferentially accumulated into proliferating cells and converted through multiple intermediates into three active metabolites: fluorodeoxyuridine monophosphate (FdUMP), fluorodeoxyuridine triphosphate (FdUTP) and fluorouridine triphosphate (FUTP)[92].

The enzymes orotate phosphoribosyltransferase (OPRT), thymidine synthase (TS) and the sequential action of uridine phosphorylase (UP) and uridine kinase (UK) facilitate functionalisation of 5FU's N1 atom to synthesise downstream active metabolites[92,105,111]. During anabolism, 5FU's N3 atom is crucial for hydrogen bonding based enzyme recognition by Uridine Monophosphate (UMP) Synthase during nucleotidic synthesis[112]. FdUMP and FdUTP drive DNA damage by TS inhibition and direct incorporation respectively[113,114], while FUTP damages RNA molecules by direct incorporation[115,116]. Both pathways disrupt essential cellular function and drive apoptosis (fig 2.3).

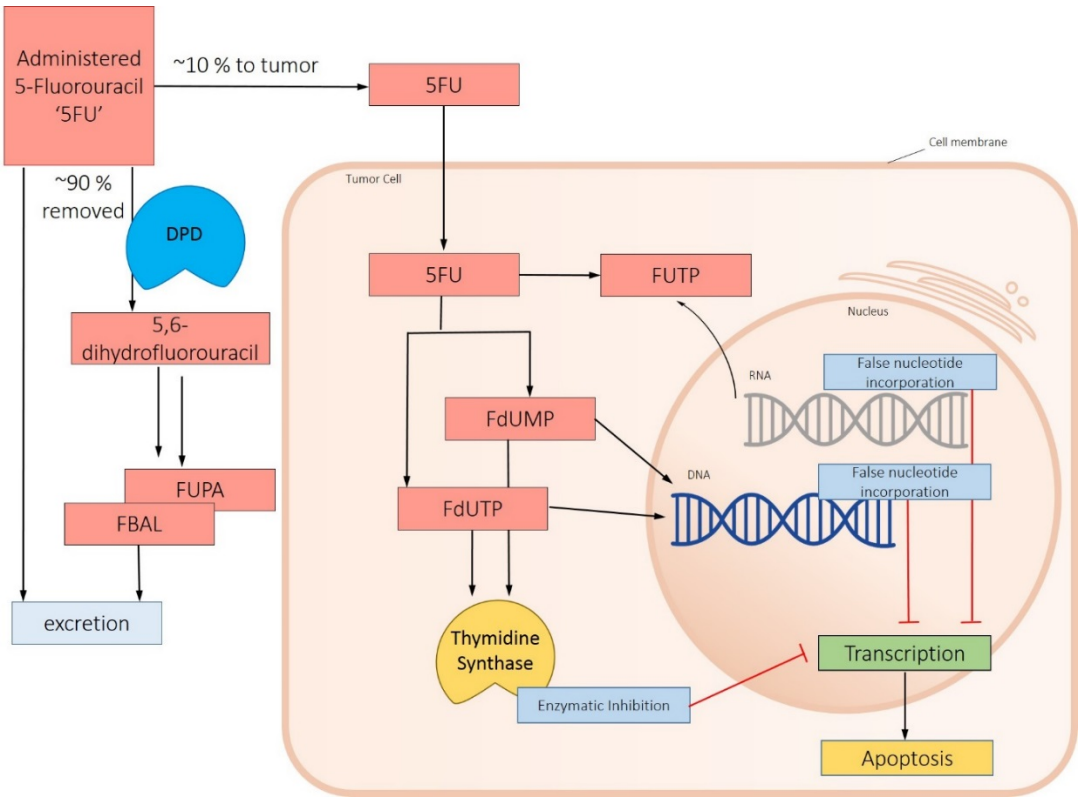

Figure 2.3 Cellular metabolism of 5-fluorouracil. Up to 90 % of administered 5-fluorouracil is catabolised to FUPA/FBAL and excreted, or excreted as the unmodified drug. The remaining ~10 % is available to accumulate in tumour cells where it is converted intracellularly into active metabolites: fluorodeoxyuridine monophosphate (FdUMP), fluorodeoxyuridine triphosphate (FdUTP) and fluorouridine triphosphate (FUTP), driving apoptosis via enzyme inhibition and DNA / RNA damage pathways.

As 5FU simultaneously undergoes multiple de-activating and activating pathways upon administration, accurately dosing the drug is a significant challenge. It is estimated that up to 80 % of patients receive non-optimal dosages of 5FU during routine treatment[117]. Dose limiting side effects such as myelosuppression and gastrointestinal toxicity events are commonly observed[118]. If prodrug design could mask 5FU from uncontrolled metabolic activation / deactivation on administration, a lower dosage of non-toxic prodrug would deliver significantly more 5FU directly to tumour tissue whilst reducing side-effects.

2.2 Current Progress with N-alkylated 5FU Prodrugs

Both endocyclic NH groups at the N1 and N3 positions have unusually low experimental pK_a values due to charge delocalisation across the pyrimidine π system arising from lactam

(keto)/lactim (enol) tautomerization[119] (scheme 2.4). Consequently, various N1 and / or N3 protected prodrugs of 5FU have been investigated[111,120], including from our laboratory[34,88].

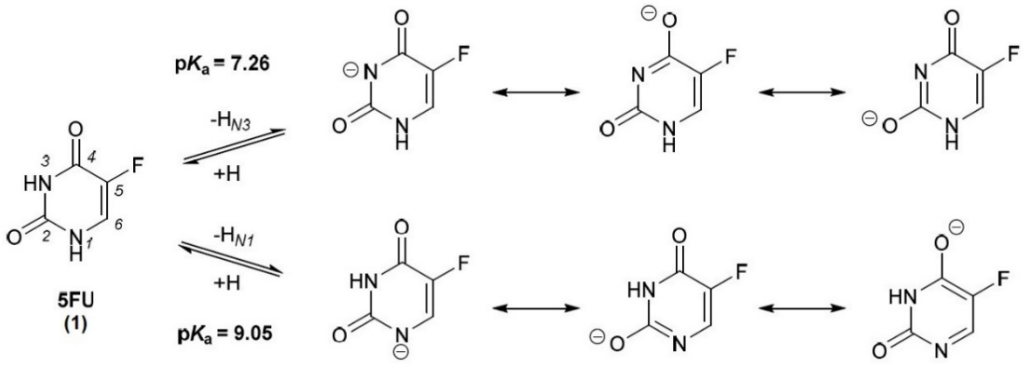

Scheme 2.4 5-fluorouracil conjugate bases. Negative charge delocalisation around the π system pyrimidine ring of 5-fluorouracil reduces the N1 and N3 experimental pK_a of 5FU

By alkylating the N1 and/or N3 position of the pyrimidine ring, we have previously deactivated 5FU using a protecting group that is both resistant to metabolic cleavage and exclusively labile to a Pd^0 source. Conversion to active drug occurs by Pd-mediated N-dealkylation in the presence of a Pd^0 catalyst in biocompatible conditions[34,88]. A semisynthetic strategy was previously used to synthesise allyl (All-), propargyl (Pro-) and benzyl (Bn-) N1 functionalised 5FU prodrugs in a one-step reaction (scheme 2.5).

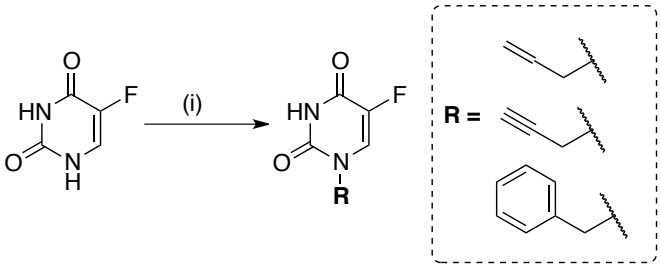

Scheme 2.5 Synthesis of N1 alkylated 5-fluorouracil prodrugs. Reagents and conditions: (i) DBU (1.2 equiv.), DMF, alkylbromide (1 equiv.), 4 °C, then RT overnight (31-40%).

N1 protected Pro-5FU was progressed as the only candidate that displayed excellent bioorthogonality ([EC_{50} (Pro-5FU) / EC_{50} (5FU)] > 500 – 700 fold reduction) and 100 % Pd-mediated conversion to 5FU after 24 hr. As the N3 position of 5FU has a lower pK_a than the

N1 position, it was predicted that an N3-alkylated 5FU would improve upon the reaction kinetics of Pd-mediated cleavage. N3 and N1,N3-*bis*-alkylated 5FU prodrugs were synthesised and tested *in vitro* for biocompatibility and Pd^0 activation, however, the conversion of N3-monoalkylated 5FU prodrug was incomplete after 24 hr, with only 26 % of an N1,N3-*bis*-alkylated 5FU prodrug converted to active 5FU in the same time period. Further investigation is required to develop an optimized Pd^0 labile prodrug of 5FU with improved kinetic reactivity.

An ideal prodrug of 5FU would retain rapid conversion to 5FU whilst removing NH bonding recognition at both N1 and N3 positions. By modifying the electronic configuration of 5FU's pyrimidine ring, a new prodrug may improve the kinetic rate of Pd-mediated dealkylation with increased lipophilicity and retained metabolic stability. More lipophilic prodrugs could be more rapidly absorbed into the Pd^0 bead, itself a hydrophobic resin, to affect faster catalytic cleavage and release of the polar 5FU product.

Rapid uptake and deprotection of prodrug by an intratumoural Pd^0 implant would be expected to increase the quantity of 5FU delivered locally to proliferating cancer cells. Therefore we expect a more lipophilic prodrug of 5FU to improve the dose efficiency and rate of catalytic conversion in a clinical model of activation. Accordingly, we set about to develop a new bioorthogonal 5FU prodrug that would:

(1) retain excellent bioorthogonality characteristics across all cell lines investigated
(2) improve lipophilicity by modification of the electronic structure of 5FU
(3) increase stability against DPD catabolic activity
(4) increase the rate of conversion to 5FU with respect to the N1,N3-*bis*-propargylated 5FU prodrug

2.3 Design and Synthesis of a Novel O-propargylated 5FU prodrug

Inspired by the tautomeric resonance forms of 5FU at physiological pH, we considered a trapped lactim-type prodrug of 5FU that would reconvert to the parent 5FU lactam form upon Pd^0 mediated cleavage (fig 2.6).

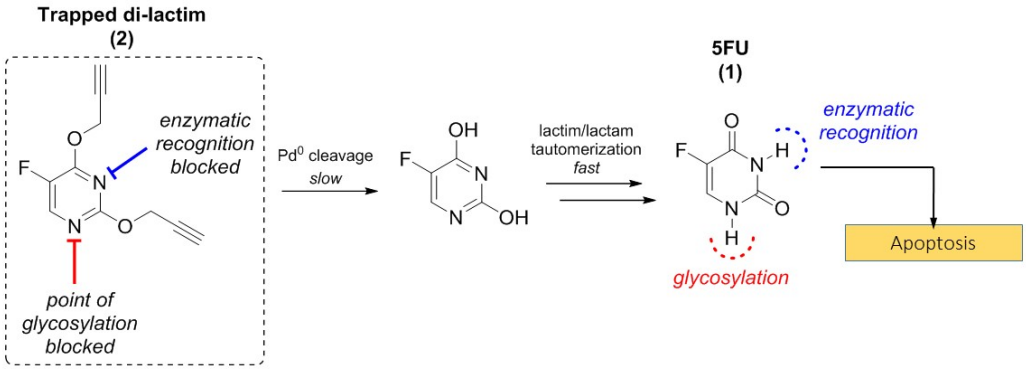

Figure 2.6 Development of a trapped di-lactim analogue of 5FU. By *bis*-O-propargylating 5FU, NH bonding interactions are removed. Pd-mediated conversion of the lactim product would rapidly undergo tautomerization to active 5FU, re-establishing the cytotoxic effect

The trapped lactim form would impose aromatic restriction to the pyrimidine ring by converting the endocyclic –NH- groups into =N-. 2,4-*bis*-propargyloxy 5-fluoropyrimidine **2** would block enzymatic interaction at N1 and N3, preventing critical NH hydrogen bonding interactions that facilitate enzymatic recognition and metabolism of 5FU. When incubated in the presence of Pd^0 it is expected that propargyl bond cleavage would produce the lactim form of 5FU, which then rapidly undergoes tautomerization to the parent drug in biocompatible conditions (i.e. at pH 7.4). Computational predictions show that O-alkylated prodrugs of 5FU display a higher clogP than N-alkylated prodrugs (fig 2.7).

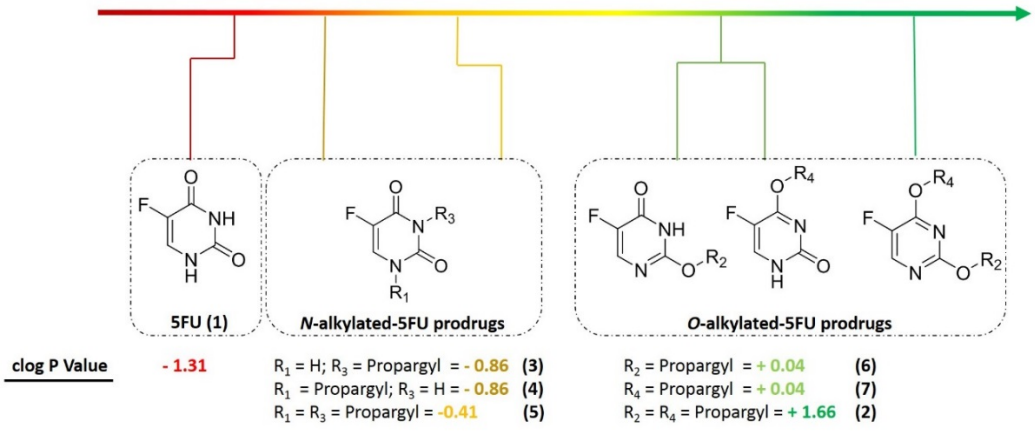

Figure 2.7. Experimental clogP of 5FU and 5FU prodrugs. Whereas N-alkylated prodrugs of 5FU have low clog P values, O-propargylated 5FU prodrugs are increased, increasing the amenability to oral bioavailability.

2 has a clogP of 1.66, an order of magnitude higher than either N1 and/or N3 functionalised 5FU prodrugs and indicating enhanced lipophilicity. It is important to note that drug candidates with logP values between 2 and 3 are generally considered to be orally available[121,122], and are likely to achieve the right balance between permeability and first-pass elimination during systemic administration.

2 was synthesised in a one-step synthetic strategy (scheme 2.8). 2,4-dichloro-5-fluoropyrimidine **8** was reacted with two equivalents of propargyl alcohol and NaH in THF to afford the diprotected product in moderate yield.

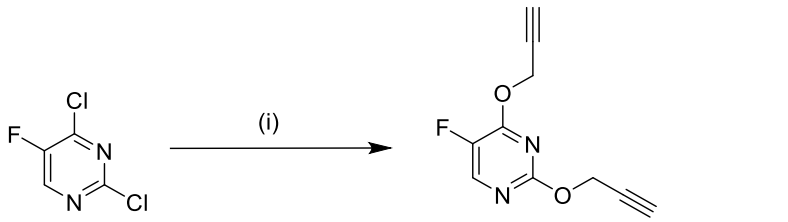

(8)

2,4-*bis*-propargyloxy-5-fluoropyrimidine (2)

Scheme 2.8 Synthesis of 5FU prodrug 2. Reagents and conditions (i) propargyl alcohol (2 equiv.), NaH (2 equiv.), THF, rt overnight (36 %)

Attempts to synthesise mono-alkylated derivatives **6** and **7** were unsuccessful. Two strategies are described (scheme 2.9)(scheme 2.10). 2-Chloro-4-(2-propargyloxy)pyrimidine **9** was isolated as the major byproduct of the reaction affording **2**. This product was synthesised in higher yield by repeating this reaction with one equivalent of propargyl alcohol and NaH. Mixing **9** together with various alkali hydroxides in a range of conditions failed to affect hydroxy substitution of the Cl atom at the C2 position (scheme 2.9).

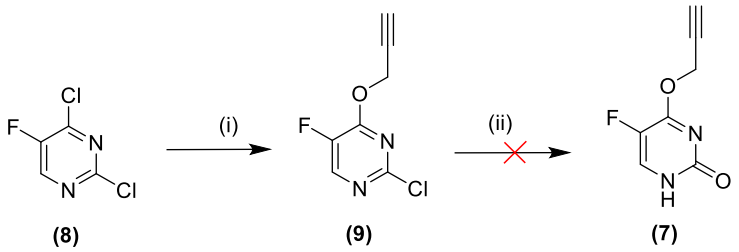

(8) (9) (7)

Scheme 2.9 1st Attempted synthesis of O-monoalkylated propargyloxy-5-fluorouracil prodrug 7. Reagents and conditions (i) propargyl alcohol (1 equiv.), NaH (1 equiv.), THF, rt overnight (50 %) (ii) alkali hydroxides: (NaOH, KOH) (1 equiv. → excess), solvents: (H_2O, MeCN, THF, MeOH or neat), variable time, heat, pressure, atmosphere.

A separate methodology was next developed to attempt synthesis of monoalkylated prodrugs directly from 5FU (scheme 2.10). First 5FU was mono-benzoylated at the N1- or N3-position. N1- benzoylation product **10** retains lactim/lactam tautomerization at the N3- site, whilst N3-benzoylation product **11** retains N1 tautomerization; each potentially allowing the distal oxygen atom to act as a nucleophile during subsequent alkylation reactions, as reported by Ludek[123,124] and others[125–127]. 1-benzoyl-5-fluorouracil **10** was prepared by stirring one equivalent of aryl acid chloride into a pre-mixed solution of one equivalent of 5FU and one equivalent of potassium hydroxide[128,129]. 3-benzyl-5-fluorouracil **11** was prepared by adding three equivalents of the aryl chloride to one equivalent of 5FU, then treating with water and concentrated HCl[129].

Mitsunobu chemistry has synthesised carbocyclic pyrimidine nucleosides from N3 benzoylated thymine starting material, with 2-alkyloxy by-products isolated during this reaction[123,125–127]. Whilst the mechanism for selective N vs O alkylation is unknown, N or O alkylation products could be selected for by altering reagents and conditions used during the Mitsunobu reaction; specifically by changing the coupling reagent[126], N3-protecting group or solvent[124]. For example, N3-benzoylated thymine and cyclopentanol treated with DIAD and PPh_3 in THF has been reported to afford the 2-alkyloxy product in a 34 % yield[124].

Accordingly we predicted that treating **10** or **11** with propargyl alcohol, DIAD, PPh_3 and THF would produce a mixture of N1/O2 alkylated products **14** and **15** or N3/O4 alkylated products **12** and **13** respectively. N- and O- alkylated products could be separated by standard

chromatography then treated with ammonia in methanol to cleave the benzoyl group and afford final products **6** or **7** (scheme 2.10).

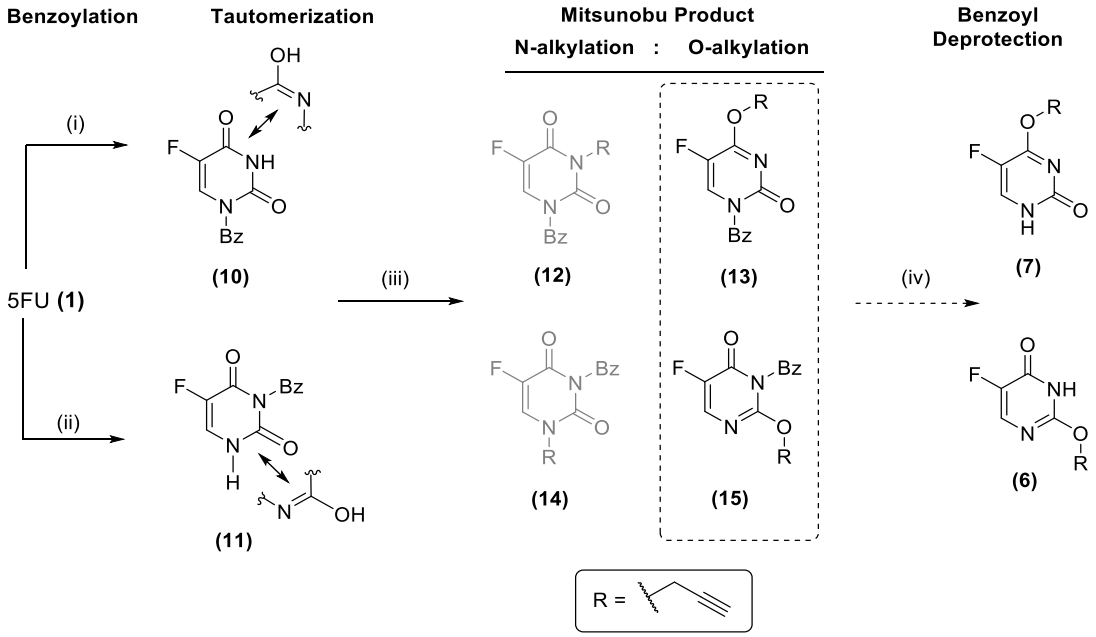

Scheme 2.10 2nd Attempted synthesis: O-monoalkylated propargyloxy-5-fluorouracil prodrugs: O vs N Alkylation of 5FU derivatives. Reagents and Conditions: (i) KOH (1 equiv.), benzyl chloroformate (1 equiv.), MeOH, MeCN, 0 °C → rt, 3 hr (19.2 %) (ii) pyridine (2.25 equiv.), BnCl (2 equiv.), MeCN, N_2, 0 °C → rt, 48 hr then in air at rt: K_2CO_3 (0.5 M), conc. acetic acid, $NaHCO_3$, 0 °C → rt, 1 hr (25.8 %) (iii) Ph_3P and DIAD (2.5 equiv.) added to propargyl alcohol (1 equiv.) and **10** or **11** in N_2, -78 °C, 24 hr. (iv) 7N NH_3 in MeOH

Unfortunately only N-alkylated products **12** and **14** were isolated from separate Mitsunobu reactions, confirmed by 2D NMR. The unexpected difficulty associated with synthesising mono-O-alkylated 5FU prodrugs **6** and **7** meant that only compound **2** was progressed into *in vitro* studies.

2.4 5FU Novel Prodrug Biocompatibility Assays

5FU is a widely utilized chemotherapeutic agent deployed against multiple indications, including in pancreatic cancer as a combination therapy and colorectal cancer as a frontline therapy. Therefore pancreatic (BxPC-3) and colorectal (HCT116) cancer cells were chosen to test the bioorthogonality of the novel prodrug **2**. Although 5FU was cytotoxic in both cell lines, **2** completely unaffected cell viability, even at 100 μM (fig 2.11). As expected, a trapped lactim prodrug was at least as biocompatible as previously synthesised N-alkylated prodrugs[34,88].

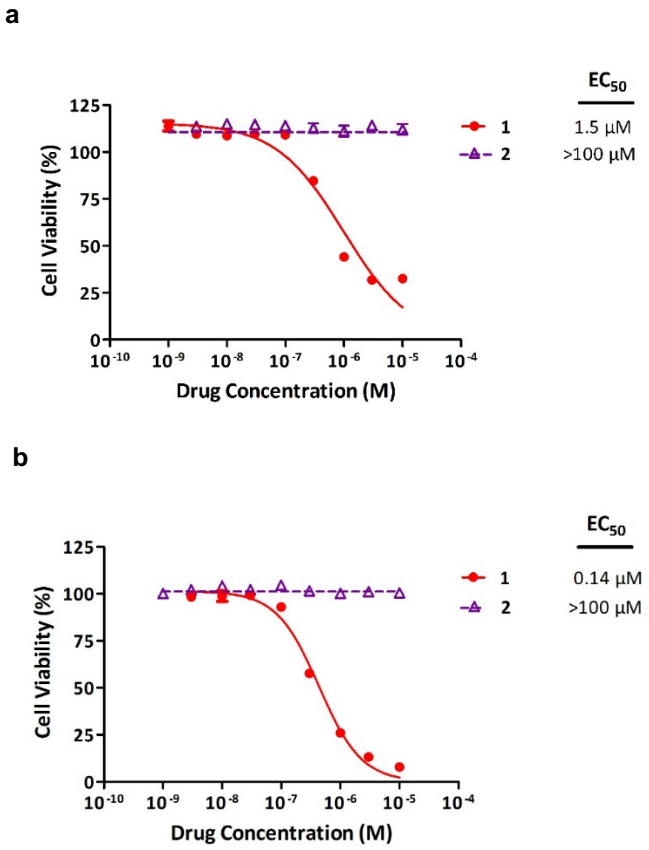

Figure 2.11 Study of 5-fluorouracil cytotoxic reduction produced by prodrug 2 in cell culture. Semilog dose − response curves and calculated EC_{50} values of **2** (dashed-purple) in comparison to unmodified **1** (solid-red) in (**a**) HCT116 cells and (**b**) BxPC-3 cells. Cell viability was measured at day 5 using PrestoBlue® reagent. Error bars: ± SD from *n* = 3

2.5 Pd-mediated 5FU Prodrug *in vitro* Conversion Study

Our lab explores the reactivity between Pd^0-functionalised devices and Pd-labile chemotherapeutic prodrugs. Previous reports have utilised a 130 µm sized Pd^0 functionalised bead catalyst de-protect prodrugs in biology[34,88,89,130,131]. This device will be utilised for Pd-mediated activation studied herein. The Pd^0 device is described in more detail in Section 4.6.

As **2** was completely non-toxic when incubated in cell culture, we investigated the sensitivity of the trapped lactam prodrug to Pd-mediated catalysis by UPLC. Initially the signal corresponding to reactants and expected prodrugs was obtained by incubating a 100 µM solution of prodrug or drug in PBS (1 mL) with a thermomixer at 1400 rpm, 37 °C. Aliquots

collected after 24 hr incubation were analysed by UPLC (fig 2.12) using a UV detector that removed the interference of salts to the signal.

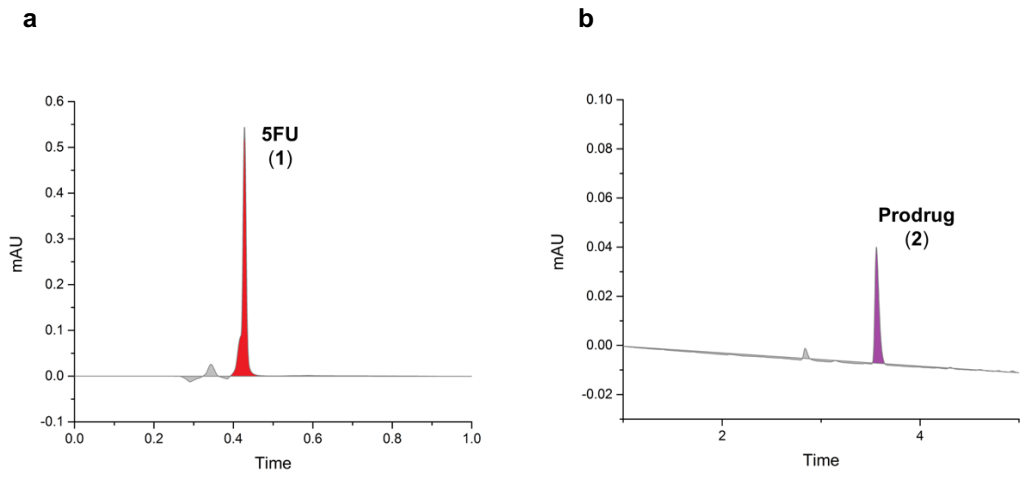

Figure 2.12 Non-biological stability assay of 5FU prodrug 2. UPLC chromatograms of (**a**) 5FU (**1**) (red) and (**b**) Prodrug (**2**) (purple) as 100 μM solutions in PBS incubated at 1400 rpm, 37 °C for 24 hr in a thermomixer. UPLC experiment was conducted with flow rate 0.4 mL / min. A = Water + 0.1 % TFA, B = Acetonitrile. Method 0 min = A:95 / B:5, 8 min = A:20 / B:80, 8.5 min = A:95 / B:5

Notably 5FU is a very polar small molecule that elutes early from the only UPLC column available for this experiment. This caused partial overlap between the peak corresponding to 5FU and the signal corresponding to general sample injection, though separation of these peaks was evident from the zoomed in image in figure 2.12 during the first min of elution time. Altering the eluent polarity (MeCN 90 – 99 %) and modifier (+/- TFA) was unable to shift the 5FU peak towards a later elution time. Furthermore, **2** gave a very weak signal despite incubating equimolar quantities of 5FU and **2** in each experiment, possibly indicating lower UV activity at 254 nm. Despite this challenge, repeated experimentation confirmed the elution of 5FU and **2** (**1** = 0.42 min), (**2** = 3.59 min). This suggested that **2** would be stable in biocompatible conditions over 24 hr in the absence of Pd^0 beads (fig 2.12).

Next, **2** was incubated in a thermomixer at 1400 rpm, 37 °C for 3, 9, 24 and 48 hr with 1 mg / mL of Pd^0 beads in 1 mL of PBS (fig 2.12). Significant generation of 5FU was observed after only 3 hr, with sustained production of the drug during a 48 hr period. Complete disappearance

of the peak corresponding to **2** at 3 hr suggests that the prodrug is rapidly "sequestered" by Pd^0 beads and gradually converted into the active drug that is then released into solution over time.

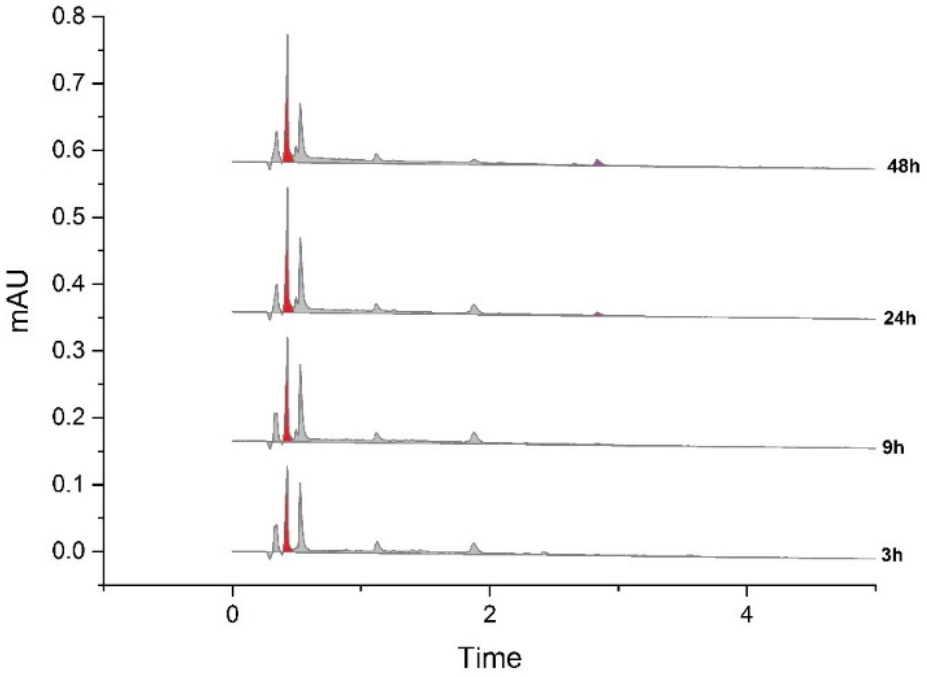

Figure 2.13 Non-biological Pd^0 conversion assay with 5FU prodrug 2. UPLC chromatogram runs over 5 minutes producing 5FU (red) from **2** (purple) as 100 µM solutions in PBS incubated with 1 mg / mL of Pd^0 beads at 1400 rpm, 37 °C for 3, 9, 24 and 48 hr in a thermomixer. UPLC experiment was conducted with flow rate 0.4 mL / min. A = Water + 0.1 % TFA, B = Acetonitrile. Method 0 min = A:95 / B:5, 8 min = A:20 / B:80, 8.5 min = A:95 / B:5. Impurities consistent with the signal produced from injection (at t = 0.25 min) and background are presented in light grey.

2.6 5FU Prodrug Biological Conversion Assay in Combination with Pd^0

2 was next assessed for BOOM activation in cell culture. Pd^0 beads, **2** or a combination of both were initially evaluated in BxPC3 cells and HCT116 cells at 1 µM and 3 µM concentrations respectively. The combination of **2** and Pd^0 beads displayed a significant cytotoxic effect across both cell lines. Neither **2** nor Pd^0 beads individually affected cell viability. This confirmed the ability of Pd^0 beads to release 5FU from the trapped lactim analogue **2** and produce a cytotoxic effect.

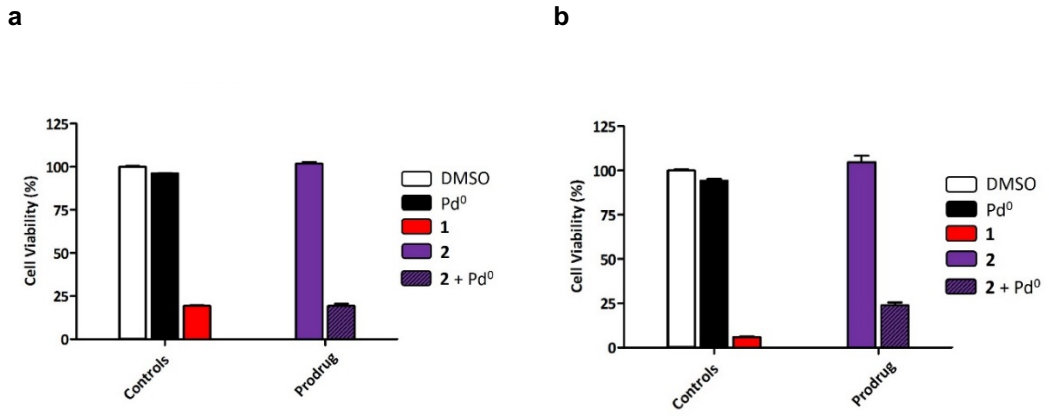

Figure 2.14 Preliminary Pd-mediated activation assay to compare activity of 5FU prodrug 2 against drug. Experiments: 0.1 % (v/v) DMSO (untreated cell control, white); 1 mg / mL of Pd^0 beads (negative control, black); 5FU (positive control, red); **2** (negative control, solid purple); and 1 mg / mL of Pd^0 beads + **2** (BOOM activation, striped purple). (**a**) BxPC3 pancreatic cancer cells incubated at 1 μM drug / prodrug, (**b**) HCT116 colorectal cancer cells incubated at 3 μM drug / prodrug. Cell viability was measured at day 5 using PrestoBlue® reagent. Error bars: ± SD from *n* = 3.

This initial BOOM activation study was expanded to test the prodrug across a concentration range (0.03 – 3 μM for BxPC3 cells), (0.3 – 30 μM for HCT116 cells) in combination with Pd^0 beads. (fig 2.15). DMSO is used as standard control vehicle for drug or prodrug in all experiments throughout this thesis. 0.1 % (v/v) DMSO is accepted as a concentration that does not accept cell viability during in vitro testing.

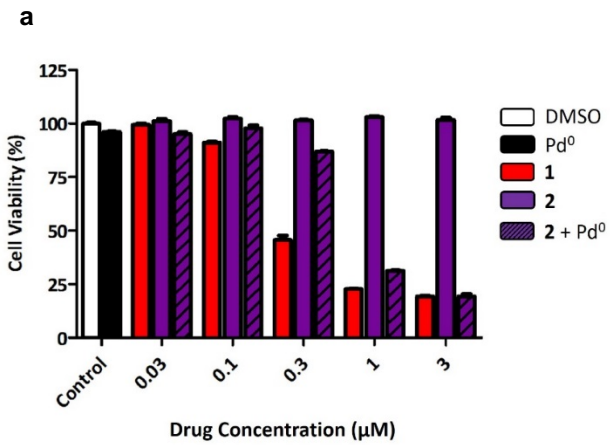

b

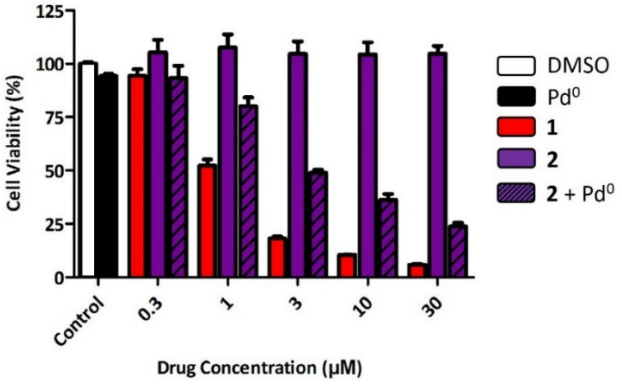

Figure 2.15 Pd-mediated activation of 5FU prodrug 2 in BxPC3 and HCT116 cell culture. Toxigenic effect of bioorthogonally activated 5FU prodrug across a concentration window in (**a**) BxPC3 and (**b**) HCT116 cells. Experiments: 0.1% (v/v) DMSO (untreated cell control, white); 1 mg / mL of Pd^0 beads (negative control, black); 5FU (positive control, red); **2** (purple); **2** + Pd^0 beads (striped purple). Drug and Prodrug concentrations 0.03 – 3 μM (BxPC3 cells), 0.3 – 30 μM HCT116 cells. Cell viability was measured at day 5 using PrestoBlue® reagent. Error bars: ± SD from *n* = 3.

This study confirmed the ability of **2** to undergo Pd-mediated cleavage to form 5FU over a range of concentrations *in vitro* (fig 2.15).

2.7 Investigating Analytical Modalities to Study 5FU Prodrug Deprotection: NMR

Over the past thirty years a variety of methodologies have been developed in the clinic to study the active drug uptake and metabolism of fluorinated antimetabolites. Positron Emission Tomography (PET) is one such imaging technique capable of detecting gamma rays produced from the positron decay of short-lived isotopes. ^{18}F is an isotope of fluorine with a 110 min half-life, producing gamma rays with discrete energy upon positron decay[132]. ^{18}F based radiotracer surrogates of 5FU have been used to study intra-tumoral uptake of ^{18}F-5FU in patients with metastatic colorectal cancer[133]. ^{19}F NMR spectroscopy is another technique used to detect the heterogeneous accumulation of 5FU in tumours. As ^{19}F is a naturally occurring stable NMR active isotope of fluorine, ^{19}F-NMR spectroscopy has been utilised to study the intratumoral half-life of 5FU in tumour tissue both in *in vivo* models[134] and in the clinic[134,135]. Whereas PET imaging can only detect the single emission of short lived ^{18}F drug surrogates, NMR is capable

of distinguishing *between* fluorinated compounds based on electronic structural differences that alter the polarization of an ^{19}F atom in a molecule. In addition, as the ^{19}F isotope of fluorine does not rapidly decay, longitudinal studies of drug and prodrug signals within a tumour would be possible.

Propargylated 5FU prodrugs will significantly modify the electronic characteristics of the pyrimidine ring, resulting in shifted NMR ^{19}F signals in prodrugs relative to 5FU. This would allow for the study of prodrug to drug turnover. An experiment was designed to visualise the ^{19}F signal of drug **1** and prodrugs **2**, **4** and **5** by NMR in a test tube that approximated the conditions of a living system. **3** was not included due to the slower kinetic rate compared with **4** as previously reported for N3-dealkylation[88].

5 mM of **1**, **2**, **4** or **5** in 0.1 % (v/v) DMSO was mixed with 10 % FBS solution in PBS (1 mL) in a thermomixer at 1400 rpm, 37 °C for 36 hr, then sonicated and transferred into a standard NMR tube. A heat sealed capillary tube of 10 % TFA solution in d-Benzene was added into the NMR tube to provide an internal reference signal and deuterated solvent for adequate locking, and the tube was submitted to NMR as a ^{19}F paramagnetic non-spin experiment (fig 2.16).

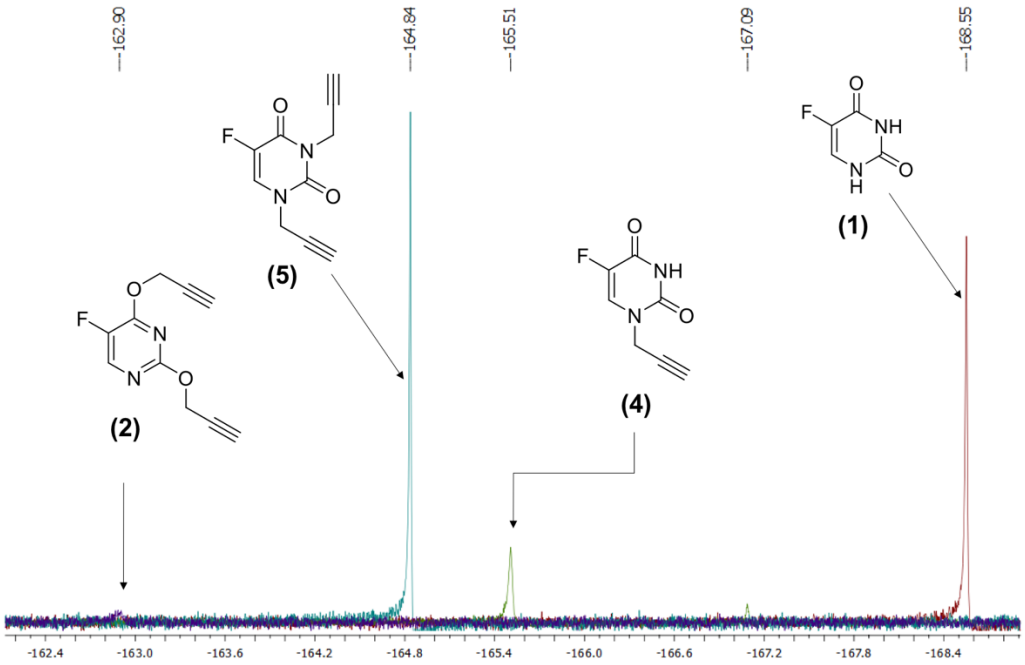

Figure 2.16 Overlaid ^{19}F NMR spectra of 5FU and prodrugs. Conditions: **1**, **2**, **4** and **5** (5 mM in 0.1 % DMSO with PBS + 10 % FBS solution (1 mL) incubated for 36 hr at 1400 rpm, 37 °C in thermomixer. Solution transferred into NMR tube with sealed capillary of 10 % TFA in d-benzene and submitted for paramagnetic non-spin ^{19}F NMR experiment.

Both N- and O-propargylation alters the electronic effect about the pyrimidine ring system, shifting the ^{19}F signal upfield (less negative) for all 5FU prodrugs. Unfortunately **2** gave a very weak ^{19}F signal at -162.90 ppm, likely due to poor solubility in H_2O at 5 mM. **4** showed an intermediate signal at -165.51 ppm. **5** displayed an excellent single peak signal at -164.84 ppm and was chosen as the model prodrug to monitor catalytic cleavage to 5FU by ^{19}F NMR spectroscopy as a proof of concept experiment.

A BOOM activation assay was next developed to monitor the conversion of **5** to 5FU by ^{19}F NMR. **5** was incubated together with Pd^0 beads under biocompatible conditions. As 5 mM does not approximate a relevant therapeutic concentration, efforts were made to optimise the experiment to retain signal resolution with reduced concentration. By increasing the length of data acquisition (from 30 min to overnight) and the scan rate (from 16 – 2046 scans) it was determined that the ^{19}F signal from a 500 μM solution of **5** in PBS would provide adequate signal to quantify conversion. As the concentration of prodrug was increased, a corresponding

increase in the amount of catalyst was required. The maximum volume of Pd^0 beads that could be loaded into a 1 mL Eppendorf and mixed efficiently (determined as 4 mg/mL) was used. A 500 µM, 0.1 % (v/v) DMSO solution of **5** in a 10 % FBS solution of PBS (1 mL) was incubated together with 4 mg of Pd^0 beads in a thermomixer at 1400 rpm, 37 °C for 5 days, then submitted for ^{19}F NMR paramagnetic non-spin analysis (fig 2.17). Initial concerns that the Pd^0 beads would interfere with the NMR analysis were overcome by the use of a non-spinning paramagnetic experiment. This reduced the likelihood that rotational movement would move Pd^0 beads into the transmission window frame of the NMR tube whilst sample scans are being accumulated.

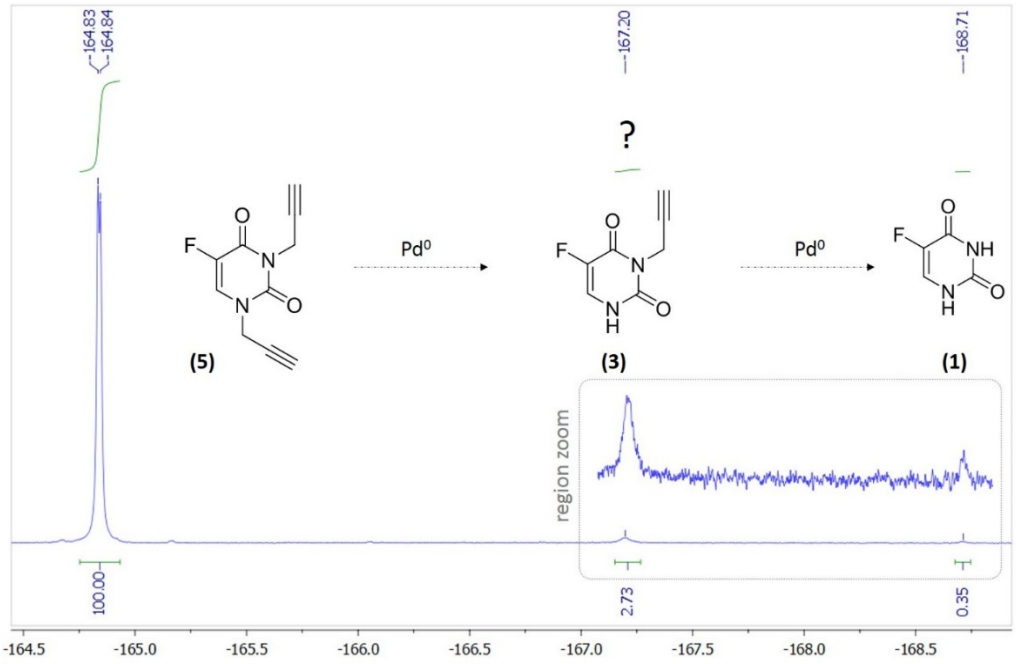

Figure 2.17 ^{19}F NMR reaction product of 5FU prodrug 5 with Pd^0 beads. Conditions: **5** (500 µM in 0.1% DMSO) incubated with 4 mg Pd^0 beads in PBS + 10 % FBS solution (1 mL) for 5 days at 1400 rpm, 37 °C in thermomixer. Solution transferred into NMR tube with sealed capillary of 10 % TFA in d-benzene and submitted for paramagnetic non-spin ^{19}F NMR experiment

After 5 days of incubation **5** was still present in large excess. While this conflicts with evidence of deprotection from previous HPLC studies[88], compound **5**'s protection kinetics were the slowest of all N-alkylated prodrugs. The lower sensitivity of NMR relative to HPLC requires a higher concentration of **5** to monitor conversion; one likely cause of an excess of reactant after

long incubation with a high quantity of the catalyst. Despite this, an intermediate at -167.20 ppm was resolved which may be the ^{19}F signal corresponding to a mono-deprotected derivative of **5** (possibly **3**), as well as presence of 5FU at -168.71 ppm. Both signals were observed in low quantity.

Our objective was to develop a sensitive ^{19}F NMR spectroscopic method to allow for the quantitative turnover of fluorinated prodrugs to drugs without perturbation. The accumulation and metabolism of 5FU and fluorinated metabolites by ^{19}F NMR spectroscopy has been previously visualised in an *in vivo* tumour model[134]. We attempted to develop a system that could accurately monitor the Pd-mediated conversion of 5FU prodrugs to 5FU using the ^{19}F signal to detect electronic changes incurred by functionalising a propargyl group to 5FU at the N1 and/or N3 and O2 and O4 positions. Whilst initial work has verified that ^{19}F NMR would be in principle capable of facilitating the analysis of a BOOM activation assay; it is clear that the experimental procedure requires further optimisation before it is progressed into more complex *ex vivo* and *in vivo* models.

2.8 Investigating Analytical Modalities to Study 5FU Prodrug Deprotection: Raman Spectroscopy

Raman Spectroscopy detects the specific vibrational signals of molecules excited by a laser. A distinct molecular spectrum (known as a fingerprint) is produced for Raman active molecules under investigation. The low intensity laser beam required for Raman Spectroscopy has historically limited signal detection in living systems. Despite this, recent developments in beam sensitivity and new molecular probes have established Raman Spectroscopy as a non-perturbing imaging technique to visualise the distribution of molecular probes in cells[136]. As biological molecules show limited Raman scattering in the 'silent region' of the spectrum (1800 – 2800 cm^{-1}), optimized bioorthogonal Raman active molecular probes have been developed to undergo silent region Raman scattering.

The alkyne group is a well suited functional group for use in Raman imaging. The alkyne group does not exist within mammalian cells, and is uniquely Raman active within the silent region of a Raman spectrum This allows for the accurate signal detection of alkyne functionalised molecules in cellular environments. Early analysis of polyacetylene natural products in carrot roots[137] and alkyne-substituted oleic acids[138] visualised alkyne functionalised molecules in living systems. 5-ethynyl-2'deoxyuridine (EdU), a pyrimidine analogue similar to an alkylated 5FU has been detected in real time during *in vitro* incubation[139–141], and the conversion of 1-ethyloxycarbonyl-5FU to 5FU has been monitored in the transdermal layer of skin[142]. We were encouraged to explore the use of Raman spectroscopy to visualise the conversion of **2** into 5FU. Raman spectroscopy was performed on dry powders of 5FU and **2** (fig 2.18).

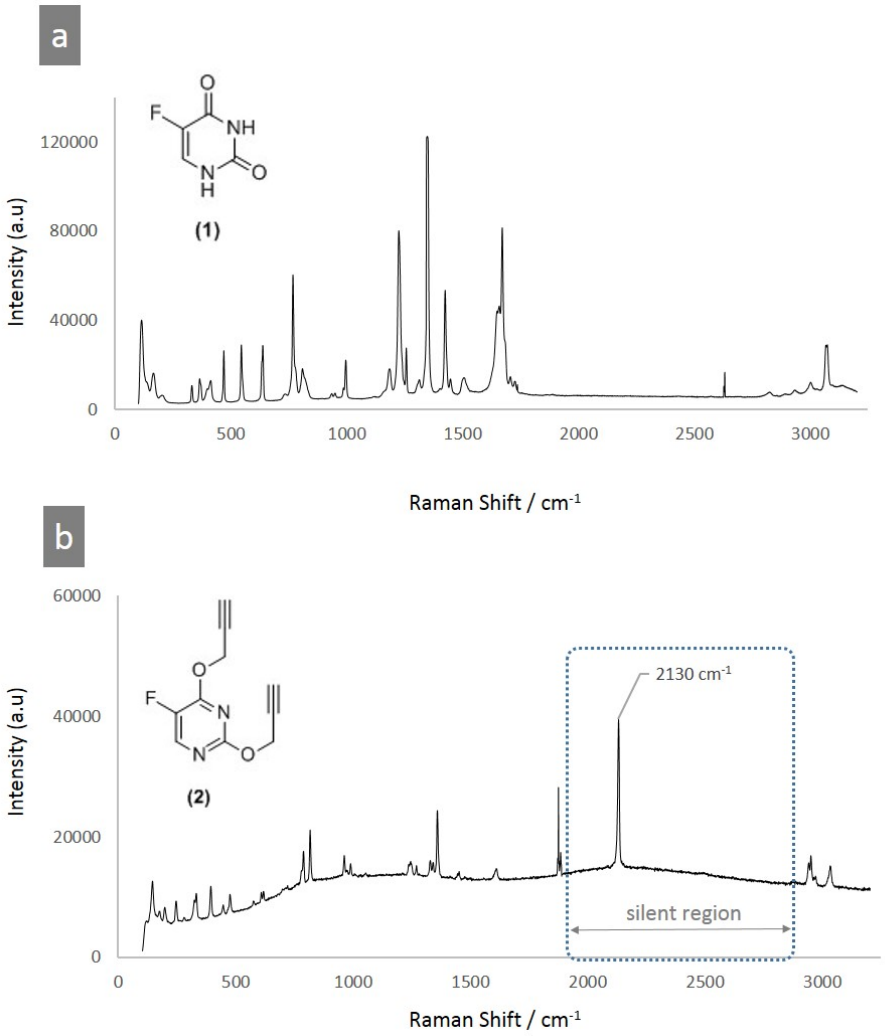

Figure 2.18 Raman Spectroscopy of 5FU and 5FU prodrug 2 as powder samples. Raman spectroscopy of (**a**) 5FU and (**b**) **2**. Raman spectra were acquired by localising beam onto an amorphous solid sample at λ_{ex} = 532 n m for 10 s using a 20x objective. Raman spectra were scaled between 0 – 120 000 counts (**a**) and 0 – 60 000 counts (**b**) and offset for clarity. The peak at 2130 cm^{-1} has been annotated and the silent region appropriately framed.

The Raman spectrum of 5FU (fig 2.18.a) is consistent with other reported spectra[140,143]. The Raman spectrum of **2** (fig 2.18.b) shows a strong alkyne signal within the silent region at 2130 cm^{-1}. An *in vitro* assay was next developed to visualise **2** in the presence of typical cellular contents at a therapeutically relevant concentration. Following analogous protocols for the imaging of Raman active molecules in cellular pellets[141,144], adenocarcinoma human alveolar basal epithelial (A549) cells were grown to confluence in a T75 flask, detached and centrifuged into a cell pellet. The supernatant was removed and the cell pellet was bathed in 1 mL of a

500 μM solution of **2** in 0.1 % (v/v) DMSO for 15 min, then the cell pellet was snap frozen in liquid nitrogen for transport, re-thawed and pipetted gently onto a glass cover for imaging. The Raman spectrum (fig 2.18) was unable to resolve peaks corresponding to cellular content or **2** across the range 0 – 3500 cm^{-1}, with the exception of a small peak at 2094 cm^{-1}. It is unclear whether this peak corresponds to the alkyne of **2**, and if so why it is slightly downshifted from the signal seen in fig 2.19. Repeated attempts to optimise the experiment consisted of bathing the cell pellet in a higher concentration of **2** (1 mM), increasing the incubation time of **2** within the cellular pellet (1 hr) and increasing the length of laser scanning time on the cover slip sample, however altering these parameters was unable to resolve other peaks.

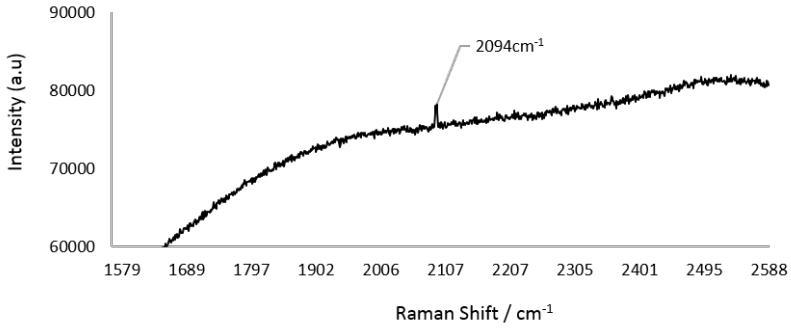

Figure 2.19 i*n vitro* Raman study of 2 in cell pellet. Spontaneous Raman spectrum recorded of A549 cells within a cellular pellet treated with **2** (1 mM, 30 min). Raman spectra were acquired by focusing beam on cellular membrane edge at λ_{ex} = 532 nm for 60 s using a 20x objective. Raman spectra were scaled between 60 000 – 90 000 counts and offset for clarity. The peak at 2094 cm^{-1} has been annotated.

One reason for this could be that **2** rapidly diffuses across the cell membrane as it is not retained by any biomolecule, an expected outcome for a bioorthogonal reagent candidate. As Raman imaging is emerging as an important tool for bioorthogonal alkyne visualisation in living systems, we attempted to leverage the unique imaging properties of the alkyne group to visualise **2** in a living system by modifying two successfully utilized protocols[141,144]. Although the alkyne signal corresponding to **2** was detected when submitted to Raman imaging as a dry powder, this did not translate into an analogous *in vitro* experiment, supporting the highly-diffusive, low retentive nature of prodrug **2**.

2.9 Conclusions

By N-alkylating endocyclic NH groups within the pyrimidine ring, our group has previously reported an N1 prodrug of 5FU, **3**, capable of selective Pd-mediated deprotection in biological environments[34]. This strategy eliminated cytotoxicity associated with 5FU in cellular assays. In the presence of a Pd^0 source, N-dealkylation produced 5FU, restoring cytotoxicity in cancer cell cultures. A clear rationale exists to alkylate 5FU at both the N1 and N3 positions[92], removing key hydrogen bonding associations and disrupting the incorporation of 5FU into antimetabolites. As the pK_a of N3 is lower than at the N1 position, N3-alkylated 5FU **4** and N-*bis*-alkylated 5FU prodrug **5** were also synthesised and tested[88]. Despite excellent biocompatibility, **4** and **5** in combination with Pd^0 released active drug more slowly than **3**.

3 and **4** display clogP values of -0.86; **5** has a clogP of - 0.4. These values are not typically associated with drug candidates amenable to administration. LogP values between 2 and 3 are desired as an optimal balance for good drug absorption or elimination during first-pass on administration. Since mono-N-alkylated 5FU prodrugs **3** and **4** still possess endocyclic NH enzymatic recognition sites, metabolism is still possible. Although bis-N-alkylated 5FU candidate **5** has no endocyclic NH enzyme recognition sites, a slow stepwise release of 5FU in the presence of a Pd^0 source may reduce the efficacy of treatment.

These suboptimal intrinsic properties may prevent N-alkylated prodrugs of 5FU from progressing into a pre-clinical study. *Bis*-O-propargylated 5FU prodrug **2** was developed to overcome this. **2** possesses improved lipophilic properties, retained biocompatibility and rapidly releases 5FU via Pd-mediated depropargylation in cell culture.

By locking into place the lactim tautomeric state of 5FU via *bis*-O-propargylation, **2** blocks NH bonding interactions required to metabolise the parent drug. **2** displayed no cytotoxicity across all tested cell lines. Non-biological UPLC studies showed that **2** was taken up by Pd^0 beads when mixed in solution, rapidly producing 5FU without the observation of mono-propargylated intermediate byproducts. This is an attractive property as conceptually Pd^0 beads inserted into a tumour would be capable of capturing free circulating **2** and catalysing the localized release

of 5FU. The lipophilicity of **2** (clogP = + 1.66) was calculated as one order of magnitude higher than **5** and two orders higher than **3** and **4**, a possible explanation as to why **2** could sequester into the lipophilic matrix of Pd^0 beads, whereas **1**, **3**, **4** and **5** do not. This clogP value is typical of drug candidates with ideal pharmacokinetic properties and amenable to oral availability, unlike the much lower clogP values of **3**, **4** and **5**.

2 and Pd^0 beads underwent BOOM activation *in vitro* across a range of concentrations. At high concentrations, **2** + Pd^0 beads is capable of matching the cytotoxic profile of 5FU, however at low concentrations an appreciable gap remains between the cytotoxicity produced by 5FU alone and that of **2** and Pd^0 beads in combination. This effect may be attributed to the time delay required for Pd^0 bead catalysis of **2** and subsequent release of 5FU into solution.

Initial attempts to utilise imaging and analytical modalities on prodrugs of 5FU were explored by NMR and Raman Spectroscopy. ^{19}F NMR spectroscopic biocompatible conversion assay in an NMR tube was expected to allow for visualisation of the real time conversion of prodrugs into intermediates and 5FU through intermediates. Unfortunately, the weak ^{19}F NMR signal observed for **2** precluded further investigation for this prodrug. Instead **5** was determined as the best candidate to test this assay. However this experiment did not produce 5FU at the rate observed by prior HPLC and suggested by cytotoxicity from *in vitro* studies. It is important to note that the concentration of **5** and Pd^0 beads were optimised for NMR studies, and do not reflect those used in HPLC and *in vitro* studies.

Raman Spectroscopy has been used to monitor the accumulation and compartmentalisation of Raman active molecules in living systems. The alkyne group has emerged as a useful tool to study functionalised alkyne bearing molecular probes in cellular biology. A modified procedure for the uptake of **2** into a cell pellet was unable to resolve a clear signal produced by alkyne in the silent region of the spectrum, suggesting that the compound is not retained by any cellular component as would occur for a bioactive compound.

2, an optimised lactim tautomerised O-alkylated prodrug of 5FU has been developed to overcome the non-drug like properties of previously reported N-alkylated BOOM 5FU prodrug candidates. With improved physicochemical properties, non-toxic and Pd^0 labile, **2** potentially represents a viable candidate for pre-clinical *in vivo* testing. Next steps will be to test *in vivo* pharmacokinetics (PK) in a rodent model to verify if key PK properties such as oral availability and plasma half life are improved over 5FU and N-alkylated prodrugs. Based on the analytical investigations performed with **2**, it is recommended to use standard HPLC studies to carry out *in vivo* ADME studies.

CHAPTER 3

Prodrugs of Gemcitabine

Gemcitabine is the second antimetabolite to be investigated for use as a Pd-labile prodrug. Previously developed prodrugs of gemcitabine focused on functionalising at the C4NH_2 and C5'OH position with Pd-labile groups. Moderate reduction in cytotoxicity with Pd-mediated activation was achieved. This chapter focuses on developing novel protecting groups to improve the cytotoxic fold change afforded from C4NH_2 and C5'OH functionalisation with retained sensitivity to Pd^0.

3.1 Gemcitabine Overview

2', 2"-difluoro 2'-deoxycytidine, commonly known as Gemcitabine (**16**), is an antimetabolite chemotherapy first approved in 1997 for the front line treatment of pancreatic cancer[145] (fig. 3.1). Since its approval as a monotherapy, gemcitabine has been the standard of care for patients with metastatic pancreatic cancer, improving overall survival and median response rates in large patient population studies relative to 5-fluorouracil, the historical standard of care[146]. Recent studies have expanded the number of indications for which gemcitabine may be used as a monotherapy or as part of a combined chemotherapeutic regime to include cancers of the lung[147], ovary[148], liver[149] and breast[150].

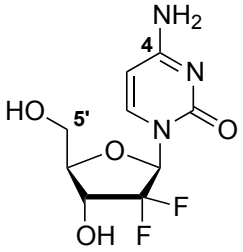

gemcitabine
(16)

Figure 3.1. Structure of gemcitabine.

Gemcitabine is a C2' di-fluorinated pyrimidine antimetabolite analogue of the nucleoside deoxycytidine. Nucleosides are critical intracellular substrates required for nucleic acid synthesis, DNA elongation and replication. As cancer cells undergo sustained proliferation and uncontrollable DNA synthesis, the demand for nucleoside uptake and metabolism is accordingly upregulated[151]. This upregulated demand for DNA metabolites has been exploited by the development of nucleoside analogues designed to mimic endogenous metabolic processes; eliciting apoptosis by competition and inhibition of key enzymes involved in nucleoside anabolism or by direct incorporation into growing DNA chains[152,153]. Selective isosteric replacement of hydrogen atoms with fluorine or isopolar replacement of hydroxy groups with fluoro groups has successfully converted a number of well-studied nucleosides into approved antimetabolite cancer medicines. Although the fluorine atom mimics the size and geometry of the hydroxy group, increased stability and electronegativity properties of the C-F bond leads to a dramatic change in the pharmacological activity of an analogue with respect to its metabolic mimic[154].

Deoxycytidine, the molecular mimic of gemcitabine, undergoes mono phosphorylation at the C5'OH position by Deoxycytidine Kinase (dCK)[155,156], thus trapping the metabolite in the cell. Following di and tri phosphorylation by other enzymes, the tri phosphorylated metabolite is then delivered into the nucleus where it is incorporated into growing DNA strands[156]. The increased rate of DNA synthesis in proliferating cancer cells corresponds to a higher demand for deoxycytidine. Gemcitabine is preferentially accumulated in cancer cells via the same dCK phosphorylation pathway. dCK recognizes gemcitabine via coordination with multiple amino acid residues conserved within the active pocket of dCK. Key enzymatic interactions take place between the C5'OH, C4-NH_2 and N3 position of gemcitabine and Glu 53, Arg 128, Asp 133 and Gln 97 residues within the active pocket of dCK[157,158] (fig 3.2). Hydrogen bonding interactions in the active pocket then catalyze an Adenosine Diphosphate (ADP) assisted rate-limiting phosphorylation at the C5'OH position to form gemcitabine monophosphate.

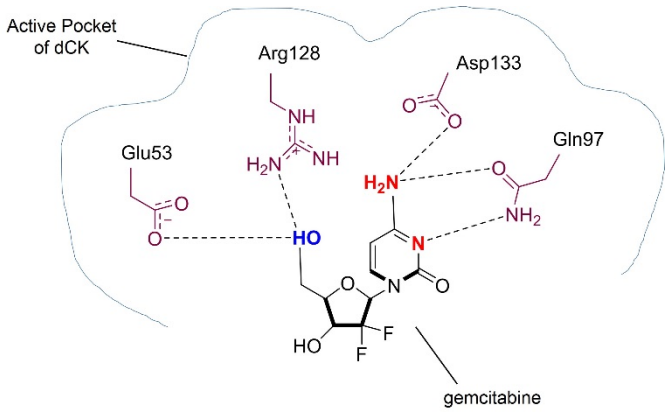

Figure 3.2 Deoxycytidine Kinase (dCK) in complex with gemcitabine. Molecular recognition sites between the C5'OH, C4NH_2 and N3 position of gemcitabine and Glu 53, Arg 128, Asp 133 and Gln 97 residues within the active pocket of dCK[110].

Subsequent di- and tri-phosphorylations by UMP/CMP kinase (CMPK1) and nucleoside-disphosphate kinase (NDPK) occur in the cellular cytoplasm. Gemcitabine diphosphate induces cytotoxicity by inhibition of ribonucleotide reductase, which depletes intracellular deoxyribonucleotide pools and starves the cell of DNA building blocks. Gemcitabine triphosphate is synthesized into elongating DNA chains, which triggers 'masked chain termination' by incorporation of deoxyribonucleotide triphosphate into the growing DNA chain, halting chain elongation and inducing apoptosis[159,160].

Gemcitabine is routinely administered by intravenous infusion at a dosage of 1,000 mg/m^2 on intermittent or recurrent days during a standard dosing cycle[161]. A family of membrane bound nucleoside transporters, including sodium dependent concentrative (CNT) and sodium-independent equilibrative (ENT) nucleoside transporters[162–164] deliver gemcitabine from blood into the cellular cytoplasm where the conversion to active metabolites occur.

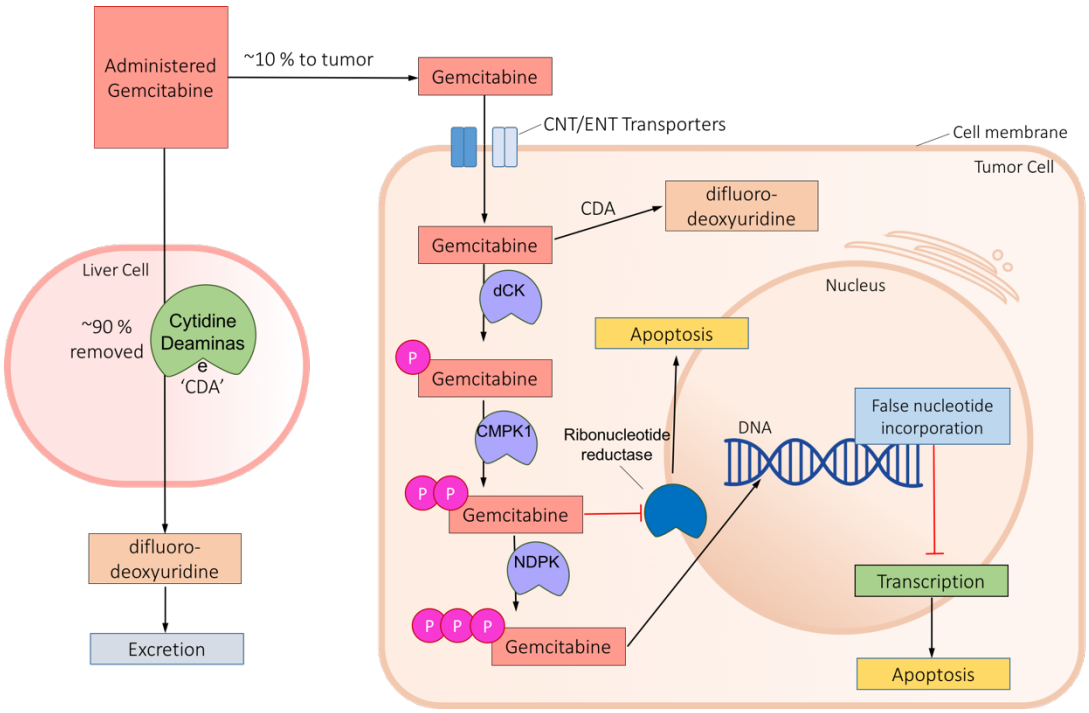

Figure 3.3. Cellular metabolism of gemcitabine. Cytidine deaminase CDA is responsible for the removal of up to 90 % of administered gemcitabine. The remaining 10 % accumulates in tumour cells where it undergoes successive phosphorylation events to mono-, di- and tri-phosphorylated gemcitabine by Deoxycytidine kinase (dCK), UMP/CMP kinase (CMPK1) and nucleoside-disphosphate kinase (NDPK). Gemcitabine diphosphate inhibits ribonucleotide reductase, depleting intracellular deoxyribonucleotide pools and starving the cell of DNA building blocks. Gemcitabine triphosphate is transported into the nucleus where it induces false nucleotide incorporation via masked chain termination.

Despite initial reports of a well-tolerated safety profile[165], increasing evidence from widespread use has shown that gemcitabine has significant off-target toxicity[166,167]. Myelosuppression is a common dose-limiting side effect, with an infrequent incidence of pulmonary toxicity[166] and rare cases of treatment induced cardiomyopathy[168]. In addition, up to 90 % of the drug is rendered biologically inert via cytidine deaminase (CDA) mediated $C4NH_2$ hydrolytic deamination to difluoro-deoxyuridine. This process takes place in most organs[169] with the majority of deactivation occurring in the liver[160] (fig 3.3).

Preclinical and clinical studies have shown that CDA upregulation increases resistance to gemcitabine treatment, whereas CDA downregulation reduces the maximum tolerated dosage that may be administered, reducing efficacy[170,171]. Further evidence has shown that genetic

variations associated with CDA expression levels in biliary tract cancer patients correlate to the efficacy of gemcitabine treatment[172].

There is a clear need to improve the pharmacokinetics and safety characteristics of this essential medicine. An optimized selectively and focally activatable gemcitabine prodrug would have the dual advantages of masking the drug to dCK activation in off target tissues and variable CDA deactivation. This would reduce side effects and allow for a precise dosage regimen to be determined independent of CDA expression variability in patient populations. Selective activation at the tumour site would deliver a high dose of gemcitabine to undergo dCK mediated metabolism into active anti-metabolites, driving a highly localized cytotoxic effect.

3.2 Current Progress with Gemcitabine Prodrugs

By reviewing the metabolic pathways of gemcitabine, a rational basis emerges for developing C5'OH and C4NH_2 masked gemcitabine prodrugs that would reduce metabolic deactivation of the drug and off-target activation and toxicity. Masking gemcitabine at the C4NH_2 position would block recognition of the drug by CDA and dCK. Our group has previously invented gemcitabine prodrugs that block this C4NH_2 group[89] using a carbamate. Separately a cholesteryl hemisuccinate C4NH_2 carbamate protected gemcitabine prodrug has been being progressed into *in vivo* studies[173–175]. This evidence suggests that C4NH_2 carbamate protected derivatives of gemcitabine are resistant to cellular cleavage.

Masking gemcitabine at the C5'OH position would block dCK mediated mono-phosphorylation at the hydroxy group. Downstream synthesis of di-, and tri-phosphorylated antimetabolites would be blocked, preventing cytotoxicity in off-target tissue. We previously concluded that C5'OH carbonate protected gemcitabine derivatives are susceptible to cleavage in cell culture[89]. A literature search does not find examples of C5'OH protected gemcitabine derivatives able to resist enzymatic cleavage during extended (> 12 hr) incubation in cell culture. One report functionalizes a targeting peptide to gemcitabine via a C5'OH carbonate group, and suggests stability from a 10 hr *in vitro* assay[176], indicating that the use of bulky

protecting groups could increase the stability of the carbonate bond. Another study concludes that an analogue of gemcitabine, a peroxy-caged-fluorodeoxy thymidine-1 was stable to enzymatic processing incubating the compound with serum for only 2 hrs[177]. No selectively labile C5'OH carbonate protecting group of gemcitabine has been capable of achieving significant resistance to enzymatic cleavage during an extended drug incubation assay.

We set out to develop a new protecting group that could (1) afford resistance to C5'OH carbonate cleavage and (2) enhance the BOOM activation profiles of previously reported $C4NH_2$ masked prodrugs of gemcitabine.

Prior work within our group developed prodrugs of **16** by incorporating allyloxycarbonyl (Alloc), propargyloxycarbonyl (Poc) and carboxybenzyl (Cbz) at both the C5'OH and $C4NH_2$ positions. This semisynthetic strategy afforded Alloc **17** and **24**, Poc **18** and **25** and Cbz **19** and **26** protected carbamate or carbonate derived prodrugs of **16**[89] (scheme 3.4).

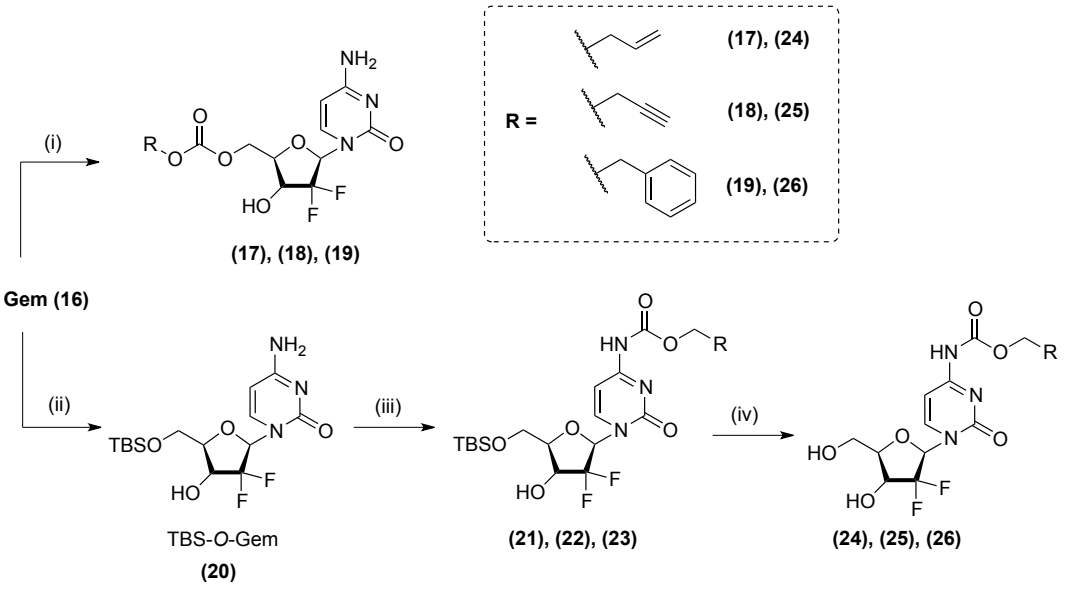

Scheme 3.4 Synthesis of reported gemcitabine prodrugs. Reagents and conditions: (i) DBU (2.5 equiv.), DMF, alkyl chloroformate (1.5 equiv.) at 4 °C, rt, overnight (47 – 53 %); (ii) TBS-Cl (1.1 equiv.), imidazole (3.5 equiv.), DMF, rt, 2.5 hr (88 %); (iii) pyridine (3.2 equiv.), DMF or THF, alkylchloroformate (1.5 equiv.) at 4 °C, rt, overnight 12 – 48 hr (42 – 69 %); (iv) TBAF (2.5 equiv.), THF, rt, overnight (62 – 92 %).

Whilst Poc, Alloc and Cbz carbamate prodrugs **24**, **25** and **26** were capable of conferring increased bioorthogonality with respect to gemcitabine in pancreatic adenocarcinoma BxPC-3 and MiaPaCa-2 cell lines (> 20 fold cytotoxic reduction)[89], carbonate protected prodrugs **17**, **18** and **19** were sensitive to metabolic activation. This was likely due to the enhanced propensity of the carbonate bond to undergo hydrolysis[178,179].

3.3 Rational Design and Incorporation of a Novel Protecting Group for Gemcitabine Prodrugs

Based on observations that; (1) Poc is superior to Alloc as a C4NH_2 protecting group for bioorthogonality and activation, (2) Cbz and Poc groups at the C4NH_2 position are resistant to metabolic cleavage in the absence of Pd^0, and (3) Poc is readily cleaved in the presence of a Pd^0 source, we designed the propargyloxybenzylcarbonyl protecting group (Pobc) (fig 3.6).

This 'self-immolative' linker combines the bioorthogonality of Cbz and Poc groups. By imposing increased steric bulk around the carbamate/carbonate bond, we sought to reduce the rate by which endogenous enzymes could cleave the protecting group. By positioning the Propargyloxy group at the ortho position, we would expect improved bioorthogonality to the carbamate with respect to para position functionalization due to increased steric bulk.

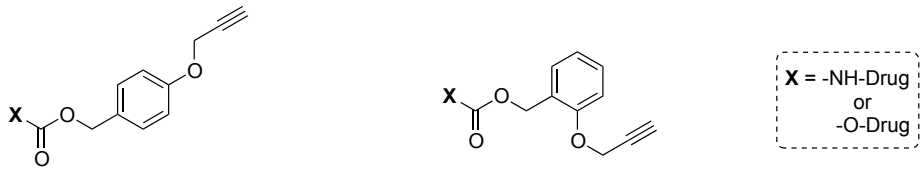

para-propargyloxybenzyl carbonyl (p-Pobc) *ortho*-propargyloxybenzyl carbonyl (o-Pobc)

Figure 3.5. The propargyloxybenzyl carbonyl (Pobc) group.

The Pobc group would also retain Pd lability via a self-immolative trigger mechanism[180–183]. Rapid O-depropargylation group triggered 1,4- or 1,6-self-immoliative benzyl elimination would take place in the presence of a Pd^0 source. The initial reaction expected to take place between a Pobc group and Pd^0 is oxidative cleavage of the propargyl group. This reaction was previously observed by mass spectroscopy[184] to produce acetol (1-hydroxyacetone), an

innocuous biological substrate present in human cells for glycogenesis[185]. O-depropargylation would then trigger benzyl elimination (the self-immolation step) (scheme 3.6).

When the leaving group of benzyl elimination is an *o*- or *p*- amino or hydroxy substituent and a good leaving group, a quinone methide and a carbamic- or carbonic- acid anion are respectively released[25] . Under biological conditions the carbamic or carbonic acid anions break down further to release CO_2. The amino or hydroxy group is subsequently protonated, and the unstable quinine methide byproduct undergoes rapid nucleophilic attack (i.e. by H_2O) to produce p- or o- hydroxybenzyl alcohol.

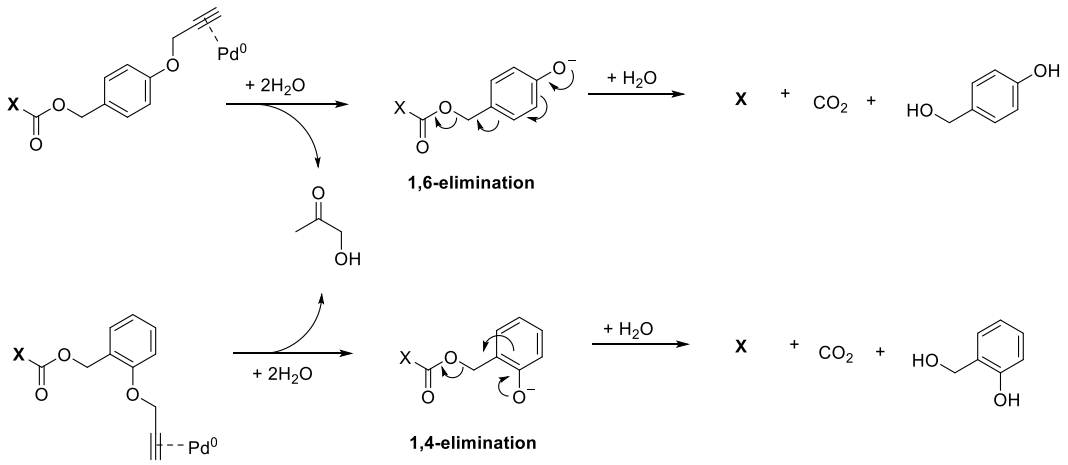

Scheme 3.6 Proposed mechanism for the Pd^0 catalysed cleavage of Pobc groups in water. Pd-mediated oxidative cleavage of the propargyl group triggers benzyl elimination to release X (an -NH_2 or –OH bearing drug), CO_2, p- or o- hydroxybenzyl alcohol and acetol.

The expected by-products resulting from Pd-mediated Pobc cleavage, 1,4- or 1,2-hydroxybenzyl alcohol, were each incubated at between 0.003 – 100 µM across a five different cancer cell lines. This confirmed that the by-product would be innocuous in cellular assays (fig 3.8). Acetol has been previously verified as non-toxic in pancreatic BxPC3 and HCT116 cancer cell lines within our group (fig 3.9). C4NH_2 carbamate gemcitabine derivatives were synthesized by incorporation of 4-nitrophenyl activated protecting groups at the NH_2 position. **27** and **28** were first alkylated using propargyl bromide and sodium carbonate. Treatment of **29** or **30** with pyridine in the presence of 4-nitrophenyl chloroformate formed the corresponding activated carbonates **31** and **32** in good yield. Separately the C5'OH position of **16** was

silylated to **20** using TBS-Cl and imidazole then treated with **31** or **32**. TBAF-mediated silyl deprotection yielded the final carbamate prodrugs **33** and **34** in low yield (scheme 3.7). C5'OH carbonate gemcitabine prodrugs were synthesized by treating gemcitabine directly with **31** or **32** in the presence of pyridine to form **35** or **36** in low yield.

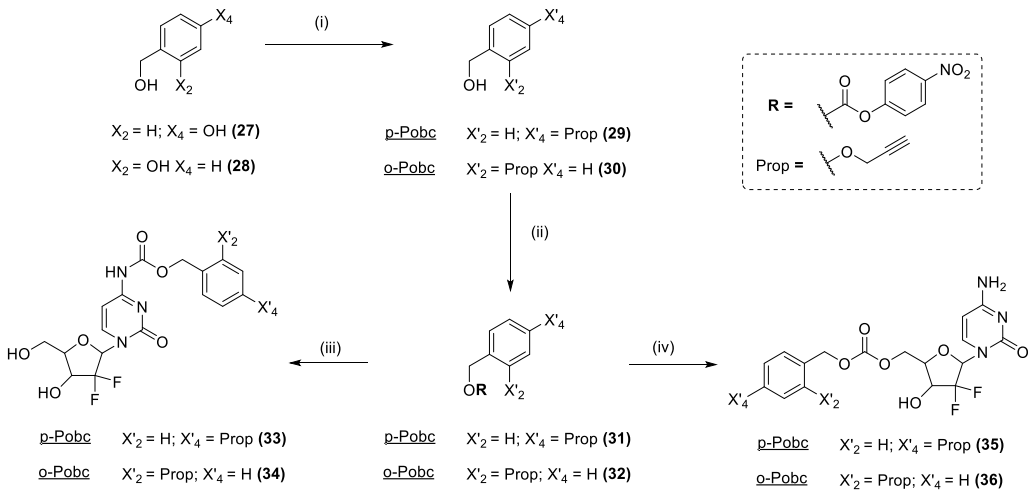

Scheme 3.7. Synthesis of novel gemcitabine prodrugs. Reagents and Conditions: (i) propargyl alcohol, Na_2CO_3, MeCN; (ii) 4-nitrophenyl chloroformate, THF (iii) TBS-O-gem **20**, pyridine, DMF, TBAF in THF (7 – 9 %) (iv) **16**, pyridine, DMF (20 – 23 %)

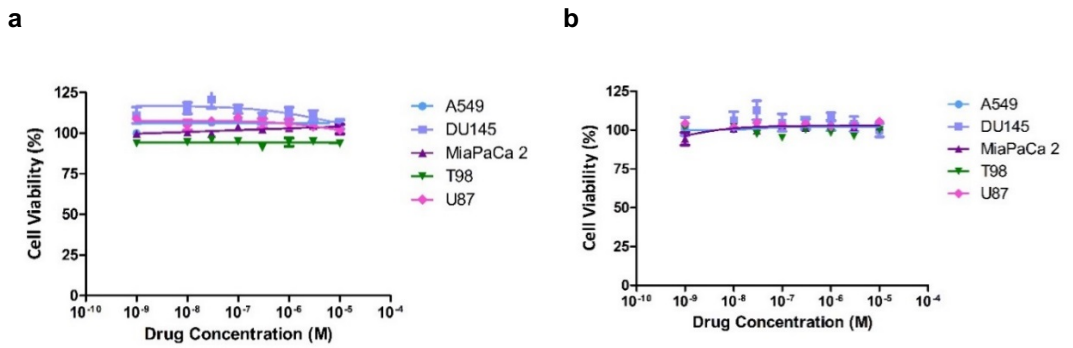

Figure 3.8 Study of hydroxybenzyl alcohol by-product cytotoxicity. (**a, b**) Toxicity effect study of (**a**) 2-hydroxybenzyl alcohol and (**b**) 4-hydroxybenzyl alcohol across multiple cancer cell lines. Cells were incubated with increasing concentration of the alcohol (0.003 – 100 μM) for 5 days and cell viability measured. Error bars represent ± standard deviation from *n* = 3.

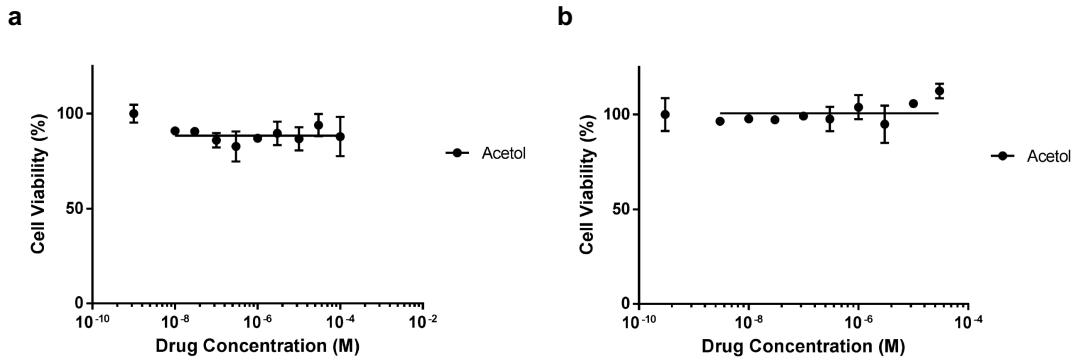

Figure 3.9 Study of acetol by-product cytotoxicity. (**a, b**) Toxicity effect study of acetol in (**a**) HCT116 and (**b**) BxPC-3 cells Cells were incubated with increasing concentrations of the alcohol (0.003 – 100 μM) for 5 days and cell viability measured. Error bars represent ± standard deviation from *n* = 3.

Therefore, incorporating p- or o-Pobc protecting group moieties at the C4NH_2 or C5' OH positions could further enhance the bioorthogonality characteristics previously reported by Poc, Alloc and Cbz prodrugs, whilst retaining sensitivity to Pd-mediated activation.

Two semisynthetic strategies were developed to incorporate o-Pobc and p-Pobc groups into gemcitabine at both the C5'OH or C4NH_2 positions via a 4-nitrophenyl carbonate precursor. **27** and **28** were first propargylated using propargyl bromide and sodium carbonate. Treatment of **29** and **30** with pyridine in the presence of 4-nitrophenyl chloroformate formed the corresponding carbonates **31** and **32** in good yield.

3.4 Gemcitabine Prodrug Biocompatibility Assays

As gemcitabine is used as a frontline treatment for pancreatic cancer, we tested our prodrugs in pancreatic cancer MiaPaCa 2 cells. Previous work in our group reported bioorthogonality fold changes by dose response curves of both carbamate and carbonate protected prodrugs against gemcitabine in MiaPaCa2 cells. Whilst carbamate protected prodrugs were significantly deactivated, carbonate prodrugs were sensitive to metabolic activation. This followed the prediction that carbonate bonds would be more susceptible to cleavage than the carbamate bond[179]. As the Pobc protecting group combines the steric hindrance afforded by Cbz and sensitivity to Pd-mediated cleavage from Poc, Poc carbamate **25** and Cbz carbamate **26** were chosen as controls for the biocompatibility study of novel prodrugs **33**-**36** in MiaPaCa2 cells (fig 3.10).

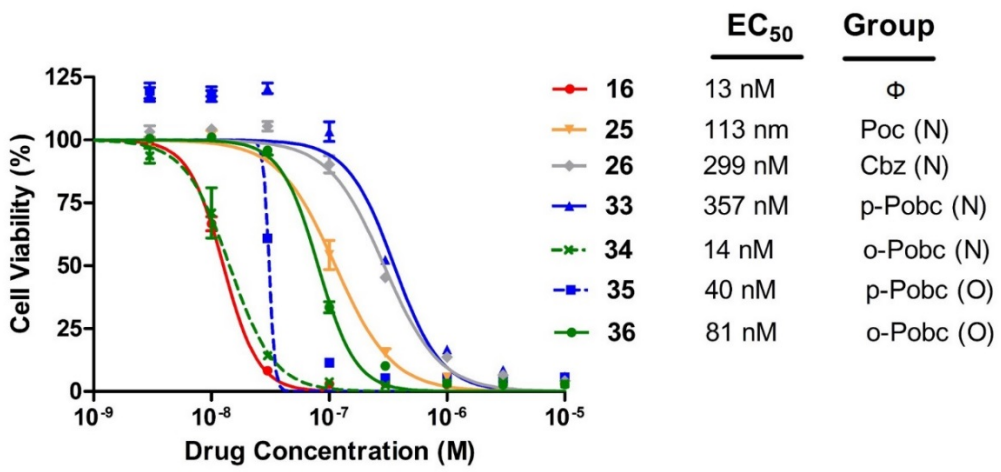

Figure 3.10. Study of gemcitabine cytotoxic reduction produced by prodrugs 25, 26 and 33 – 36 in cell culture. Semilog dose−response curves and calculated EC_{50} values of **25** (solid-yellow), **26** (solid-grey), **33** (solid-blue), **34** (dashed-green), **35** (dashed-blue) and **36** (solid-green) in comparison to those of unmodified gemcitabine **16** (solid-red) in MiaPaCa-2 cells. Cell viability was measured at day 5 using PrestoBlue® reagent. Error bars: ± SD from n = 3

As shown in fig 3.10, carbamate protected prodrug **33** displayed improved reduction of cytotoxicity relative to Gemcitabine [EC_{50} (**33**) / EC_{50} (**16**) ~ 27], slightly outperforming Poc [EC_{50} (**33**) / EC_{50} (**25**) ~ 3] and Cbz [EC_{50} (**33**) / EC_{50} (26) > 1] controls. On the contrary, **34** displayed a cytotoxic effect equivalent to that of gemcitabine. The carbonate protected prodrug

36 displayed a reduction of cytotoxicity relative to gemcitabine [EC_{50} (**36**) / EC_{50} (**16**) ~ 6], while **35** only displayed a limited reduction in cytotoxicity as compared against drug [EC_{50} (**35**) / EC_{50} (**16**) ~ 3]. For the purpose of this study **33** shows the best safety profile, whilst the reduction of toxicity obtained with the carbonate prodrug **36** was noteworthy given the widely reported low stability of this group.

3.5 Pd-mediated Gemcitabine Prodrug *in vitro* Conversion Study

Having determined that **33** and **36** confer enhanced bioorthogonality to gemcitabine by masking the free amino and hydroxy group respectively, the next step was to determine sensitivity of the Pobc group to Pd-mediated catalysis. As in Chapter 2, a heterogeneous Pd source would be utilised as the catalyst. Pd^0 functionalised beads (130 μm average diameter) were prepared according to a reported protocol[34] to test the susceptibility of the best prodrug candidates to undergo Pd-mediated activation.

Quantitative analysis of prodrug cleavage via UPLC analysis presented unexpected challenges. When any of **32** - **36** were directly injected into the UPLC machine at therapeutically relevant concentrations (10 – 1000 μM), broad bimodal peak distributions were consistently observed by UV-Vis detection. Fine-tuning by altering drug concentration, solvent mixture ratios and elution rate did not change this distinct peak distribution pattern, Thus the resolution of separate peaks corresponding to generation of drug from prodrug was not possible. **33** and **36** were therefore progressed directly into an *in vitro* BOOM assay. **33** and **36** were incubated in combination with Pd^0 beads in MiaPaCa-2 cells against **26** and **25** as a negative and positive control respectively. An initial assay was conducted at 30 nM to observe the effect of Pd^0 bead incubation on prodrugs (fig 3.11).

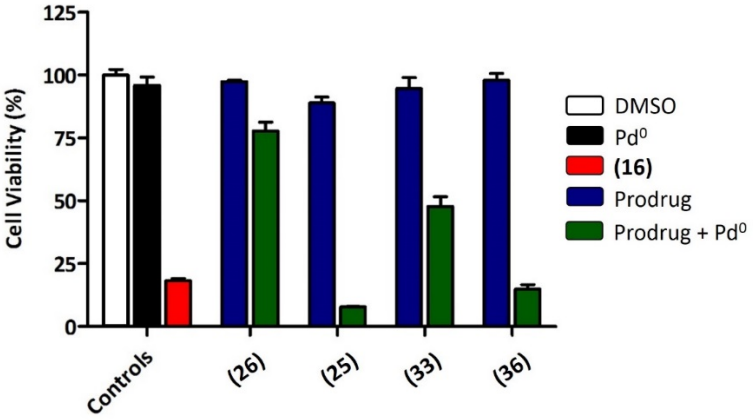

Figure 3.11 Preliminary Pd-mediated activation assay to compare activity of gemcitabine prodrugs 25, 26, 33 and 36 against drug in MiaPaCa-2 cells. Experiments: 0.1% (v/v) DMSO (untreated cell control, white); 1 mg/mL of Pd^0 beads (negative control, black); gemcitabine **16** (30 nM, positive control, red); **26**, **25**, **33** and **36** (30 nM, negative control, blue); and 1 mg/mL of Pd^0 beads + **26**, **25**, **33** and **36** (30 nM, BOOM activation, green). Cell viability was measured at day 5 using PrestoBlue® reagent. Error bars: ± SD from *n* = 3.

As previously reported **25** was capable of releasing drug upon Pd^0 bead incubation, whereas **26** was resistant to cleavage[89]. A significant cytotoxic effect was observed when **33** and **36** were incubated in combination with Pd^0 beads, suggesting that Pd^0 beads were able to cleave Pobc masked **33** and **36** to release cytotoxic **16**. Encouraged by this preliminary study, **33** and **36** were next tested for BOOM activation across a range of concentrations (0.003 – 0.3 μM) in combination with Pd^0 beads in MiaPaCa-2 cells (fig 3.12). Pd^0 beads were able to release **16** from **25**, **33** and **36** across a therapeutic range, with **26** being resistant to Pd-mediated cleavage.

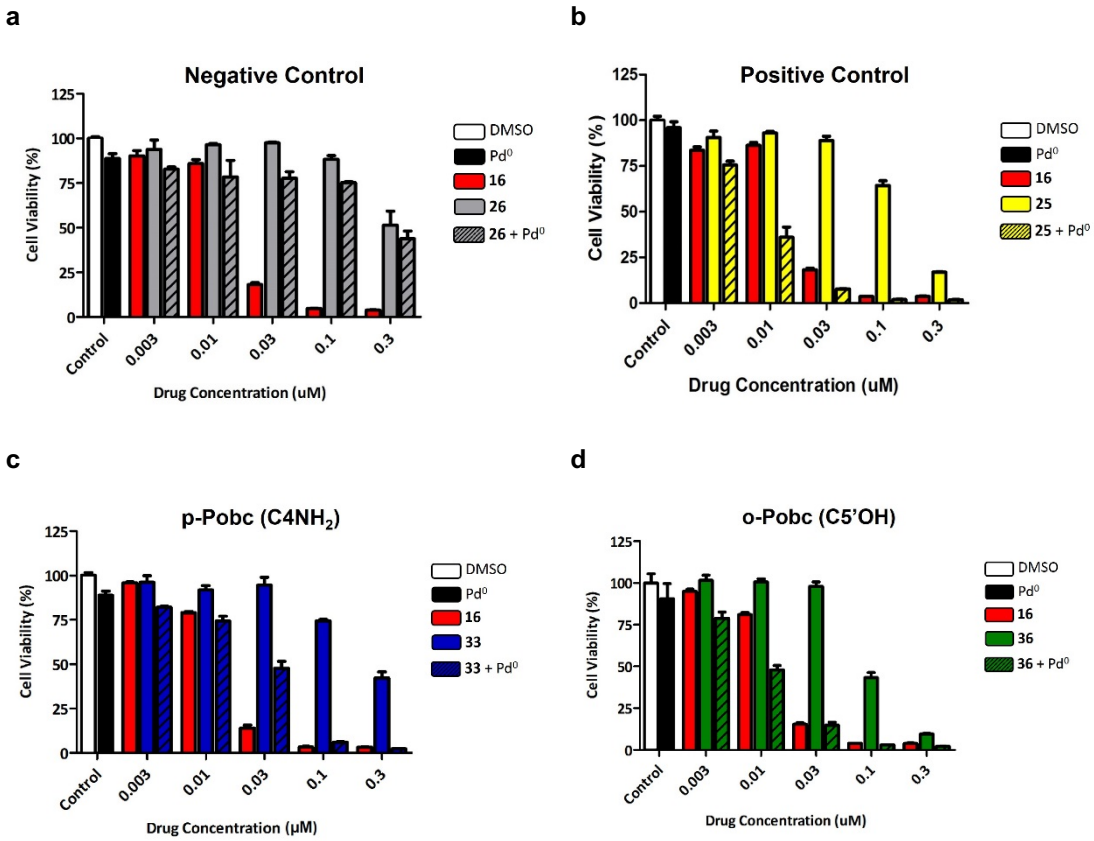

Figure 3.12 Pd-mediated activation of gemcitabine prodrugs in MiaPaCa-2 cell culture. Toxigenic effect of Pd-activated gemcitabine prodrugs across a concentration window in MiaPaCa-2 cells. Experiments: 0.1 % (v/v) DMSO (untreated cell control, white); 1 mg/mL of Pd^0 beads (negative control, black); **16** (positive control, red); Prodrug (**26**, grey) (**25**, yellow), (**33**, blue) and (**36**, green); Prodrug + Pd^0 beads (**26**, striped grey) (**25**, striped yellow), (**33**, striped dark blue) and (**36**, striped green). Drug and Prodrug concentrations 0.003 – 0.3 µM. Cell viability was measured at day 5 using PrestoBlue® reagent. Error bars: ± SD from *n* = 3.

3.6 Conclusions

Prodrugs of gemcitabine have been designed based on mechanism of action studies to remove biological interaction with dCK and CDA, two key enzymes responsible for unwanted metabolism[155–158,160]. $C4NH_2$ carbamate prodrugs of gemcitabine are considered to be resistant to enzymatic cleavage, whereas C5'OH hydroxy group carbonate derivatives of gemcitabine are not[173].

Gemcitabine **16** has been previously investigated as a drug candidate amenable to BOOM chemotherapy[89]. Poc, Alloc and Cbz protecting groups were functionalised to **16** at the C4NH2 and C5'OH positions and tested *in vitro*. The N-Poc derivative **25** improved bioorthogonality with respect to **16**, and was cleaved to release drug in the presence of Pd^0 beads. The N-Cbz derivative **26** was also capable of reducing inherent cytotoxicity, however was resistant to Pd-mediated cleavage. The best reported N-protecting group for **16** was capable of eliciting a 23 fold decrease in cytotoxicity. No O-protecting group was bioorthogonal during a 5 day biocompatibility assay.

In this work, the Pobc protecting group was designed and incorporated via a semisynthetic strategy at the $C4NH_2$ and C5'OH positions of gemcitabine. The introduction of an N-Pobc (functionalised at the amino group of the pyrimidine ring) was sought to further enhance bioorthogonality observed in Poc and Cbz group masking. An O-Pobc (functionalised at the hydroxyl group) was also developed to improve the stability of the labile carbonate. Expected by-products of Pd-mediated Pobc cleavage were tested for bioorthogonality and found to be non-toxic across a broad range of cell types.

The N-Pobc prodrug **33** was found to be slightly more biocompatible than N-Cbz and N-Poc groups [EC_{50} (**33**) / EC_{50} (**25**) ~ 3], [EC_{50} (**33**) / EC_{50} (**26**) > 1], reducing the cytotoxicity of the prodrug 27 fold relative to the unmodified drug **16**. The o-Pobc prodrug **36** displayed a 6-fold reduction in cytotoxicity relative to gemcitabine. Both **33** and **36** were sensitive to Pd-mediated deprotection over a range of concentrations, validating the use of Pobc as a novel protecting group for BOOM prodrug protection strategies.

Although this study validates the use of Pobc, a novel protecting group capable of generating prodrugs that exhibit low inherent cytotoxicity and high sensitivity to palladium mediate activation, the enhancement afforded relative to previous carbamate strategies is marginal and not sufficient to progress Pobc derivatives of **16** into a preclinical *in vivo* models.

CHAPTER 4

Prodrugs of Doxorubicin

Doxorubicin will be investigated as the next new drug candidate amenable to masking and Pd-mediated activation. Protecting groups designed and incorporated into gemcitabine will be functionalised to the C3' amino group of the drug and tested for biocompatibility and sensitivity to Pd. The observation of prodrug and drug "sequestration" into established Pd^0 devices will lead to optimization – new Pd^0 devices capable of preferentially accumulating prodrug and releasing drug will be reported.

4.1 Doxorubicin Overview

Doxorubicin (dox) **37** is an anthracycline antitumour antibiotic used alone or in combination for the treatment of a wide range of haematological malignancies, carcinomas and soft tissue sarcomas[188] (fig. 4.1). A powerful cytotoxic drug with severe side effects, dox has been the subject of intense research since its discovery as an antitumour agent over 40 years ago[189,190], reflecting both the importance of this drug and its complex cytotoxicity profile.

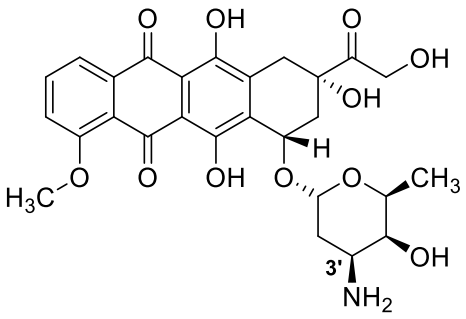

Doxorubicin (Dox)
(37)

Figure 4.1 Structure of doxorubicin.

In standard therapy dox is dosed as a single rapid intravenous infusion once every 21 days at or below 550 mg/m^2 [191]. Once administered, dox diffuses passively into the cellular cytoplasm[192,193] where it exerts cytotoxic effect via numerous distinct pathways (fig 4.2). At cellular and mitochondrial membranes, dox induces lipid peroxidation by way of complexing with Fe^{2+}, inducing mitochondrial DNA damage and apoptosis through the production of Reactive Oxygen Species (ROS)[194]. Dox inhibits transcription directly by irreversibly binding to Topoisomerase II (TopoII)[195] and adducting with DNA, which is classically considered its main cytotoxic mode of action[196]. Furthermore, dox impairs Ca^{2+} processing in the endoplasmic and sarcoplasmic reticulum, one of the key contributions to its off-target side effect in heart tissue[197,198]. Dox cytotoxicity produces multiple effects on cellular physiology, whereby a multitude of processes that each disrupt cellular function operate together to induce apoptosis in rapidly dividing tumour cells[199,200].

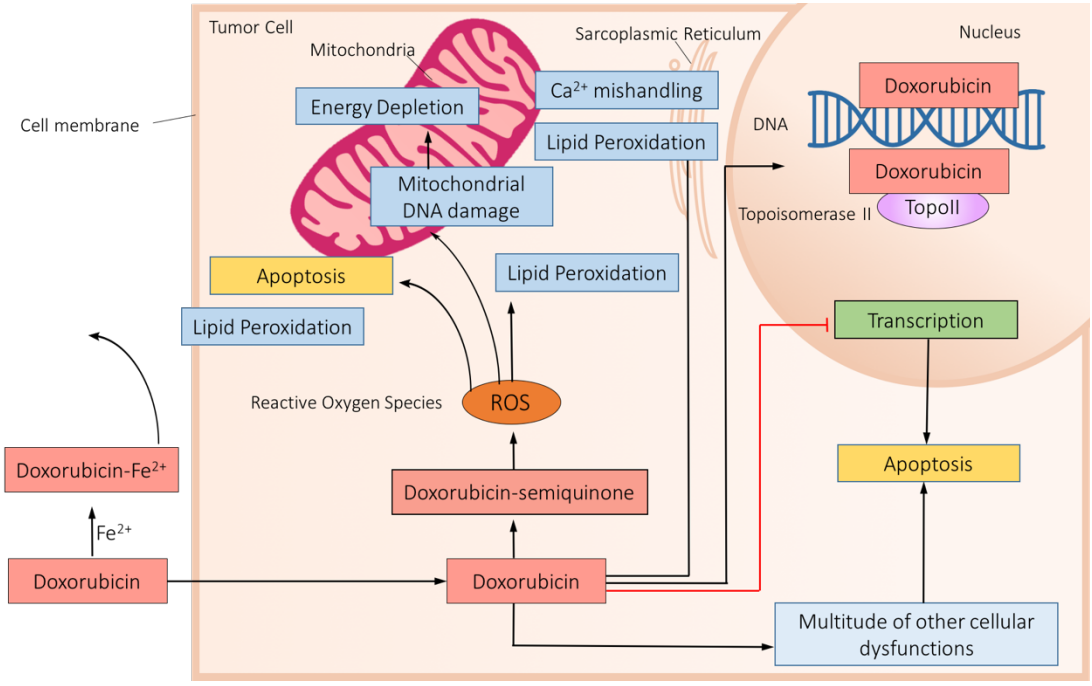

Figure 4.2 Doxorubicin mechanism of action. Doxorubicin chemotherapy has a range of effects on tumour cells. Dox complexes with Fe^{2+} causing lipid peroxidation across and within cellular membranes. Dox irreversibly binds to Topoisomerase II (TopoII) and adducts with DNA. By producing Reactive Oxygen Species (ROS), Doxorubicin-semiquinone induces mitochondrial DNA damage and energy depletion as well as impaired Ca^{2+} processing in the endoplasmic and sarcoplasmic reticulum. These processes work in concert to drive apoptosis in tumour cell populations.

Early studies of anthracycline antitumour activity investigated the ability of dox to intercalate into the DNA double helix and form DNA adducts[201]. Once taken up by the tumour cell, the planar ring structure of dox intercalates between adjacent DNA base pairs. The relationship between dox cytotoxicity and DNA adduct formation is a well-established property of this drug[202], with the N3' amino group forming key interactions between DNA strands within the dox-DNA adduct and along the minor groove of DNA during intercalation[203,204].

Dox irreversibly binds to DNA Topoisomerases (Topo)[205,206], ubiquitous enzymes in biology that control access to DNA supercoiling and entanglement during transcription and replication of the cell cycle. A recent study implicated Topo II β, a key enzyme also conserved across all mammalian cells as the essential driver of dox-induced cardiotoxicity in mice[207]. The primary amino group at the C3' position of the sugar moiety of dox plays an essential role in the formation of the TopoII-dox-DNA complex[205].

A multitude of moderate to severe side effects are observed in patients when dox is directly injected as the hydrochloride salt[208–210]. Dox is primarily dose limited due to the immediate risk of acute cardiac toxicity incidence at higher dosages[200]. As a result, much of the research pertaining to anthracycline development has focused on suppressing cardiotoxicity during administration of the drug[211]. Attempts to limit cardiac toxicity by altering aspects of the dosage rate or excipient formulations of dox have shown only limited clinical benefit[212,213]. Despite concerted efforts to improve the side-effect profile, ~ 10 % of patients will develop cardiomyopathy post administration, a chronic degeneration of cardiac tissue which may lead to fatal myocardial infarction[214].

4.2 The Rational Design Basis for Masking the C3' Amino Group of Doxorubicin

As much evidence supports the role of dox's C3' amino group in eliciting cytotoxicity, this functional group remains a focus for chemical modification. Prodrugs of dox that mask and

selectively de-protect this functional group have been developed. Below are three key examples that prompted the rational basis for our prodrug design.

A peptidyl moiety was conjugated to the NH_2 at C3' of dox as a selective substrate of an upregulated intratumoural enzyme known as plasmin[215] (Fig 4.3.a). When plasmin cleaves the peptidyl masking group, dox would be released and accumulate in tumour tissue expressing high levels of the enzyme. The (Boc-Val-Leu-Lys)-dox prodrug masked the amino group at C3' by acylation to a short poly peptide via the C terminal of a Lysine. The peptidyl group incorporated a D configured Boc-protected terminal valine, which was expected to retain plasmin induced hydrolysis whilst preventing off target activation by other endogenous amino peptidases. Boc-Val-Leu-Lys-dox was six fold less toxic than the unmodified drug in a Rous sarcoma virus transformed chicken embryo fibroblast toxicity assay. This moderate improvement in toxicity came at the cost of significantly reduced dox potency from slow release, observed in a subsequent *in vivo* B16 Melanoma treatment assay. We noted the author's suggestion that a cleavable spacer moiety between the drug and peptide may contribute to improved substrate metabolism by plasmin hydrolysis.

Subsequently an antibody directed enzyme prodrug therapy (ADEPT) strategy reported a dox prodrug that incorporates a spacer moiety linked to the amino group at C3' position, designed to be cleaved in the presence of glycosidases[216]. Conceptually this ADEPT strategy is as follows. A covalently bonded monoclonal antibody (MAb)-glycosidase complex would be administered and target tumour cells by MAb receptor-antigen recognition, resulting in elevated levels of glycosidase in tumour tissue. Next, dox prodrug would be administered, with the protected amino group masking drug activity during systemic circulation. Selective cleavage of the prodrug in the presence of the tumour-MAb bound glycosidase releases dox locally at the site of tumour. Accordingly, glucuronide, the sugar substrate of glycosidase was attached to dox through a self-immolative spacer group between the drug and sugar moiety. The linked spacer group, an ortho- or para-hydroxybenzylcarbamate derivative was expected to spontaneously eliminate after enzymatic cleavage (fig 4.3.b). Significant cytotoxic reduction of the dox prodrugs was observed in L1210 Leukemia cells *in vitro* in the absence of

glycosidase. The hydroxybenzylcarbamate spacer group was also reported as stable in human plasma. In the presence of 0.1 μg / mL E. Coli β-glucuronidase, the ortho-substituted prodrug underwent rapid enzymatic hydrolysis followed by spacer elimination to release dox.

More recently, a bioorthogonal dox deprotection strategy utilized a similar reactivation strategy[217]. By masking the amino group with a benzyl azide functional group (fig 4.3.c), a dox prodrug decreased growth inhibition in A431 human vulvar skin squamous carcinoma cells. A cytotoxic effect was re-established by the repeated infusion of a phosphine derivative into cell culture, releasing dox via the Staudinger reaction. Further evidence that such prodrug was capable of bioorthogonal deprotection was reported in 2014 when a strain-promoted 1,3-dipolar cycloaddition reaction between the same N-p-azidobenzyl dox (Fig 4.3.c) and a trans-cyclooctene (TCO) was reported to proceed *in vitro* at two orders of magnitude faster than the Staudinger reaction[218].

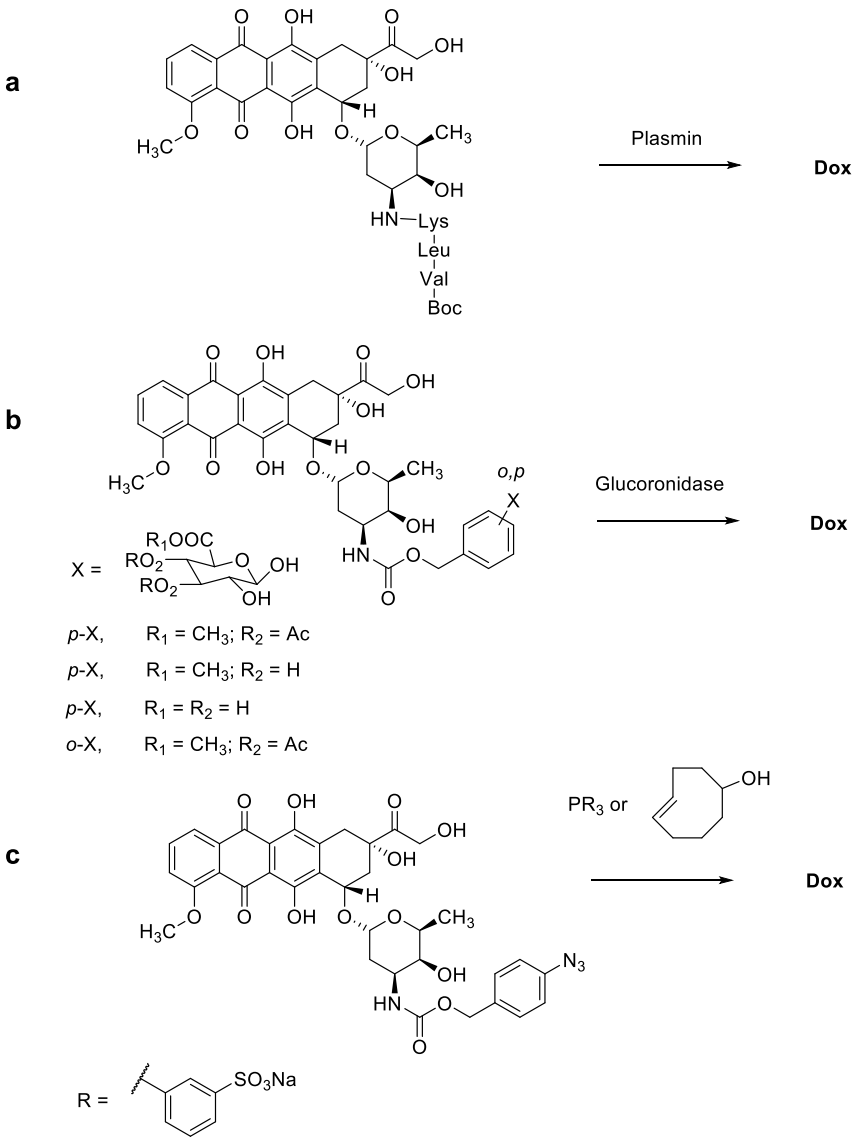

Figure 4.3 C3' amino-protected prodrugs of doxorubicin. (**a**) A Boc-Val-Leu-Lys-dox prodrug was capable of releasing drug in the presence of plasmin, an upregulated enzyme in tumour tissue. (**b**) A dox prodrug masked with a spacer linked glucuronide promoiety released drug via glucoronidase hydrolysis followed by linker self-immolation; and (**c**) A dox prodrug masked with benzyl azide and unmasked by phosphine derivatives (Staudinger reduction) or trans-cyclooctene (a strained promoted 1,3-dipolar cycloaddition) followed by linker self-immolation.

These key publications focused our attention toward the development of bioorthogonal dox prodrugs by masking the amino group at C3' with promoieties capable of selective deprotection by Pd^0 bead catalysis.

4.3 Synthesis of Novel Doxorubicin Prodrugs

Prodrugs were generated by using the novel propargyloxybenzylcarbonyl (Pobc) group described in Chapter 3. The Pobc group was incorporated to increase steric hindrance whilst providing sensitivity to Pd^0 catalysis, as suggested by preliminary evidence from *in vitro* assays reported in Chapter 3 with gemcitabine prodrugs.

The propargyloxycarbonyl (Poc) group was also chosen to mask the amino group of dox, as Poc deprotection has been utilized previously[34,89,219] to conduct bioorthogonal Pd-mediated cleavage on fluorophores, proteins and chemotherapeutics. The carboxybenzyl (Cbz) group was chosen to mask dox with a metabolically stable group non-responsive to oxidative Pd catalysis. The Cbz group is labile to Pd catalysts in the presence of H_2[220]. In the absence of a hydrogen source, i.e. in a biocompatible conditions, we have observed that the Cbz group is highly resistant to cleavage[89]. As a benzyl group imparts increased steric bulk relative to a propargyl group, it would be expected that an N-Cbz masked dox prodrug would increase steric hindrance about the carbamate bond, improving stability to metabolic cleavage.

All dox prodrugs were synthesized in a semisynthetic strategy using 4-nitrophenyl activated protecting groups (scheme 4.4). **27** and **28** were first alkylated using three equivalents of propargyl bromide and sodium carbonate to yield **29** and **30** in 30 % and 99 % respectively. Treatment of **29**, **30**, **38** or **39** with excess pyridine in the presence of 4-nitrophenyl chloroformate formed the corresponding activated carbonates **31**, **32**, **40** and **41** in 72 – 75 % yield. Each reaction was undertaken in the dark at 0 °C, to reduce the possibility of polymerization. Each moiety was added to dox in the presence of pyridine in dry DMF under nitrogen to yield carbamate prodrugs **42**, **43**, **44**, and **45** in 45 – 64 % yield.

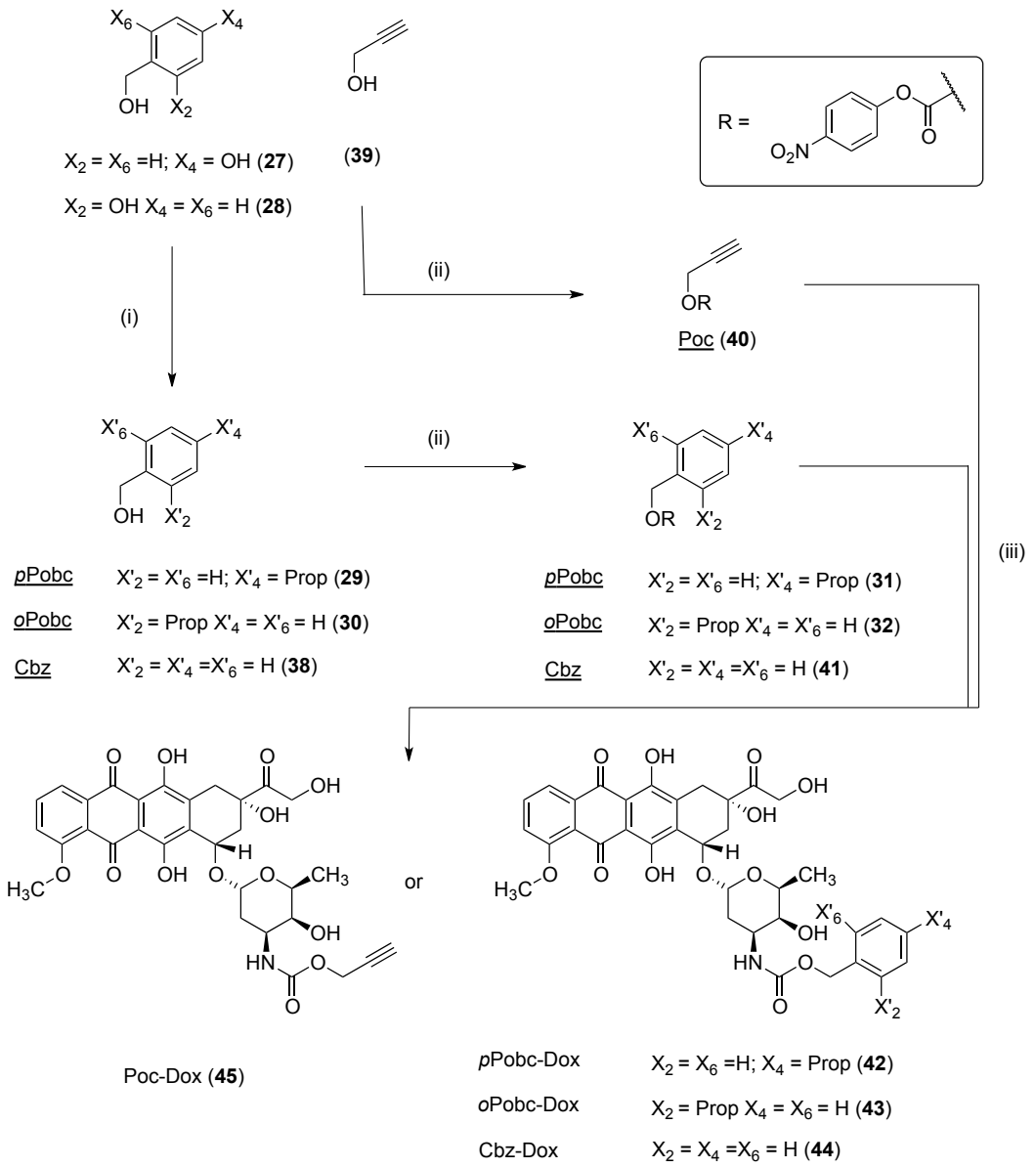

Scheme 4.4 Synthesis of doxorubicin prodrugs 42, 43, 44 and 45. Reagents and Conditions: (i) propargyl bromide (3 equiv.), Na_2CO_3, toluene; reflux overnight (30 – 99 %); (ii) 4-nitrophenyl chloroformate (1.1 equiv.), pyridine (excess) THF, 0 °C, dark, overnight (72 – 75 %); (iii) doxorubicin (1.5 equiv.), pyridine, DMF, N_2, rt, overnight (45 – 64 %)

4.4 Doxorubicin Prodrug Biocompatibility Assays

Glioblastoma U87 and Prostate cancer DU145 cell lines were chosen as cancer cell models due to the use of dox in associated indications as a first-line or adjuvant drug alone or in combination therapy. Dose-response studies were conducted on dox and each of **42**, **43**, **44**, and **45** in cell culture (fig 4.5).

a

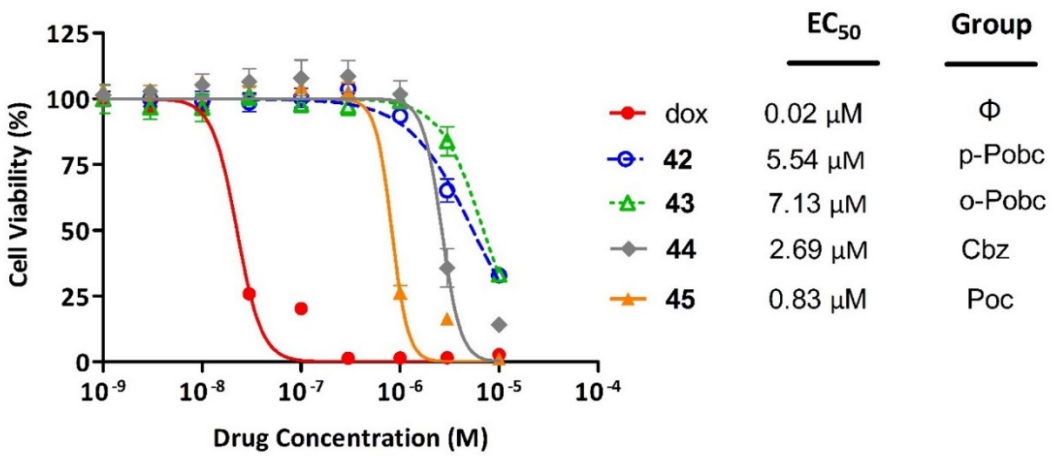

b

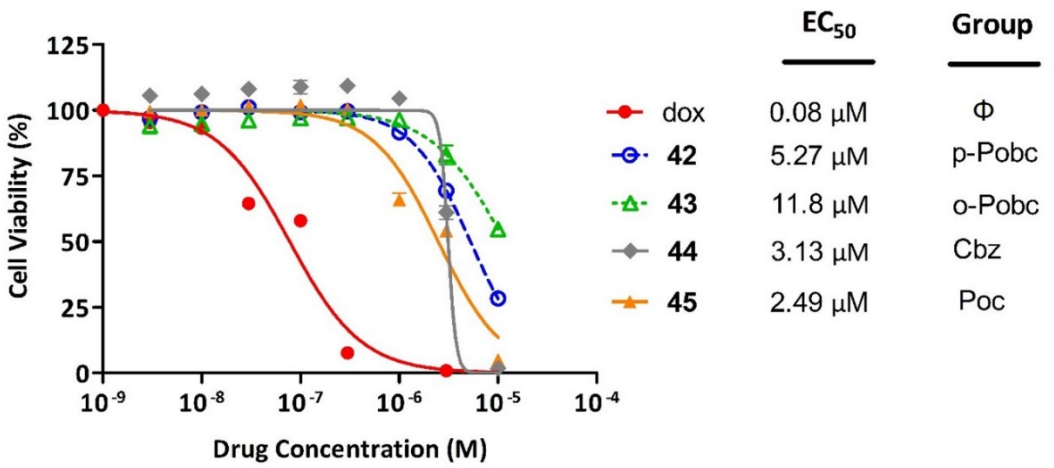

Figure 4.5 Study of doxorubicin cytotoxic reduction produced by 42 - 45 prodrugs in cell culture. Semilog dose−response curves and calculated EC_{50} values of prodrugs **42** (dashed blue), **43** (dashed green) **44** (solid grey), and **45** (solid orange) in comparison to those of unmodified dox (solid red) in (**a**) DU145 and (**b**) U87 cells. Cell viability was measured at day 5 using PrestoBlue® reagent. Error bars: ± SD from *n* = 3

All prodrugs showed a significant reduction in cytotoxicity relative to dox. As predicted, the Poc group conferred the least steric hindrance to the carbamate bond, resulting in a narrower therapeutic window [EC_{50} (**45**) / EC_{50} (dox) ~ 31(U87); 36(DU145)]. Notably, the two Pobc derived prodrugs displayed much higher reduction of cytotoxicity [EC_{50} (**42**) / EC_{50} (dox) ~

64(U87); 242(DU145)], [EC_{50} (**43**) / EC_{50} (dox) ~ 134(U87); 310(DU145)], superior to that of the Cbz prodrug [EC_{50} (**44**) / EC_{50} (dox) ~ 40(U87); 117(DU145)].

4.5 Design of the *bis*-o-Pobc Protecting Group

As **43** was found to be the most efficient group for dox deactivation, we further envisioned functionalizing a *bis*-2,6-propargyloxybenzylcarbonyl (*bis*-o-Pobc) group to the amino group at the C3' position. The introduction of a second propargyloxy group was intended to simultaneously enhance steric hindrance and increase the propensity of Pd-mediated moiety self-immolation by virtue of two available trigger groups instead of one (scheme 4.6).

a

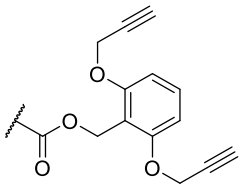

The *bis*-o-Pobc group

b

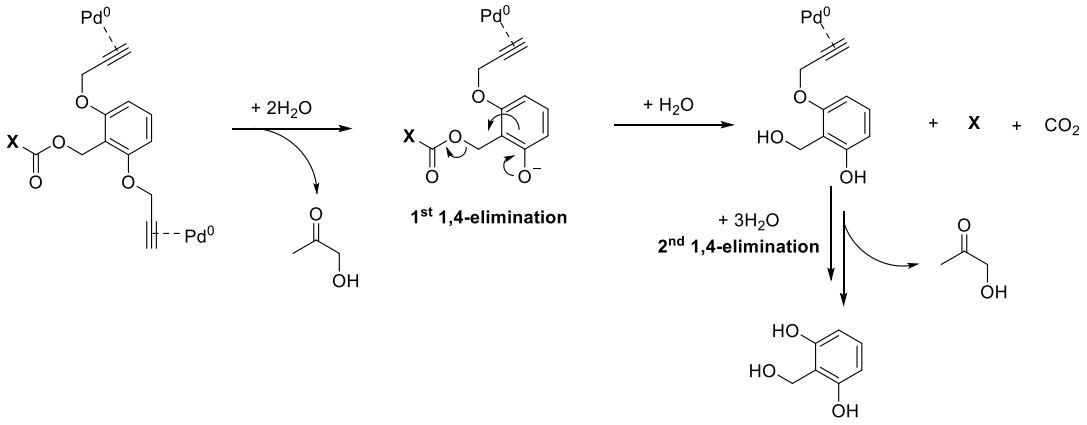

Scheme 4.6 The *bis*-2,6-propargyloxybenzylcarbonyl (*bis*-o-Pobc) group. (**a**,**b**) A proposed mechanism for the Pd^0 catalysed cleavage of the bis-o-Pobc groups in water. Pd-mediated oxidative cleavage of the propargyl groups trigger benzyl elimination to release X (an $-NH_2$ or –OH drug), CO_2, 2,6-dihydroxybenzyl alcohol and two equivalents of acetol.

A semisynthetic strategy was developed to incorporate *bis*-o-Pobc (scheme 4.7). **46** was propargylated at each of the hydroxyl positions using propargyl bromide and sodium carbonate. The carboxylic group was then reduced to alcohol **48** by lithium aluminium hydride. Treatment with 4-nitrophenyl chloroformate in the presence of pyridine formed the corresponding carbonate **49**. Adding **49** to dox in the presence of pyridine yielded carbamate prodrug **50** in moderate yield.

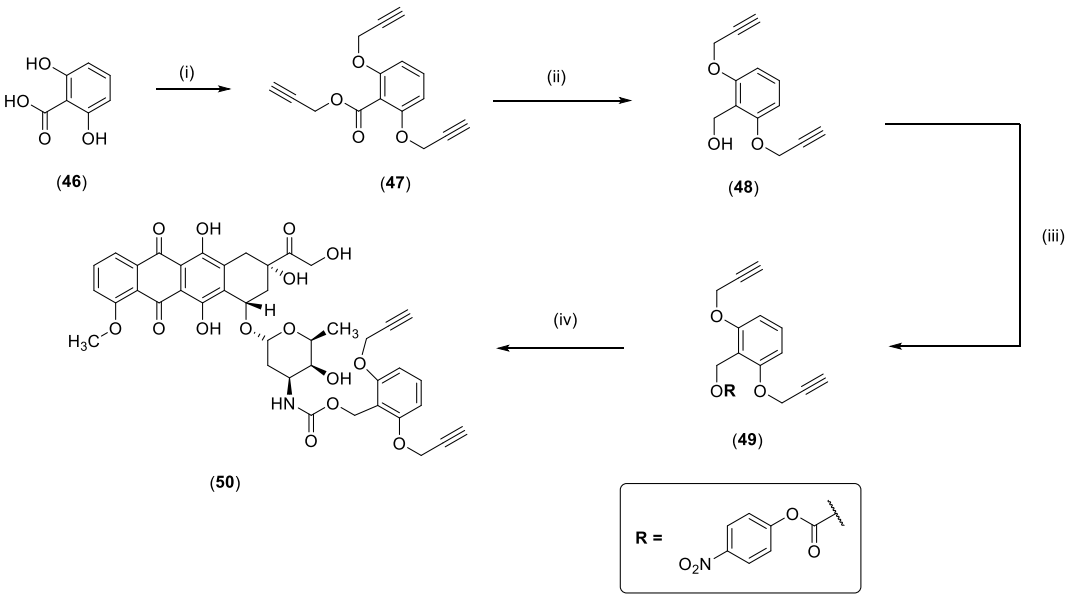

Scheme 4.7 Synthesis of doxorubicin prodrug 50. Reagents and Conditions: (i) propargyl bromide (0.25 equiv.), Na_2CO_3, toluene, 4 °C, overnight (44 %); (ii) $LiAlH_4$, THF, 10 % NaOH, 0 °C, overnight (63 %); (iii) 4-nitrophenyl chloroformate (1.1 equiv.), pyridine, THF (86.5 %), rt, overnight; (iv) doxorubicin, pyridine, DMF, N_2, 0 °C overnight (30 %)

A dose-response study was conducted on **50** and dox in Glioblastoma U87 and Prostate cancer DU145 cell lines (fig 4.8).

a

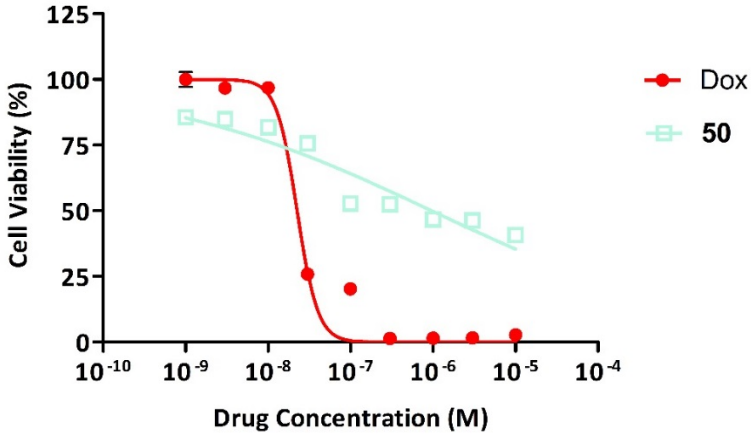

b

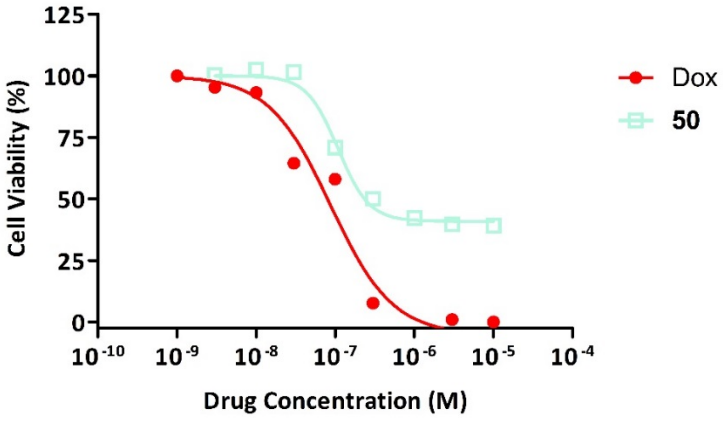

Figure 4.8 Study of doxorubicin cytotoxic reduction produced by prodrug 50 in cell culture. Semilog dose−response curves and calculated EC_{50} values of prodrug **50** (light blue), in comparison to that of unmodified dox (solid red) in (**a**) DU145 and (**b**) U87 cells. Cell viability was measured at day 5 using PrestoBlue® reagent. Error bars: ± SD from *n* = 3

Although **50** reduced cytotoxicity with respect to dox, the effect was not as prominent as with either **42** or **43**. It was noted that **50** was practically insoluble in standard solutions of cell media when added in a 0.1 % (v/v) DMSO solution at concentrations above 1 μM, which may account for the unusual semi-log dose response curves at concentrations above 1 μM. This precluded the ability to reliably assess the EC_{50} value of **50** at concentrations above 1 μM. Nevertheless, as **50** was considerably less cytotoxic to cells than dox it progressed together with prodrugs **42** – **45** into Pd-mediated prodrug conversion studies.

4.6 Reviewing the Pd Device

Next, prodrugs of dox will be progressed into *in vitro* activation studies. As this section reports both on the Pd-mediated activation of dox prodrugs, as well as the subsequent development of novel Pd^0 beads that enhance conversion and release kinetics of drug, a small update on the current state of Pd catalysis in our lab is provided herein.

Palladium is a versatile transition metal that has revolutionized the last 50 years of organometallic chemistry[221,222]. Widespread application comes from the fact that Pd and Pd complexes are capable of adducting to many organic molecule classes; including alkenes, alkynes, dienes and CO, as well as alkyl, aryl and vinyl halides[221]. Adduct formation is capable of forming or cleaving carbon-carbon bonds, depending on the system in question. Pd has four oxidation states (Pd^{II}, Pd^0, Pd^{IV} and Pd^{I}); allowing for the metal to function as an electrophile (Pd^{II}) or nucleophile (Pd^0). Pd^0 emerges as an attractive catalyst candidate to conduct bioorthogonal carbon cleavage reactions due to a low toxicity profile and broad scope of activity in standard carbon-heteroatom cleavage chemistry[223]. Pd^0 catalysts have been investigated for their capability to deprotect prodyes and prodrugs in biological systems [224,225].

We have utilized a previously reported methodology to routinely synthesise and encapsulate Pd^0 nanoparticles into polyethylene glycol-polystyrene (PEG-PS) microspheres (beads) of regular size[81]. These Pd^0 beads have formed the basis of the BOOM Pd^0 labile prodrug and probe deprotection strategy for the past five years[33,34,81,89,90,130]. As the library of prodrugs amenable to Pd^0 dependant deprotection continues to expand, a corresponding focus on advancing the Pd^0 device is necessary. This will ensure that optimally functional forms of both the device and the therapeutic are at hand as BOOM chemotherapy progresses into the development of pre-clinical assays.

4.7 Design, Synthesis and Characterization of Pd^0 Functionalized Beads

Pd^0 nanoparticles are highly reactive and efficient catalysts due principally to their high surface area to volume ratio[226]. Several drawbacks however preclude their direct use in complex living systems. The difficulty of positioning or administering a homogenous catalysts for site selective activation presents the most obvious challenge: undesired distribution of a soluble catalyst about the organism may lead to toxicity (i.e. via unwanted organ accumulation), low activation in the tissue of interest (as a result of off target accumulation and poor distribution) and/or rapid clearance (by immune system mediated phagocytosis and removal from the bloodstream). Encapsulating individual Pd^0 nanoparticles within a solid support system as a heterogeneous catalyst would allow for the surgical insertion of a device directly into the tissue of interest. Ideally the device would function as a bio-inert medical insert loaded with immobilized Pd^0 nanoparticles that would localise the effect of catalysis to the target tissue.

An immobilization technique was initially reported[227], then subsequently optimised[228,229] for the encapsulation of Pd^0 nanoparticles into 130 μm diameter PEG-PS microspheres. NovaSyn TG® amino resins (130 μm diameter) are treated with $Pd(OAc)_2$ (3 equivalents.) causing the resin to change colour from translucent to dark orange. Resin bound $Pd(OAc)_2$ is then reduced to Pd^0 in a 10 % hydrazine monohydrate solution in MeOH, affecting a subsequent colour change to black. Addition of Fmoc-Glu(OH)-OH via a standard Oxyma/DIC amide coupling procedure physically entraps Pd^0 to the resin. This protocol reliably synthesises comparable batches of Pd^0 beads that may be stored at 4 °C for up to 12 months with no observed reduction in catalytic efficiency. Our group has previously undertaken extensive studies to characterise and image these beads. Once synthesised, each batch undergoes a ninhydrin test and Scanning Electron Microscopy (SEM) (fig 4.9) alongside a standard catalytic efficiency assay using an activatable molecular probe[89]. Suitable batches are directly utilized in standard BOOM activation assays with no further preparation.

a **b**

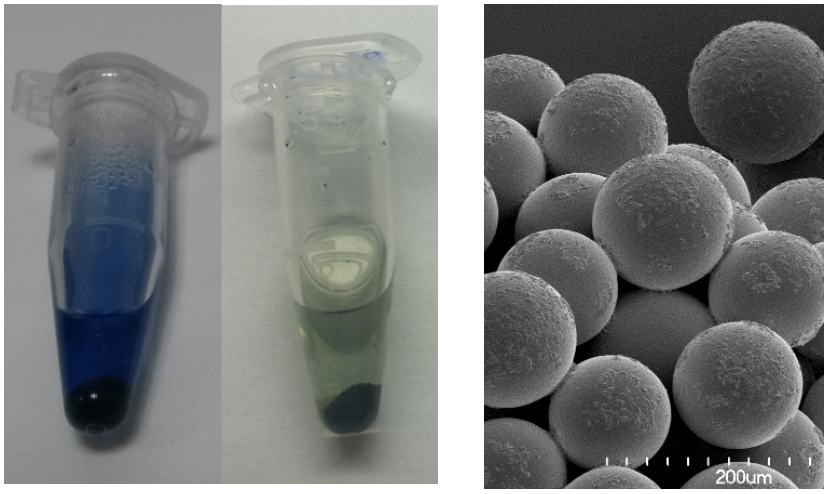

Figure 4.9 Assessment of 130 µm diameter Pd^0 beads for coupling and size homogeneity. (**a**) Ninhydrin test to determine the efficacy of the final coupling reaction in accordance with a standard solid phase peptide synthesis protocol[33]. Left sample dyed blue due to incomplete Oxyma/DIC amide coupling reaction. Clear solution from right sample shows complete coupling[81,230] (**b**) Scanning Electron Microscopy of successfully Oxyma/DIC amide coupled 130 µm diameter Pd^0 beads to determine homogeneity in bead size and shape using a Hitachi S-4700 scanning electron microscope

4.8 Non-biological Pd-mediated Doxorubicin Prodrug Conversion Study

Having determined that Poc, Cbz, p-Pobc, o-Pobc and *bis*-o-Pobc groups confer reduced bioactivity by masking the C3' amino group of dox, the next step was to determine the sensitivity of each of these groups to standard Pd^0 bead mediated catalysis. This was achieved by first incubating **42**, **43**, **44**, **45** and **50** at 100 µM in PBS solution in a thermomixer at 1400 rpm, 37 °C for 48 hr then submitting 50 µL aliquots to UPLC analysis to determine the elution time of each compound (fig 4.10).

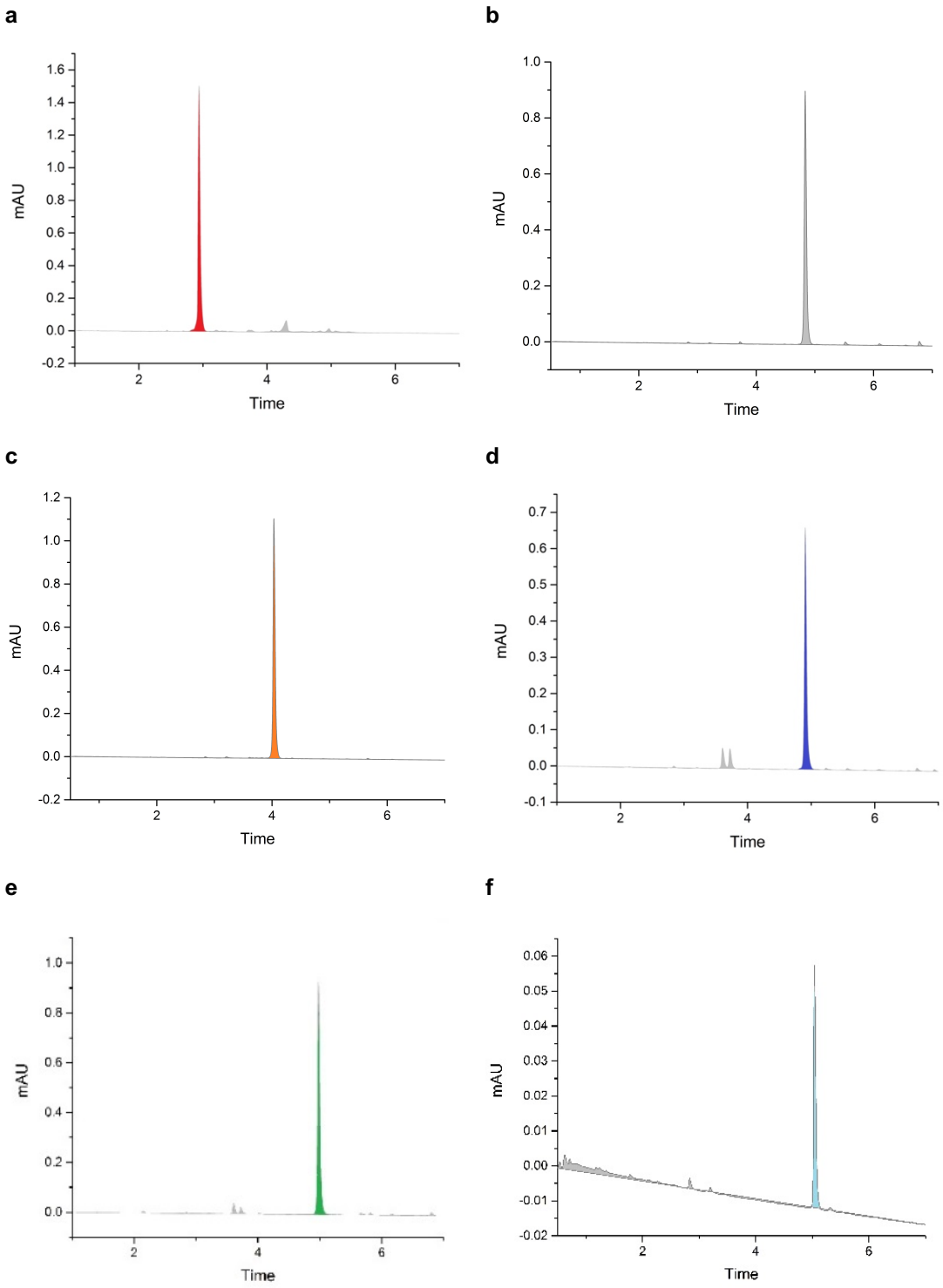

Figure 4.10 Non-biological stability assay of doxorubicin prodrugs 42 – 45 and 50. UPLC chromatograms of (**a**) dox (red), (**b**) **44** (dark grey), (**c**) **45** (orange), (**d**) **42** (dark blue), (**e**) **43** (green) and (**f**) **50** (light blue) as 100 μM solutions in PBS incubated at 1400 rpm, 37 °C for 48 hr. Impurities consistent with background are highlighted in light grey across all chromatograms.

Each of **42 – 45** and **50** were stable in PBS after 48 hr. Retention times were assigned, dox (retention time **37** = 2.9 min) and prodrugs (retention time **44** = 4.8 min, **45** = 4.1 min, **42** = 4.9 min, **43 =** 5.0 min and **50** = 5.1 min). Next, 1 mg / mL of 130 μm Pd^0 beads was added to each prodrug mixture and the experiment repeated over a 48 hr period (fig 4.11).

a

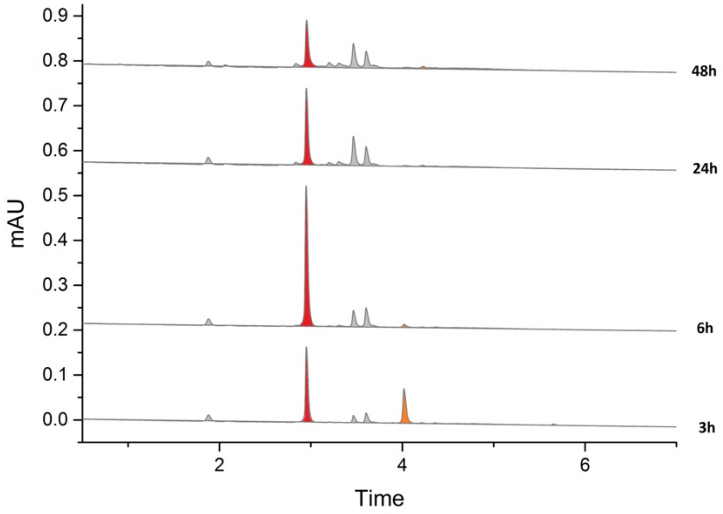

b

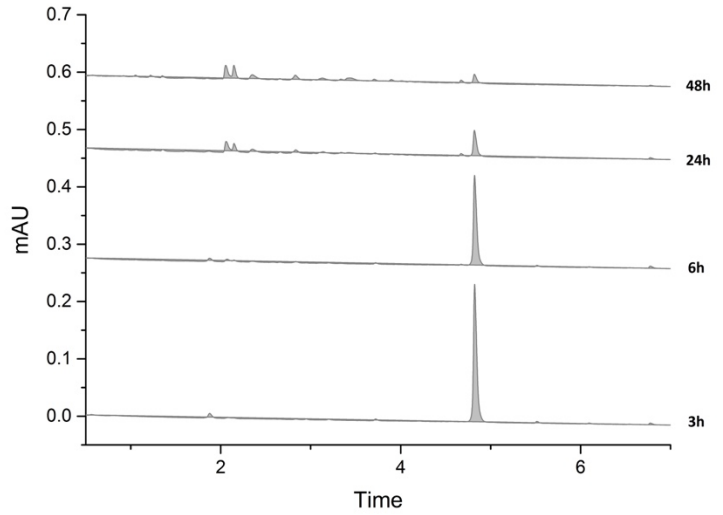

c

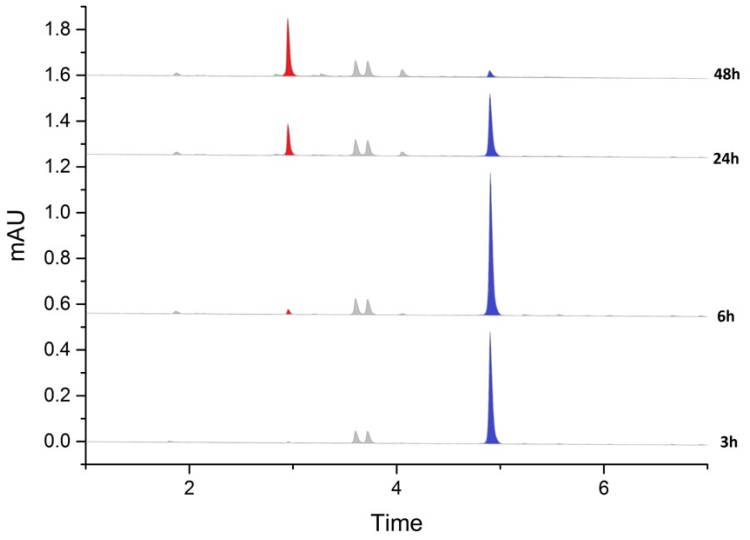
1.8
1.6
1.4
1.2
1.0
0.8
0.6
0.4
0.2
0.0
mAU
48h
24h
6h
3h
2
4
6
Time

d

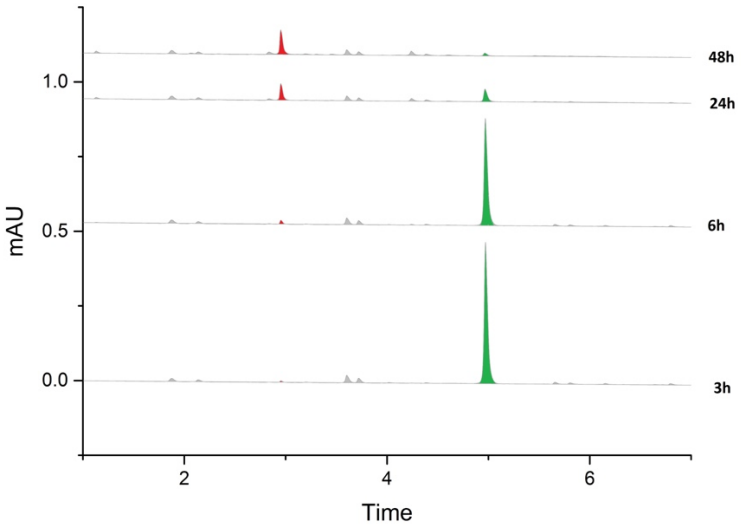
1.0
0.5
0.0
mAU
48h
24h
6h
3h
2
4
6
Time

e

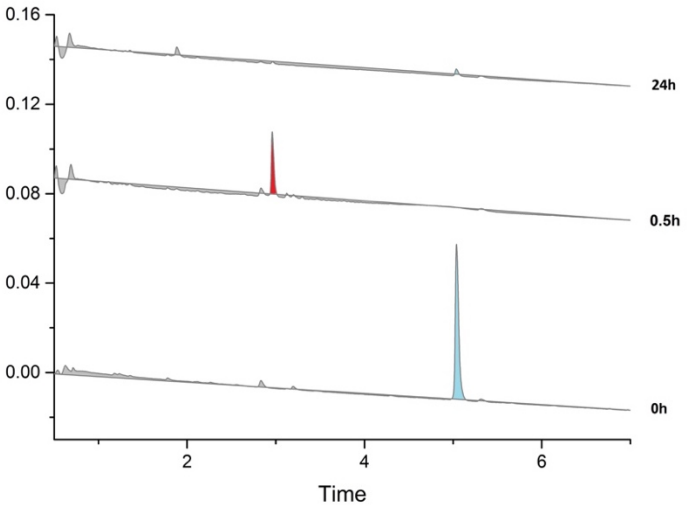
0.16
0.12
0.08
0.04
0.00
24h
0.5h
0h
2
4
6
Time

Figure 4.11 Non-biological conversion assay of doxorubicin prodrugs 42 – 45 and 50 in combination with 130 μm Pd^0 beads. UPLC chromatograms producing doxorubicin (red) from dox prodrugs of (**a**) **45** (orange), (**b**) **44** (grey), (**c**) **42** (dark blue), (**d**) **43** (green) and (**f**) **50** (light blue) as 100 μM solutions in PBS incubated with 1 mg / mL of 130 μm Pd^0 beads at 1400 rpm, 37 °C for 3, 6, 24 and 48 hr (a-d) or 0, 0.5 and 24 hr (e). Impurities consistent with background are highlighted in light grey across all chromatograms.

Figure 4.11 confirms the Pd^0-mediated cleavage of **45**, **42**, **43** and **50**, with each prodrug producing dox to varying degrees over 48 hr. **44** was unmodified by Pd^0 catalysis, as predicted by previous studies and in accordance with the inability of Pd^0 to cleave the Cbz group in the absence of a hydrogen source. By-products were not observed.

One effect consistently observed was the reduction (or total disappearance) of either dox and/or prodrugs. This is seen in fig 4.11, whereby the signal for **44** (fig 4.11a), **42** (fig 4.11c) and **43** (fig 4.11d) diminishes over time without the equimolar generation or growth of other peaks (including dox). Further evidence is seen with **45** (fig 4.11b), whereby dox is rapidly produced then shrinks over time, and in the UPLC chromatogram of **50** (fig.4.11e) with peaks corresponding to both prodrug and drug absent after t = 48 hr. Despite this, significant quantities of dox was generated from prodrugs on incubation with a Pd^0 source. The proposed reason for this inconsistency is addressed in detail in section 4.10.

4.9 Pd-mediated Doxorubicin Prodrug *in vitro* Conversion Study

An *in vitro* BOOM assay was next conducted to test the extent to which conversion to dox would take place in combination with Pd^0 in a living system. Each of **42** – **45** and **50** was initially incubated at 1 μM in combination with 130 μm Pd^0 beads in prostate cancer DU145 cells (fig 4.12).

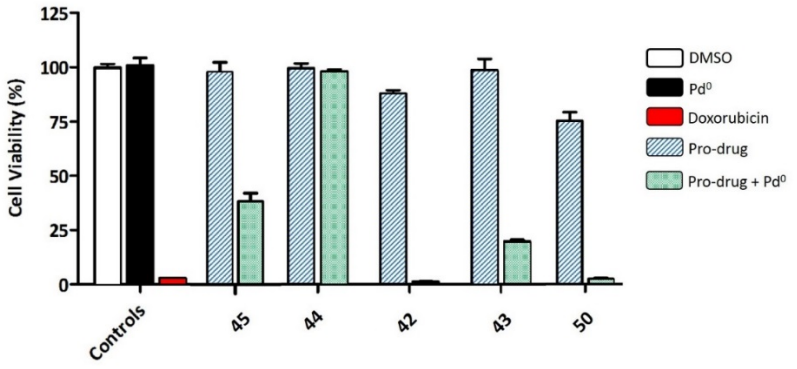

Figure 4.12 Preliminary Pd-mediated activation assay to compare activity of doxorubicin prodrugs 42-45 and 50 against drug in DU145 cells. Experiments: 0.1% (v/v) DMSO (untreated cell control, white); 1 mg/mL of 130 μm Pd^0 beads (negative control, black); dox (1 μM, positive control, red); **45**, **44**, **42**, **43** and **50** (1 μM, negative control, blue striped); and 1 mg / mL of Pd^0 beads + **45**, **44**, **42**, **43** and **50** (1 μM, BOOM activation, green checked). Cell viability was measured at day 5 using PrestoBlue® reagent. Error bars: ± SD from *n* = 3.

Whilst neither Pd^0 beads nor prodrugs affected cell viability individually, a significant cytotoxic effect was observed in combination. This assay confirmed the ability of 130 μm Pd^0 beads to cleave Poc, p-Pobc, o-Pobc and *bis*-o-Pobc protecting groups from a carbamate *in situ* to release dox. The Cbz group was resistant to cleavage as observed by UPLC studies and included as a negative control.

Each prodrug was next tested for BOOM activation across a range of therapeutically relevant drug concentrations in combination with 130 μm Pd^0 beads in prostate cancer DU145 cells (fig 4.13) and glioma U87 cells (fig 4.14).

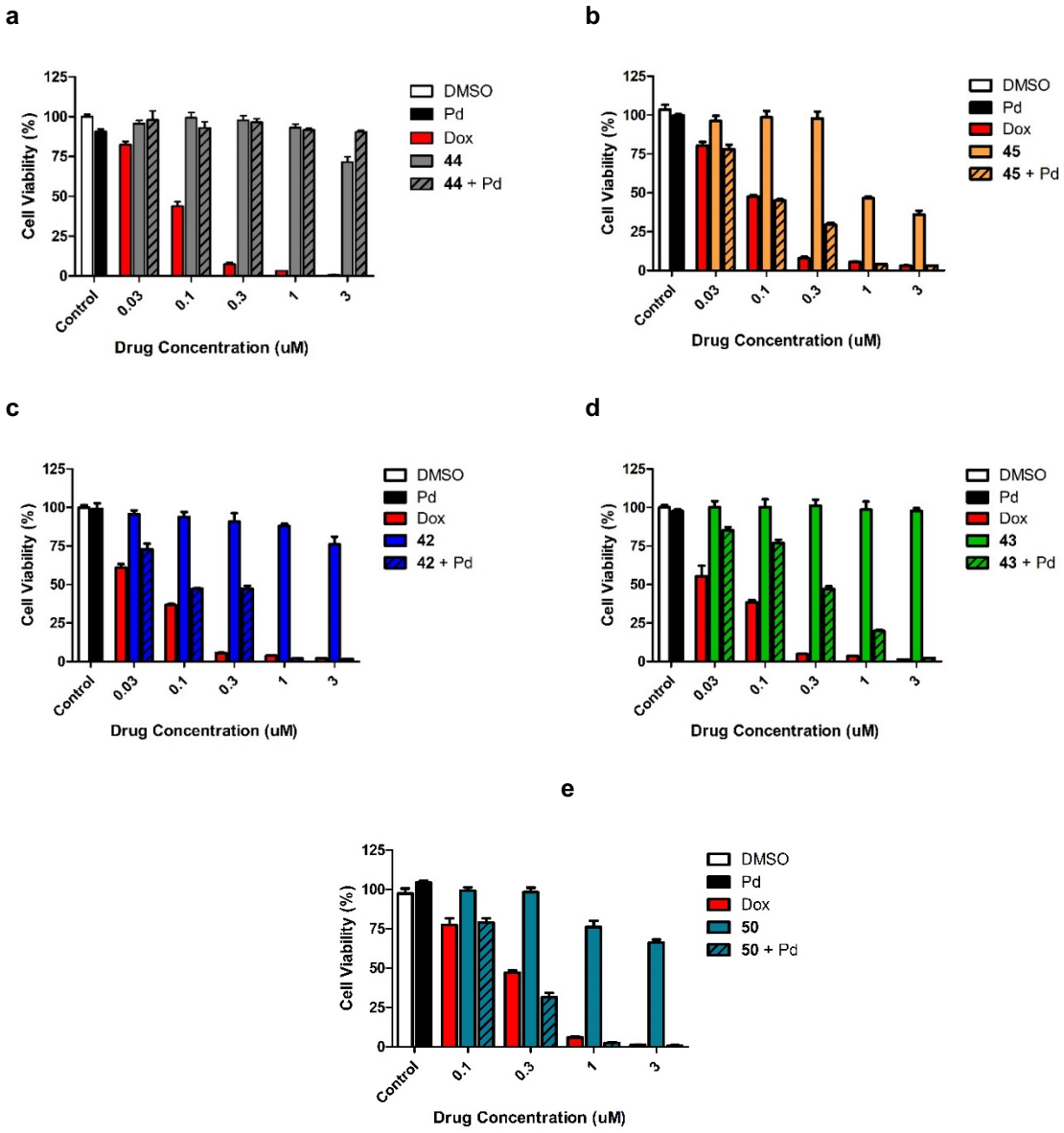

Figure 4.13 Pd-mediated activation of doxorubicin prodrugs in DU145 cell culture. Toxigenic effect of Pd-activated doxorubicin prodrugs across a concentration window in DU145 cells. Experiments: 0.1 % (v/v) DMSO (untreated cell control, white); 1 mg / mL of 130 µm Pd^0 beads (negative control, black); doxorubicin (positive control, red); Prodrug (**a**) **44**, grey, (**b**) **45**, orange, (**c**) **42**, dark blue, (**d**) **43**, green and (**e**) **50**, light blue; Prodrug + 130 µm Pd^0 beads (**a**) **44**, striped grey, (**b**) **45**, striped orange, (**c**) **42**, striped dark blue, (**d**) **43**, striped green and (**e**) **50**, striped light blue. Drug and Prodrug concentrations 0.03 – 3 µM (**42** - **45**), 0.1 – 3 µM (**50**). Cell viability was measured at day 5 using PrestoBlue® reagent. Error bars: ± SD from *n* = 3.

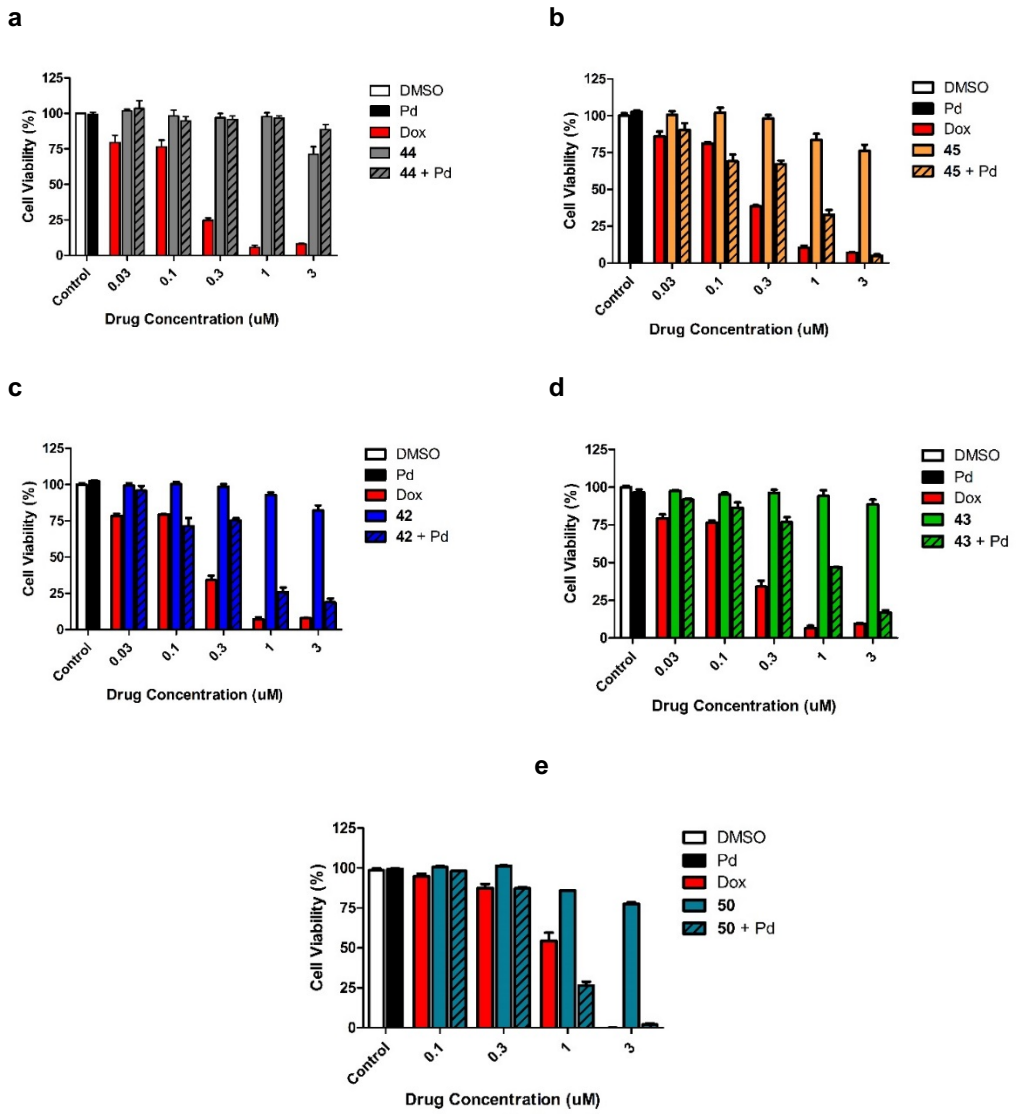

Figure 4.14 Pd-mediated activation of doxorubicin prodrugs in U87 cell culture. Toxigenic effect of Pd-activating doxorubicin prodrugs across a concentration window in U87 cells. Experiments: 0.1 % (v/v) DMSO (untreated cell control, white); 1 mg / mL of 130 μm Pd^0 beads (negative control, black); doxorubicin (positive control, red); Prodrug (**a**) **44**, grey, (**b**) **45**, orange, (**c**) **42**, dark blue, (**d**) **43**, green and (**e**) **50**, light blue; Prodrug + 130 μm Pd^0 beads (**a**) **44**, striped grey, (**b**) **45**, striped orange, (**c**) **42**, striped dark blue, (**d**) **43**, striped green and (**e**) **50**, striped light blue. Drug and Prodrug concentrations 0.03 – 3 μM (**42** - **45**), 0.1 – 3 μM (**50**). Cell viability was measured at day 5 using PrestoBlue® reagent. Error bars: ± SD from n = 3.

These studies (fig 4.13) (fig 4.14) confirm the ability of Pd^0 beads to release dox from each of **45**, **42**, **43** and **50** when incubated in combination across a broad therapeutic range. Although 130 μm Pd^0 beads incubated with **45**, **42** and **43** released significant levels of dox, these combinations were unable to elicit a cytotoxic response equivalent to dox alone in either cell line. **50** in combination with the 130 μm Pd^0 beads displayed a strong cytotoxic effect

comparable to dox, an indication consistent with the increased speed that **50** undergoes Pd^0-mediated cleavage (fig 4.11.e).

4.10 The Sequestration Effect of Doxorubicin and Prodrugs on Activation

The incomplete activation observed in BOOM *in vitro* assays and UPLC studies suggests that 130 μm Pd^0 beads do not activate prodrugs with optimal efficiency. In the routine process of UPLC sample preparation it was observed that after mixing for 30 min, the solution of all dox prodrugs and 130 μm Pd^0 bead + dox prodrug combinations would change colour from bright red to clear, with Pd^0 beads dyed dark red. This effect was not observed when dox and 130 μm Pd^0 beads where incubated together (fig 4.15).

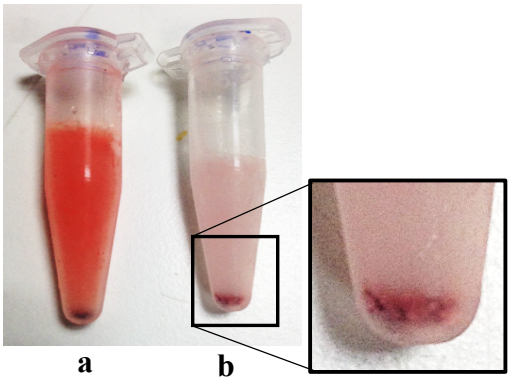

Figure 4.15 Sequestration of doxorubicin prodrugs by 130 μm Pd^0 beads. Experiment: separate solutions of (**a**) 100 μM dox and 1 mg / mL of 130 μm Pd^0 beads and (**b**) 100 μM **42** and 1 mg/mL 130 μm Pd^0 beads were stirred in 1 mL solutions of PBS at 37 °C for 30 min then flash frozen in liquid nitrogen and photographed.

Whereas rapid sequestration of prodrug into the Pd^0 bead from the surrounding environment is a highly attractive property for localised treatment (i.e. by absorbing administered prodrug from the bloodstream and accumulating it into the catalyst within the target tissue), this effect may be conversely limiting the catalytic effect during *in vitro* studies and thereby reducing the release (both physical and chemical) of the active drug.

4.11 Design and Synthesis of Novel Pd^0 Beads for Enhanced Activation

To overcome the catalytic inefficiency observed, we developed a library of Pd^0 beads across a range of sizes. We expected beads of smaller diameter (i.e. below 130 μm) would have both a smaller total internal volume available to sequester prodrug, and a greater surface area to volume ratio to increase reactivity. Using Merck Millipore's commercial catalogue of NovaSyn TG® amino beads, naked resins of varying size (10 μm – 110 μm diameter) were purchased and incorporated into the standard Pd^0 bead synthetic methodology by simply replacing the 130 μm diameter bead with a variable sized bead batch in the synthetic protocol. The author would like to acknowledge here that Dr Ana Pérez-López synthesised batches of Pd^0 beads according to the below protocol to allow for analysis.

Pd^0-functionalized beads were prepared from NovaSyn TG NH_2 HL resin (110 μm diameter (0.4 mmol NH_2/g)), (75 μm diameter (0.4 - 0.6 mmol NH_2/g)) and TentaGel® M NH_2 Monosized Amino TentaGel Microspheres (110 μm, 30 μm, 20 or 10 μm diameters) (0.2 - 0.3 mmol NH_2/g)) as described in Section 4.7. To confirm that the structural integrity of the bead had not been compromised during the synthesis, SEM images confirmed the spherical shape and size distribution of each batch of beads (fig 4.16).

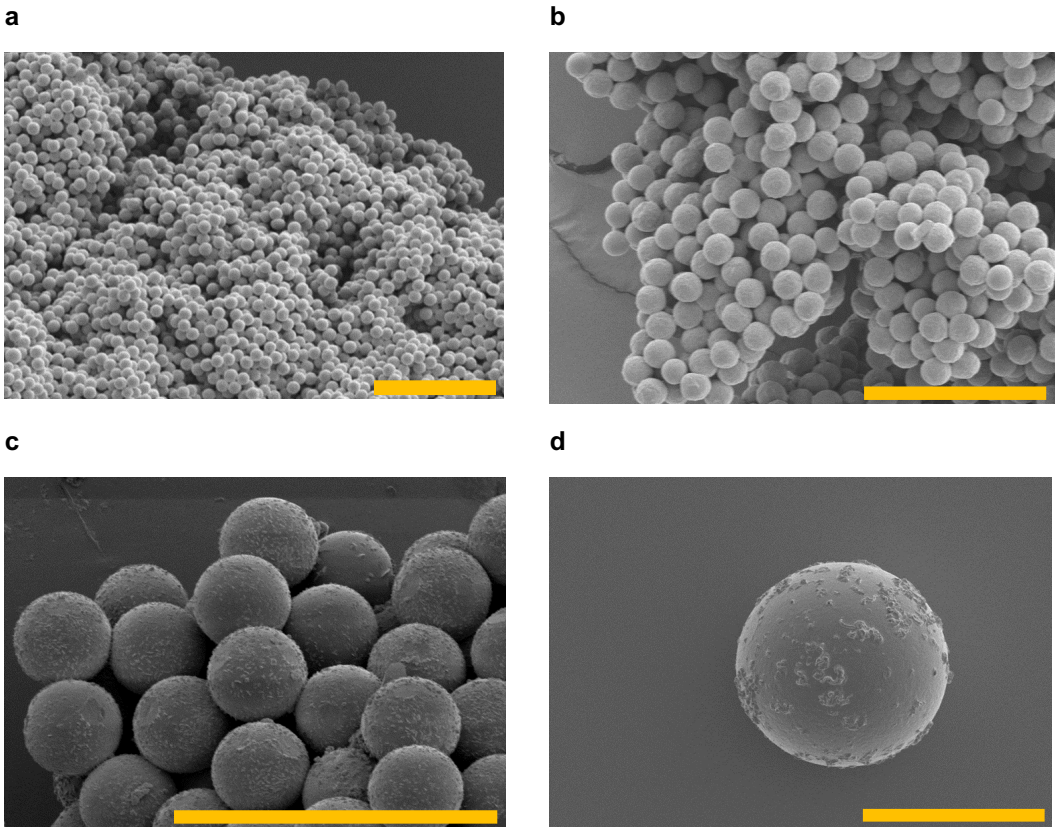

Figure 4.16 Scanning Electron Microscopy images of variable sized Pd^0 beads. (**a**) 10 µm Pd^0 beads (x 300 mag) (**b**) 20 µm Pd^0 beads (x 450 mag) (**c**) 30 µm Pd^0 beads (x 800 mag) and (**d**) 110 µm Pd^0 beads (x 450 mag) (scale bar = 100 µm)

Inductively Coupled Plasma Optical Emission Spectrometry (ICP-OES) was used to determine the loading of Pd^0 functionalized into the respective beads. ICP-OES is a standard technique used for the detection of trace metals in a sample by measuring the characteristic electromagnetic radiation emission spectra of known metals (i.e. Pd) produced via inductively coupled plasma excitation. Using this process an unknown concentration of metal sample may be determined against a standard curve. Accordingly, Dr Ana Pérez-López prepared a sample for ICP-OES analysis. Each pre-prepared Pd^0 bead batch was digested in a 10 % solution of nitric acid and heated overnight. The resultant mixture was diluted then submitted for ICP-OES to determine the respective loading of Pd in each of the beads (table 4.17).

Pd bead diameter	Loading of Pd (mmol/g)	Error ±
110 µm	0.42	0.0022
75 µm	0.52	0.0028
30 µm	0.19	0.0012
20 µm	0.06	0.0008
10 µm	0.07	0.0007

Table 4.17 Pd loading in variable sized beads. Pd loading (mmol / g) of Pd-beads calculated according to the amount of Pd-functionalized beads (mg) and the atomic weight of Pd (106.42 amu) by ICP-OES.

4.12 Testing the Catalytic Properties of 30 µm Pd^0 Beads in a Biological System

To determine the catalytic effect of each of the beads, a previously reported Pd^0-mediated *bis*-N,N'-propargyloxycarbonyl-rhodamine 110 (Poc-Rho) deprotection assay was tested against each batch of different sized beads[34]. This experiment was conducted by Dr Ana Pérez-López. Poc-Rho was prepared from Rhodamine 110 chloride as previously described[89], then 10 µM was dissolved in individual solutions containing PBS (1 mL) and incubated together with 1 mg of each 10 – 110 µm sized Pd^0-functionalized beads. The mixture was shaken at 1200 rpm and 37 °C in a thermomixer, then reaction crudes were scanned for Rhodamine 110 fluorescence signal at 6 hr by a standard multilabel plate reader (fig 4.18).

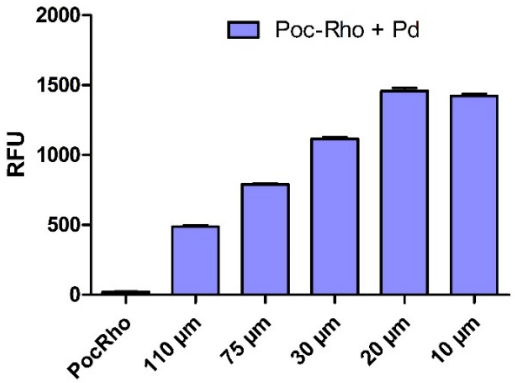

Figure 4.18 Fluorescent analysis of Pd-mediated Poc-Rho activation assay in PBS. Experiment: *bis*-N,N'-propargyloxycarbonyl-rhodamine 110 (Poc-Rho) (10 μM) in 0.1 % DMSO was converted into Rhodamine 110 by Pd^0-functionalized beads (1 mg/mL) of varying size after incubation in PBS (1 mL) for 6 hr at 1200 rpm and 37 °C in the Thermomixer. As a negative control, Poc-Rho in 0.1 % DMSO in the absence of Pd^0 beads was incubated under the same conditions. Fluorescence signal was measured at $\lambda_{ex/em}$ 480/535 nm. Error bars: ± SD from n = 8.

Observing an inverse relationship between catalytic effect and bead size, we were encouraged to repeat this experiment with addition of Fetal Bovine Serum (FBS). FBS is a complex milieu of enzymes that approximates the demands that biology would apply on the catalytic effect for each bead. Accordingly, Dr Ana Pérez-López conducted a Pd-mediated Poc-Rho deprotection assay was again tested by dissolving Poc-Rho (10 μM) in a 10 % FBS in PBS solution (1 mL), shaken at 1200 rpm and 37 °C in a thermomixer, then monitored for Rhodamine 110 fluorescence signal at 6 hr by a standard multilabel plate reader (fig 4.19).

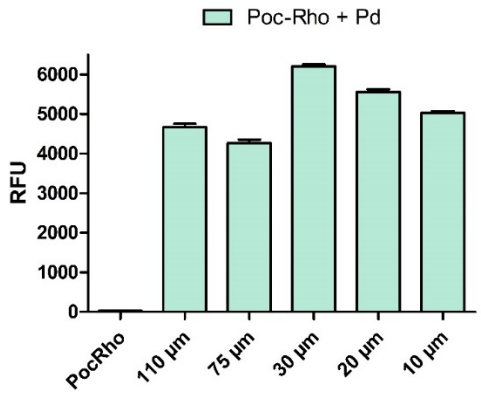

Figure 4.19 Fluorescent analysis of Pd-mediated Poc-Rho activation in PBS with FBS serum added. Experiment: *bis*-N,N'-propargyloxycarbonyl-rhodamine 110 (Poc-Rho) (10 μM) in 0.1 % DMSO was converted into Rhodamine 110 by Pd^0-functionalized beads (1 mg / mL) of varying size after incubation with 10 % Fetal Bovine Serum in PBS (1 mL) for 6 hr at 1200 rpm and 37 °C in the Thermomixer. As a negative control, Poc-Rho in 0.1 % DMSO in the absence of Pd^0 beads was incubated under the same conditions. Fluorescence signal was measured at $\lambda_{ex/em}$ 480/535 nm. Error bars: ± SD from n = 8.

An overall trend towards increasing catalytic activity in smaller beads was observed, with 30 μm beads outperforming other candidates. Although 10 and 20 μm beads also displayed good reactivity, studies have investigated the propensity of small particles[231], including polystyrene microspheres[232,233] of up to 10 μm in diameter to be engulfed by various phagocytes *in vitro*

and *in vivo*. As phagocytosis would have a detrimental effect on the function and positioning of Pd^0 beads in a living system, 30 μm diameter beads were selected as an optimal candidate on the basis of excellent reactivity and size characteristics.

4.13 Biocompatibility of 30 μm Pd^0 Beads *in vitro*

Once the catalytic effect of the new Pd^0 beads had been established, the next step was to validate biocompatibility across a diverse range of cell types *in vitro*. Pd^0 beads were incubated in DU145 and U87 cancer cell lines with increasing concentration and monitored for cell viability by adding PrestoBlue® reagent after 5 days and analysing with spectrofluorometry (fig 4.20). It was determined that 30 μm Pd^0 beads were at least as biocompatible as 130 μm Pd^0 beads in both cell lines, with cytotoxicity only observed across each cell line at concentrations above 1 mg/mL Pd^0 bead.

a

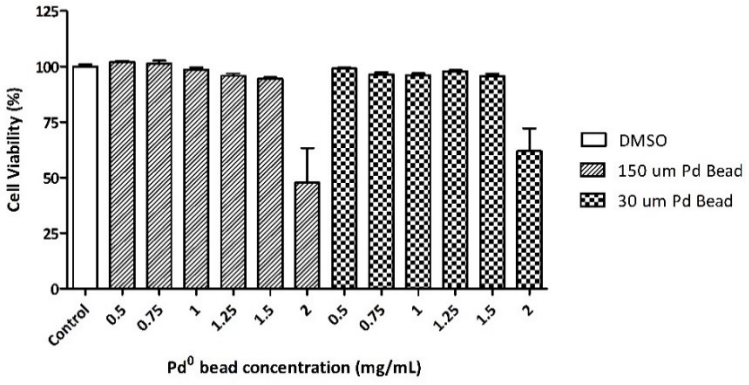

b

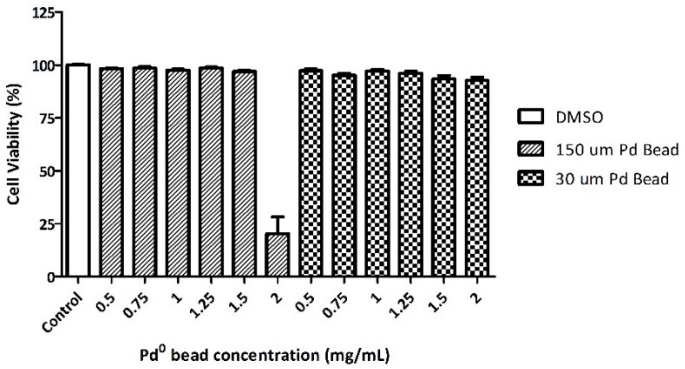

Figure 4.20 Biocompatibility of 30 µm vs 130 µm Pd^0 beads in cell culture. Study of the unspecific cytotoxic effect induced by incubating increasing concentrations (0.5 mg / mL – 2 mg / mL) of 30 µm Pd^0 beads (hatched) vs 130 µm Pd^0 beads (checked) in (**a**) DU145 and (**b**) U87 cell culture. Cell viability was measured at day 5 using PrestoBlue® reagent. Error bars: ± SD from *n* = 6.

4.14 Non-biological Pd-mediated Doxorubicin Prodrug Conversion Study with 30 µm Pd^0 Beads

Having validated the safety and reactivity of the 30 µm Pd^0 beads in biocompatible conditions, we progressed the beads into a non-biological Pd^0 mediated *in vitro* dox prodrug conversion assay. **42**, **43** and **50** were incubated at 100 µM in 0.1 % DMSO together with 1 mg/mL of the 30 µm Pd^0 beads in a thermomixer at 1400 rpm, with 50 µL aliquots taken and analysed by UPLC over a 24 hr period (fig 4.21).

a **b**

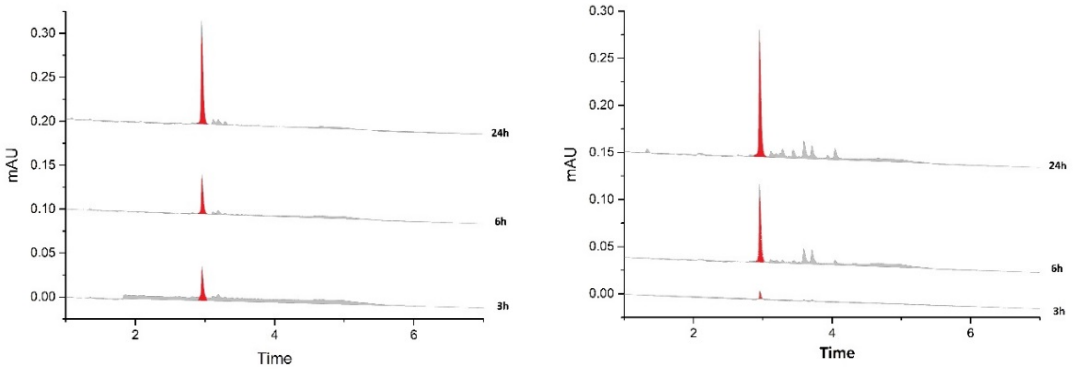

c

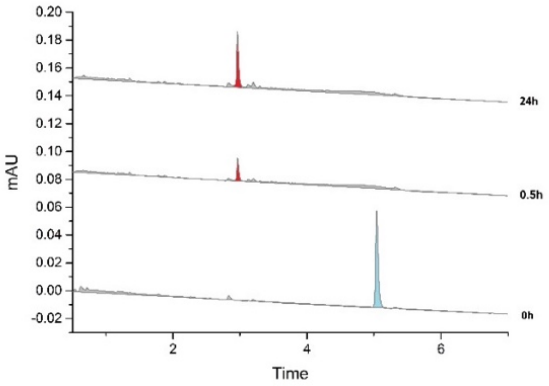

Figure 4.21 Non-biological conversion assay of doxorubicin prodrugs 42, 43 and 50 in combination with 30 μm Pd^0 beads. UPLC chromatograms producing doxorubicin (red) from prodrugs of (**a**) **42**, (**b**) **43,** and (**c**) **50** (light blue) as 100 μM solutions in PBS incubated with 1 mg / mL of 130 μm Pd^0 beads at 1400 rpm, 37 °C for 3, 6 and 24 hr (**a, b**) and 0, 0.5 and 24 hr (**c**). Impurities consistent with background are highlighted in light grey across all chromatograms.

Prodrug peaks were determined as in Section 4.8 by submitting a 100 μM concentration of each sample mixed with 0.1 % DMSO to UPLC and determining retention time off the column. Peaks were then assigned accordingly to each aliquot run by UPLC analysis. 30 μm Pd^0 beads are capable of rapidly generating high concentrations of dox in biocompatible conditions over short periods of time (fig 4.21). Whereas 130 μm Pd^0 beads were observed to sequester prodrug and drug simultaneously, 30 μm Pd^0 beads selectively sequesters prodrug alone, a significant advantage over the original Pd devices.

4.15 Pd-mediated conversion of Doxorubicin prodrugs with 30 μm Pd^0 beads in cancer cell culture

Next, **42** and **43** were separately incubated with 1 mg / mL of 30 μm Pd^0 beads in a BOOM activation assay across three therapeutically relevant concentrations in DU145 (fig 4.19) and U87 (fig 4.20) cells, to determine whether 30 μm Pd^0 beads were capable of producing a superior catalytic effect to that observed with 130 μm Pd^0 beads *in vitro*.

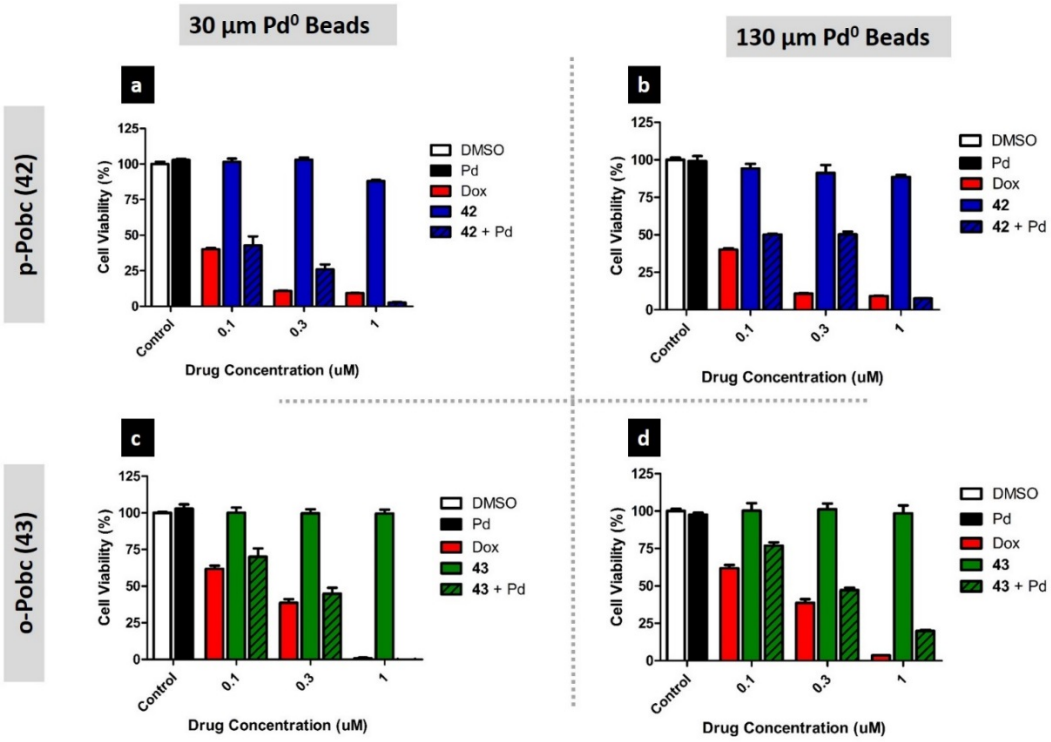

Figure 4.22 Comparative Pd-mediated activation of doxorubicin prodrugs 42 and 43 with 30 µm vs 130 µm Pd^0 beads in DU145 cell culture. Toxigenic effect of Pd-mediated activating dox prodrugs across a concentration window in DU145 cell culture. Experiments: 0.1 % (v/v) DMSO (untreated cell control, white); 1 mg / mL of (**a,c**) 30 µm or (**b,d**) 130 µm Pd^0 beads (negative control, black); Drug (doxorubicin positive control - red); Prodrug (**42** - blue), (**43** – green); Prodrug + (**a,c**) 30 µm or (**b,d**) 130 µm Pd^0 beads (**42** + Pd^0 beads - striped blue), (**43**-Dox + Pd^0 beads – striped green). Drug and Prodrug concentrations 0.1 – 1 µM. Cell viability was measured at day 5 using PrestoBlue® reagent. Error bars: ± SD from *n* = 3.

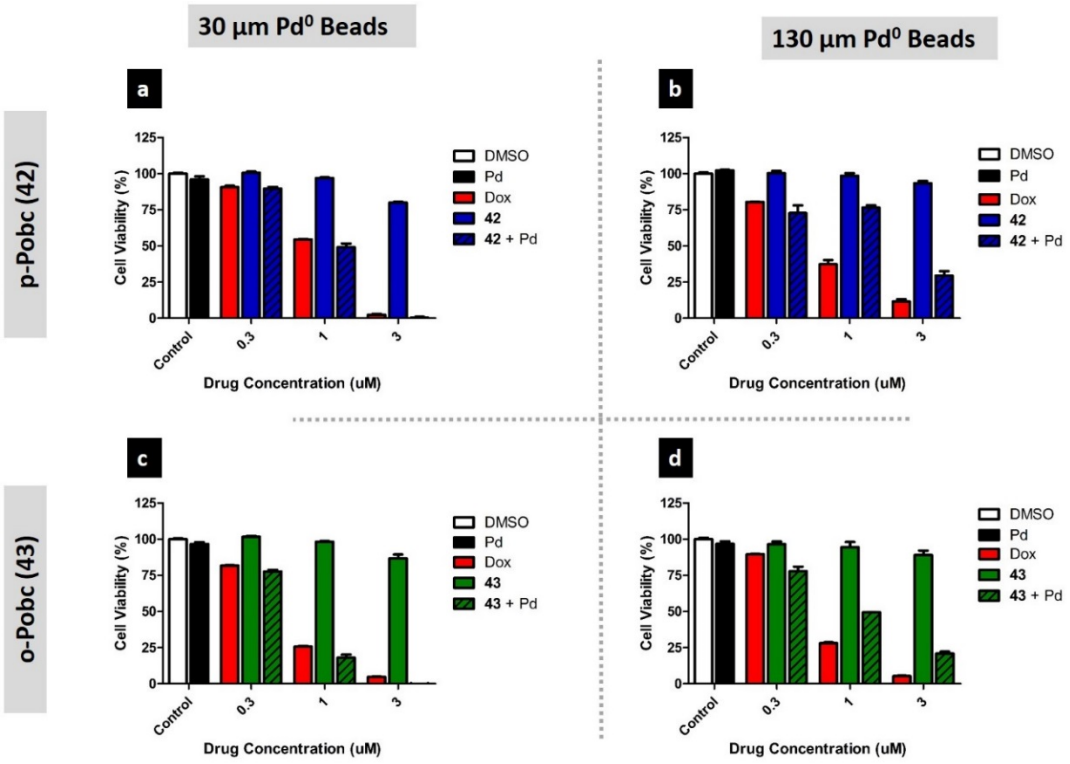

Figure 4.23 Comparative Pd-mediated activation of doxorubicin prodrugs 42 and 43 with 30 µm vs 130 µm Pd^0 beads in U87 cell culture. Toxigenic effect of Pd-mediated activating dox prodrugs across a concentration window in U87 cell culture. Experiments: 0.1 % (v/v) DMSO (untreated cell control, white); 1 mg / mL of (**a,c**) 30 µm or (**b,d**) 130 µm Pd^0 beads (negative control, black); Drug (dox positive control - red); Prodrug (**42** - blue), (**43** – green); Prodrug + (**a,c**) 30 µm or (**b,d**) 130 µm Pd^0 beads (**42** + Pd^0 beads - striped blue), (**43** + Pd^0 beads – striped green). Drug and Prodrug concentrations 0.1 – 1 µM. Cell viability was measured at day 5 using PrestoBlue® reagent. Error bars: ± SD from *n* = 3.

Remarkably the 30 µm Pd^0 beads released dox from **42** and **43** sufficiently to produce a cytotoxic effect almost identical to the active drug when incubated in combination whilst remaining bioinert when incubated alone with cells. The extent to which 30 µm Pd^0 beads improved the reactivity of the assay is shown as semi-log dose response curves with EC_{50} values for dox, **42** and **43** in combination with 130 µm Pd^0 beads or 30 µm Pd^0 beads (fig 4.24 and fig 4.25).

a

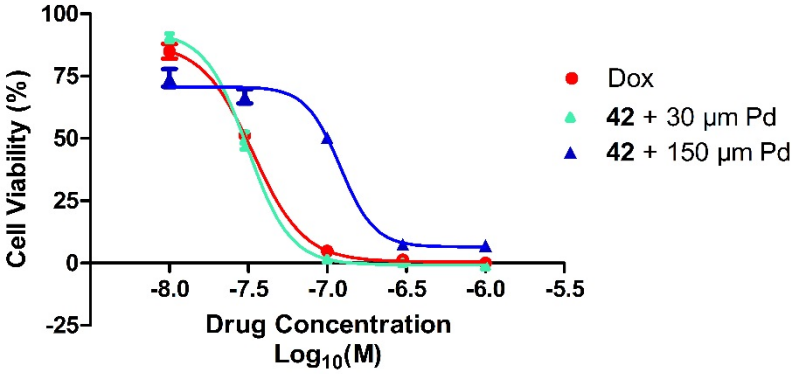

b

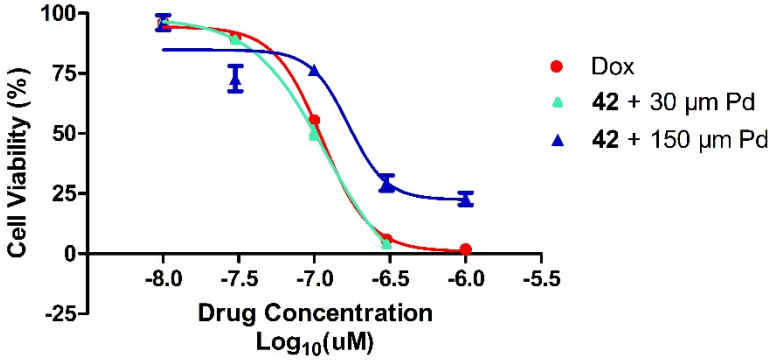

c

	doxorubicin	**42** + **30 µm Pd^0 Beads**	**42** + **130 µm Pd^0 Beads**
EC_{50} (DU145)	33.8 nM	31.3 nM	120.7 nM
EC_{50} (U87)	112.5 nM	118.2 nM	168.1 nM

Figure 4.24 Pd-mediated activation of 42 with 30 µm Pd^0 beads. Semi-log dose response curves of dox (red), **42** + 130 µm Pd^0 beads (dark blue) and **42** + 30 µm Pd^0 beads (light blue) in (**a**) DU145 and (**b**) U87 cell culture. Error bars represent ± standard deviation from *n* = 3. EC_{50} values reported as an inlaid table for each condition in (**c**).

a

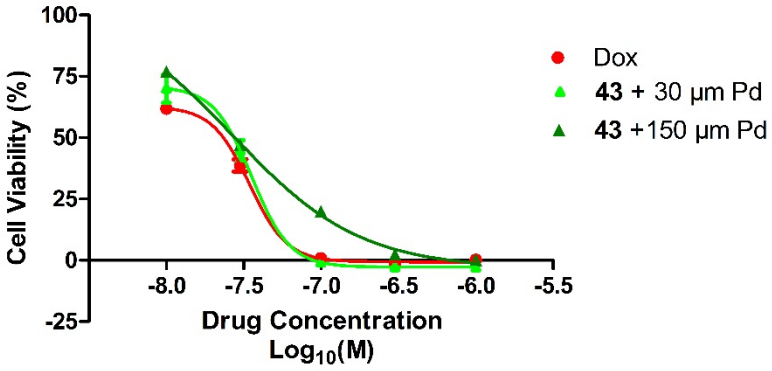

b

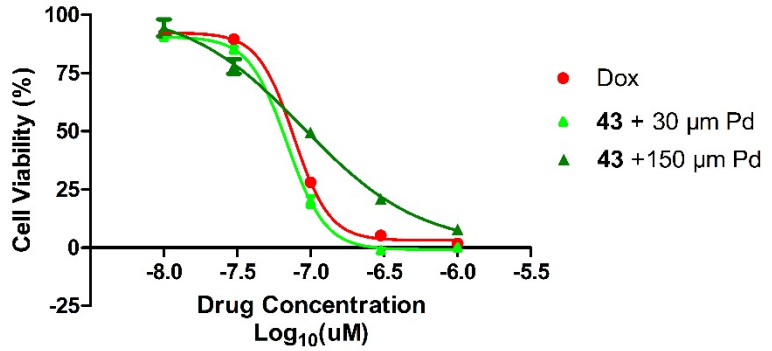

c

	doxorubicin	**43** + **30 µm Pd^0 Beads**	**43** + **130 µm Pd^0 Beads**
EC_{50} (DU145)	16.5 nM	21.1 nM	27.6 nM
EC_{50} (U87)	76.7 nM	69.0 nM	88.7 nM

Figure 4.25 Pd-mediated activation of 43 with 30 µm Pd^0 beads. Semi-log dose response curves of dox (red), **43** + 130 µm Pd^0 beads (dark green) and **43** + 30 µm Pd^0 beads (light green) in (**a**) DU145 and (**b**) U87 cells. Error bars represent ± standard deviation from *n* = 3. EC_{50} values reported as an inlaid table for each condition in (**c**).

4.16 Conclusions

Previously reported mechanistic insights have concluded that the C3' amino group of dox plays a key role in eliciting cytotoxicity[202–205]. Numerous prodrug strategies have reported the successful masking and deprotection of amino bearing protecting groups in living systems[215–

[218]. Encouraged by the deactivation and activation profiles of Gemcitabine prodrugs **25**, **26**, **33** and **34**, Poc, Cbz and Pobc groups were incorporated at the C3' amino position of dox to determine the influence of steric bulk on prodrug activity. A direct relationship between the reduction of bioactivity and increasing steric bulk around the carbamate group was observed in biocompatibility assays. EC_{50} values for prodrugs **42** - **45** were consistent with this hypothesis in two distinct cancer cell cultures [EC_{50} ~ Dox << **45** < **44** < **42** < **43**)], concluding that the o-Pobc protecting group was capable of providing the greatest protection to the carbamate group at the C3' position against biological cleavage.

Having validated Pobc as an excellent protecting group in dox deactivation, we next designed and incorporated a *bis*-o-Pobc protecting group at the C3' amino of dox, with the expectation of outperforming both **42** and **43** by virtue of increased steric bulk. Unexpectedly, prodrug **50** was insoluble at concentrations higher than 1 μM, and for this reason it was not possible to determine an accurate EC_{50} for **50**. **45**, **44**, **42**, **43** and **50** were subjected to non-biological Pd-mediated conversion assays in the presence of 130 μm Pd^0 beads. As expected, **44** was resistant to Pd-mediated catalysis, whereas **44**, **42**, **43** and **50** released dox. Notably **45** rapidly released dox, whereas **42** and **43** were more slowly catalysed. **50** underwent extremely rapid conversion to dox, with significant quantities produced within 30 minutes of incubation in combination with a Pd^0 source.

Cell viability assays were performed to quantify the cytotoxicity elicited from dox release in a biological system. In these preliminary studies there remained a significant gap in cytotoxicity between the combined dox prodrug with Pd^0 beads and unmodified dox. 130 μm Pd^0 beads were observed to rapidly sequester both prodrug and drug when incubated in combination. This may be attributed to the cytotoxicity gap, as activated drug trapped within the internal matrix of the Pd^0 bead is unable to induce cytotoxicity until it is released back into solution.

We looked to overcome this problem by developing smaller Pd^0 beads with a higher surface area to volume ratio. Pd^0 functionalized amino beads of sizes between 10 – 110 μm were

synthesised and quantified according to standard practices. 30 μm Pd^0 beads rapidly deprotected Poc-Rho when incubated together with a 10 % Fetal Bovine Serum solution. This signalled that the 30 μm Pd^0 beads would be capable of catalysis in a biological system. Whereas 10 μm and 20 μm Pd^0 beads were also capable of good catalysis in the presence of serum, their small size may cause elimination by phagocytosis in a living system. We expected an equimolar quantity of 30 μm Pd^0 beads would provide an increased rate of catalysis with less sequestration of lipophilic prodrugs into a small internal matrix in comparison to the 130 μm Pd^0 beads.

Dox prodrug candidates were incubated with 30 μm Pd^0 beads and their reactivity analysed by UPLC. Remarkably, the new Pd^0 beads were capable of rapidly sequestering and converting prodrugs **42**, **43** and **50** into active dox, which was released into solution. This is an attractive feature for a new Pd^0 device that would conceptually pull prodrug out of circulation at the site of activation, whereby it is converted and quickly released as active drug at the intended site of treatment. BOOM activation in cancer cell culture using 30 μm Pd^0 beads provided comparable EC_{50} values between the combinations of Pd-beads and prodrugs **42** and **43** and unmodified dox across two cell lines. This optimised BOOM activation capacity warranted further investigation. Dox prodrugs and the optimised Pd^0 device were together progressed into preclinical *in vivo* and *ex vivo* assays, explored in Chapter 5.

CHAPTER 5

Validation in Complex Models

This chapter will detail efforts towards the development of more clinically relevant prodrug activation assays. A library of Pd-labile prodrugs previously reported in our lab and within this thesis constitute the list of potential candidates to employ. Although N- and O-alkylated prodrugs of 5FU are completely biocompatible in cell culture and capable of Pd-mediated deprotection, a relatively high concentration of the parent drug is required to elicit an anticancer effect. Poc, Alloc and Pobc functionalised Pd-labile prodrugs of the more potent antimetabolite gemcitabine did not exhibit cytotoxic fold changes sufficient to progress into animal model studies. A floxuridine prodrug previously reported embodied an ideal candidate for *in vivo* investigation, and will be utilised for a pilot study of Pd-mediated intratumoural activation. Subsequently, prodrugs of doxorubicin, a more widely used chemotherapeutic, will be used for an *in vivo* / *ex vivo* biocompatibility and activation assay using optimised Pd^0 beads.

First, a multicellular tumour spheroid (MCTS) model was developed to assess the biocompatibility and activation of prodrugs and Pd^0 beads in a three dimensional *in vitro* cell culture. Second, an embryonic zebrafish assay will study dox and prodrugs *in vivo* for their ability to prevent cardiac oedema. Third, an *ex vivo* mouse prostate cancer assay will study the capacity of novel Pd^0 beads to activate Pd-labile prodrugs and a fluorescent probe after short and extended Pd^0 bead intratumoural *in vivo* incubation.

5.1.1 Three-dimensional cell culture overview

BOOM prodrugs, probes and their respective by-products have previously been validated for biocompatibility / activation via standard cell based studies[34,88–90,130,131]; a process that involves culturing and treating cellular monolayers on a two-dimensional (2D) plastic surface. Whilst undeniably efficient, scalable and reproducible[234,235], this method does not accurately reflect the physiology of cancer tissue in a living organism. Morphological, metabolic and phenotypic

changes arise from growing cells as 2D monolayers, and as the absence of cell-cell and cell-matrix interactions prevents the development of a tumour microenvironment (TME)[236,237], *in vitro* assays do not fully represent native state cellular function. The TME (including an extracellular matrix, growth factors, cytokines and chemokines) is known to play a crucial role in both the proliferation of cancer[238,239] and the efficacy of chemotherapeutic response[240,241], including for 5FU[242–244], gemcitabine[245–247] and doxorubicin[248]. Furthermore, a 2D cellular monolayer assay does not provide insight into the physical interaction and cytotoxicity produced by introducing a Pd^0 bead into a cellular environment. As BOOM chemotherapy requires the precise positioning of an extracellular catalyst proximal to tumour tissue to induce cytotoxicity, the effect of physically forcing Pd^0 beads into a tumour via microsurgery followed by prolonged incubation within tissue is not yet known.

Three-dimensional (3D) cell cultured assays allow for cell-cell and cell-matrix interactions that develop a TME and morphological features suggested to closely resemble that found in *in vivo* tumour biology[237,249,250]. A 3D cell cultured assay would allow for the study of biocompatibility and BOOM activation in a system closely approximating native tumour tissue. If patient tumour samples were readily available, a tumour tissue explant culture method would be one viable way of developing a 3D BOOM chemotherapeutic model. This method allows the study of preserved sections of *in vivo* tumour, where patient derived tumour biopsies are incubated on a collagen surface in media and treated with test compounds[251]. Unfortunately, natural intratumoural and intertumoural heterogeneity, rapid degradation of excised tissue and accessibility to fresh samples hinder the tumour tissue explant method as a simple means of studying BOOM chemotherapy in a representative 3D system. MCTS provide a viable alternative without the need for patient biopsy samples (fig 5.1.1).

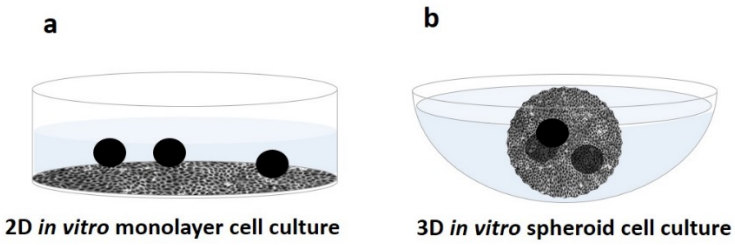

Figure 5.1.1 Illustrative example of a two-dimensional (2D) vs three-dimensional (3D) *in vitro* BOOM assay. (**a**) A 2D model does not produce a tumour microenvironment (TME), and Pd^0 beads are not embedded within the monolayer, preventing the study of bead-cell interface toxicity. (**b**) A 3D model, represented here by a multicellular tumour spheroid (MCTS), possesses a TME representative of an *in vivo* tumour, and allows for the study of toxicity at the bead-cellular interface by embedding Pd^0 beads within the spheroid.

MCTS are heterogeneous multicellular aggregates that cluster and grow together, typified by hypoxic regions, necrotic cores and physiochemical gradients when spheroid diameters exceed 500 μm[252]. MCTS recapitulate to reflect the TME of an *in vivo* tumour with equivalent cellular signalling, gene expression and growth kinetics profiles[253]. As 2D cell cultures can be stimulated to reorganise into MCTS via a variety of techniques[237,249,250,254–256] an MCTS model was chosen to develop and optimise a 3D cell culture BOOM assay.

5.1.2 MCTS Assay Optimization

An ideal MCTS assay would reproduce comparably sized spheroids in a standard 96-well suspension culture that may be incubated with compounds and/or Pd^0 beads. MCTS have been capable of taking up nm sized nanoparticle formulations[257–259], 100 – 200 nm PEG micelles[260,261] and 5 μm microspheres[254], however a method for the uptake of 130 μm diameter objects into an MCTS is not reported in literature. Accordingly, MBA-231 MCTS were co-cultured together with individual 130 μm Pd^0 beads according to a modified MCTS formation methodology[249] adapted by the Edinburgh Cancer Discovery Unit and imaged by widefield microscopy (fig 5.1.2).

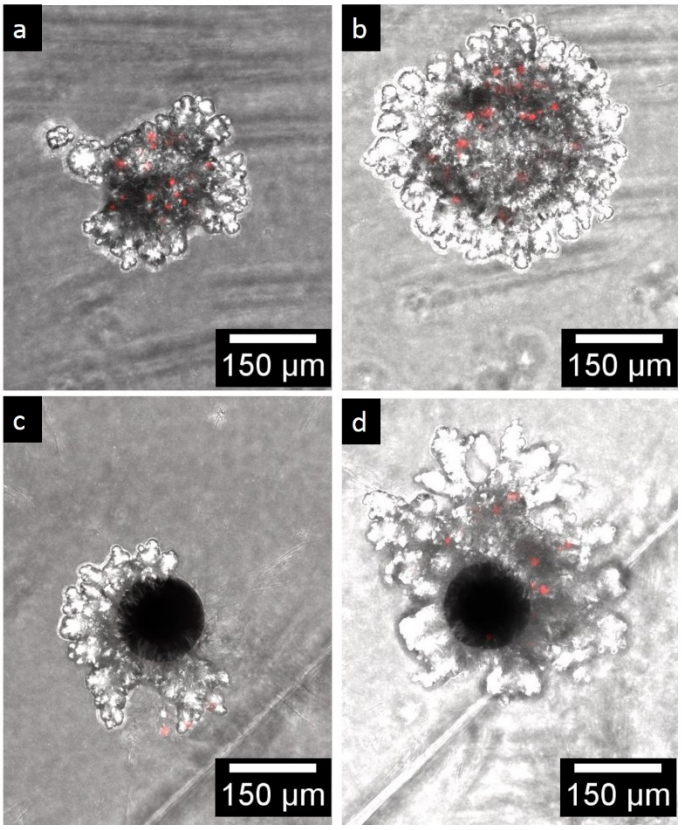

Figure 5.1.2. MCTS single Pd^0 bead incubation model. Protocol: 10,000 human breast adenocarcinoma MB231 cells (without bead, **top row**) and with 130 µm Pd^0 bead (**bottom row**) in fresh media with 2 % Matrigel® were dispensed into each well of a 96-well Corning ULA® U-bottom plate at 4 °C. The plate was centrifuged and incubated under standard conditions, and 2 µL of a 0.3 mM DRAQ7™ stock solution was added to each well after 3 days. Individual spheroids were imaged by widefield microscopy with transmitted light and a Cy5 far-red filter at day 5 (**a,c**) and day 8 (**b,d**).

By measuring the DRAQ7™ apoptosis signal it was determined that localised toxicity was not produced when a 130 µm Pd^0 bead was incubated within an MBA-231 MCTS over 48 hr incubation time. Importantly the Pd^0 bead-cellular interface did not show an increased rate of apoptosis with respect to typical background cell death in growing spheroids observed in an untreated MCTS. Adding 1 mg / mL of 130 µm Pd^0 beads (~ fifteen beads per well) during formation of the MCTS did not appear to induce additional cytotoxicity, however the morphology of the growing spheroid was altered (fig 5.1.3).

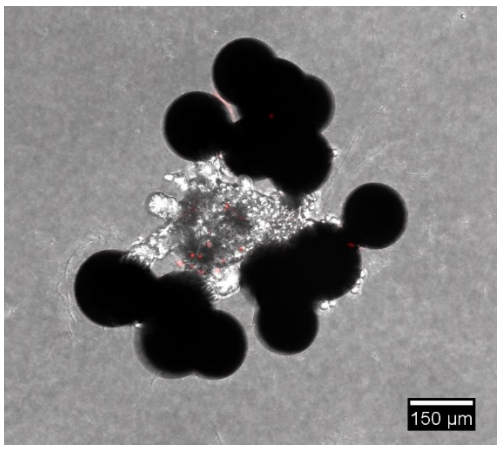

Figure 5.1.3. MCTS Pd^0 bead incubation model with increased catalyst loading. Protocol: 10,000 human breast adenocarcinoma MB231 cells and 1 mg / mL of 130 µm Pd^0 beads in fresh media with 2 % Matrigel® were dispensed into each well of a 96-well Corning ULA® U-bottom plate at 4 °C. The plate was centrifuged then incubated under standard conditions and 2 µL of a 0.3 mM DRAQ7™ stock solution was added to each well after 3 days. Spheroids were imaged by widefield microscopy with transmitted light and a Cy5 far-red filter at day 8.

5.1.3 MCTS BOOM Activation Assay

A BOOM MCTS assay was next developed to test the biocompatibility and activation of prodrugs in a 3D cell culture system. Glioblastoma U87 were chosen as the preferred MCTS cell culture type based on the following attributes. U87 cells were found to form large spheroids with minimal cell death and the absence of a necrotic core after 10 days of incubation (fig 5.1.4.a). This is important as a necrotic core produces a region of localised apoptosis that may overlap with the cytotoxic effect generated from Pd-mediated prodrug activation within the MCTS. Dox produces a strong cytotoxic effect to U87 cells in 2D *in vitro* studies (dox EC_{50} = 78 nM) whilst **43** reduces the cytotoxicity of dox by 134 fold (fig 4.5.b) and undergoes Pd-mediated activation with both 30 µm or 130 µm Pd^0 beads (4.22.c,d).

Accordingly 100 µM of **43** or dox was added with DRAQ7™ to pre-prepared U87 MCTS with or without 1 mg / mL of 75 µm or 130 µm Pd^0 beads and incubated for 5 days (fig 5.1.4). 75 µm Pd^0 beads were used in this assay as they showed comparable catalytic reactivity with respect to the 130 µm Pd^0 beads (figure 4.18). At this stage the optimal 30 µm beads had not yet been determined as the best candidate to effect Pd-mediated activation.

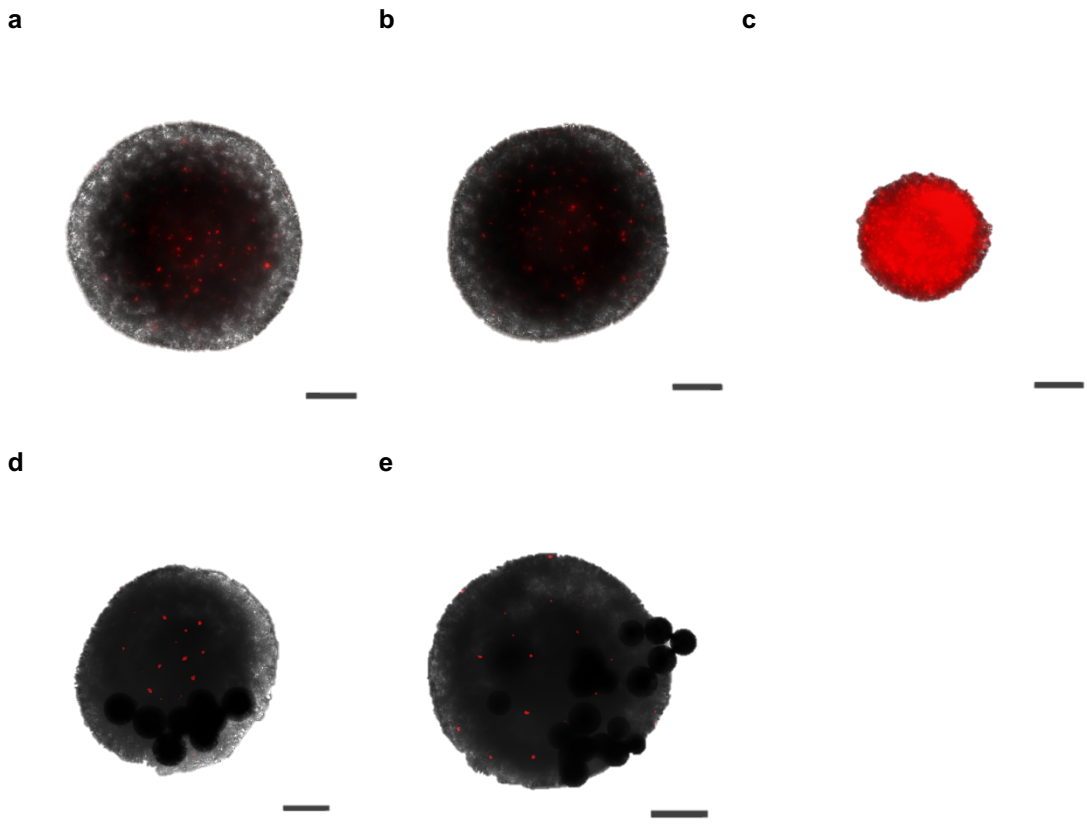

Figure 5.1.4. MCTS prodrug activation using 43 + Pd^0 beads. Protocol: 10,000 Glioblastoma U87 cells and DMEM media containing 2 % Matrigel® and no beads or 1 mg / mL of 75 µm or 130 µm Pd^0 beads were dispensed into each well of a 96-well Corning ULA® U-bottom plate at 4 °C. The plate was then centrifuged and incubated under standard conditions. At day 3 wells were examined by microscope to exclude non-formed MCTS or those that had not taken up the Pd^0 bead. Media was replaced with a solution containing 3 µM DRAQ7™, 0.1 % (v/v) DMSO, drug or prodrug. (**a**) 0.1 % DMSO, (**b**) 100 µM **43**, (**c**) 100 µM dox, (**d**) 100 µM **43** + 1 mg / mL 130 µm Pd^0 beads and (**e**) **43** + 1 mg / mL + 75 µm Pd^0 beads. Wells were imaged by widefield microscopy with transmitted light and a Cy5 far-red filter at day 10, and images were modified using ImageJ. Scale bar = 250 µm

MCTS incubated with 0.1 % DMSO produced a low cytotoxic effect scattered throughout the spheroid typically also observed with untreated growing spheroids (fig 5.1.4.a). **43** alone did not produce any cytotoxic effect at 100 µM (fig 5.1.4.b), whereas dox produced a strong cytotoxic effect, confirmed by DRAQ7™ apoptosis staining and the reduced size of the MTCS (Fig 5.1.4.c). However the combination of **43** + 130 µm Pd^0 beads (fig 5.1.4.d) or **43** + 75 µm Pd^0 beads (fig 5.1.4.e) was unable to produce a cytotoxic effect. To investigate whether this was due to the addition of Matrigel® during spheroid formation, 100 µM **43** in 0.1 % (v/v) DMSO + 1 mg / mL 75 µm Pd^0 beads was pre-incubated in cell media for 72 hr then used to

replace the media of a preformed non-Pd incubated MCTS at day 3 and incubated for an additional 7 days (fig 5.1.5).

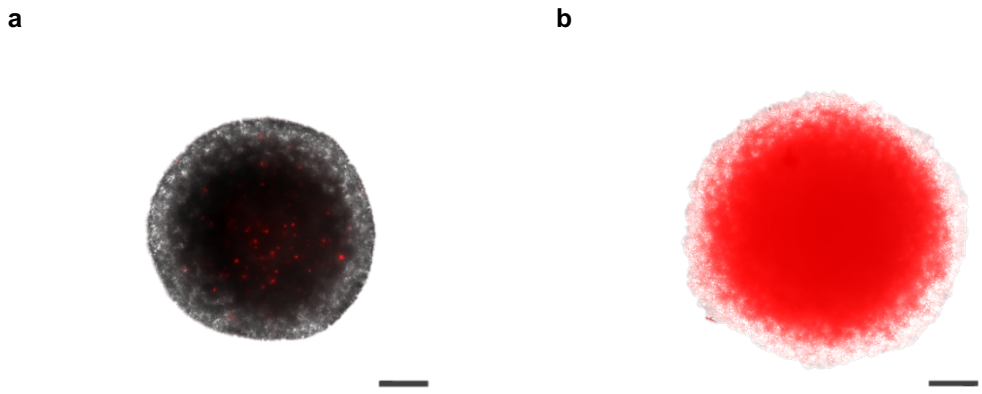

Figure 5.1.5. MCTS prodrug activation using pre-incubated 43 + 75 µm Pd^0 beads. Protocol: 10,000 Glioblastoma U87 cells and DMEM media containing 2 % Matrigel® were dispensed into each well of a 96-well Corning ULA® U-bottom plate at 4 °C. The plate was then centrifuged and incubated under standard conditions. At day 3 wells were examined by microscope to exclude non-formed MCTS. Media was replaced with a pre-incubated solution containing (**a**) 3 µM DRAQ7™, 0.1 % (v/v) DMSO or (**b**) 3 µM DRAQ7™, 0.1 % (v/v) DMSO, 100 µM **43** and 1 mg / mL 75 µm Pd^0 beads. Wells were imaged by widefield microscopy with transmitted light and a Cy5 far-red filter at day 10, and images were modified using ImageJ. Scale bar = 250 µm

A strong cytotoxic effect was confirmed by DRAQ7™ staining, however the MCTS was of an equivalent size to the untreated control. This may be because less dox was generated from the pre-incubated sample over 72 hrs than wells treated with 100 µM dox. Whilst Pd^0 beads were capable of catalysing **43** to dox in media to elicit a cytotoxic effect to MCTS, **43** was unable to undergo Pd-mediated catalysis when Pd^0 beads were embedded for 3 days in a MCTS. One possibility for this is that the Matrigel® required for spheroid formation prevents the flow of **43** into Pd^0 beads for conversion. Matrigel® is a highly viscous glue that may block the porous membrane framework of PEG resins from efficiently sequestering **43**. This study was developed as an initial step towards the development of a bridging *in vitro* to *in vivo* validation assay. Although prodrug activation was not observed, two key outcomes were achieved. The first was that **43** is non-toxic at 100 µM to a cell culture model recapitulating an *in vivo* tumour environment. The second is that Pd^0 beads may be incubated together in direct contact with tumours for extended periods of time without producing cytotoxicity. These observations will serve to inform the subsequent *in vivo* / *ex vivo* study reported in Section 5.3.

5.2.1 Zebrafish as a model animal for doxorubicin induced cardiomyopathy

As described in Chapter 4.1, doxorubicin (dox) is intrinsically dosage limited by cardiotoxicity[207]. Dexrazoxane is an approved adjuvant co-administered with dox used to mitigate cardiotoxic effect[262]. However this adjuvant therapy reduces the efficacy of dox treatment[263] and may cause secondary malignancies[264]. As a result it was restricted from the European market in 2011[265]. Dox treatment strategies capable of alleviating cardiotoxicity with retained efficacy are therefore essential to improve the safety profile of this essential medicine. An *in vivo* cardiac model is required to study the effect of prodrugs vs. dox on treatment-induced cardiomyopathy. Zebrafish have undergone extensive cardiovascular developmental and disease based studies[266–269] with the embryonic heart possessing key molecular, cellular and structural similarities with the human heart during early development[270,271] (fig 5.2.1).

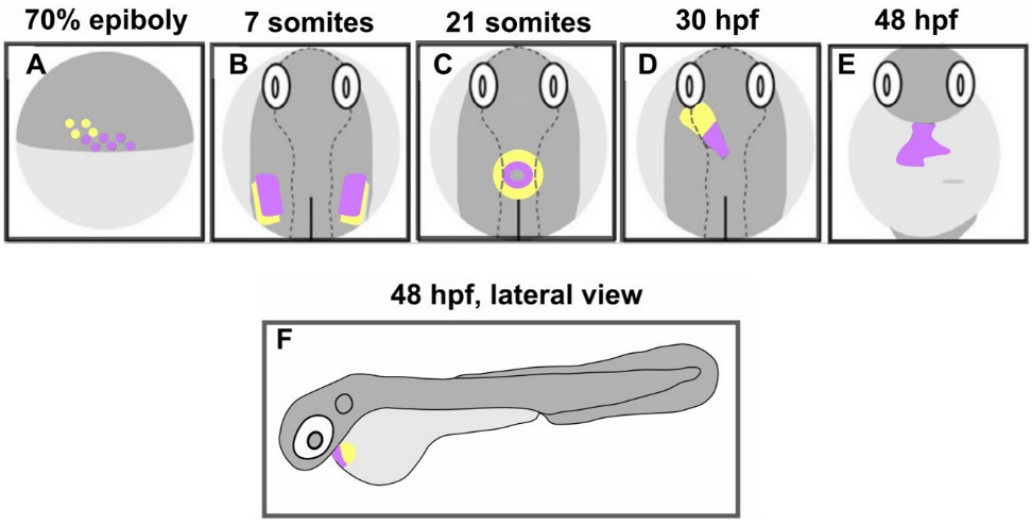

Figure 5.2.1. Phases of heart formation in the zebrafish embryo. (**A**) Schematic lateral view, dorsal to the right, of the late blastula. Ventricular (purple) and atrial (yellow) myocardial progenitor cells are spatially organized within bilateral marginal zones at this stage. (**B–D**) Schematic dorsal views, anterior up, depicting the locations of ventricular (purple) and atrial (yellow) cardiomyocytes during cardiac morphogenesis. (**B**) Myocardial progenitors migrate to form bilateral heart fields. (**C**) The process of cardiac fusion recruits cardiomyocytes to the embryonic midline, where they form a cardiac cone. (**D**) Continued migration of cardiomyocytes elongates the cardiac cone to create the heart tube. (**E-F**) Schematic frontal view (**E**), and lateral view (**F**) anterior up, depicting the morphologically distinct ventricle (purple)

and atrium (yellow) that are separated by a constriction at the atrioventricular canal following chamber emergence. Adapted from reference[272] Copyright (2011) Methods in Cell Biology.

Zebrafish provide an attractive model for heart development. Cardiac contraction commences after 24 hours post fertilisation (hpf). Inducing cardiovascular specific defect or injury during the first week of zebrafish embryogenesis does not cause embryonic lethality[266], as the embryo obtains sufficient oxygenation by diffusion alone through the skin at this time[270]. As embryos are transparent, cardiac damage can be monitored on live specimens through a conventional widefield microscope. A zebrafish cardiotoxicity assay was thus developed for the study of dox and **43** on zebrafish cardiac oedema.

5.2.2 Zebrafish doxorubicin induced cardiac oedema assay

Zebrafish embryos were initially treated with 20 μM or 40 μM dox between 12 - 72 hpf according to a reported protocol[273], and pericardial area relative to whole body surface area was determined as a ratio to infer cardiac oedema from a population of viable fish of each condition (fig 5.2.2).

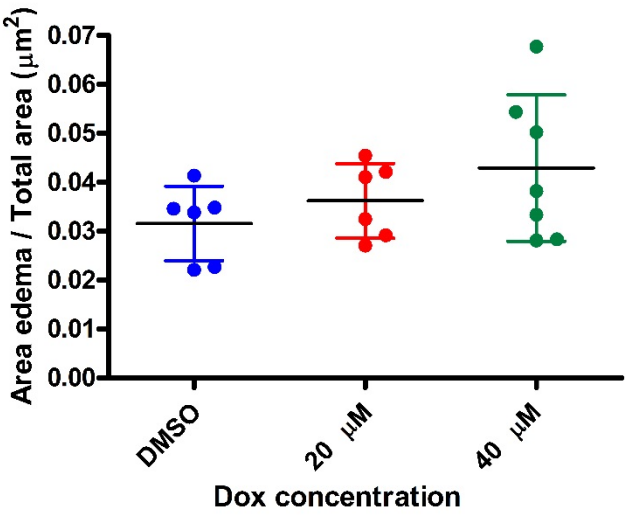

Figure 5.2.2 Initial study of doxorubicin induced cardiac oedema on the zebrafish embryonic heart. Protocol: zebrafish embryos were incubated between 12 hpf and 72 hpf in E3 medium containing DMSO (0.1 %) or dox at 20 μM or 40 μM. Embryos were kept in 6-well plates (15 embryos / well; 2 wells / condition) at 28.5 °C with dead embryos removed daily.

This initial study showed that a positive trend was induced on the relative size of the cardiac region with increasing dox concentration during 3 days of treatment. During the course of this study, spectrofluorometric analysis of the zebrafish embryo at 72 hpf determined that significant quantities of dox was absorbed by the chorion, an acellular envelope surrounding the egg. By removal of the chorion (de-chorionation) and further modification of the assay by way of treating zebrafish embryos with 50 µM dox between 24 - 120 hpf, a pronounced cardiac oedema phenotype was produced.

This modified protocol was used for a subsequent *in vivo* assay to monitor the effect of **43** vs. dox on zebrafish cardiac oedema. Dechorionated embryos were treated with 0.1 % DMSO in E3 media and 50 – 200 µM of dox or **43** between 24 hpf and 120 hpf and the pericardial oedema relative to body surface area was determined (fig 5.2.3).

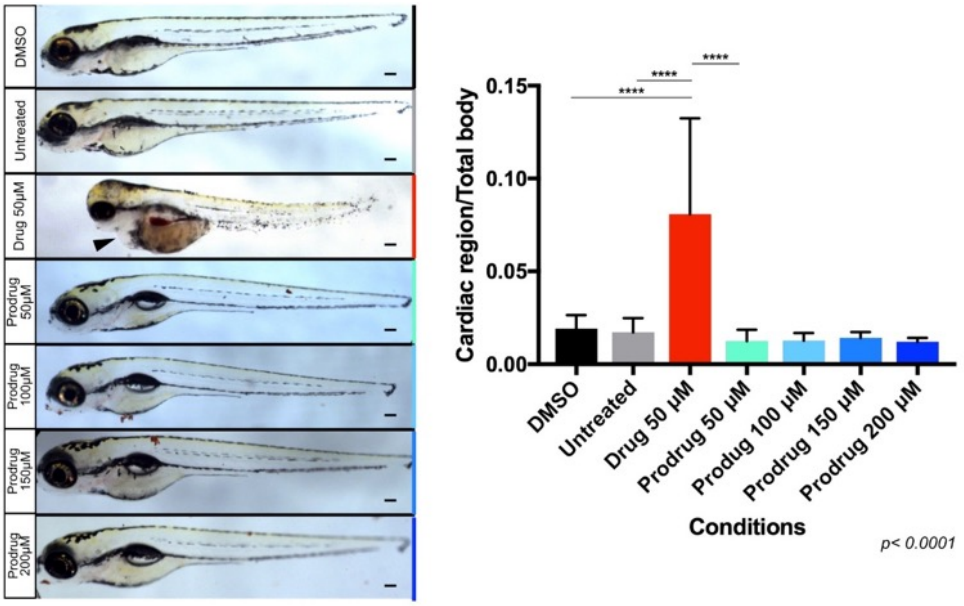

Figure 5.2.3 Study on the potential cardioprotective properties of 43 on embryonic zebrafish cardiac tissue. Left panel - lateral view study on the effect of dox and **43** on embryonic zebrafish cardiac tissue between 24 - 120 hpf. Lateral view of 120 hpf larvae exposed to E3 medium, a 0.1 % DMSO solution, 50 µM dox and 50 µM, 100 µM, 150 µM and 200 µM of **43**. Pericardiac oedema indicated by black arrow for dox treated population. Right Panel - histogram displaying cardiac area / total body area ratio as an estimate of pericardial oedema formation for populations of fish in E3 media alone untreated (grey), 0.1 % DMSO (black), 50 µM dox (red) and 50 – 200 µM **43** (light to dark blue with increasing concentration). Zebrafish populations treated with > 50 µM dox died during incubation and were excluded from analysis. Results are expressed as mean SEM of three independent experiments (15 fish for

each experiment). Asterisks indicate significant differences between dox and DMSO, untreated, and prodrug exposed animals.

A pronounced cardiac oedema was produced when zebrafish embryos were treated with dox at 50 μM. Notably, no cardiac oedema was observed in fish incubated with increasing concentrations of **43** (fig 5.2.3. and fig 5.2.4.a). Conditions of dox above 50 μM are not included as populations treated with 100 μM, 150 μM and 200 μM died within 3 days of treatment, whereas no dose-dependent lethal effect was observed with prodrug **43** (fig 5.2.4.b).

a

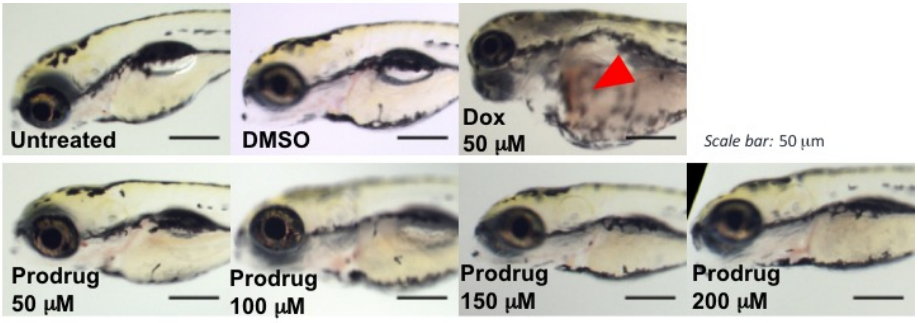

b

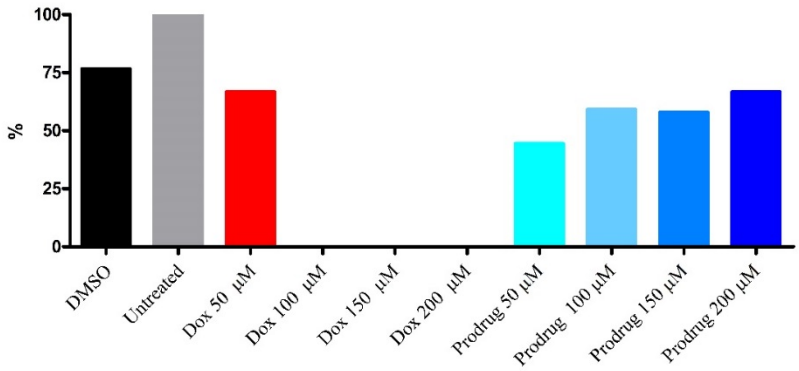

Figure 5.2.4 Dose-dependent viability effects of exposure to dox or 43 between 24 - 120 hpf. (**a**) Lateral view of 120 hpf larvae exposed to untreated E3 media, a 0.1 % DMSO (black), 50 μM dox and 50 – 200 μM **43**. Cardiac oedema indicated by red arrow absent in other images. Pericardial oedema is evident at both concentrations. Scale = 50 μm (**b**) Viability of embryonic zebrafish populations treated with untreated E3 media (grey), a 0.1 % DMSO (black), 50 μM dox or 50 – 200 μM **43** between 24 – 120 hpf, expressed as a percentage of viable fish remaining at 5 days post fertilisation after incubating 15 fish per condition.

Fluorescence microscopy confirmed the presence of **43** in zebrafish at 120 hpf, however it is important to note that an equivalent dose of dox accumulates within the fish much more

abundantly (fig 5.2.5). The reduced uptake/retention of **43** at 50 μM with respect to dox is consistent with the reduced ability of **43** to engage with the expected targets of the active drug. Therefore, **43** is expected to diffuse between and within cells whilst dox is retained and accumulated. Significant quantities of **43** was observed in the yolk of zebrafish incubated at 200 μM, which indicated that the higher lipophilicity of the yolk (which is rich in lipid content) causes more retention of the prodrug.

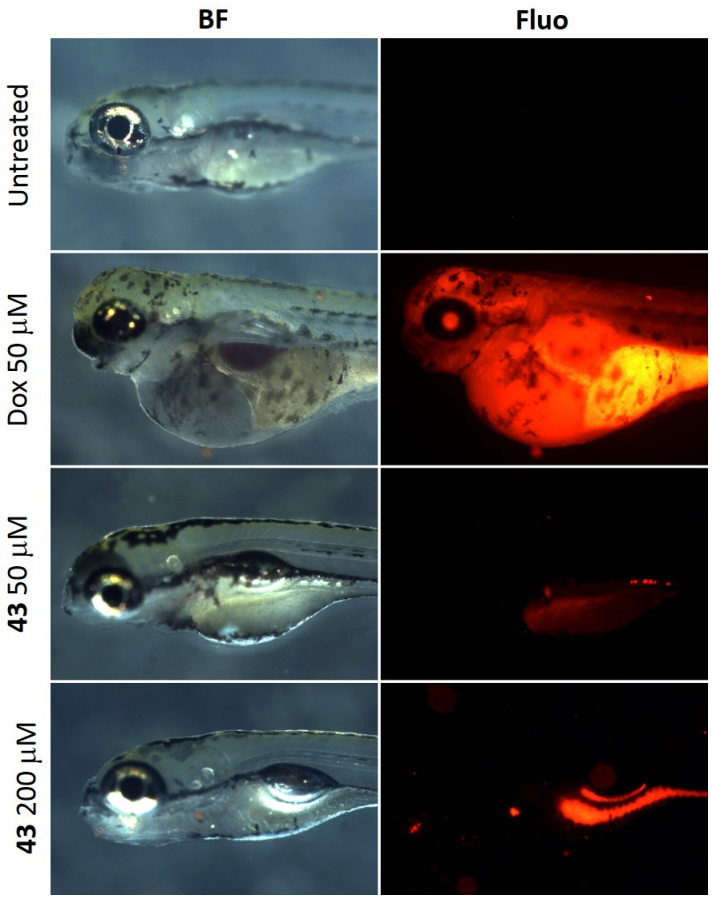

Figure 5.2.5 Fluorescence study of prodrug and drug uptake into zebrafish. Lateral view fluorescence study on the absorption of dox and **43** on embryonic zebrafish cardiac tissue at 120 hpf. Lateral view zoom of 120 hpf larvae exposed to untreated medium (E3), 50 μM dox, 50 μM **43** and 200 μM **43**. Representative images of *n* = 15 fish per condition

This zebrafish cardiac oedema was developed to study the potential cardio protective effect produced by administering **43** vs. dox in an *in vivo* embryonic zebrafish model. Whereas dox

produced a large oedema at 50 μM and was lethal at all higher concentrations, **43** did not significantly affect embryonic viability, nor did it induce oedema during 5 days incubation even at 200 μM. A future *in vivo* BOOM activation study that systemically administers **43** in a rodent model should carefully analyse the extent to which cardiomyopathy is induced against an equivalent dosage of dox.

5.3.1 *in vivo* / *ex vivo* prodrug activation assay overview

The BOOM chemotherapeutic concept was next progressed into a pre-clinical animal model activation study. An N3 masked prodrug of floxuridine, 3-propargylfloxuridine (Pro-FUdR), developed previously within our lab[90] (fig 5.3.1) was initially investigated in combination with 130 μm Pd^0 beads for an *in vivo* Pd^0 bead injection / *ex vivo* drug treatment pilot study. As a result of significant assay optimisation, dox prodrugs **42**, **43** and 30 μm Pd^0 beads emerged as the preferred candidates based on cytotoxicity, fluorescence attributed activation and catalysis respectively.

The efficacy of a BOOM chemotherapeutic treatment strategy is predicated on the sustained long term catalytic activity of the Pd^0 bead implant. An *in vivo* catalytic performance study is important to assess the long term effect of intratumoural catalyst implantation. Therefore a longitudinal *in vivo* Pd^0 injection / *ex vivo* activation assay was developed to study the effect of short vs. prolonged intratumoural Pd^0 bead injection followed by Pd-mediated probe/prodrug activation. This investigation also lead to the development of a non-perturbing microsurgical technique; an ultrasound guided intratumoural injection protocol for the precise insertion of catalytic beads into the prostates of anaesthetized mice.

5.3.2 Pilot study of intratumoural Pd-mediated floxuridine prodrug activation

Floxuridine (FUdR) is an antimetabolite chemotherapy administered in advanced colorectal, stomach, kidney and metastatic liver cancer indications despite significant side-effect[274,275]. Monophosphorylated-FUdR inhibits thymidylate synthetase (TS), reducing the cellular reservoir of thymine nucleoside reserves and halting DNA synthesis[49]. Triphosphoylated-

FUdR is incorporated predominantly into DNA where it prevents chain elongation and triggers cellular apoptosis[50]. N3 masked prodrugs of FUdR have been reported to reduce cytotoxicity and undergo selective activation by enzymatic action[277] or via induced electromagnetic radiation in the presence of hypoxic conditions[278–281]. Pro-FUdR previously underwent biocompatibility and BOOM activation *in vitro* assays under normal and hypoxic conditions[90]. Pro-FUdR was capable of > 6,000 fold cytotoxic reduction across two cell lines (fig 5.3.1.b). In combination with 130 µm Pd^0 beads, a strong cytotoxic effect was observed corresponding to almost quantitative rescue of the parent drug via the Pd-mediated N3 dealkylation of Pro-FUdR (fig 5.3.1.c).

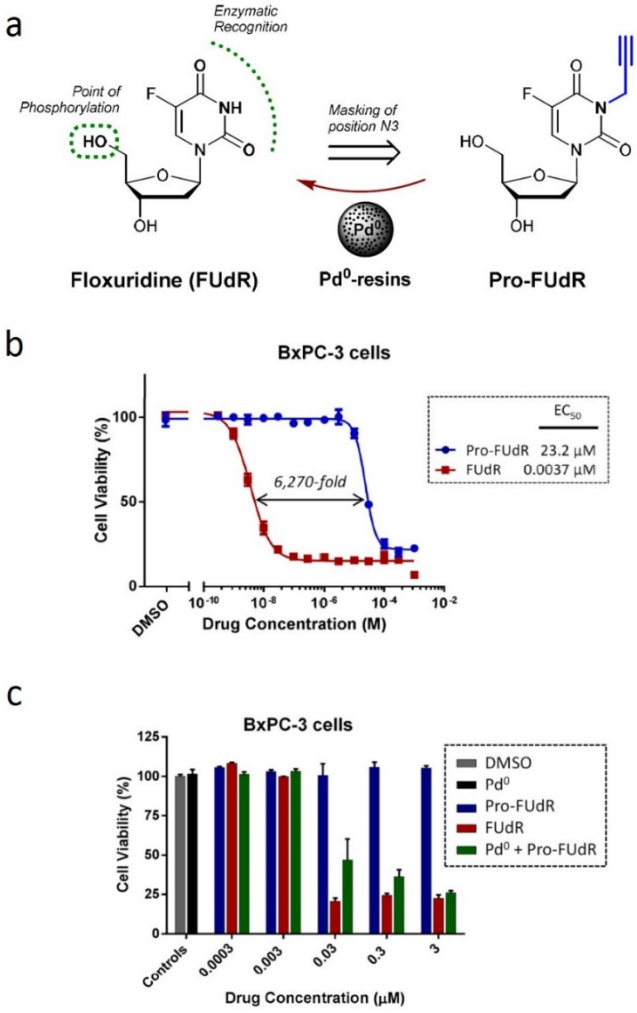

Figure 5.3.1 Design and assessment of a biocompatible N3 alkylated Floxuridine prodrug *in vitro*. (**a**) Schematic overview of the Pd-mediated release of Floxuridine (FUdR) from 3-propargylfloxuridine (Pro-FUdR) by Pd^0 beads. (**b**) Cytotoxic effect of Pro-FUdR (blue) in comparison to unmodified FUdR (red) on BxPC-3 cells measured by semi log dose

response curves of increasing drug concentrations (0.0003 - 1,000 μM) to calculate corresponding EC_{50} values. Cell viability was determined at day 5 using PrestoBlue® reagent and a fluorescent microplate reader. Error bars: ± SD from *n* = 3. (**c**) Study of BOOM activation in a dose response study of cell viability after 5 days of treatment with BxPC-3 cells. Experiments: 0.1 % (v/v) DMSO (untreated cell control; grey), 0.67 mg / mL of Pd^0 beads (negative control; black); 0.0003 – 3 μM of Pro-FUdR (negative controls; blue); 0.0003 – 3 μM of FUdR (positive controls; red) and Pd^0 beads + Pro-FUdR (BOOM generation assay; in green).

Due to the remarkable bioorthogonality fold change and sensitivity to Pd-mediated catalysis *in vitro*, Pro-FUdR was chosen as the first candidate to undergo a proof of concept *in vivo* / *ex vivo* prodrug activation assay.

Conducting metal catalyst implantation on a mouse prostate cancer model bears homology with brachytherapy, an established intratumoural metal implantation treatment protocol commonly used in the clinic[282]. Brachytherapy is a type of radiotherapy in which a radioactive source (notably including Pd seeds[283]) is implanted directly into a tumour (fig 5.3.2). A localised radioactive emission causes cell death within a pre-determined zone dependant on the dose rate (related to the half-life of the radioactive source) and radioactive source positioning.

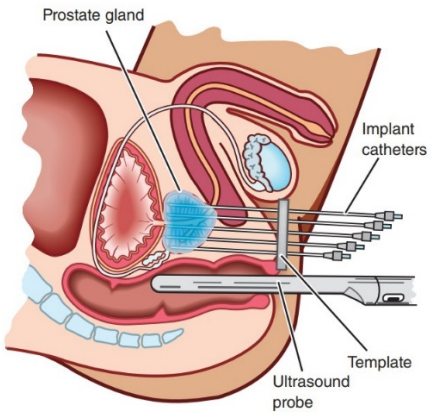

Figure 5.3.2 High Dose Rate (HDR) Brachytherapy treatment protocol for prostate cancer. Image reprinted from open source CRUK prostate cancer infographic. (Copyright 2016 CRUK)

Brachytherapy is commonly performed on prostate tumours due to ease of accessibility and the ability to precisely position the radioactive source via ultrasound guidance. As the BOOM chemotherapeutic concept approximates the clinical protocol of brachytherapy, a mouse

prostate cancer model was designed. The first step was to determine whether the FUdR / Pro-FUdR cytotoxic fold change would be observed for BxPC3 pancreatic adenocarcinoma cells. A biocompatibility assay conducted by Dr Mark Salji confirmed that whilst FUdR produced a strong cytotoxic effect (EC_{50} = 8 nM), Pro-FUdR had no effect on cell viability at the maximum assay concentration of 1 µM (safety window >125-fold). FUdR and Pro-FUdr were progressed into an *in vivo* intratumoural Pd^0 bead injection / *ex vivo* prodrug activation study. ~ 1 x 10^9 CWR22 prostate cancer cells were injected into the prostate of male mice and grown to approximately 1 cm^3 tumours in accordance with standard protocols. 1 mg / mL of 130 µm Pd^0 beads was suspended in 50 µL sterile PBS and injected by a 1 mL syringe fitted with 9 mm gauge needle into the centre of a freshly excised CWR22 prostate cancer tumour (fig 5.3.3).

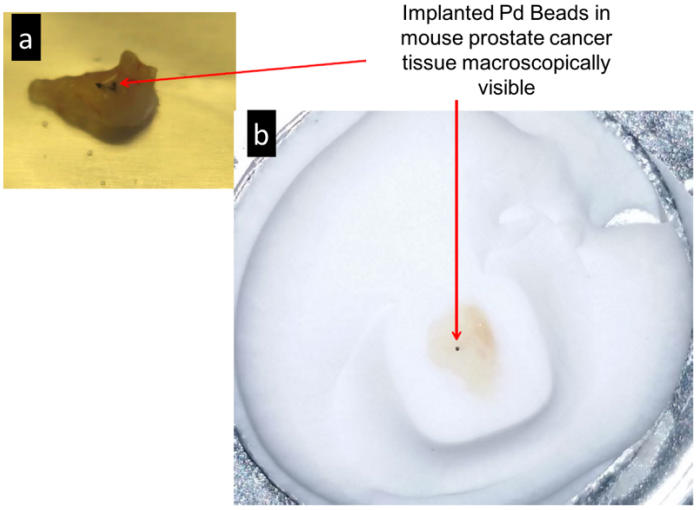

Figure 5.3.3 Observing the outcome of Pd^0 bead injections on tumour tissue samples. (**a**) A freshly excised 1 cm^3 CWR22 prostate tumour with injected Pd^0 beads (**b**) Lateral view of a 1 mm thick CWR22 prostate tumour slice section imaged during tissue fixation process with an individual Pd^0 bead.

Whole tumours were immediately soaked in RPMI media containing 0.1 % DMSO as a vehicle control or 100 µM Pro-FUdR and incubated under standard conditions for 48 hrs. Tumours were then sliced into 1 mm sections and embedded in paraffin wax for immunohistochemistry (IHC) staining (fig 5.3.4).

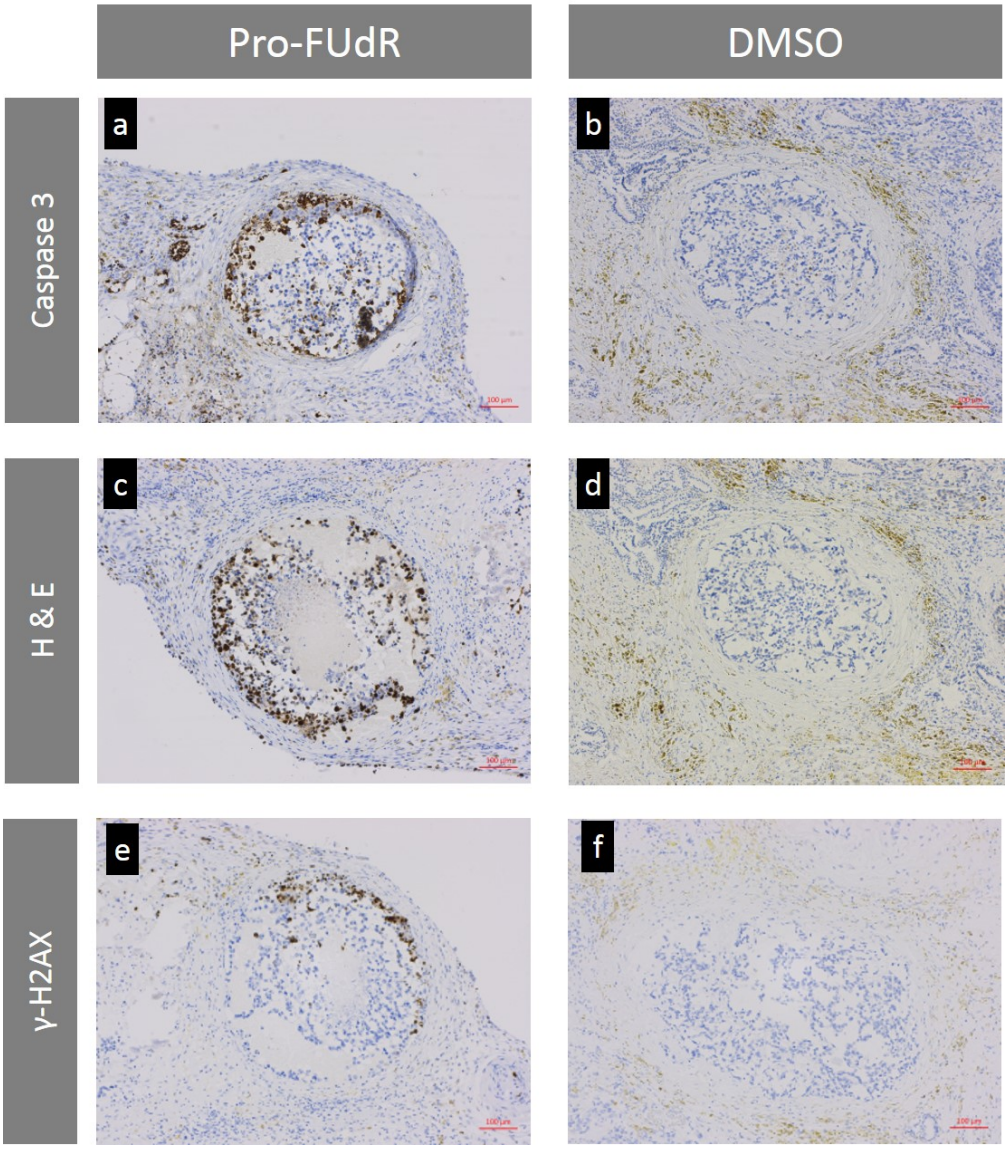

Figure 5.3.4 Immunohistochemistry staining of an intratumoural Pro-FUdR Pd-mediated activation assay Caspase 3 (**a,b**), hematoxylin and eosin (H & E) (**c,d**) and γ-H2AX (**e,f**) staining of CWR22 prostate tumours injected with 1 mg 130 μm Pd^0 beads in 50 μL PBS then excised and incubated for 48 hr in 0.1 % DMSO control or 100 μM Pro-FUdR and sliced into 1 mm sections for tissue processing. Apoptosis is identified according to each staining technique; (Caspase 3 (**a,b**); H & E (**c,d**) and γ-H2AX (g,h) – dark brown circles). Note the circular fibroblast ring present in each slice corresponding to needle injection. Pd^0 beads are absent due to the use of xylene during the tissue processing protocol.

Each panel of figure 5.3.4 shows a 1 mm tumour section sliced perpendicular to the axial plane of needle injection. The circular fibroblast ring in each image measures 9 mm in diameter, corresponding to the needle injection. Pd^0 beads present in tumour slices prior to fixation (fig 5.3.4) are unexpectedly absent from each image. This was due to the use of xylene, a conventional tissue fixation solvent used to clear unwanted tissue debris, dissolving Pd^0 beads

due to their polystyrene composition. Only the spaces left by implanted Pd^0 beads are visible (fig 5.3.5).

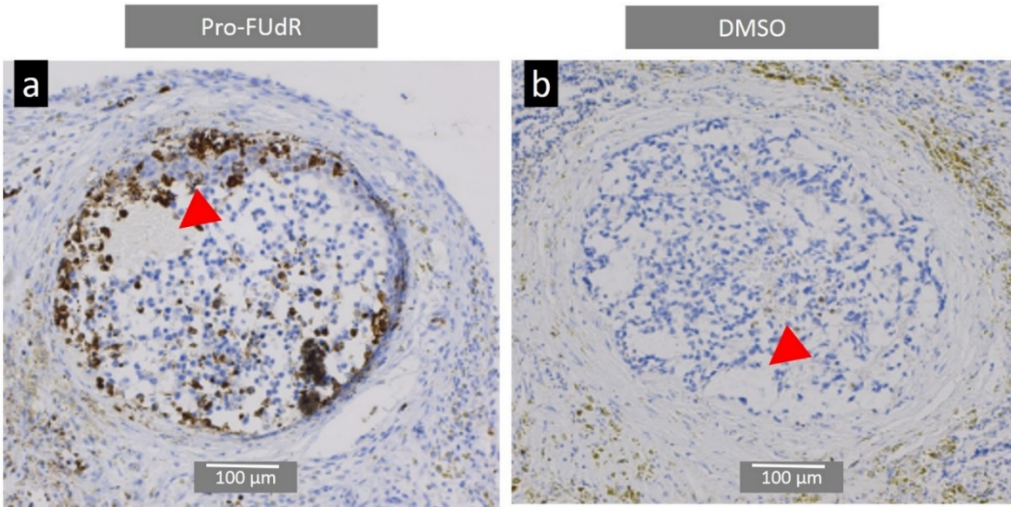

Figure 5.3.5 Proposed site of Pd^0 beads within a caspase 3 stained CWR22 prostate tumour tissue slice Red arrows indicate the space left by dissolved Pd^0 beads injected within the needle tract of a CWR22 prostate tumour in (**a**) 100 µM Pro-FUdR and (**b**) 0.1 % DMSO control treated tissue slices.

IHC indicates dark brown stains within the needle injection region and surrounding blank areas, proposed as the sites of individual Pd^0 beads, which were subsequently dissolved by xylene. Cellular activation of the caspase 3 pathway is a hallmark of apoptosis, and is indicated by a dark brown stain in cells undergoing apoptotic cell signalling. Hematoxylin and eosin (H & E) stain is another major determinant of single-cell necrosis/ apoptosis death, and is observed here by cellular morphology and dark stained colour associated with cell death. γ-H2AX staining also resolves localised regions of apoptotic activity by a dark brown stain in individual cells undergoing double stranded DNA breaks, an expected outcome of incorporating phosphorylated derivatives of FUdR into the cell.

Localised apoptotic regions present in Pro-FUdR treated samples (fig 5.3.4. left panels) were absent in DMSO treated samples (fig 5.3.4. right panels). This effect was therefore attributed to the activation of Pro-FUdR in combination with Pd^0 beads, and not due to needle injury or Pd^0 bead induced cytotoxicity within the tumour. The concerted cytotoxic effect between Pro-

FUdR and Pd^0 beads is further evidenced by the confined distribution of apoptotic cells within the fibroblast ring, the only region that Pd^0 beads were present in each sample, and the absence of cytotoxicity at the outer surface of tissue slices, which would be exposed to high concentration of the prodrug alone. Subsequently a new xylene free tissue fixation method was developed that would allow for the visualisation of the Pd^0 beads within tumour tissue (fig 5.3.6).

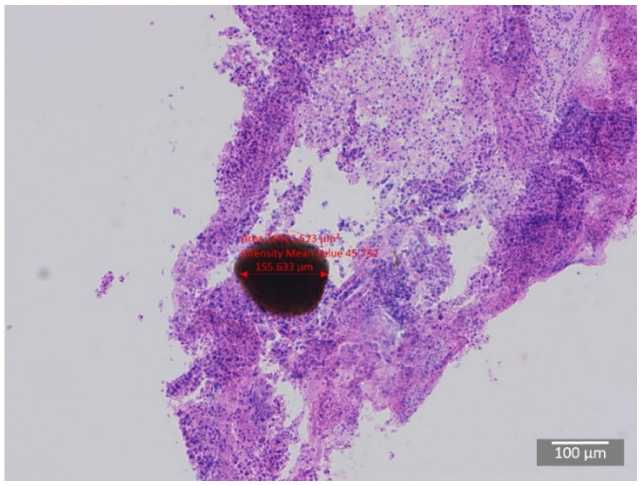

Figure 5.3.6 Xylene free histology for Pd^0 bead visualisation. Histology of a 1 mm^2 CWR22 tumour tissue slice mixed with a solution of Pd^0 beads and fixed using a xylene free freezing protocol.

This pilot study highlighted key areas for assay optimisation. First, FUdR and Pro-FUdR are not fluorescent molecules, the study of BOOM activation was ultimately confined to IHC. An ideal prodrug/drug candidate would possess fluorescent properties that could open the possibility for real time imaging of prodrug/drug biodistribution, interaction with the catalyst and cellular uptake by confocal microscopy. Although IHC identified localised regions of cell death, an accompanying fluorescing non-toxic live imaging apoptotic stain solution would also allow for the real-time observation of apoptosis within tissue samples.

Second, injecting a solution of 130 µm Pd^0 beads through a standard 1 mL syringe fitted with a 9 mm needle gauge was procedurally complex, as beads would fall out of suspension and settle within the syringe during the injection procedure. Smaller Pd^0 beads were anticipated to remain in suspension longer, allowing for a more controlled infusion of Pd^0 beads into the tumour. Pd^0 bead implantation was carried out by simply injecting a solution containing the

catalyst into a freshly excised tumour. Access to injection guiding equipment would allow for the precise intratumoural placement of Pd^0 beads into an anaesthetised mouse with minimal perturbation. This experimental setup would more closely approximate a clinical Pd^0 bead injection protocol.

5.3.3 Optimising an intratumoural *in vivo* Pd^0 bead implantation / *ex vivo* activation assay

Dox prodrugs **42** and **43** were selected for use in this assay. Dox is an anticancer therapy approved across several prostate cancer indications[284–286], and is a potent cytotoxin in human prostate DU145 cells *in vitro* studies (dox EC_{50} = 23 nM) (fig 4.5.a). **42** and **43** reduce the cytotoxic profile of dox *in vitro* by 240 and 310 fold respectively, with both prodrugs sensitive to Pd^0 bead mediated activation consistent with conversion of prodrug to drug after 5 days incubation (fig 4.25).

30 μm Pd^0 beads were selected on the basis of good biocompatibility (fig 4.20), selective prodrug **42** and **43** sequestration (fig 4.21 a,b) and rapid drug release (fig 4.25). In addition it is expected that smaller Pd^0 beads will remain suspended in solution for a longer period, simplifying the injection protocol. Dox and prodrugs are highly fluorescent, allowing for fluorescence microscopy of incubated tissue samples in combination with dox and prodrugs. 4',6-diamidino-2-phenylindole (DAPI) is a non-permanent nuclear stain that emits fluorescence in the blue range. DAPI cell penetration is significantly enhanced in cells that have lost membrane integrity. By binding to DNA and emitting a strong fluorescent signal, cellular populations that are undergoing cell death fluoresce with much stronger intensity than healthy cells. Accordingly, DAPI staining solution will be used as an accompanying non overlapping live imaging fluorescent apoptotic stain for the real-time observation of apoptosis within treated samples.

As sustained catalytic efficiency is a key consideration for *in vivo* prodrug activation, the catalytic effect of Pd^0 beads will also be investigated in parallel by use of a fluorescent probe - Bis-N,N'-Poc-Rhodamine 110 (Poc-Rho) and its Pd^0 activated product Rhodamine 110 (Rho),

in a probe activation study. First a longitudinal *in vivo* intratumoural Pd^0 bead injection / *ex vivo* probe activation assay was designed. This study investigated the effect of short vs. prolonged intratumoural Pd^0 bead incubation followed by treating the resulting explant tissue with a Pd-labile probe. Subsequently an *ex vivo* prodrug activation study was conducted. A schematic of this workflow is presented in figure 5.3.7

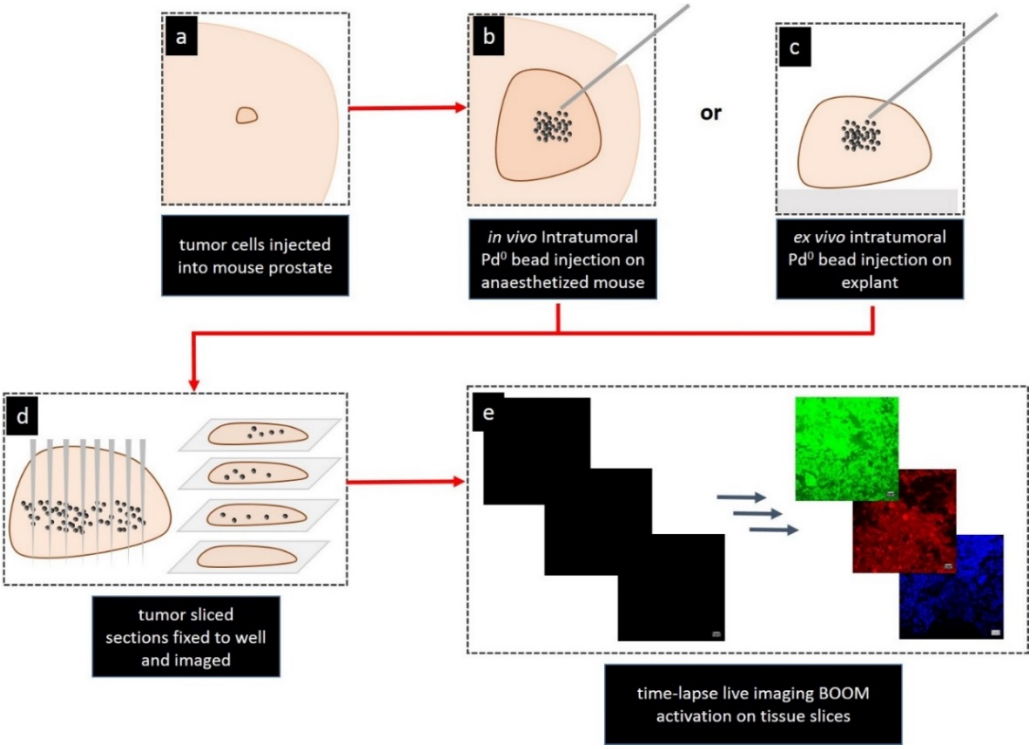

Figure 5.3.7 Schematic representation of *in vivo* Pd^0 implantation / *ex vivo* activation assay. (**a**) 1 x 10^9 DU145 prostate cancer cells were injected into nude mice prostates and grown to ~ 1 cm^3. (**b**) Mice were anaesthetised and 1 mg of 30 µm Pd^0 beads in 25 µL of sterile PBS was injected *in vivo* by ultrasound guidance into the DU145 tumour and incubated in the live mouse for 3 weeks then excised; or (**c**) tumours were resected and injected immediately *ex vivo* with 1 mg of 30 µm Pd^0 beads in 25 µL of PBS. (**d**) Excised tumours were sliced into 1 mm sections using a sectioned slicer matrix then fixed into 24 well plates using tissue glue and soaked in media containing prodrugs, probes or control. (**e**) Time-lapse live imaging of tissue slices by confocal microscopy monitored fluorescence increase attributed to Pd-mediated activation.

5.3.4 Development of an ultrasound guided in-vivo Pd^0 bead injection protocol

1 mg of 30 µm Pd^0 beads was suspended in 25 µL of sterile PBS solution and injected via ultrasound guided subcutaneous injection into prostate tumours. 30 µm Pd^0 beads remained

suspended in solution during the injection procedure. A shadowed region within the tumour was identified for Pd^0 bead placement, as this region was expected as a lower density, spongy material that would more efficiently absorb the injection volume. Pd^0 beads displayed strong echogenicity under ultrasound and were easily observed as intensely bright spots in the plane of detection (fig 5.3.8). Controlled administration of the Pd^0 beads directly into tumour was performed over a 30 s period. The injected region was monitored for an additional 10 min to ensure that Pd^0 beads were not leaking from the tumour into the extratumoural space, then the mouse was transferred for recovery.

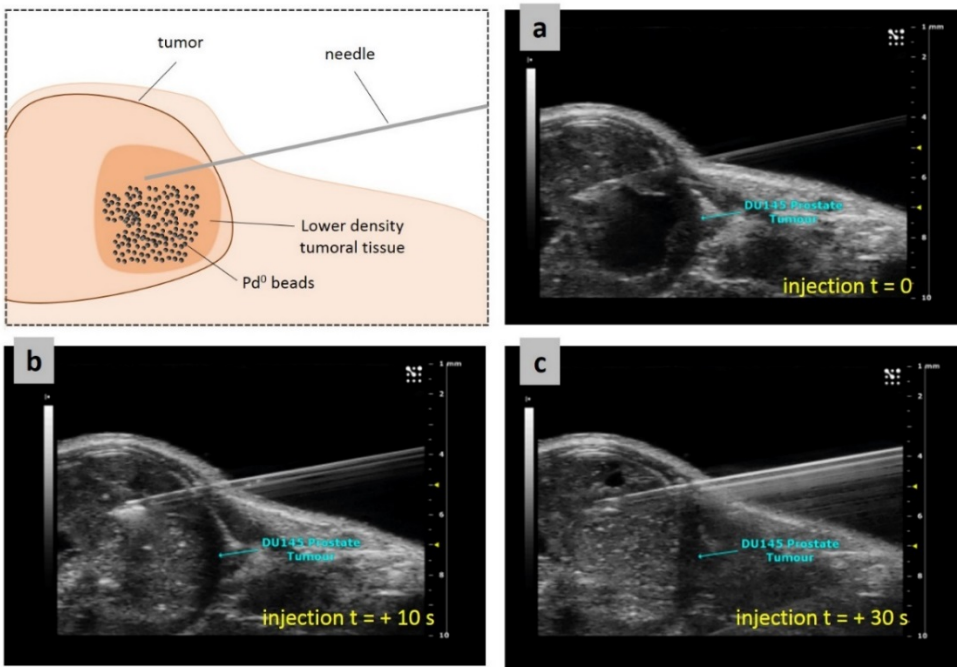

Figure 5.3.8 Subcutaneous ultrasound guided intratumoural prostate injection of 30 µm Pd^0 beads into anaesthetized mouse Top Left Panel: a schematic of the injection protocol to insert 1 mg of Pd^0 beads suspended in 25 µL into a tumour. Images captures during injection at (**a**) t = 0 s, (**b**) t = + 10 s and (**c**) t = + 30 s from the beginning of the injection. After t = + 30 s the 25 µL solution had been completely injected into the tumour mass.

After 3 weeks, a Pd^0 incubated tumour was removed and sliced in half to study the extent of Pd^0 distribution (fig 5.3.9). Pd^0 beads injected via this protocol were well retained within the injection site and highly concentrated along the needle injection tract. Examination of tissues

surrounding the injection site concluded that no Pd^0 beads had been ejected from the tumour during incubation (fig 5.3.9).

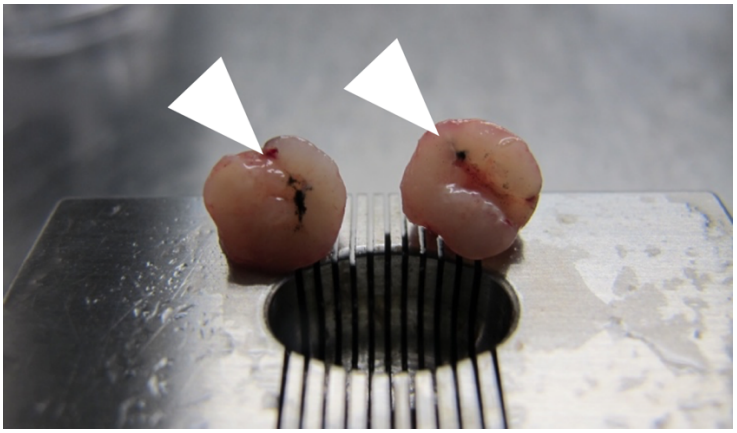

Figure 5.3.9 Resected tumor halved to visualise intratumoral Pd-implant distribution. 1 cm^3 mouse tumour implanted with Pd^0 beads via ultrasound guided syringe, incubated for 3 weeks then resected and sliced in half.

5.3.5 *ex vivo* Pd-mediated probe activation

The catalytic activity of Pd^0 beads implanted via this procedure were next assessed by an *in vivo* implantation / *ex vivo* probe activation assay using the non-fluorescent probe bis-N,N'-propargyloxycarbonylrhodamine 110 (Poc-Rho). Poc-Rho was selected as an off-on fluorescence probe capable of undergoing selective Pd-mediated activation *in vivo*[89] (fig 5.3.10).

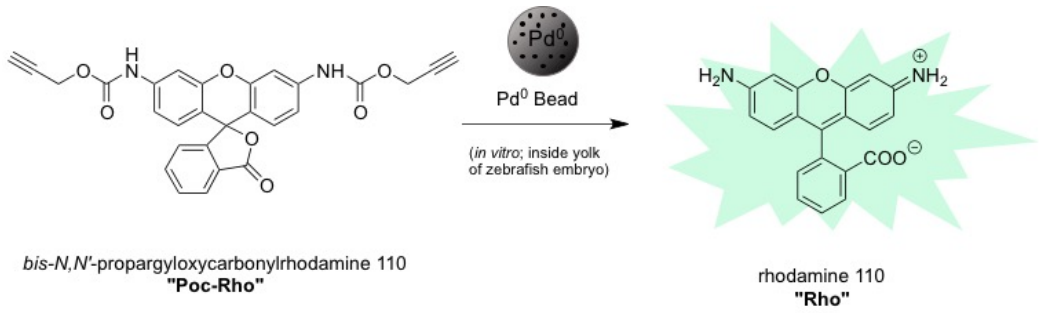

Fig 5.3.10 Conversion schematic of non-fluorscent bis-N,N'-propargyloxycarbonylrhodamine 110 (Poc-Rho) into fluorescent rhodamine 110 (Rho) by Pd-mediated carbamate cleavage.

Tissue samples containing no Pd^0 beads, short or +3 week incubated Pd^0 beads were soaked in media containing 100 μM Poc-Rho and monitored for fluorescence by live cell-imaging confocal microscopy over 63 hr (fig 5.3.11).

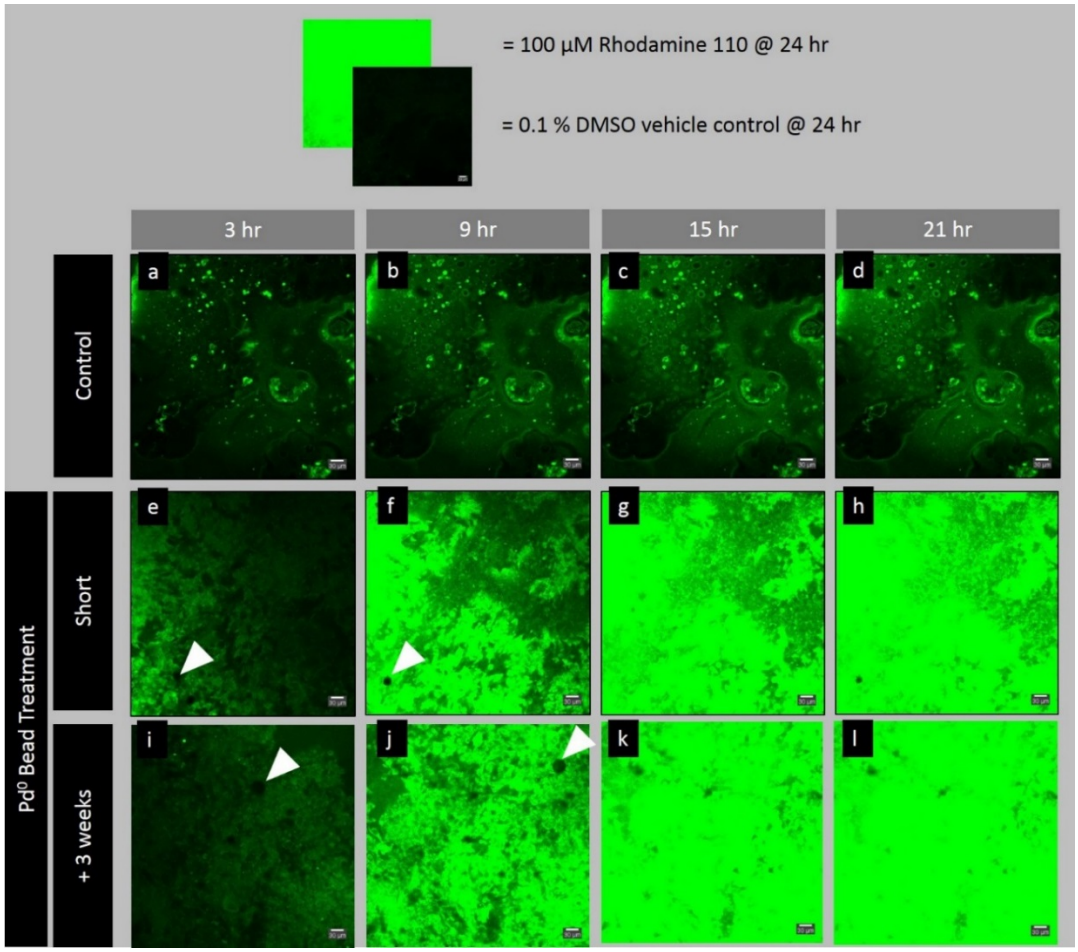

Figure 5.3.11 *ex vivo* Pd-mediated carbamate cleavage of *bis*-N,N'-Poc-Rhodamine 110 incubated with *in vivo* Pd^0 bead injected prostate tumour samples. Pd^0 beads were injected and tissue samples prepared according to the procedure described in Section 5.3.1 (short) or Section 5.3.4 (+ 3 weeks). Time-lapse images of fixed tissue samples incubated under standard conditions and treated with 100 μM Poc-Rho alone (**a - d**), 100 μM Poc-Rho + acutely administered Pd^0 beads (**e – h**) or 100 μM Poc-Rho + 3 week incubated Pd^0 beads (**i - l**) every 3 hrs for 21 hr.

In the absence of Pd^0 beads, Poc-Rho undergoes slow conversion to Rho over a 21 hr period (fig. 5.3.12. a - d), showing the relative stability of this carbamate bond to be cleaved over time within the tumour environment. Individual Pd^0 beads can be observed within injected tissue slices as highlighted by the white arrows in (fig. 5.3.11. e,f) and (fig. 5.3.11. i,j). Pd^0 beads that

underwent intratumoural incubation for 3 weeks prior to treatment did not appear to have a reduced catalytic effect. Both short and 3 week incubated Pd^0 beads samples rapidly converted Poc-Rho to Rho after 9 hrs, and signal saturation in both tissue slices within 21 hrs (fig. 5.3.11. e - h, i - l).

This study coupled with Pd^0 bead distribution observations provide key insight into the non-perturbing effect of the catalyst. Pd^0 beads may be injected into a tumour mass using the conventional microsurgical technique of ultrasound guided injection. As Pd^0 beads are highly echogenic, this procedure allows for the visualisation of Pd^0 beads within a tumour. Once injected, Pd^0 beads are retained within the tumour where they remain highly concentrated along the needle injection tract. No leakage is observed from the injection site into surrounding tissue, with mice bearing Pd-incubated tumours progressing with no additional effect attributed to the injection protocol or intratumoural presence of the catalyst during an 8 week study. Intratumoural incubated Pd^0 beads are capable of rapidly converting Poc-Rho at a rate comparable to freshly injected Pd^0 beads. This further validates the bioorthogonality of the catalyst, as extended exposure to biology does not interfere with the catalytic conversion properties of the non-toxic Pd^0 beads. This is a key finding for the validation of a BOOM chemotherapeutic concept, whereby the catalyst is capable of retained Pd-mediated prodrug activation during repeated prodrug administration, lasting perhaps months or until remission is achieved.

5.3.6 *ex vivo* tumour explant drug/prodrug biocompatibility study

The next step was to investigate the fluorescence spectra of dox prodrugs for *in vivo* imaging. Dox and prodrugs retained a broad fluorescence emission, with a local maxima at 597 nm (fig 5.3.12).

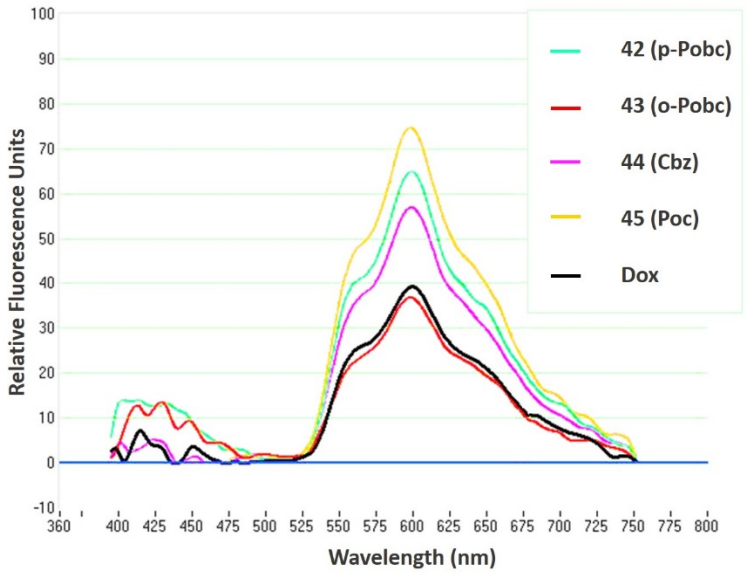

Figure 5.3.12 Fluorescence spectra of dox and prodrugs Protocol: dox and prodrugs were incubated at 10 μM in PBS and the fluorescence spectra were collected using a Nanodrop™ 3300 Fluorospectrometer with an excitation wavelength of 365 nm.

As shown in figure 5.3.12, fluorescence signals prevent the resolution of prodrug to dox conversion due to significant overlap. Red channel fluorescence imaging will be limited to providing information regarding the biodistribution and potential Pd^0 bead sequestration of drug/prodrug. 4',6-diamidino-2-phenylindole (DAPI) was chosen as a non-overlapping cell death marker that fluoresces when bound to DNA (absorption maxima 358 nm, emission maxima 461 nm). A 0.1 % (v/v) DMSO control and 100 μM solutions of Dox, **42** or **43** in RPMI media were incubated under standard conditions together with prepared tumour tissue samples according to the protocol described in figure 5.3.8 and monitored for DAPI and drug/prodrug fluorescence by live-imaging confocal microscopy over 63 hr (fig 5.3.13-15).

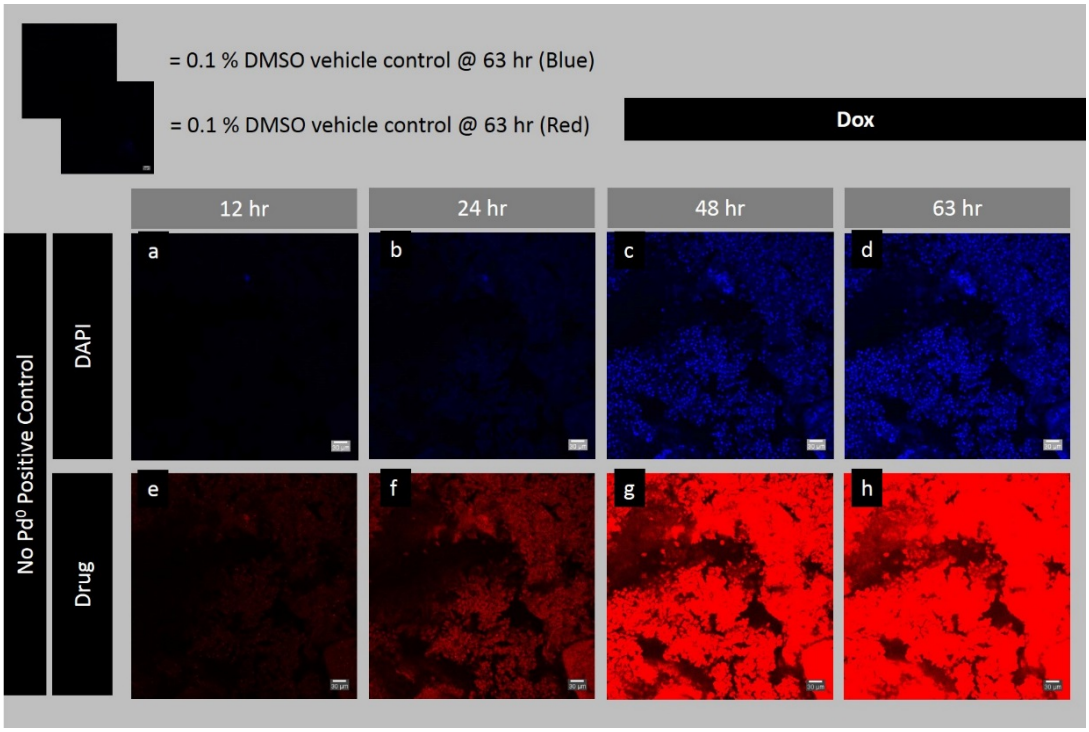

Figure 5.3.13 *ex vivo* biocompatibility study of dox in prostate tumour samples. Time-lapse images of a fixed tissue sample incubated under standard conditions and treated with 100 μM Dox. Images taken every 3 hr from t = 0 – 63 hr under blue fluorescent channel (for DAPI) (**a** - **d**) and red fluorescent channel (for dox) (**e** - **h**) fluorescence, modified by ImageJ. Scale bar = 30 μm. *n* = 2 tissue slices.

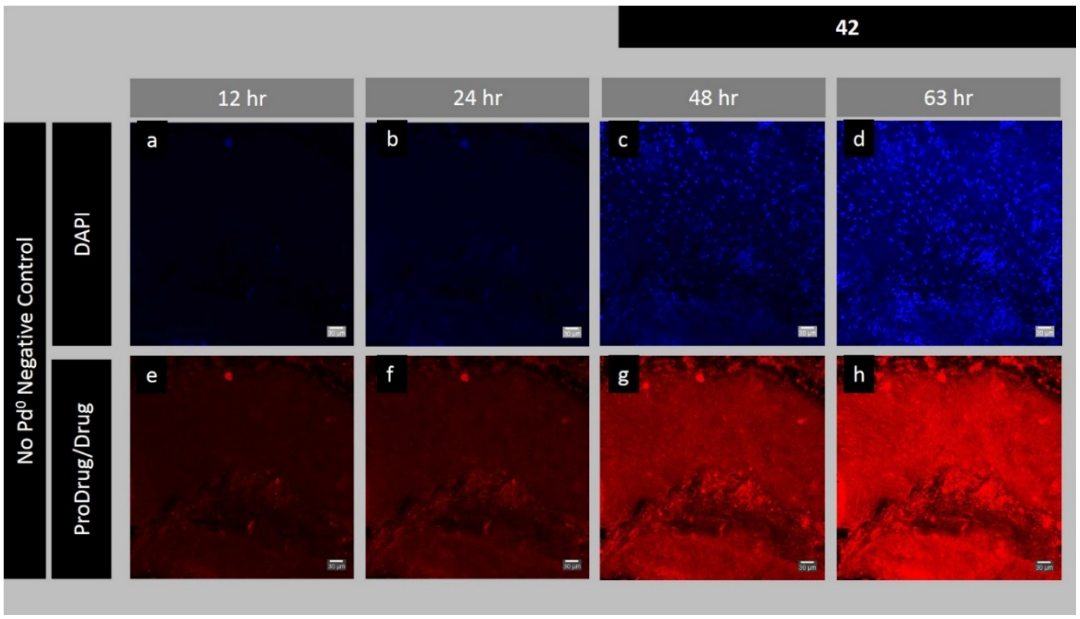

Figure 5.3.14 *ex vivo* biocompatibility study of 42 in prostate tumour samples. Time-lapse images of a fixed tissue sample incubated under standard conditions and treated with 100 μM **42**. Images taken every 3 hr from t = 0 – 63 hr under blue fluorescent channel (for DAPI) (**a** - **d**) and red fluorescent channel (for **42**) (**e** - **h**) fluorescence, modified by ImageJ. Scale bar = 30 μm. *n* = 2 tissue slices.

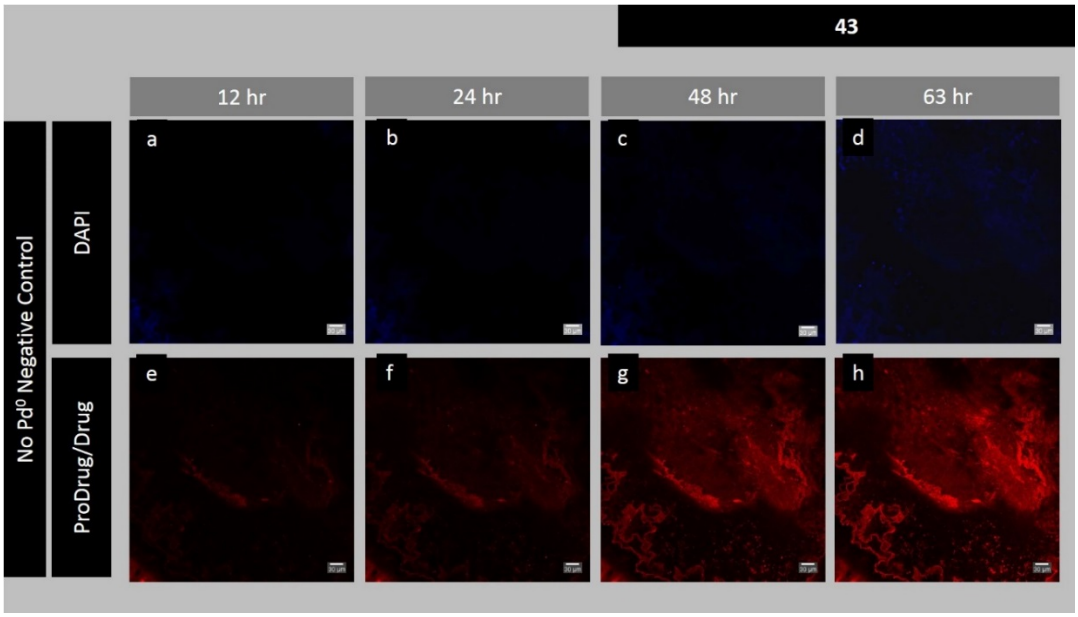

Figure 5.3.15 *ex vivo* biocompatibility study of 43 in prostate tumour samples. Time-lapse images of a fixed tissue sample incubated under standard conditions and treated with 100 μM **43**. Images taken every 3 hr from t = 0 – 63 hr under blue fluorescent channel (for DAPI) (**a** - **d**) and red fluorescent channel (for **43**) (**e** - **h**) fluorescence, modified by ImageJ. Scale bar = 30 μm. *n* = 2 tissue slices.

Control tumour samples treated with 0.1 % (v/v) DMSO vehicle displayed no fluorescence signal during 63 hr (fig 5.3.13, top left panels). This suggested that the protocol developed for tumour tissue resection and preparation did not induce cytotoxicity. Dox distributed evenly throughout tissue samples and appeared to accumulate within individual cellular nuclei, producing bright fluorescence spots overlapping with the DAPI stain. Cell death was first observed after 48 hr. This suggests an initial step whereby dox concentrates within the cell over time, with accumulated cellular damage then triggering rapid cell death.

The fluorescence signal corresponding to **42** in the red channel produced a distribution pattern discernibly different from that associated with dox (fig 5.3.14). Whereas the signal accumulated over time, intense spots representing the nuclear accumulation of dox were not observed, however cell death was patently observed after 48 hr. This may indicate that, whilst resistant to metabolic cleavage, the cell death produced after 48 hr is due to **42** alone inducing

cytotoxicity in its inactive form. This indicates that a 100 μM solution of **42** is not biocompatible in tumour tissue at 100 μM during a 3 day study.

As with **42**, the fluorescence signal associated to **43** was discernibly different to that of dox (fig 5.3.15). **43** may be taken up more slowly into tumour tissue, observed by a relatively weaker fluorescence signal. A weak DAPI signal was observed after soaking the tissue sample in 100 μM of **43** after 63 hr. This is consistent with the increased safety profile attributed to enhanced steric bulk for the o-Pobc protection strategy (see Chapter 4). The EC_{50} of **43** in *in vitro* biocompatibility assays are 1.3 fold and 2.3 fold higher than **42** in DU145 and U87 cells, with over 300 fold reduction in cytotoxicity with respect to dox. **43** was non-toxic to zebrafish during 5 days incubation at 200 μM, and did not induce cytotoxicity to a MCTS during 7 days at 100 μM. As a result, **43** was progressed into an intratumoural *in vivo* Pd^0 bead implantation / *ex vivo* prodrug activation assay.

5.3.7 Intratumoural *in vivo* Pd^0 bead implantation / *ex vivo* prodrug activation assay

Tissue samples containing shortly incubated or 3 week incubated 30 μm Pd^0 beads were soaked in media containing 100 μM of **43** and monitored for fluorescence attributed to drug/prodrug distribution (red channel) or DAPI staining (blue channel) by live-imaging confocal microscopy over 63 hr (fig 5.3.16) (fig 5.3.17).

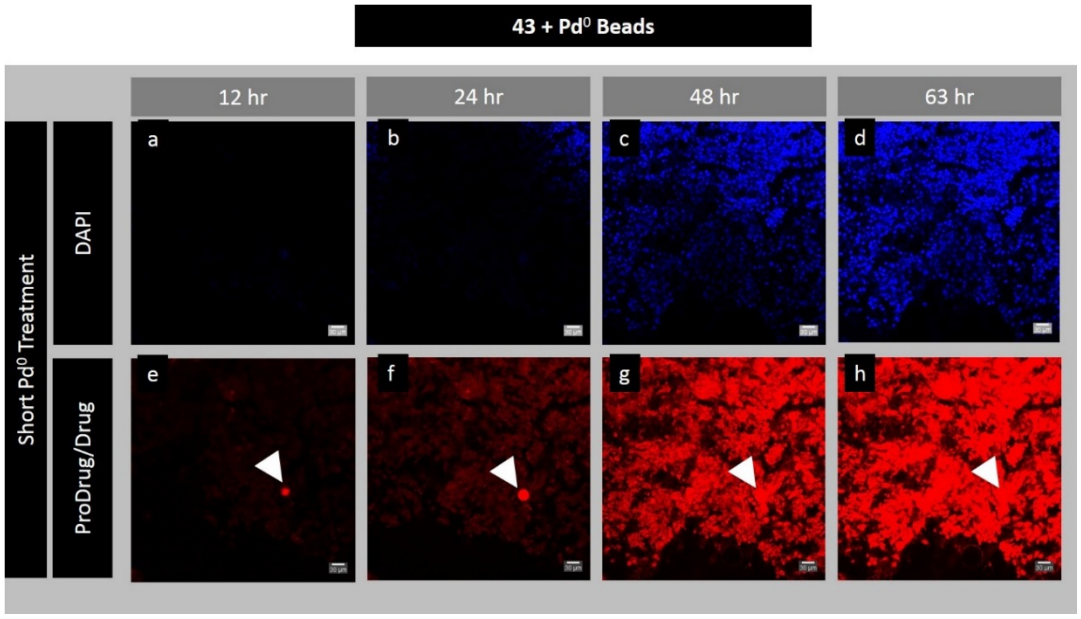

Figure 5.3.16 *ex vivo* Pd^0-mediated carbamate cleavage of 43 with shortly administered *in vivo* Pd^0 bead injection into prostate tumour samples. 30 μm Pd^0 beads were injected and tissue excised according to procedure described in Section 5.3.1. Representative time-lapse images of fixed tissue samples incubated under standard conditions and treated with 100 μM **43** + shortly administered Pd^0 beads in red (**a – d**), and blue (**e – h**) fluorescence channels. Images captured every 3 hrs for 63 hr and modified by ImageJ. Scale bar = 30 μm. *n* = 2 tissue slices.

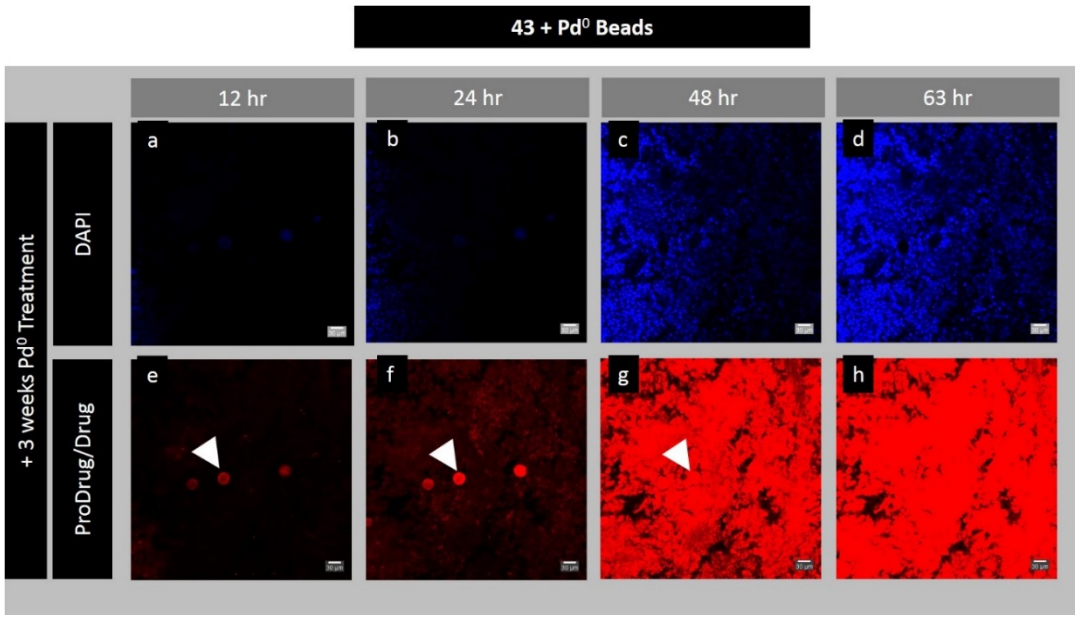

Figure 5.3.17 *ex vivo* Pd^0-mediated carbamate cleavage of 43 with 3 week incubated *in vivo* Pd^0 bead injections into prostate tumour samples. Pd^0 beads were injected and tissue excised according to procedure described in Section 5.3.4. Representative time-lapse images of fixed tissue samples incubated under standard conditions and treated with 100 μM **43** + 3 week Pd^0 beads in red (**a – d**), and blue (**e – h**) fluorescence channels. Images were captured every 3 hrs for 63 hr and modified by ImageJ. Scale bar = 30 μm. *n* = 2 tissue slices.

Remarkably, the prodrug sequestration effect observed in section 4.15 is clearly evident for all combinations of **43** and Pd^0 beads, indicated by white arrows in figure 5.3.16, figure 5.3.17 and below (fig 5.3.18).

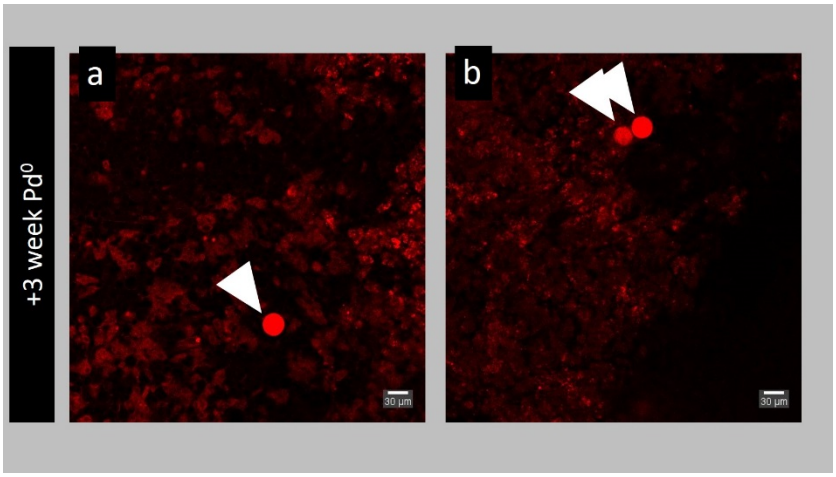

Figure 5.3.18 Sequestration effect of Prodrug 43 within + 3 week incubated Pd^0 bead injections into prostate tumour samples. (**a**,**b**) **43** is rapidly sequestered into 30 µm Pd^0 beads, shown by fluorescing bead. Images of two samples (**a**,**b**) captured at + 36 hr during a 100 µM **43** treatment study.

The *in vivo* injection of Pd^0 beads followed by immediate *ex vivo* BOOM activation of **43** resulted in a strong cytotoxic effect. DAPI staining showed a clear cytotoxic response after 48 hr incubation. The DAPI cytotoxic signal produced is not localised around individual beads, but rather increases across the frame from 48 – 63 hr (fig 5.3.16 & 5.3.17 panels c & d). This is likely due to the variable density of tissue within each explant. Active dox expelled from beads is absorbed by solution and evenly distributes about the well. Thinner peripheral sections of tissue are more exposed to solution and uptake a relatively higher proportion of drug compared with denser regions. The red fluorescence signal attributed to **43** or dox in both short and prolonged Pd^0 bead incubation shows a biodistribution pattern more closely approximating that of the active drug, overlapping with DAPI (fig 5.3.18), which suggests that dox is chemically released by Pd-mediated activation and is responsible for observed cell death.

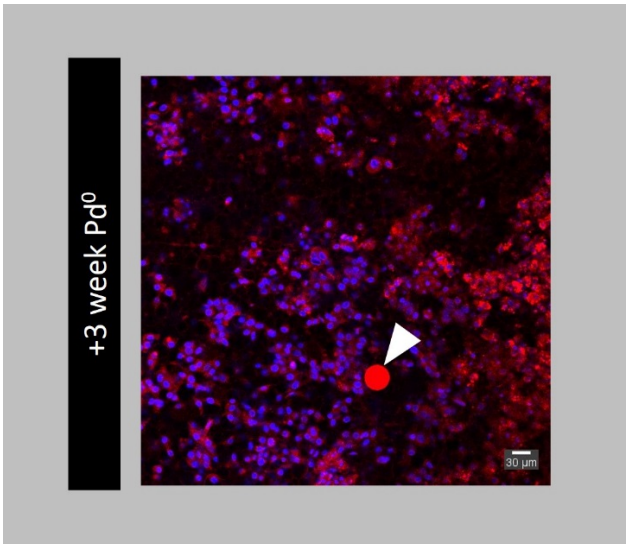

Figure 5.3.19 Fluorescence signal merge (blue and red channels) corresponding to dox induced cellular cytotoxicity.

42 + Pd^0 beads produced an effect similar to that seen with **43**, however the underlying cytotoxicity induced by **42** alone precluded an independent analysis of BOOM induced cytotoxicity. The *in vivo* / *ex vivo* combination of **42** + Pd^0 beads was not reported for this reason. Prodrug **43** preferentially and rapidly sequesters into Pd^0 beads administered into a prostate tumour. **43** then undergoes Pd-mediated conversion to dox, which is released into the interstitial space and accumulates in tumour cells inducing cytotoxicity. A comparable effect is observed between short and prolonged intratumoural incubation of Pd^0 beads within a live mouse for 3 weeks. This study provides *in vivo* evidence that BOOM chemotherapy could be used for administration and selective activation of a prodrug within tumour over an extended timeframe.

5.3.8 Conclusions

Various biological assays have been developed to explore and validate BOOM chemotherapy in complex biological systems. A 3D cell culture MCTS assay provided evidence that **43** alone would not induce cytotoxicity to an *in vivo* tumour at 100 µM. This was higher than the cytotoxic effect observed in a 2D *in vitro* experiment (EC_{50} = 7.13 µM). By embedding Pd^0 beads into pre-formed spheroids and monitoring for cytotoxicity using DRAQ7™ it was confirmed that Pd^0

beads in direct contact with cellular surfaces were non-toxic. Ultimately prodrug activation in this assay was not achieved, attributed to the use of Matrigel®, a highly viscous glue required for the structural architecture of the growing spheroid. Matrigel® may have prevented **43** from accessing the Pd^0 bead, or from the effective release of dox into solution post conversion. By separately incubating a 100 μM solution of **43** in combination with 1 mg / mL of Pd^0 beads for 72 hrs then replacing the media of a pre-formed spheroid with this mixture a strong cytotoxic effect was observed, further supporting the likelihood that Matrigel® was preventing effective prodrug uptake into individual Pd^0 beads.

An *in vivo* zebrafish cardiotoxicity assay was designed to study the effect of **43** on cardiac oedema. 50 μM dox induced large cardiac oedema's in embryonic zebrafish, with 100 % lethality in all populations incubated at > 50 μM dox. **43** did not induce lethality or observed cardiac oedema even up to 200 μM – well above the theoretical maximum therapeutic dosage prescribed in a clinical dox dosing regimen. Fluorescence microscopy determined that **43** was less readily absorbed and retained by zebrafish with respect to dox.

An *in vivo* microsurgery injection protocol was developed to insert a BOOM catalyst into the prostate tumour of an anaesthetized mouse. Ultrasound guided injection enhanced control over the injection process. Pd^0 beads were revealed to be highly echogenic. Ultrasound would be an ideal modality for the non-invasive visualisation of Pd^0 bead biodistribution within a tumour. Pd^0 beads were retained within the tumour, where they remained highly concentrated within the intratumoural needle tract during 3 weeks of incubation. An off-on fluorescence probe, Poc-Rho, was utilized in an initial *in vivo* / *ex vivo* probe activation assay to study the effect of short vs extended Pd^0 bead incubation within live tumour tissue samples. Extended intratumoural incubation did not reduce the underlying catalytic turnover rate achieved by Pd^0 beads. Rapid activation of Poc-Rho was achieved in combination with both acutely administered and + 3 week incubated Pd^0 beads.

An *ex vivo* tumour biocompatibility study showed that **43** was relatively non-toxic at 100 μM. This was consistent with spheroid and zebrafish studies, and may be attributed to the enhanced steric hindrance afforded by an ortho positioned propargyl group on the Pobc protecting group. This lead to the *in vivo* injection / *ex vivo* prodrug activation study of prodrug **43**. Intratumourally injected Pd^0 beads in short or extended incubation settings were both capable of rapidly sequestering **43** to rapidly release active drug at sufficient concentration to induce cytotoxicity in tumour tissue within 48 hr.

The next step will be to conduct an *in vivo* Pd^0 implantation and prodrug administration BOOM activation assay to evaluate the performance of this optimised system. This would allow for the study of **43** biodistribution and pharmacokinetics, as well as the ability for systemically circulated prodrug to be sequestered and converted by intratumourally inserted Pd^0 beads. Furthermore, an embryonic zebrafish cardiac oedema study has laid the foundation for a parallel study on the *in vivo* effect of **43** on cardiomyopathy during localised BOOM activation. The methodology for precise intratumoural Pd^0 bead implantation, tissue preparation and analysis in a rodent model has been optimised. **43** was validated as an ideal candidate for the study of Pd-mediated prodrug activation *in vivo* by three complex biological assays.

CHAPTER 6

Conclusions and Future Work

Bioorthogonal chemistry unlocks new and transformative ways to undertake the non-perturbing chemoselective making and breaking of chemical bonds in biology. Conducting chemistry within a biological system imposes extraordinary demands on chemical reactivity, and as such the scope of early bioorthogonal chemistry was initially confined to a limited number of reactions. Early investigations primarily focused on developing novel reaction partners to probe biology, allowing for the chemoselective study of recombinant proteins[10], cellular surfaces[11] and metabolic processes[23]. Since these and other landmark advances, a wide range of bespoke reaction partners have emerged. The field of bioorthogonal chemistry is now furnished with a rich catalogue of reaction partners for chemistry in the living cell. Despite the advent of non-metallic strain promoted reactions, bioorthogonal metal catalysts have already emerged as a novel subtype of bioorthogonal chemistry due in most part to dramatic improvements in ligand design and encapsulation methods that reduce the underlying toxicity of the metal whilst improving the rate of catalysis.

To this extent, our group has focused on the use of Palladium (Pd) chemistry to conduct biocompatible covalent bond breaking. By immobilizing Pd^0 nanoparticles onto matrix resin beads through a solid support chemical interaction with PEG-PS polymers, various drugs and probes have been unlocked in cellular culture, including within the embryonic yolk sac[89] and even in the intracranial space of live zebrafish[131]. This catalytic system provides the basis for a new prodrug approach to chemotherapy, whereby the chemospecific transformation of a small molecule, such as a chemotherapeutic, may be focused by a device implanted within a target tissue. Both the method of delivering cancer therapeutics as well as the therapeutic window of many small molecule cancer drugs is sub-optimal. Conventional chemotherapy administers ‘free’ drug into the body via an oral or intravenous administration route. Intravenous administration ensures that the patient receives rapid systemic administration of the drug, whereas oral drugs must overcome absorption barriers resulting in increased

pharmacokinetic variability[287]. The activity of some non-targeting chemotherapies may be regulated to an extent by modification of the excipient formula and method of delivery, however off-target effects are an inevitable outcome when potent molecules circulate systemically throughout the body. Whereas targeting chemotherapies were envisaged to prevent side-effects by virtue of molecular design, a new era of targeted therapies has done little to remove this underlying problem. Several clinical trials have reported increased incidence of severe treatment induced side effect caused by targeted medicines with no corresponding improvement in treatment efficacy.

Treatment induced side-effects cause detrimental harm to the body and force dose-limitations which in turn reduce the efficacy of treatment. Many drugs are administered with adjuvants designed to reduce off-target effects, however some adjuvants are themselves toxic and known to reduce the underlying efficacy of treatment. Thus a non-ideal balancing act is required to maximize the tolerated dosage of a drug whilst managing acute side-effects that may themselves be life threatening.

A strategy that masks the cytotoxicity of a drug until it reaches the site of tumour could alleviate this intractable drawback. Furthermore, if suitable modification of the molecule results in a prodrug that preferentially accumulates into the metal catalyst where it is converted and released, the effective dosage delivered to the target tissue may be dramatically higher than the systemically circulating dose. To that extent BOOM chemotherapy emerges as an attractive potential treatment strategy. Considerable effort has developed new methods of delivering molecules to tumours with improved pharmacokinetic and biodistributive properties[288–292]. Typical drug delivery systems applied to the chemotherapeutic space include lipid-based carriers (miscelles, lipid-drug emulsions and complexes), polymer-drug conjugates and polymer microsphere products[288]. Polymeric microspheres have undergone extensive investigation as drug carriers capable of synthetic modification[293], high loading capability[294] and controllable drug release and/or activation in living systems[291]. Polyethylene glycol (PEG) constitutes the majority of polymeric microsphere drug delivery systems[288]. Drug eluting

polymeric microspheres have altered the PK, biodistribution and efficacy of multiple chemotherapeutics[295–297] including microsphere formulations of 5FU[298], gemcitabine[299] and doxorubicin[300–302]. The non-toxic Pd catalyst employed in this thesis is constituted of resin formulations employed in many promising drug delivery PEGylated microsphere systems that would be highly relevant in the clinical setting.

The work of this thesis progresses the BOOM chemotherapeutic concept into pre-clinical evaluation, by improving various aspects concerning bioorthogonal reactivity of the catalyst against a library of novel anticancer prodrugs. Three anticancer drugs were investigated.

The first of these was 5-fluorouracil (5FU). Each of the endocyclic NH groups of 5FU plays a key role in enzymatic recognition for the biosynthesis of active metabolites that induce an antiproliferative effect[92,105,108,111]. By mono-alkylating 5FU at the N1 or N3 position (prodrugs **3** and **4**), and bis-alkylating at both (prodrug **5**), the cytotoxic profile of the parent molecule was completely removed and subsequently restored by N-dealkylation in the presence of Pd beads[34,88]. Of these **5** is capable of simultaneously blocking both N1 enzyme mediated glycosylation and N3 mediated catabolism. **5** however displays a slow stepwise release of 5FU in the presence of a Pd source, which may result in the release of inactive mono-alkylated 5FU derivatives into tumour tissue, reducing the effectiveness of treatment. Furthermore, the clogP of **5** is – 0.4, not ideal for bioavailability or the development of an oral chemotherapeutic. **2** was developed as an optimised lactim trapped *bis*-O-propargylated analogue of **5**. Like **5**, **2** displayed no cytotoxicity. Unlike **5** however, **2** was sequestered within Pd beads when mixed in solution, which then rapidly released 5FU without the appearance of mono-propargylated intermediates. This sequestration effect was due to increased lipophilicity, as **2** has a clogP of + 1.66. The synergistic cytotoxicity produced when **2** was incubated together with Pd beads together in cell culture was comparable to that of 5FU.

The preferential sequestration of lipophilic prodrugs into the polymeric matrix of the catalyst resin is in fact a highly attractive feature for BOOM prodrug activation. Conceptually, the

intratumoural implanted catalyst may be capable of pulling a lipophilic prodrug out of systemic circulation by sequestration, then converting and locally expelling the hydrophilic drug product. This would serve as a means of concentrating treatment to the site of the catalytic implant. **2** represents an optimised physicochemical, biocompatible prodrug of 5FU capable of prodrug activation in the presence of a Pd source. **2** should next be progressed into an *in vivo* pharmacokinetic study.

Gemcitabine was the second antimetabolite investigated for use as a BOOM reaction partner. Gemcitabine is expected to undergo strong binding affinity within the active pocket of deoxycytidine kinase (dCK), with key recognition between amino acid residues and gemcitabine's C5'OH and C4NH_2 groups during initial phosphorylation and subsequent activation[160]. In addition, gemcitabine is rapidly deactivated by cytidine deaminase (CDA) hydrolytic deamination via C4NH_2 mediated enzymatic recognition[169]. These mechanisms have lead to the investigation of various alkyl carbamate and carbonate protected prodrugs that were expected to produce a pharmacophoric blockade to C5'OH and C4NH_2 groups. No carbonate protected gemcitabine prodrug has been previously found to be resistant to metabolic cleavage, whereas Alloc, and Poc carbamate protected prodrugs produced a moderate reduction in cytotoxicity with lability to a Pd source[89].

By incorporating together aspects of the Poc and Cbz protecting groups, we designed a novel Propargyloxybenzylcarbonyl (Pobc) protecting group. Pobc would be capable of enhanced bioorthogonality afforded by steric bulk to restrict enzymatic cleavage. Pobc would also retain Pd lability by propargyloxy trigger initiated benzyl elimination. A palladium-triggered 'self-immolation' event liberates the active drug along with the non-toxic by-products[180–183] acetol[89,184] and hydroxybenzyl alcohol, both of which were confirmed as non-toxic in cell culture, as well as the benign gas CO_2. A semisynthetic strategy was capable of masking the C5'OH and C4NH_2 functional groups of gemcitabine. **33**, the p-Pobc functionalised C4NH_2 promoiety was capable of 27 fold reduction in cytotoxicity against gemcitabine, a meaningful improvement over Poc functionalisation at the same site (EC50 (**33**) / EC50 (**25**) ~ 3. o-Pobc

was expected to outperform p-Pobc in terms of reduced cytotoxic fold change by virtue of increased steric bulk about the carbamate, however curiously **34** exhibited cytotoxicity similar to gemcitabine. The C5'OH o-Pobc masked prodrug **36** however produced a slight improvement over previously reported alkyloxycarbonyl functionalised prodrugs, although the cytotoxic fold change provided a narrow therapeutic window to observe the effect produced by Pd-mediated conversion to the active drug. Carbonate protected prodrugs of gemcitabine are not likely capable of withstanding extended incubation in cell culture.

A synergistic effect was produced when **33** or **36** were incubated in combination with Pd beads, suggesting that Pobc functinalised prodrugs were capable of Pd-mediated 'self-immolation'. Although the bioorthogonal fold change achieved with Pobc functionalised gemcitabine prodrugs was not sufficient to progress candidates into animal studies, this study provided a proof of concept for the design, synthesis and activation of the Pobc group for use in the next drug candidate. As the activity of gemcitabine is determined by multiple amino acid residue interactions within an active pocket, functionalising at one of C5'OH or C4NH_2 may not provide a pharmacophoric blockade strong enough to completely restrict enzymatic recognition, metabolic cleavage and subsequent activation of the drug. A bi-functionalised prodrug of gemcitabine may further enhance the bioorthogonality fold change by simultaneously blocking both active sites.

Poc, Cbz and Pobc promoieties were next functionalised to the C3' amino of doxorubicin via a semisynthetic strategy. Dox is a widely used chemotherapeutic that induces severe off target side effects due to the broad range of pathways involved in eliciting cytotoxicity[197,198,195,196,199,200]. The C3' amino group is established as a key functional group involved in the cytotoxic response[203–205]. Various C3' acyl and carbamate functionalised prodrugs have been developed that were capable of effectively reducing cytotoxicity[215–217]. By N-functionalising doxorubicin with Poc, Cbz and Pobc promoieties, a direct correlation between increased steric bulk and reduced cytotoxicity was observed in cell culture.

Both Pobc-functionalised dox prodrugs displayed > 100 fold reduction in cytotoxicity, achieving our self-imposed goal in terms of therapeutic window, with o-Pobc prodrug **43** approximately twice as bioorthogonal as p-Pobc prodrug **42**. This suggests that masking the C3' amino group of dox with a more sterically hindered carbamate protecting group provides an effective pharmacophoric blockade against DNA intercalation and TopoII binding. This lead to the development of *bis*-o-Pobc protected prodrug **50**, which was expected to further enhance the bioorthogonality of this candidate with respect to o-Pobc (due to steric bulk) and Pd-lability (by adding an additional trigger group to the aryl ring). **50** was only capable of producing a moderate reduction in cytotoxicity fold change, whilst increased lipophilicity hindered subsequent *in vitro* study.

42, **43**, **45** and **50** underwent Pd-mediated carbamate cleavage by HPLC analysis, demonstrating dox release in combination with Pd beads. During this study, dox and prodrugs were also observed to undergo sequestration into the Pd^0 bead. Whereas prodrug sequestration remains a desired outcome, sequestration and retention of the active drug product within the bead as well may ultimately limit the dosage of dox exposed to the tumour tissue. *In vitro* prodrug activation assays showed a cytotoxicity gap remained when prodrugs and Pd^0 beads were incubated together, an effect likely attributed to the combined effect of dox sequestration and the time-delay resulting from slower catalytic turnover rate. This lead to the development of novel 30 μm Pd^0 beads. When incubated in combination with **42** and **43** in HPLC studies and cell culture, 30 μm Pd^0 beads were capable of increased catalytic effect, selective sequestration of prodrug alone and rapid release of dox into solution.

Three variations of the the novel Pobc moiety have been revealed as versatile functional groups capable of effectively masking drugs and then reactivating them in the presence of Pd^0 catalysts. Future work should elucidate the general catalytic mechanism of activation that occurs between alkene, alkyne and Pobc groups together with Pd catalysts. The characterisation and assignment of all products generated from this catalytic system needs identification prior to advancing confidently into preclinical assays. Further investigation is

required specifically of the *bis*-o-Pobc functional group. The expected enhancement to the biocompatibility of Doxorubicin via steric bulk was not observed in **50**, although it is clear that the incorporation of a second propargyl group dramatically enhances Pd lability. As *ortho* and *para* Pobc groups were unable to enhance the biocompatibility of Gemcitabine beyond that of Poc incorporation, biocompatibility induced by adding *bis*-o-Pobc at amine and/or hydroxyl positions of Gemcitabine should be considered.

A multicellular tumour spheroid (MCTS) model was next developed to allow for the direct study of Pd bead cytotoxicity on a cellular interface that recapitulated an *in vivo* tumour. This model would also provide information on a representative cytotoxicity fold gap for dosing a subsequent *ex vivo* tumour implant. **43** and Pd^0 beads alone did not induce any cytotoxicity. In combination, the expected toxigenic effect was not observed, perhaps due to the necessary addition of Matrigel®, a viscous gel required for spheroid formation that would coat the Pd^0 beads, possibly preventing prodrug entry into the spheroid.

As dox is often dose limited by virtue of cardiomyopathy, an *in vivo* embryonic zebrafish cardiac oedema assay was developed to investigate the potential cardio protective effect of **43** on heart tissue. A pronounced cardiac oedema was observed after 120 hpf when zebrafish embryos were incubated with 50 μM dox, with 100 % lethality occurring at higher concentrations. **43** did not cause significant lethality or observed cardiac oedema at any concentration tested (up to 200 μM). It is important to note that treatment with **43** showed reduced retention of the prodrug into the zebrafish embryo with respect to dox, corresponding to the reduced ability of **43** to engage with the molecular targets of dox. At 200 μM significant quantities of prodrug is observed without producing oedema, which is consistent with the inability of prodrug to interact with the molecular targets of the active drug.

A pre-clinical animal model was next investigated to observe, for the first time, the BOOM activation of chemotherapeutic prodrugs by intratumoural inoculated Pd^0 beads within a living tumour explant. A pilot study injected freshly excised mouse prostate tumours with 130 μm Pd

beads then incubated whole tumours with a previously reported prodrug of floxuridine, 3'propargylfloxuridine (Pro-FUdR). Crucially, the apoptotic effect observed by immunohistochemistry resolved a cytotoxic effect localised to the Pd^0 bead injection region.

Significant optimisation of this study was then undertaken to develop a non-invasive microsurgery protocol capable of accurately injecting the more effective 30 μm Pd^0 beads into prostate tumours of live mice. Ultrasound guided injection of Pd^0 beads into prostate tumours *in vivo* allowed for the precise implantation of catalyst into tumour without any observed effect on the overall viability of the mouse. Pd^0 beads were retained within the tumour at high concentration within the needle injection tract.

The catalytic activity of Pd^0 beads was assessed by incubating Pd-containing tumour slices with an off-on fluorescence probe, bis-N,N'-propargyloxycarbonylrhodamine 110 (Poc-Rho), and equating the fluorescence signal produced as a determinant of catalytic effect. Poc-Rho was activated with comparable rate in all Pd-containing tissue slices, even in samples that contained Pd^0 bead in the tumor *in vivo* for over 20 days, suggesting that the catalytic effect produced by Pd^0 beads could be sustained over extended incubation within a tumour. This finding presents an important step forwards for the development of catalysts amenable to long term chemotherapeutic activation within a patient.

42 and **43** were chosen as drug precursors to undergo a prodrug activation assay in combination with 30 um Pd^0 beads using the optimised microsurgery protocol. At 100 μM, dox produced significant cytotoxicity during a 63 hr window with a distinctive biosdistribution pattern corresponding to cellular uptake of the drug. Although the biodistrubution pattern for **42** was discernibly different, significant cytotoxicity was also observed at 100 uM. This suggests that cytotoxicity was induced by **42** alone and not the activated drug. **43** alone produced almost no cytotoxicity after 63 hr at 100 μM, with a biodistribution pattern showing low retention of the prodrug into tumour cells. In combination with 30 μm Pd^0 beads, **43** produced a strong cytotoxic effect comparable to dox. The sequestration effect observed in

Chapter 4 was clearly visualised during this study, with **43** rapidly accumulating into individual Pd^0 beads, causing them to 'light up' in a fluorescence study in preference to the surrounding tissue. The subsequent release of dox into the local environment was consistent with the marked cytotoxic effect and intense localised cellular fluorescence signal observed from treatment of dox alone.

This body of work has contributed to the development of potentially clinically viable prodrug and metal catalyst reaction partners. By masking established chemotherapeutics with novel protecting groups (Pobc functionalisation) and masking strategies (lactim trap), new and improved prodrug candidates are available. Parallel optimisation of the Pd^0 device, including a minimally invasive microsurgical protocol for the prolonged non-invasive *in vivo* incubation of the catalyst in a tumour, has generated a preliminary procedure for an *in vivo* BOOM chemotherapeutic activation study.

The incision and incubation of Pd beads into mouse prostate tumor has apparently had no short term observable affect on the viability of the mouse or the activity of the catalyst. The evident next step towards validating this assay would be to develop excipient formulae of the *bis*-protected 5FU prodrug **2** and the oPOBC-amine protected Doxorubicin prodrug **43** to conduct pharmacokinetic dosing studies to determine the maximum tolerated dosage of each drug before toxicity and side effect are observed.

Once this dosage window is determined, *in vivo* activation of the prodrug could be studied by first conducting intratumoral *in vivo* Pd^0 bead implantation, followed by intravenous dosing (i.e. via intraperitoneal injection) of the prodrug into the mouse. The efficacy of treatment would be determined by control populations that are treated with either prodrug alone or Pd^0 beads alone. Efficacy on dissection should assess the impact of treatment on tumor volume as well as key organs associated with drug related toxicity (i.e. the myocardium of heart tissue for Doxorubicin, the gastrointestinal tract for 5FU).

Depending on the resources at hand, parallel studies should be conducted by repeated injecting mouse populations with prodrugs during staggered time points to determine the

efficacy of treatment after extended incubation of Pd^0 beads. Future work must validate the *in vivo* generation of BOOM activated drugs over longer time periods and in more relevant animal models.

The surgical procedure for incision of a Pd device into the prostate tumors of mice should next be progressed into larger animal models. As porcine and canine anatomy is more representative of human structure, function and scale, success in the mouse assays should progress into either of these model systems.

CHAPTER 7

Methods

7.1 Chemistry

7.1.1 Chemicals

All chemicals were purchased from Sigma Aldrich, VWR International Ltd or Fisher Scientific UK Ltd unless otherwise stated. Doxorubicin HCl was purchased from Cambridge Biosciences Ltd, Gemcitabine HCl was purchased from Fluorochem Ltd.

7.1.2 Chromatography

Compounds were purified by manual flash column chromatography with commercially available silica gel (220 – 440 mesh, Sigma-Aldrich). Columns and solvents used to elute and purify the products varied depending on the amount of starting material used and polarity of compounds. R_f values were determined on Merck aluminium backed TLC Silica gel 60 F254 sheets. Compounds were visualized using a UV6L-58 Mineralight UV emitter at 254 nm. Semi-preparative high-performance liquid chromatography (Semi-prep HPLC) was performed using a Waters 600E pump and a Waters 486 tuneable absorbance detector equipped with a Phenomenex Luna C18(2), 5 µm, 250 x 21.2 mm column, with compounds detected using an evaporative light scattering detector (ELSD) and UV detector. All solvents used were HPLC grade. Method: eluent A, H_2O and formic acid (0.1 %); eluent B, acetonitrile and formic acid (0.1 %); A/B = 95 : 5 to 5 : 95 in 30 min. Ultra-performance liquid chromatography (UPLC) was performed using a Waters Acquity UPLC PDA with a 50 x 2.4 mm Waters BEH C18 1.7 µm column, with compounds detected using an evaporative light scattering detector (ELSD) and UV detector. All solvents used were HPLC grade. Method: eluent A, H_2O and formic acid (0.1 %); eluent B, acetonitrile; A/B = 95 : 5 to 20 : 80 in 8 min, 95 : 5 in 8.5 minutes.

7.1.3 Nuclear Magnetic Resonance

^{1}H and ^{13}C NMR were recorded at ambient temperature on Bruker Avance III 400 Mhz, 500 Mhz or 600 Mhz spectrometers from the Edinburgh University School of Chemistry. All chemical shifts are reported relative to the solvent peak in parts per million (δ).

7.1.4 Mass Spectrometry

High Resolution Mass Spectra (HRMA) were obtained using a Bruker 3.0 T Apex II Spectrometer under electron spray ionisation (ESI) conditions. Low Resolution Mass Spectra (LRMS) was obtained using an Agilent 1100 HPLC Modular System coupled to an Agilent Technologies 6130 Quadrupole LC/MS Mass Spectrometer under electron spray ionisation (ESI) conditions.

7.1.5 Scanning Electron Microscopy Imaging

Samples were fixed in a solution of 3 % glutaraldehyde in 0.1 M sodium cacodylate buffer (pH 7.3) for 2 hr, then washed in 3 x 10 min changes of 0.1 M sodium cacodylate buffer. Samples were then fixed in 1 % osmium tetroxide in 0.1 M sodium cacodylate buffer for 45 min. A further three 10 min washes were performed in 0.1 M sodium cacodylate buffer. Dehydration in graded concentrations of acetone (50 %, 70 %, 90 %, and 3 x 100 %) for 10 min each was followed by critical point drying using liquid CO_2. After mounting on aluminium stubs with carbon tabs attached, the specimens were sputter coated with 20 nm gold palladium and viewed using a Hitachi S-4700 scanning electron microscope. Preparation was performed with help from Stephen Mitchell from the School of Biological Sciences.

7.1.6 Synthesis & Characterization of Pd^0 beads

NovaSyn TG amino resins HL of variable diameter (10 µm, 20 µm, 30 µm, 75 µm, 110 µm and 130 µm) (1,000 mg, 0.39 mmol NH_2 per gram) and palladium acetate (263 mg, 1.17 mol) were added into a 25 mL Biotage microwave vial (Biotage). Next, toluene (10 mL) was added to the vial and heated to 80 °C under stirring for 10 min. The mixture was then stirred at room temperature (rt) for an additional 2 hr. The resins were filtered and washed with dichloromethane (DCM) (5 x 20 mL) and methanol (MeOH) (5 x 20 mL). Resins were dispersed

in 10 % hydrazine monohydrate in MeOH (10 mL) and stirred at room temperature for 25 min. The resins were again filtered and washed with MeOH (5 x 20 mL) and DCM (5x 20 mL). Resins were added to a solution of Fmoc-Glu(OH)-OH (216 mg, 0.59 mmol), Oxyma (166 mg, 1.17 mmol), N,N'-diisopropylcarbodiimide (DIC) (148 mg, 1.17 mmol) with DCM/dimethylformamide (DMF) (2 : 1, 9 mL) and stirred for 2 hr at rt. The resins were filtered and washed with DCM (5 x 20 mL), MeOH (5 x 20 mL) and H_2O (5 x 20 mL) and dried in an oven at 40 °C for 3 days. Completed coupling was verified by ninhydrin test after the last MeOH wash. Pd^0 beads were prepared together with Dr Ana Pérez-Lopéz and Dr Belén Rubio Ruiz. SEM images were performed at the School of Biological Sciences and Pd^0 quantification (by inductively coupled plasma-optical emission spectrometry) was performed by Dr Lorna Eades from the School of Chemistry. Resins were previously characterized using X-ray diffractometry (Bruker D2 PHASER with LYNXEYE detector (Bruker), Cu radiation source at 30 kV, 10 mA and a Ni filter) by Dr Carmen Torrez-Sanchez from the Additive Manufacturing Research Group at Loughborough University before and after Pd^0-functionalization.

7.1.7 Synthesis and characterization of 5-fluorouracil prodrugs

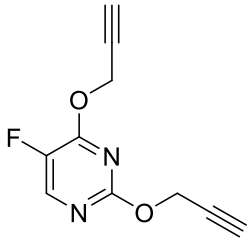

*Synthesis of 5-fluoro-2,4-bis-propargylpyrimidine (**2**)*. Sodium hydride (60 % dispersion in mineral oil) (120 mg, 3 mmol) was added to dry THF (10 mL) at 4 °C and stirred rapidly for 30 min. Propargyl alcohol (97 μL, 1.8 mmol) was added to dry THF (5 mL), and then added dropwise to the stirring mixture. An evolution of gas was observed with a slight exotherm, then the flask was sealed and flushed with nitrogen. A gas tight syringe containing 5-fluoro-2,4-dichloropyrimidine (100 mg, 0.6 mmol) mixed with dry THF (5 mL) was added dropwise at 4 °C, then warmed to rt whilst stirring for 12 hr. The resulting mixture was partitioned between DCM (50 mL) and H_2O (50 mL), acidified with acetic acid and separated. The organic layer was reduced by rotary evaporation then purified via flash chromatography (12.5 % ethyl acetate in hexane) The synthetic method described gave white crystals (0.45 mg, 0.22 mmol, 36 % yield); ^{1}H NMR (500 MHz, $CDCl_3$) δ 8.13 (s, 1H), 5.06 (d, J = 2.5 Hz, 2H), 4.94 (d, J = 2.4 Hz, 2H). 2.53 (t, J = 2.4 Hz, 1H), 2.4 (d, J = 2.4 Hz, 1H). ^{13}C NMR (126 MHz, $CDCl_3$) 158.5 (C), 158.4 (C), 143.2 – 142.2 (d, $J_{C\text{-}F}$ = 255.4 Hz C), 144.2 – 143.9 (d, $J_{C\text{-}F}$ = 20.6 Hz CH), 78.3 (C), 77.4 (C) 76.2 (CH), 75.0 (CH), 55.7 (CH_2), 55.1 (CH_2) HRMS (m/z): $[M+H]^+$ calcd for $C_{10}H_7FN_2O_2$ $[M+H]^+$: 207.0564, found: 207.0561

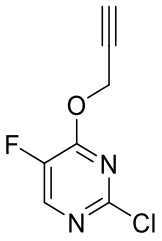

*Synthesis of 2-chloro-5-fluoro-4-propargylpyrimidine (**9**)* Sodium hydride (60 % dispersion in mineral oil) (120 mg, 3 mmol) was added to dry THF (10 mL) at 4 °C and stirred rapidly for 30 min. Propargyl alcohol (32 μL, 0.6 mmol) was added to dry THF (5 mL), and then added dropwise to the stirring mixture. An evolution of gas was observed with a slight exotherm, then the flask was sealed and flushed with nitrogen. A gas tight syringe containing 5-fluoro-2,4-dichloropyrimidine (100 mg, 0.6 mmol) mixed prior with dry THF (5 mL) was added dropwise at 4 °C, then left to warm whilst stirring for 12 hr. The resulting mixture was partitioned between DCM (50 mL) and H_2O (50 mL), acidified with acetic acid and separated. The organic layer was reduced by rotary evaporation then purified via flash chromatography (12.5 % ethyl acetate in hexane). The synthetic method described gave white crystals (55.9 mg, 0.3 mmol, 50 % yield) ^{1}H NMR (500 MHz, $CDCl_3$) δ 8.22 (d, J = 2.1 Hz, 1H), 5.08 (d, J = 2.5 Hz, 2H), 2.57 (t, J = 2.5 Hz, 1H). ^{13}C NMR (126 MHz, $CDCl_3$) δ 158.2 (d, $J_{C\text{-}Cl}$ = 11.5 Hz CCl), 153.2 (d, $J_{C\text{-}Cl}$ = 4.8 Hz C), 145.9 (d, $J_{C\text{-}F}$ = 265.3 Hz C), 144.8 (d, $J_{C\text{-}F}$ = 20.1 Hz CH), 76.6 (CH), 76.5 (C), 55.7 (CH_2) HRMS (m/z): $[M+H]^+$ calcd for $C_7H_4ClFN_2O$ $[M+H]^+$: 187.0069, found: 187.0086

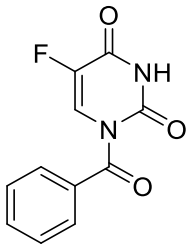

*Synthesis of 1-benzoyl-5-fluoropyrimidine-2,4(1H,3H)-dione (**10**)* 5-fluorouracil (1.37g, 10 mmol) was added to a solution of potassium hydroxide (0.69 g, 10 mmol) in MeOH (50 mL). The suspension was stirred at rt for 20 min, then concentrated and resuspended in acetonitrile (50 mL), stirred for 30 min then added portion wise to a solution of benzoyl chloride (1.4 g, 10 mmol) in acetonitrile (50 mL) at 0 °C. The reaction mixture was allowed to warm to rt and stirred for 3 hr, then filtered via vacuum filtration. The resulting crude product was washed with cold DCM (3 x 20 mL) then purified via flash chromatography (25 % ethyl acetate in hexane). The synthetic method described gave white crystals in agreement with cited reference[128]. (450 mg, 1.92 mmol, 19.2 % yield) ^{1}H NMR (500 MHz, DMSO) δ 12.05 (s, 1H), 8.26 (d, J = 6.7 Hz,

1H), 7.85 (dd, *J* = 8.3, 1.2 Hz, 2H), 7.70 – 7.62 (m, 1H), 7.56 – 7.47 (m, 2H).[13]C NMR (126 MHz, DMSO) δ 169.1 (C), 157.7 (d, $J_{C\text{-}F}$ = 26.8 Hz C), 148.3 (C), 141.2 (d, $J_{C\text{-}F}$ = 235.2 Hz C), 133.6 (C), 132.9 (CH), 129.5 (CH), 124.6 (d, $J_{C\text{-}F}$ = 36.4 Hz CH), 76.5 (CH), 76.5 (C), 55.7 (CH_2). HRMS (m/z): $[M+H]^+$ calcd for $C_{11}H_7FN_2O_3$ $[M+^{23}Na_1]^+$: 257.0333, found: 257.0327

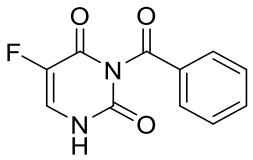

*Synthesis of 3-benzoyl-5-fluoropyrimidine-2,4(1H,3H)-dione (**11**)* Benzoyl chloride (2.13 mL, 18.9 mmol) was added to a stirring mixture of 5-fluorouracil (1.00 g, 9.1 mmol) and pyridine (3.06 mL, 38 mmol) in anhydrous acetronitrile (20 mL) at 0 °C under nitrogen. The mixture was allowed to warm to rt and stirred for 48 hr, then concentrated by rotary evaporation, re-dissolved in DCM (200 mL), washed with cold H_2O (3 x 50 mL) and re-concentrated. The resulting residue was dissolved in 1,4-dioxane (25 mL) and treated with aqueous potassium carbonate (0.5 M, 20 mL in H_2O) at 0 °C. After stirring at rt for 30 min the pH was slowly lowered to 5 by dropwise addition of concentrated acetic acid. The solution was concentrated by rotary evaporation, then treated with saturated sodium bicarbonate (100 mL) and stirred for 1 hr. The solution was then cooled to 0 °C, filtered by vacuum and washed with cold H_2O (5 x 20 mL) and the crude product was purified via flash chromatography (50 % ethyl acetate in hexane). The synthetic method described gave white crystals in agreement with cited reference[129] (550 mg, 2.34 mmol, 25.8 % yield) ^{1}H NMR (601 MHz, DMSO) δ 11.53 (s, 1H), 8.08 (d, *J* = 6.1 Hz, 1H), 8.04 (dd, *J* = 8.4, 1.1 Hz, 2H), 7.80 (tt, *J* = 7.6, 1.2 Hz, 1H), 7.65 – 7.58 (m, 2H).[13]C NMR (151 MHz, DMSO) δ 168.6 (C), 156.8 (C), 156.6 (C), 148.6 (C), 140.3 (C), 138.7 (C), 135.7 (C), 130.9 (CH), 130.5 (CH), 129.5 (CH), 127.5 (CH). HRMS (m/z): $[M+H]^+$ calcd for $C_{11}H_7FN_2O_3$ $[M+^{23}Na_1]^+$: 257.0333, found: 257.0340

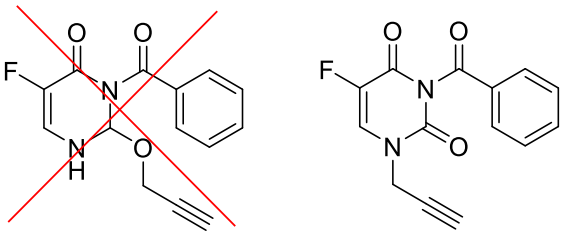

*Attempted synthesis of 3-benzoyl-5-fluoro-2-(prop-2-yn-1-yloxy)-2,3-dihydropyrimidin-4(1H)-one (**15**); Synthesis of 3-benzoyl-5-fluoro-1-(prop-2-yn-1-yl)pyrimidine-2,4(1H,3H)-dione (**14**)*

DIAD (333 uL,1.6 mmol) was added to a solution of PPh_3 (420 mg, 1.6 mmol) in THF (20 mL) at 0 °C under nitrogen. After 30 min the mixture was cooled to -78 °C and a solution of propargyl alcohol (35 uL, 0.64 mmol) and 3-benzoyl-5-fluoropyrimidine-2,4(1H,3H)-dione (150 mg, 0.64 mmol) in THF (20 mL) was added by gas tight syringe. The mixture was allowed to warm to rt then concentrated under reduced pressure and purified via flash chromatography (25 → 100 % ethyl acetate in hexane). The synthetic method described gave white crystals (25.6 mg, 0.09 mmol, 14.7 % yield) ^{1}H NMR (500 MHz, $CDCl_3$) δ 7.93 (dd, *J* = 8.3, 1.1 Hz, 2H), 7.73 – 7.63 (m, 2H), 7.52 (t, *J* = 7.9 Hz, 2H), 4.58 (d, *J* = 2.5 Hz, 2H), 2.60 (t, *J* = 2.5 Hz, 1H).^{13}C NMR (126 MHz, $CDCl_3$) δ 167.1 (C), 156.2 (d, $J_{C\text{-}F}$ = 27.1 Hz C), 148.0 (C), 140.4 (d, $J_{C\text{-}F}$ = 241.1 Hz C), 135.7 (C), 131.0 (C), 130.8 (C), 129.4 (C), 126.7 (d, $J_{C\text{-}F}$ = 33.8 Hz CH), 77.1 (C), 75.2 (C), 37.7 (CH_2).

7.1.8 Synthesis and characterization of Pd^0 labile moieties

Synthesis of propargyloxy-benzyl alcohol derivatives. Potassium carbonate (4.70 g 34 mmol) was added to a solution of o-hydroxybenzyl alcohol or p-hydroxybenzyl alcohol (2.50 g, 20 mmol) or 2,6-dihydroxybenzyl alcohol (2.80 g, 20 mmol) dissolved in acetonitrile (50 mL). After stirring for one hr at rt, the mixture was treated dropwise with propargyl bromide (2.93 mL as 80 % (v/v) in toluene, 35 mmol) and heated to reflux for 48 hr. The solution was then filtered, concentrated *in vacuo*, and the crude was purified via flash chromatography (30 % ethyl acetate in hexane)

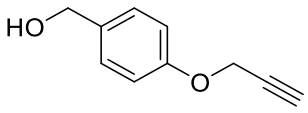

*p-propargyloxybenzyl alcohol (**29**)* The synthetic method described using p-hydroxybenzyl alcohol gave a viscous bright yellow liquid (3.7 g, 99 % yield); R_f = 0.36 (30 % ethyl acetate in hexane) ^{1}H NMR (500 MHz, $CDCl_3$) δ 7.19 (d, *J* = 8.8 Hz, 2H), 6.93 – 6.85 (m, 2H), 4.60 (d, *J* = 2.6 Hz, 2H), 4.44 (s, 2H), 3.73 (s, 1H), 2.55 (t, *J* = 2.4 Hz, 1H). ^{13}C NMR (126 MHz, $CDCl_3$) δ 156.6 (C), 133.9 (C), 128.3 (2 x CH), 114.6 (2 x CH), 78.5 (C), 75.7 (CH), 63.9 (CH_2), 55.6 (CH_2). HRMS (m/z): $[M+Na]^+$ calcd for $C_{10}H_{10}O_2$ $[M+Na]^+$: 185.0573, found: 185.0576

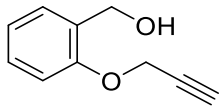

*o-propargyloxybenzyl alcohol (**30**)*. The synthetic method described using o-hydroxybenzyl alcohol gave a viscous dark yellow liquid (1.0 g, 30 % yield); R_f = 0.37 (30 % ethyl acetate in hexane) ^{1}H NMR (500 MHz, $CDCl_3$) δ 7.34 (dd, *J* = 7.5, 1.7 Hz, 1H), 7.28 – 7.22 (m, 1H), 6.99 (td, *J* = 7.4, 0.9 Hz, 1H), 6.94 (d, *J* = 8.3 Hz, 1H), 4.68 – 4.61 (m, 4H), 3.42 (s, 1H), 2.57 (t, *J* = 2.4 Hz, 1H). ^{13}C NMR (126 MHz, $CDCl_3$) δ 154.8 (C), 129.7 (CH), 128.4 (C), 128.2 (CH), 121.3 (CH), 111.6 (CH), 78.5 (C), 75.7 (CH), 60.3 (CH_2), 55.7 (CH_2). HRMS (m/z): $[M+Na]^+$ calcd for $C_{10}H_{10}O_2$ $[M+Na]^+$: 185.0573, found: 185.0573

Synthesis of p-nitrophenyl-carbonate moieties. A solution of 4-nitrophenylchloroformate (0.48 g, 2.4 mmol) in dry DCM (8 mL) was added dropwise to a solution of the alcohol (2.2 mmol) and pyridine (0.19 mL, 2.4 mmol) in DCM (8 mL) at 0 °C under nitrogen in the dark. The mixture was stirred from 0 °C to rt overnight with TLC monitoring at t = 0 hr, 0.5 hr, 2 hr and 20 hr to indicate full consumption of the alcohol. After concentrating *in vacuo,* the crude residue was re-dissolved in ethyl acetate (70 mL), washed with H_2O (2 x 50 mL) and brine (2 x 50 mL),

dried over $MgSO_4$ and re-concentrated *in vacuo,* and the crude was purified via flash chromatography (50 % DCM in hexane).

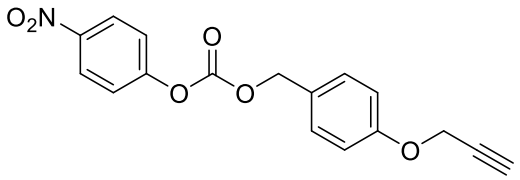

*p-nitrophenyl-p-propargyloxybenzyl carbonate (**31**).* The synthetic method described using p-propargyloxybenzyl alcohol gave an off white oil that solidified to a white solid when below 20 °C (0.54 g, 1.65 mmol, 75 % yield); R_f = 0.20 (50 % DCM in hexane) ^{1}H NMR (500 MHz, $CDCl_3$) δ 8.28 – 8.24 (m, 2H), 7.42 – 7.38 (m, 2H), 7.38 – 7.35 (m, 2H), 7.03 – 6.98 (m, 2H), 5.24 (s, 2H), 4.71 (d, *J* = 2.4 Hz, 2H), 2.53 (t, *J* = 2.4 Hz, 1H). ^{13}C NMR (126 MHz, $CDCl_3$) δ 158.3 (C), 155.7 (C), 152.6 (C), 145.5 (C), 130.7 (2 x CH), 127.4 (2 x CH), 125.4 (CH_2), 121.9 (2 x CH), 115.3 (2 x CH), 78.4 (C), 75.9 (CH), 70.9 (CH_2), 56.0 (CH_2). HRMS (m/z): $[M+Na]^+$ calcd for $C_{17}H_{13}O_6N_1$ $[M+Na]^+$: 350.0635, found: 350.0646

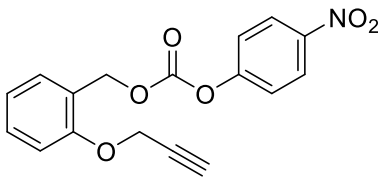

*p-nitrophenyl-o-propargyloxybenzyl carbonate (**32**).* The synthetic method described using o-propargyloxybenzyl alcohol gave an off white oil that solidified to a white solid when kept below 20 °C (0.52 g, 1.59 mmol, 72 % yield); R_f = 0.19 (50 % DCM in hexane) ^{1}H NMR (500 MHz, $CDCl_3$) δ 8.28 – 8.23 (m, 2H), 7.44 – 7.36 (m, 4H), 7.08 – 7.01 (m, 2H), 5.39 (s, 2H), 4.78 (d, *J* = 2.4 Hz, 2H), 2.53 (t, *J* = 2.4 Hz, 1H). ^{13}C NMR (126 MHz, $CDCl_3$) δ 155.9 (C), 155.8 (C), 152.5 (C), 145.4 (C), 130.6 (CH), 130.5 (C), 125.4 (2 x CH), 123.4 (CH), 121.9 (2 x CH), 121.7

(CH), 112.4 (CH), 78.4 (C), 76.0 (CH), 66.6 (CH_2), 56.3 (CH_2). HRMS (m/z): $[M+Na]^+$ calcd for $C_{17}H_{12}O_6N_1$ $[M+Na]^+$: 350.0635, found: 350.0590

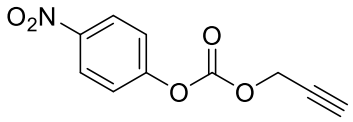

*p-nitrophenylpropargyloxy carbonate (**40**).* The synthetic method described using propargyl alcohol gave white crystals in agreement with cited reference[217] (0.31 g, 1.40 mmol, 64 % yield); R_f = 0.29 (50 % DCM in hexane) ^{1}H NMR (500 MHz, $CDCl_3$) δ 8.32 – 8.25 (m, 2H), 7.44 – 7.38 (m, 2H), 4.88 (d, *J* = 2.5, 2H), 2.62 (t, *J* = 2.5, 1H). ^{13}C NMR (126 MHz, $CDCl_3$) δ 155.5 (C), 152.1 (C), 145.7 (C), 125.5 (2 x CH), 121.9 (2 x CH), 77.4 (C), 76.9 (CH), 56.6 (CH_2). HRMS (m/z): $[M+Na]^+$ calcd for $C_{10}H_7O_5N_1$ $[M+Na]^+$: 244.0216, found: 244.0206

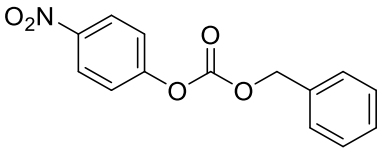

*p-nitrophenyl benzyl carbonate (**41**).* The synthetic method described using benzyl alcohol gave white crystals in agreement with cited reference[217] (0.41 g, 1.5 mmol, 68 % yield); R_f = 0.34 (50 % DCM in hexane) ^{1}H NMR (500 MHz, $CDCl_3$) δ 8.30 – 8.26 (m, 2H), 7.48 – 7.36 (m, 7H), 5.30 (s, 2H). ^{13}C NMR (126 MHz, $CDCl_3$) δ 155.6 (C), 152.6 (C), 145.5 (C), 134.3 (C), 129.2 (2 x CH), 129.0 (CH), 128.9 (2 x CH), 125.5 (2 x CH), 121.9 (2 x CH), 71.2 (CH_2). HRMS (m/z): $[M+Na]^+$ calcd for $C_{14}H_{11}O_5N_1$ $[M+Na]^+$: 296.0529, found: 296.0507

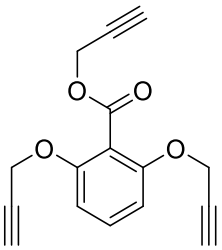

*o-bis-propargyloxybenzoate (**47**)* o-dihydroxybenzoic acid (6.96 g, 45.0 mmol) and potassium carbonate (30.5 g, 220 mmol) was suspended in dry DMF (40 mL) and stirred for 30 mins at 0 °C. Propargyl bromide (21 mL, 80 % (v/v) in toluene, 16.8 mmol) was added dropwise and the reaction was warmed to ambient temperature and stirred for three days. The reaction was diluted with H_2O (300 mL) and extracted with diethyl ether (6 x 200 mL). The combined organic phases were washed with brine, dried over $MgSO_4$ and concentrated *in vacuo* to yield a brown oil (5.37 g 20.1 mmol, 44%), used without further purification. ^{1}H NMR (400 MHz, $CDCl_3$) δ 7.32 (t, *J* = 8.4 Hz, 1H), 6.76 (d, *J* = 8.4 Hz, 2H), 4.91 (d, *J* = 2.5 Hz, 2H), 4.71 (d, *J* = 2.5 Hz, 4H), 2.51 (t, *J* = 2.4 Hz, 2H), 2.50 (t, *J* = 2.5 Hz, 1H); ^{13}C NMR (126 MHz, $CDCl_3$) δ 165.1 (C), 156.0 (C), 131.3 (CH), 114.0 (CH), 106.8 (C), 78.2 (C), 77.7 (C), 76.2 (CH), 75.2 (CH), 57.0 (CH_2), 52.9 (CH_2).

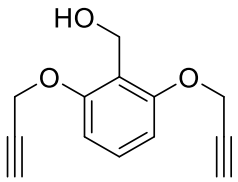

*o-bis-propargyloxyphenyl methanol (**48**)* o-bis-propargylbenzoate (5.37 g, 20.1 mmol) was dissolved in THF and cooled to 0 °C for the addition of $LiAlH_4$ (24 mL, 1 M in THF, 24 mmol) before warming to ambient temperature and stirring overnight. The reaction was quenched at 0 °C with 10 % NaOH (40 mL), then stirred for 30 mins. The aqueous phase was extracted with DCM (3 x 70 mL) and the combined organic phases were washed with brine (40 mL), dried over $MgSO_4$ and concentrated *in vacuo*. The crude residue was purified via flash column chromatography (30 % ethyl acetate in hexane) to yield a white solid (2.74 g, 12.6 mmol, 63%). ^{1}H NMR (500 MHz, $CDCl_3$-*d*) δ 7.24 (t, *J* = 8.4 Hz, 1H), 6.72 (d, *J* = 8.4 Hz, 2H), 4.81 (d, *J* = 6.7 Hz, 2H), 4.74 (d, *J* = 2.4 Hz, 4H), 2.51 (t, *J* = 2.4 Hz, 2H), 2.37 (t, *J* = 6.7 Hz, 1H). ^{13}C NMR

(126 MHz, $CDCl_3$) δ 162.5 (CH), 155.7 (CH), 129.1 (C), 106.6 (2 x CH), 78.5 (2 x C), 75.82 (2 x CH) 56.6 (2 x CH_2), 54.4 (2 x CH_2); HRMS (ES^+) calcd for $C_{13}H_{12}O_3$ $[M+H]^+$: 217.0865, found: 217.0859

Synthesis of p-nitrophenyl-carbonate moiety. A solution of 4-nitrophenylchloroformate (0.48 g, 2.4 mmol) in dry DCM (8 mL) was added dropwise to a solution of o-*bis*-propargyloxybenzyl alcohol (2.2 mmol) and pyridine (0.19 mL, 2.4 mmol) in DCM (8 mL) at 0 °C under nitrogen in the dark. The mixture was stirred from 0 °C to rt overnight with TLC monitoring at t = 0 hr, 0.5 hr, 2 hr and 20 hr to indicate full consumption of the alcohol. After concentrating *in vacuo,* the crude residue was re-dissolved in ethyl acetate (70 mL), washed with H_2O (2 x 50 mL) and brine (2 x 50 mL), dried over $MgSO_4$ and re-concentrated *in vacuo,* and the crude was purified via flash chromatography (50 % DCM in hexane).

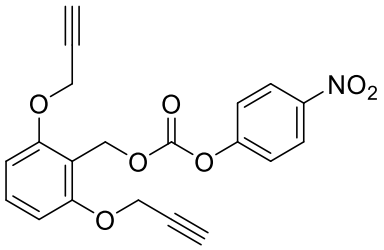

*p-nitrophenyl-o-bis-propargyloxybenzyl carbonate (**49**)* The synthetic method described gave a white solid when below 20 °C (0.80g, 2.1 mmol, 86.5 %); R_f = 0.3 (25 % ethyl acetate in hexane) ^1H NMR (500 MHz, $CDCl_3$) δ 8.29 – 8.23 (m, 2H), 7.44 – 7.40 (m, 2H), 7.35 (t, *J* = 8.4 Hz, 1H), 6.75 (d, *J* = 8.4 Hz, 2H), 5.49 (s, 2H), 4.76 (d, *J* = 2.4 Hz, 4H), 2.52 (t, *J* = 2.4 Hz, 2H). ^{13}C NMR (126 MHz, $CDCl_3$) δ 157.6 (C), 156.0 (C), 152.6 (C), 145.4 (C), 131.2 (CH), 125.4 (2 x CH), 122.0 (2 x CH), 112.1 (2 x CH), 106.2 (2 x CH), 78.4 (2 x C), 76.0 (2 x CH), 60.7 (2 x CH_2), 56.7 (CH_2). HRMS (m/z): $[M+Na]^+$ calcd for $C_{20}H_{15}O_7N$ $[M+Na]^+$: 404.0741, found: 404.0763.

7.1.9 Synthesis and characterization of gemcitabine prodrugs

Synthesis of carbamate protected gemcitabine prodrugs. Gemcitabine HCl (500 mg, 1.67 mmol) was dissolved in a stirred solution of dry DMF (5 mL) with imidazole (397 mg, 5.84 mmol) and tert-butyldimethylsilyl chloride (302 mg, 2.00 mol) and stirred at rt overnight. The mixture was concentrated *in vacuo*, dissolved in ethyl acetate (50 mL) and washed with H_2O (50 mL). The aqueous layer was then washed two more times with ethyl acetate and the organic layers were collected, washed with brine (150 mL), dried over $MgSO_4$, concentrated *in vacuo* then purified via flash chromatography (8 % methanol in DCM) and directly used in the next step. Dry pyridine (35.5 µL, 440.7 µmol) was added drop wise to a solution of TBS-gemcitabine (60 mg, 162 µmol) and the p-nitrophenyl carbonate moiety (106 mg, 324 µmol), propargyl chloroformate (37.8 µL, 390 µmol) or benzyl chloroformate (33.6 µL, 390 µmol) in dry THF (2 mL) with rapid stirring, and the reaction monitored by TLC (5 % methanol in DCM) at t = 1 hr, 6 hr and 24 hr, monitoring for formation of product at R_f = 0.13 (10 % methanol in DCM). After 24 hr the mixture was concentrated *in vacuo*, and the crude was purified via flash chromatography (0 → 5 % methanol in DCM). The carbamate protected TBS-gemcitabine (15 µmol) was dissolved in dry THF (2 mL) and TBAF (30 µL, 101.8 µmol) was added. The solution was stirred rapidly for 24 hr, then concentrated *in vacuo* and the crude was purified via flash chromatography (0 → 5 % methanol in DCM)

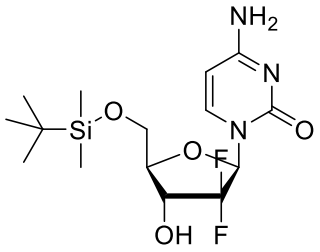

*4-amino-1-(5'-(((tert-butyldimethylsilyl)oxy)methyl)-3',3'-difluoro-4'-hydroxytetrahydrofuran-2-yl)pyrimidin-2(1H)-one (**20**)* The synthetic method described above gave a white powder in agreement with cited reference[34] (552 mg, 1.34 mmol, 88 % yield); R_f = 0.35 (2.5 % methanol in DCM). ^{1}H NMR (500 MHz, DMSO) δ 7.63 (d, *J* = 7.5 Hz, 1H), 7.38 (s, 2H), 6.31 (d, *J* = 5.1, 1H), 6.14 (t, *J* = 7.7 Hz, 1H), 5.76 (d, *J* = 7.5 Hz, 1H), 4.19 – 4.06 (m, 1H), 3.95 (d, *J* = 11.8 Hz, 1H), 3.90 – 3.77 (m, 2H), 0.90 (s, 9H), 0.09 (d, *J* = 2.1 Hz, 6H). ^{13}C NMR (126 MHz, DMSO)

δ 165.6 (C), 154.6 (C), 139.9 (CH), 123.0 (t, $J_{C\text{-}F}$ = 258.3 Hz, C), 94.5 (CH), 83.5 (t, $J_{C\text{-}F}$ = 31.5 Hz, CH), 79.8 (CH), 68.2 (t, $J_{C\text{-}F}$ = 22.7 Hz, CH), 60.7 (CH_2), 25.7 (CH_3), 18.0 (C), -5.5(CH_3), -5.6 (CH_3). MS (ESI) m/z: $C_{15}H_{25}F_2N_3O4Si$ 378.0 [M+H]+.

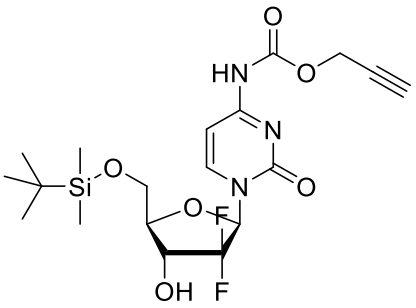

*Propargyloxy(1-(5'-(((tert-butyldimethylsilyl)oxy)methyl)-3',3'-difluoro-4'-hydroxytetrahydrofuran-2-yl)-2-oxo-1,2-dihydropyrimidin-4-yl)carbamate (**22**).* The synthetic method described above gave a white powder in agreement with cited reference[34] (335.5 mg, 0.73 mmol 44 % yield); (R_f = 0.6, 10 % methanol in DCM). ^{1}H NMR (500 MHz, MeOD) δ 8.30 (d, *J* = 7.6 Hz, 1H), 7.29 (d, *J* = 7.6 Hz, 1H), 6.25 (t, *J* = 6.7 Hz, 1H), 4.84 (d, *J* = 2.5 Hz, 2H,), 4.33 – 4.24 (m, 1H), 4.10 (d, *J* = 12.0 Hz, 1H,), 4.03 – 3.90 (m, 2H), 2.99 (t, *J* = 2.3 Hz, 1H), 0.98 (s, 9H,), 0.17 (s, 6H,). ^{13}C NMR (126 MHz, MeOD) δ 165.3 (C), 157.3 (C), 154.6 (C), 145.0 (CH), 123.9 (t, $J_{C\text{-}F}$ = 259.6 Hz, C), 96.9 (CH), 86.2 (t, $J_{C\text{-}F}$ = 32.8 Hz, CH), 82.5 CH), 77.7 (C), 76.9 (CH), 69.6 (t, $J_{C\text{-}F}$ = 22.7 Hz, CH), 61.7 (CH2), 54.3 (CH_2), 26.4 (CH_3), 19.3 (C), -5.4 (CH_3), -5.5 (CH_3). MS (ESI) m/z: $C_{19}H_{27}F_2N_3O_6Si$ 460.2 $[M+H]^+$.

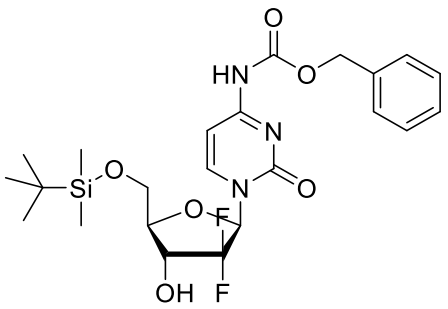

*Benzyl(1-(5'-(((tert-butyldimethylsilyl)oxy)methyl)-3',3'-difluoro-4'-hydroxytetrahydrofuran-2-yl)-2-oxo-1,2-dihydropyrimidin-4-yl)carbamate (**23**).* The synthetic method described above gave a white powder in agreement with cited reference[34] (358.8 mg, 0.70 mmol, 42 % yield) (R_f = 0.53, 10 % methanol in DCM). ^{1}H NMR (500 MHz, $CDCl_3$) δ 8.11 (d, *J* = 7.5 Hz, 1H), 7.40 – 7.32 (m, 5H), 6.40 – 6.32 (m, 1H), 5.22 (s, 2H), 4.41 – 4.31 (m, 1H), 4.07 – 4.00 (m, 2H), 3.90 (dd, *J* = 11.9 Hz, 2.2 Hz, 1H), 0.93 (s, 9H), 0.12 (s, 6H). ^{13}C NMR (126 MHz, DMSO) δ 162.9 (C), 154.9 (C), 152.4 (C), 144.4 (CH), 135.0 (C),128.9 (CH), 128.4 (CH), 122.3 (t, J_{C-F} = 258.3 Hz, C), 95.5 (CH), 84.6 (t, J_{C-F} = 32.8 Hz, CH), 81.6 (CH), 69.3 (t, J_{C-F} = 26.5 Hz, CH), 68.2 (CH_2), 60.7 (CH_2), 26.0 (CH_3), 18.5 (C), -5.4 (CH_3). MS (ESI) m/z: $C_{23}H_{31}F_2N_3O_6Si$ 534.1 $[M+Na]^+$.

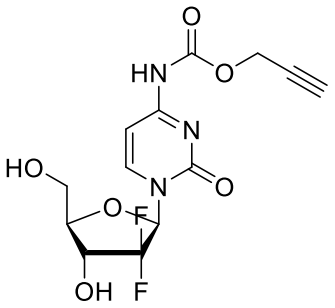

*Propargyloxy(1-(3',3'-difluoro-4'-hydroxy-5'-(hydroxymethyl)tetrahydrofuran-2-yl)-2-oxo-1,2-dihydropyrimidin-4-yl)carbamate (**25**).* The synthetic method described above gave a white powder in agreement with cited reference[34] (4.5 mg, 15 µmol, 99 % yield); R_f = 0.41 (10 % methanol in DCM). ^{1}H NMR (500 MHz, DMSO) δ 11.06 (s, 1H), 8.25 (d, *J* = 7.6 Hz, 1H), 7.08 (d, *J* = 7.55 Hz, 1H), 6.30 (d, *J* = 6.5 Hz, 1H), 6.16 (t, *J* = 7.4 Hz, 1H), 5.29 (t, *J* = 5.5 Hz, 1H), 4.80 (d, *J* = 2.4 Hz, 2H), 4.26 – 4.13 (m, 1H), 3.89 (dt, *J* = 8.5 Hz, 3.1 Hz, 1H), 3.84 – 3.63 (m, 2H), 3.62 (t, *J* = 2.4 Hz, 1H). ^{13}C NMR (126 MHz, DMSO) δ 163.3 (C), 153.9 (C), 152.4 (C), 144.6 (CH), 122.9 (C), 94.8 (CH), 84.1 (CH), 81.0 (CH), 78.2 (CH), 78.2 (C) 68.4 (CH), 58.8 (CH), 53.01 (CH_2). MS (ESI) m/z 344.0 $[M-H]^-$. HRMS (m/z): $[M - H]^-$ calcd for $C_{13}H_{12}O_6N_3F_2$, 344.0700; found 344.0719.

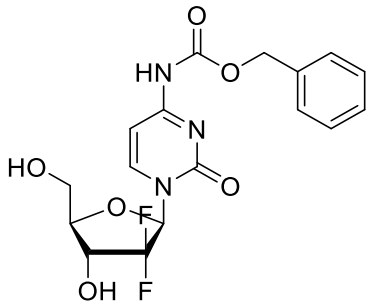

*Benzyl(1-(3',3'-difluoro-4'-hydroxy-5'-(hydroxymethyl)tetrahydrofuran-2-yl)-2-oxo-1,2-dihydropyrimidin-4-yl)carbamate (**26**).* The synthetic method described above gave a white powder in agreement with cited reference[34] (5.9 mg, 15 µmol, 99 % yield); R_f = 0.33 (10 % methanol in DCM). ^{1}H NMR (500 MHz, DMSO) δ 10.98 (s, 1H), 8.23 (d, *J* = 7.6 Hz, 1H), 7.45 – 7.32 (m, 5H), 7.11 (d, *J* = 7.6 Hz, 1H), 6.31 (d, *J* = 6.5 Hz, 1H), 6.16 (t, *J* = 7.4 Hz, 1H), 5.29 (t, *J* = 5.5 Hz, 1H), 5.20 (s, 2H), 4.25 – 4.13 (m, 1H), 3.88 (dt, *J* = 8.5 Hz, 3.1 Hz, 1H), 3.84 – 3.62 (m, 2H).^{13}C NMR (126 MHz, DMSO) δ 163.4 (C), 154.0 (C), 153.0 (C), 144.5 (CH), 135.8 (C),), 128.5 (CH), 128.2 (CH), 128.0 (CH), 122.9 (t, J_{C-F} = 259.6 Hz, C), 94.9 (CH), 84.1 (t, J_{C-F} = 30.2 Hz, CH), 81.0 (CH), 68.4 (t, J_{C-F} = 22.7 Hz, CH), 66.7 (CH2), 58.8 (CH_2). HRMS (m/z): $[M - H]^-$ calcd for $C_{17}H_{16}O_6N_3F_2$, 396.1013; found 396.1016.

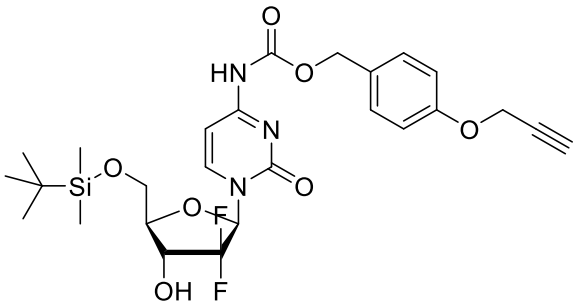

p-propargyloxybenzyl(1-(5'-(((tert-butyldimethylsilyl)oxy)methyl)-3',3'-difluoro-4'-hydroxytetrahydrofuran-2-yl)-2-oxo-1,2-dihydropyrimidin-4-yl)carbamate. The synthetic method described above gave a white powder (8.5 mg, 15 µmol, 9 % yield); R_f = 0.30 (2.5 % methanol in DCM). ^{1}H NMR (500 MHz, MeOD) δ 8.26 (d, *J* = 7.7 Hz, 1H), 7.38 – 7.35 (m, 2H),

7.31 (d, *J* = 7.7 Hz, 1H), 7.00 – 6.97 (m, 2H), 6.24 (t, *J* = 6.7 Hz, 1H), 5.16 (d, *J* = 1.4 Hz, 2H), 4.72 (d, *J* = 2.4 Hz, 2H), 4.28 (td, *J* = 12.5, 8.7 Hz, 1H), 4.09 (d, *J* = 12.0 Hz, 1H), 4.00 (dt, *J* = 8.7, 2.2 Hz, 1H), 3.92 (dd, *J* = 12.1, 2.3 Hz, 1H), 2.92 (t, *J* = 2.4 Hz, 1H), 0.97 (s, 9H), 0.16 (s, 6H). ^{13}C NMR (126 MHz, MeOD) δ 165.34 (C), 159.34 (C), 157.3 (C), 154.5 (CH), 144.8 (C), 131.12 (CH), 129.8 (C), 123.89 (t, J_{C-F} = 258.8 Hz C), 116.0 (CH), 97.90 (CH), 86.2 (t, J_{C-F} = 32.5 Hz CH), 82.5 (CH), 79.67 (C), 76.8 (CH), 69.67 (d, J_{C-F} = 22.9 Hz CH), 68.55 (CH_2), 61.67 (CH_2), 56.6 (CH_3), 26.4 (CH_3), 18.5 (C), -5.4 (CH_3). HRMS (m/z): $[M+Si]^+$ calcd for $C_{26}H_{34}O_7N_3F_2+Si^{28}$ 566.2129 found 566.2155

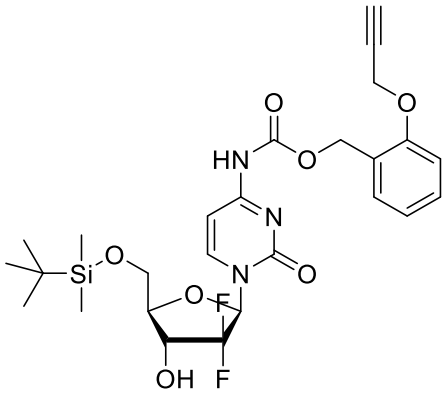

o-propargyloxybenzyl(1-(5'-(((tert-butyldimethylsilyl)oxy)methyl)-3',3'-difluoro-4'-hydroxytetrahydrofuran-2-yl)-2-oxo-1,2-dihydropyrimidin-4-yl)carbamate. The synthetic method described above gave a white powder (6.4 mg, 11.3 µmol, 6.9 % yield); R_f = 0.28 (2.5 % methanol in DCM). ^{1}H NMR (500 MHz, MeOD) δ 8.26 (d, *J* = 7.7 Hz, 1H), 7.43 (dd, *J* = 7.5, 1.6 Hz, 1H), 7.39-7.32 (m, 2H), 7.16 –7.12 (m, 1H), 7.03 (td, *J* = 7.5, 1.0 Hz, 1H), 6.27 (t, *J* = 6.8 Hz, 1H) 5.35 - 5.25 (m, 2H), 4.82 (d, *J* = 2.4 Hz, 2H), 4.31 (td, *J* = 12.5, 8.7 Hz, 1H), 4.12 (d, *J* = 12.0 Hz), 4.03 (dt,*J* = 8.7, 2.3 Hz, 1H), 3.95 (dd, *J* = 12.1, 2.4 Hz, 1H), 2.96 (t, *J* = 2.4 Hz, 1H), 1.00 (s, 9H), 0.19 (s, 6H). HRMS (m/z): $[M+Si]^+$ calcd for $C_{26}H_{34}O_7N_3F_2+Si^{28}$ 566.2129 found 566.2147

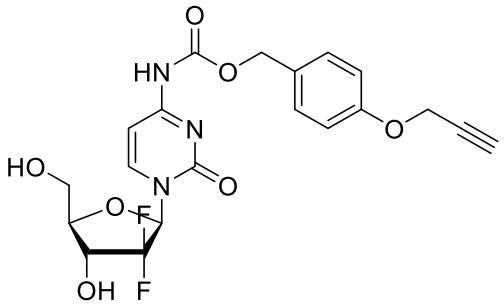

*p-propargyloxybenzyl(1-(3',3'-difluoro-4'-hydroxy-5'-(hydroxymethyl)tetrahydrofuran-2-yl)-2-oxo-1,2-dihydropyrimidin-4-yl)carbamate (**33**).* The synthetic method described above gave a white powder (6.7 mg, 15 µmol, 99 % yield); R_f = 0.42 (5 % methanol in DCM). ^{1}H NMR (601 MHz, MeOH) δ 8.30 (d, *J* = 7.7, 1H), 7.39 – 7.36 (m, 2H), 7.35 (d, *J* = 7.6, 1H), 7.01 – 6.97 (m, 2H), 6.29 – 6.19 (m, 1H), 5.17 (s, 2H), 4.73 (d, *J* = 2.4, 2H), 4.30 (td, *J* = 12.1, 8.7, 1H), 4.02 – 3.91 (m, 2H), 3.81 (dd, *J* = 12.7, 3.0, 1H), 2.93 (t, *J* = 2.4, 1H). ^{13}C NMR (151 MHz, MeOH) δ 165.6 (C), 159.5 (C), 157.6 (C), 154.7 (C), 145.8 (CH), 131.3 (CH), 130.0 (C), 125.8 – 124.1 (C), 116.2 (CH), 97.2 (CH), 83.1 – 82.9 (CH), 79.8 (C), 77.0 (CH), 70.9 – 70.0 (C), 68.6 (CH_2), 60.4 (CH_2), 56.8 (CH_2). HRMS (m/z): $[M+Na]^+$ calcd for $C_{20}H_{19}O_7N_3F_2$+Na^{23} 474.1083 found 474.1083

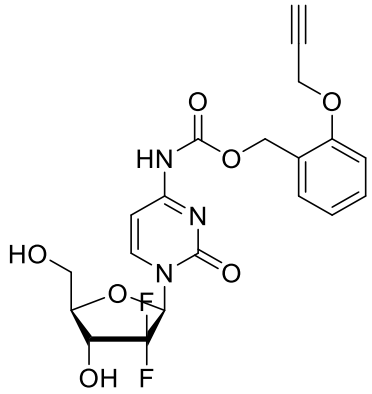

*o-propargyloxybenzyl(1-(3',3'-difluoro-4'-hydroxy-5'-(hydroxymethyl)tetrahydrofuran-2-yl)-2-oxo-1,2-dihydropyrimidin-4-yl)carbamate (**34**).* The synthetic method described above gave a white powder (5.1 mg, 11.3 µmol, 99 % yield); R_f = 0.40 (5 % methanol in DCM). ^{1}H NMR (601 MHz, MeOH) δ 8.31 (d, *J* = 7.7 Hz, 1H), 7.40 (dd, *J* = 7.5, 1.3 Hz, 1H), 7.38 – 7.29 (m, 2H),

7.11 (d, *J* = 8.3 Hz, 1H), 7.00 (t, *J* = 7.5 Hz, 1H), 6.33 – 6.18 (m, 1H), 5.28 (s, 2H), 4.80 (d, *J* = 2.4 Hz, 2H), 4.36 – 4.24 (m, *J* = 12.1, 8.8 Hz, 1H), 4.03 – 3.92 (m, 2H), 3.87 – 3.77 (m, 1H), 2.94 (t, *J* = 2.4 Hz, 1H). ^{13}C NMR (151 MHz, MeOH) δ 165.6 (C), 157.6 (C), 157.3 (C), 155.3 (C), 145.8 (CH), 131.2 (CH), 131.1 (C), 125.8 (CH), 124.5 (CH), 124.1 - 122.5 (CH), 113.6 (CH), 97.2 (CH), 83.0 – 82.9 (CH), 79.8 (C), 77.1 (CH), 70.9 – 69.9 ($J_{C\text{-}F}$ = 24.2 Hz CH), 64.4 (CH_2), 60.4 (CH_2), 57.2 (CH_2). HRMS (m/z): $[M+Na]^+$ calcd for $C_{20}H_{19}O_7N_3F_2+Na^{23}$ 474.1083 found 474.1105

Synthesis of carbonate protected gemcitabine prodrugs. Triethylamine (33 µL, 33 µmol) was added dropwise to a solution of gemcitabine HCl (50 mg, 0.17 µmol) in anhydrous DMF (1 mL) and stirred rapidly for 10 min. The p-nitrophenyl carbonate moiety (120 mg, 33 µmol) was added and the reaction monitored by TLC (10 % methanol in DCM) at t = 1 hr, 6 hr and 24 hr monitoring for formation of product at R_f = 0.13 (10 % methanol in DCM). After 24 hr, the reaction was concentrated *in vacuo*, and the crude was purified via flash chromatography (0 → 5 % methanol in DCM)

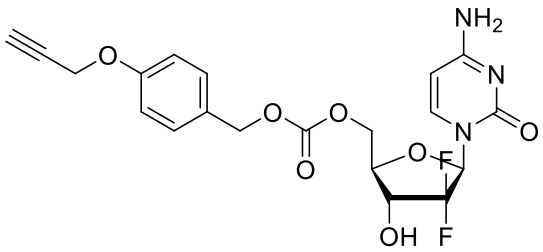

*(5'-(4-amino-2-oxopyrimidin-1(2H)-yl)-3',3'-difluoro-4'-hydroxytetrahydrofuran-2-yl)methyl (p-propargyloxybenzyl) carbonate (**35**)* The synthetic method described above using p-nitrophenyl-p-propargyloxybenzyl carbonate gave a pale yellow oil (17.2 mg, 38.1 µmol, 23 % yield); R_f = 0.26 (10 % methanol in DCM). ^{1}H NMR (500 MHz, MeOD) δ 8.30 (d, *J* = 7.7 Hz, 1H), 7.39 – 7.36 (m, 2H), 7.35 (d, *J* = 7.7 Hz, 1H), 7.02 – 6.96 (m, 2H), 6.30 – 6.19 (m, 1H), 5.17 (s, 2H), 4.73 (d, *J* = 2.4 Hz, 2H), 4.34 – 4.24 (m, *J* = 20.7, 12.1 Hz, 1H), 4.02 – 3.93 (m, 2H), 3.81 (dd, *J* = 12.6, 3.1 Hz, 1H), 2.93 (t, *J* = 2.4 Hz, 1H). ^{13}C NMR (126 MHz, MeOD) δ

165.6 (C), 159.5 (C), 157.6 (C), 154.7 (C), 145.8 (CH), 131.3 (CH), 130.0 (C), 124.1 (t, $J_{C\text{-}F}$ = 258.0 Hz C), 116.2 (CH), 97.2 (CH), 87.0 – 86.1 (CH), 83.2 – 82.6 (CH), 79.8 (C), 77.0 (CH), 70.7 – 70.0 (CH), 68.6 (CH_2), 60.4 (CH_2), 57.8 (CH_2). HRMS (m/z): $[M+Na]^+$ calcd for $C_{20}H_{19}O_7N_3F_2+Na^{23}$ 474.1083 found 474.1083

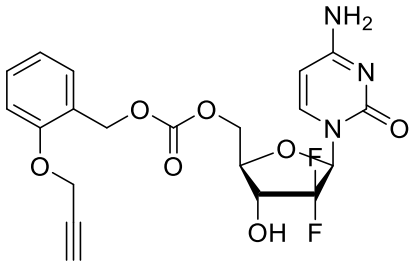

*(5'-(4-amino-2-oxopyrimidin-1(2H)-yl)-3',3'-difluoro-4'-hydroxytetrahydrofuran-2-yl)methyl (o-propargyloxybenzyl) carbonate (**36**)* The synthetic method described above using p-nitrophenyl-2-propargyloxybenzyl) carbonate gave a pale yellow oil (15.5 mg, 34.3 µmol, 20 % yield); R_f = 0.13 (10 % methanol in DCM). ^{1}H NMR (500 MHz, MeOD) δ 8.30 (d, *J* = 7.7 Hz, 1H), 7.39 (d, *J* = 7.5 Hz, 1H), 7.37 – 7.31 (m, 2H), 7.11 (d, *J* = 8.3 Hz, 1H), 7.00 (t, *J* = 7.5 Hz, 1H), 6.30 – 6.18 (m, 1H), 5.27 (s, 2H), 4.79 (d, *J* = 2.3 Hz, 2H), 4.37 – 4.25 (m, *J* = 12.1, 8.8 Hz, 1H), 4.01 – 3.92 (m, 2H), 3.81 (dd, *J* = 12.7, 3.1 Hz, 1H), 2.94 (t, *J* = 2.4 Hz, 1H). ^{13}C NMR (126 MHz, MeOD) δ 165.6 (C), 157.6 (C), 157.3 (C), 154.7 (C), 145.7 (CH), 131.2 (CH), 131.1 (C), 126.0 (C), 125.6 (CH) 124.1 (t, $J_{C\text{-}F}$ = 259.1 Hz C), 122.5 (CH), 113.6 (CH), 97.2 (CH), 86.9 – 86.2 (CH), 83.0 – 82.9 (CH), 79.8 (C), 77.1 (CH), 70.6 – 70.1 (CH), 64.4 (CH_2), 60.4 (CH_2), 57.2 (CH_2). HRMS (m/z): $[M+Na]^+$ calcd for $C_{20}H_{19}O_7N_3F_2+Na^{23}$ 474.1083 found 474.1083

7.1.10. Synthesis and characterization of doxorubicin prodrugs

Synthesis of doxorubicin prodrugs. A solution of the p-nitrophenyl carbonate moiety (1.5 equiv) in anhydrous DMF (2 mL) was flushed with nitrogen after stirring for 10 minutes, then syringed into a flask containing a solution of doxorubicin HCl (20 mg, 36.8 µmol) and triethylamine (7.5 µL, 55.2 µmol) in anhydrous DMF under nitrogen at rt. The reaction was monitored by TLC

(10 % methanol in DCM) to observe complete consumption of doxorubicin. After 20 hr, the reaction was diluted with H_2O (50 mL) and extracted with ethyl acetate (4 x 50 mL). The combined organic extracts were concentrated down to a volume of ~100 mL, then washed successively with saturated $NaHCO_3$ (2 x 50 mL), H_2O (2 x 50 mL) and brine (2 x 50 mL), dried over $MgSO_4$, concentrated *in vacuo* with the water bath kept below 40 °C and the crude was purified via flash chromatography (0 → 2 % methanol in DCM)

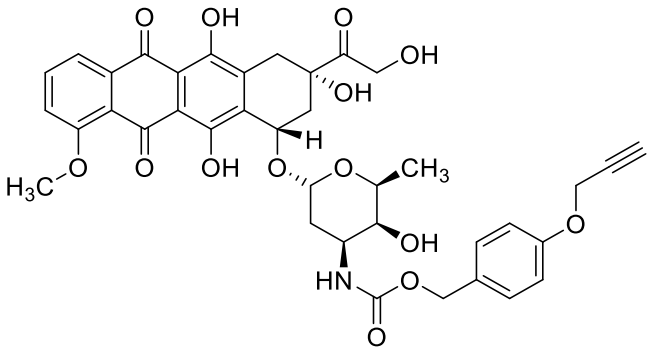

*N-(p-propargyloxybenzyl) carbamate doxorubicin (**42**).* The synthetic method described using p-nitrophenyl-p-propargyloxybenzyl carbonate gave a bright red clumpy powder (17.3 mg, 23.6 µmol, 64 % yield); R_f = 0.25 (2 % methanol in DCM) ^{1}H NMR (500 MHz, CDCl3) δ 13.96 (s, 1H), 13.23 (s, 1H), 8.03 (dd, *J* = 7.7, 1.0 Hz, 1H), 7.81 – 7.76 (m, *J* = 8.3, 7.8 Hz, 1H), 7.39 (dd, *J* = 8.5, 0.7 Hz, 1H), 7.24 (s, 1H), 6.92 (d, *J* = 8.0 Hz, 2H), 5.49 (d, *J* = 3.9 Hz, 1H), 5.28 (s, 1H), 5.10 (d, *J* = 8.3 Hz, 1H), 4.97 (s, 2H), 4.76 (s, 2H), 4.66 (s, 2H), 4.53 (s, 1H), 4.17 – 4.10 (m, 1H), 4.08 (s, 3H), 3.91 – 3.80 (m, 1H), 3.66 (s, 1H), 3.27 (dd, *J* = 18.8, 1.8 Hz, 1H), 3.05 – 2.97 (m, 2H), 2.49 (t, *J* = 2.4 Hz, 1H), 2.33 (dt, *J* = 14.5, 1.8 Hz, 1H), 2.17 (dd, *J* = 14.7, 4.0 Hz, 1H), 1.93 (d, *J* = 4.2 Hz, 1H), 1.87 (dd, *J* = 13.5, 4.8 Hz, 1H), 1.76 (td, *J* = 13.3, 4.2 Hz, 1H), 1.28 (d, *J* = 6.6 Hz, 3H), 1.25 (s, 1H). ^{13}C NMR (126 MHz, $CDCl_3$) δ 214.0 (C), 187.3 (C), 186.9 (C), 161.2 (C), 157.6 (C), 156.3 (C), 155.8 (C), 157.7 (C), 135.9 (CH), 135.7 (C), 133.7 (C), 134.0 (C), 130.1 (CH), 129.6 (C), 121.1 (C), 120.0 (CH), 118.6 (CH), 115.1 (C), 111.8 (C), 111.8 (C), 100.9 (CH), 78.6 (CH), 77.4 (CH), 76.8 (C), 75.7 (C), 69.8 (CH), 69.7 (CH), 67.4 (CH), 66.6 (CH), 65.7 (CH_2), 56.8 (CH_3), 55.9 (CH_2), 47.1 (CH), 35.8 (CH_2), 34.2 (CH_2), 30.0 (CH_2), 17.0 (CH_3) HRMS (m/z): $[M+Na]^+$ calcd for $C_{38}H_{37}O_{14}N_1Na_1$ 754.2106 found 754.2130.

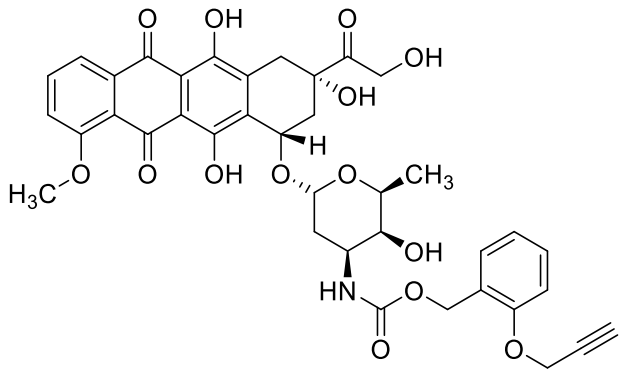

*N-(o-propargyloxybenzyl carbamate) doxorubicin (**43**).* The synthetic method described using p-nitrophenyl-o-propargyloxybenzyl carbonate gave a dark red clumpy powder (12.1 mg, 16.5 µmol, 45 % yield); R_f = 0.25 (2 % methanol in DCM). ^{1}H NMR (500 MHz, $CDCl_3$) δ 13.98 (s, 1H), 13.25 (s, 1H), 8.04 (dd, *J* = 7.7, 1.0 Hz, 1H), 7.82 – 7.75 (m, *J* = 8.4, 7.8 Hz, 1H), 7.39 (dd, *J* = 8.5, 0.7 Hz, 1H), 7.33 – 7.27 (m, 1H), 7.01 – 6.93 (m, 2H), 5.51 (d, *J* = 3.9 Hz, 1H), 5.33 – 5.27 (m, 1H), 5.15 – 5.08 (m, 3H), 4.76 (s, 2H), 4.70 (s, 2H), 4.55 (s, 1H), 4.14 (dd, *J* = 12.3, 6.2 Hz, 1H), 4.08 (s, 3H), 3.92 – 3.82 (m, 1H), 3.68 (s, 1H), 3.28 (dd, *J* = 18.8, 1.5 Hz, 1H), 3.03 (d, *J* = 18.8 Hz, 2H), 2.48 (s, 1H), 2.34 (d, *J* = 14.7 Hz, 1H), 2.17 (dd, *J* = 14.7, 4.0 Hz, 1H), 1.88 (dd, *J* = 13.5, 5.0 Hz, 1H), 1.77 (td, *J* = 13.3, 4.2 Hz, 2H), 1.29 (d, *J* = 6.6 Hz, 3H), 1.25 (s, 1H). ^{13}C NMR (126 MHz, $CDCl_3$) δ 214.0 (C), 187.3 (C), 186.9 (C), 161.2 (C), 156.3 (C), 155.9 (C) 155.9 (C), 155.6 (C), 135.9 (CH), 135.7 (C), 133.7 (C), 130.0 (CH), 129.5 (CH), 125.6 (CH), 121.6 (C), 121.1 (CH), 120.0 (CH), 118.6 (CH), 112.3 (C), 111.8 (C), 111.6 (C), 111.5 (CH), 100.9 (CH), 78.7 (C), 77.4 (CH), 76.8 (C), 75.7 (C), 69.8 (CH), 69.7 (CH), 67.4 (CH), 65.7 (CH), 62.2 (CH_2), 56.9 (CH_3), 56.3 (CH_2), 47.1 (CH), 35.8 (CH_2), 34.2 (CH_2), 30.1 (CH_2), 17.0 (CH_3). HRMS (m/z): $[M+Na]^+$ calcd for $C_{38}H_{37}O_{14}N_1Na_1$ 754.2106 found 754.2130.

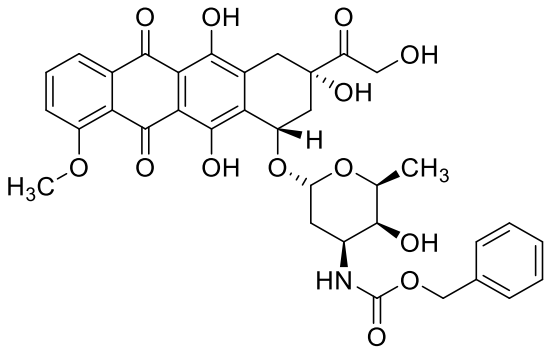

*N-(carboxybenzyl) doxorubicin (**44**).* The synthetic method described using p-nitrophenyl-benzyl carbonate gave a dark red powder (17.3 mg, 25.5 µmol, 94 % yield); R_f = 0.25 (2 % methanol in DCM). ^{1}H NMR (500 MHz, $CDCl_3$) δ 13.96 (s, 1H), 13.23 (s, 1H), 8.03 (dd, *J* = 7.7, 1.0 Hz, 1H), 7.78 (dd, *J* = 8.3, 7.9 Hz, 1H), 7.39 (dd, *J* = 8.6, 0.7 Hz, 1H), 7.34 – 7.26 (m, 5H), 5.50 (d, *J* = 3.9 Hz, 1H), 5.28 (s, 1H), 5.14 (d, *J* = 8.4 Hz, 1H), 5.03 (s, 2H), 4.82 – 4.70 (m, 2H), 4.54 (s, 1H), 4.14 (dd, *J* = 13.6, 7.2 Hz, 1H), 4.08 (s, 3H), 3.92 – 3.82 (m, 1H), 3.67 (s, 1H), 3.27 (dd, *J* = 18.8, 1.9 Hz, 1H), 3.00 (d, *J* = 18.8 Hz, 2H), 2.33 (d, *J* = 14.7 Hz, 1H), 2.19 – 2.14 (m, 1H), 1.88 (dd, *J* = 13.5, 4.8 Hz, 1H), 1.77 (td, *J* = 13.2, 4.1 Hz, 1H), 1.29 (d, *J* = 6.6 Hz, 3H), 1.25 (s, 1H). ^{13}C NMR (126 MHz, $CDCl_3$) δ 214.0 (C), 187.3 (C), 186.9 (C), 161.2 (C), 156.3 (C), 155.8 (C), 155.7 (C), 136.5 (C), 135.9 (CH), 135.7 (C), 133.7 (C), 128.7 (C), 128.3 (CH), 121.0 (C), 120.0 (CH), 118.6 (CH), 111.8 (C), 111.6 (C), 100.9 (CH), 77.4 (C), 76.8 (CH), 69.8 (CH), 69.7 (CH), 67.4 (CH), 66.9 (CH), 65.7 (CH_2), 56.8 (CH_3), 47.1 (CH), 35.8 (CH_2), 34.2 (CH_2), 31.1 (CH_2), 17.0 (CH_3). HRMS (m/z): $[M+Na]^+$ calcd for $C_{35}H_{35}O_{13}N_1Na_1$ 700.2001 found 700.1988

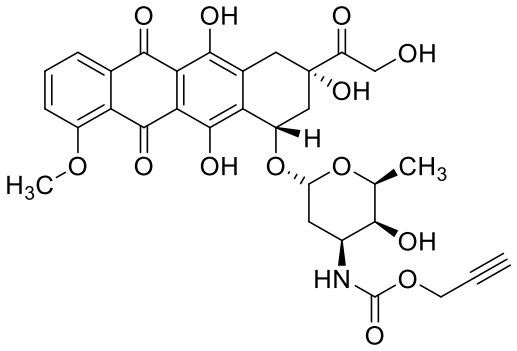

*N-propargyloxy carbamate doxorubicin (**45**).* The synthetic method described using p-nitrophenyl-propargyloxy carbonate gave a dark red powder (12.4 mg, 19.8 µmol, 73 % yield); R_f = 0.25 (2 % methanol in DCM). ^{1}H NMR (500 MHz, CDCl3) δ 13.96 (s, 1H), 13.21 (s, 1H), 8.03 (dd, *J* = 7.7, 1.0 Hz, 1H), 7.81 – 7.74 (m, 1H), 7.39 (d, *J* = 8.0 Hz, 1H), 5.50 (d, *J* = 3.8 Hz, 1H), 5.28 (s, 1H), 5.21 (d, *J* = 8.5 Hz, 1H), 4.76 (d, *J* = 1.8 Hz, 2H), 4.61 (d, *J* = 2.2 Hz, 2H), 4.51 (s, 1H), 4.14 (q, *J* = 6.3 Hz, 1H), 4.08 (s, 3H), 3.91 – 3.83 (m, 1H), 3.67 (s, 1H), 3.26 (dd, *J* = 18.8, 1.7 Hz, 1H), 2.99 (d, *J* = 18.8 Hz, 2H), 2.42 (d, *J* = 2.1 Hz, 1H), 2.33 (d, *J* = 14.7 Hz, 1H), 2.17 (dd, *J* = 14.7, 4.1 Hz, 1H), 1.88 (dd, *J* = 13.5, 5.1 Hz, 1H), 1.78 (td, *J* = 13.3, 4.2 Hz, 1H), 1.29 (d, *J* = 6.6 Hz, 3H), 1.25 (s, 1H).^{13}C NMR (126 MHz, CDCl3) δ 214.0 (C), 187.3 (C), 186.8 (C), 161.2 (C), 156.3 (C), 155.8 (C), 154.8 (C), 135.9 (CH), 135.7 (C), 133.7 (C), 121.0 (C), 120.0 (C), 118.6 (CH), 111.8 (C), 111.6 (C), 100.8 (CH), 78.2 (CH), 77.4 (CH), 76.8 (C), 74.8 (C), 69.8 (CH), 69.7 (CH), 67.4 (CH), 65.7 (CH_2), 56.8 (CH_3), 52.7 (CH_2), 47.3 (CH), 35.8 (CH_2), 34.2 (CH_2), 30.5 (CH_2), 17.0 (CH_3). HRMS (m/z): $[M+Na]^+$ calcd for $C_{31}H_{31}O_{13}N_1Na_1$ 648.1687 found 648.1677

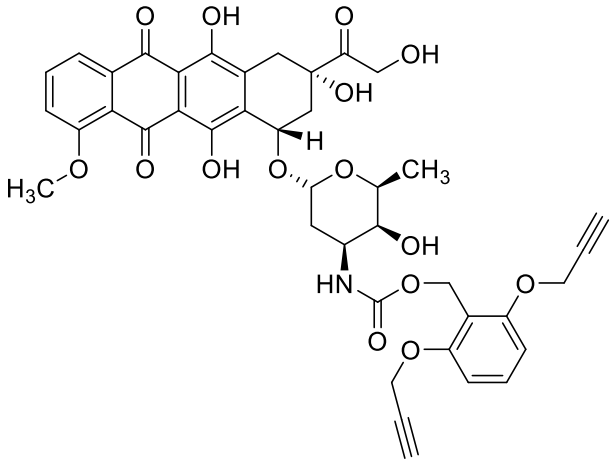

*o-bis-propargyloxybenzyl) carbamate doxorubicin (**50**)* The synthetic method described using *p*-nitrophenyl-*o-bis*-propargyloxybenzyl- carbonate gave a crude powder that was then further purified by semi-prep HPLC to afford a dark red clumpy powder (14 mg, 11 µmol, 30 % yield); R_f = 0.52 (2 % methanol in DCM). ^{1}H NMR (500 MHz, $CDCl_3$) δ 13.97 (s, 1H), 13.26 (s, 1H), 8.05 (d, *J* = 7.7 Hz, 1H), 7.79 (t, *J* = 8.1 Hz, 1H), 7.39 (d, *J* = 8.5 Hz, 2H), 7.24 (s, 1H), 6.70 (d, *J* = 5.5 Hz, 2H), 5.50 (d, *J* = 3.3 Hz, 1H), 5.30 (s, 1H), 5.25 – 5.14 (m, 2H), 5.03 – 4.92 (m, 2H), 4.76 (s, 2H), 4.69 (s, 4H), 4.13 (s, 1H), 4.08 (s, 3H), 3.88 (s, 1H), 3.70 (s, 1H), 3.16 (dd, *J* = 126.2, 18.6 Hz, 2H), 2.46 (s, 2H), 2.25 (dd, *J* = 88.8, 14.5 Hz, 2H), 1.79 (ddd, *J* = 27.8, 16.8, 7.2 Hz, 2H), 1.31 – 1.24 (m, 3H).^{13}C NMR (126 MHz, $CDCl_3$) δ 214.0 (C), 187.1 (C), 187.0 (C), 161.1 (C), 157.5 (C), 156.2 (C), 155.9 (C), 155.7 (C), 135.7 (CH), 135.6 (C), 133.7 (C), 133.6 (C), 130.1 (CH), 121.0 (C), 119.9 (CH), 118.5 (CH), 114.0 (C), 111.7 (C), 111.5 (C), 106.3 (CH), 100.7 (CH), 78.5 (CH), 77.2 (CH), 76.6 (C), 75.6 (C), 69.5 (CH), 69.5 (CH), 67.3 (CH), 65.6 (CH_2), 56.7 (CH_3), 56.5 (CH_2), 56.2 (CH_2), 47.0 (CH), 35.7 (CH_2), 34.1 (CH_2), 30.2 (CH_2), 16.9 (CH_3). HRMS (m/z): $[M+Na]^+$ calcd for $C_{41}H_{39}O_{15}N_1Na_1$ 808.2212 found 808.2186.

7.2 Biology Methods

7.2.1 Cell culture

Cell lines were grown in culture media supplemented with 10 % Fetal Bovine Serum (FBS) and 2 mM L-glutamine, then incubated in a tissue culture incubator at 37 °C and 5 % CO_2. Human adenocarcinomic alveolar basal epithelial A549 cells (a gift from Dr. Simon Wilkinson), human prostate cancer DU145 cells (a gift from Dr. Neil Carragher), human glioblastoma multiforme U87 cells (a gift from Dr. Noor Gamon), human glioblastoma multiforme T98 cells (a gift from Dr. Margaret Frame), human pancreatic carcinoma MiaPaCa-2 cells (a gift from Dr. Simon Wilkinson) and human colorectal carcinoma HCT116 cells (a gift from Dr Van Schaeybroeck) were cultured in Dulbecco's modified Eagle's media (DMEM). Human pancreas adenocarcinoma BxPC-3 cells (a gift from Dr Mark Duxbury) were cultured in Roswell Park Memorial Institute (RPMI) media.

7.2.2 Non Biological Pd^0 mediated Conversion Study

All stock drug samples (100 mM in DMSO) were dissolved in PBS (1 mL) for a final concentration of 100 μM with 1 mg of 30 μm or 150 μm Pd^0 beads and shaken at 1200 rpm, 37 °C in a Thermomixer. 50 μL aliquots were removed at reported time intervals and monitored by analytical UPLC using a UV detector. Ultra-performance liquid chromatography (UPLC) was performed using a Waters Acquity UPLC PDA with a 50 x 2.4 mm Waters BEH C18 1.7 μm column, with compounds detected using an evaporative light scattering detector (ELSD) and UV detector. All solvents used were HPLC grade. Method: eluent A, H_2O and formic acid (0.1 %); eluent B, acetonitrile; A/B = 95 : 5 to 20 : 80 in 8 min, 95 : 5 in 8.5 minutes.

7.2.3 Bioorthogonal Comparative Study of Prodrug to Parental Drug

Cells were seeded in a 96 well plate format at the appropriate cell concentration (2000 cells/well for DU145 cells and U87 cells, 1,000 cells/well for MiaPaCa-2 cells, 3000 cells/well for HCT116 cells and T98 cells and 2500 cells/well for A549 and BxPC-3 cells), and incubated

for 48 hr before treatment. Each well was then replaced with fresh media containing drug or prodrug and incubated for 5 days. Untreated cells were incubated with DMSO (0.1 % v/v). PrestoBlue® cell viability reagent (10 % v/v) was added to each well and the plate incubated for 1 hr. Fluorescence emission was detected using a PerkinElmer Victor2 multilabel reader (excitation filter at 540 nm and emissions filter at 590 nm). All conditions were normalized to the untreated cells (100 %) and curves fitted with GraphPad Prism 5 using a sigmoidal variable slope curve.

7.2.4 Pd^0-Mediated Dealkylation of Prodrugs in Cell Culture

Cells were plated as described and incubated for 48 hr prior to treatment. Wells were then replaced with fresh media containing Pd^0-beads. For 130 μm diameter Pd^0 bead studies, appropriate wells were replaced containing 0.67 mg/mL – (BxPC3 cells) or 1 mg/mL – (DU145 cells, U87 cells, MiaPaCa2 cells and HCT116 cells) with DMSO (0.1 % v/v). For 30 μm diameter Pd^0 bead studies, appropriate wells was replaced with fresh media containing 0.6 mg/mL – (DU145 cells, U87 cells) with DMSO (0.1 % v/v). For doxorubicin assays; wells were replaced with media containing prodrugs **42** – **45**, **50** (30 - 3000 nM) with DMSO (0.1 % v/v); doxorubicin **37** (30 - 3000 nM) with DMSO (0.1 % v/v); or a combination of Pd^0 beads and prodrugs **42** – **45**, **50** (30 - 3000 nM) with DMSO (0.1 % v/v). Untreated cells were incubated with Pd^0 beads and DMSO (0.1 % v/v), and DMSO (0.1 % v/v) alone. For gemcitabine assays; wells were replaced with media containing prodrugs **24** – **26**, **33** - **36** (3 - 300 nM) with DMSO (0.1 % v/v); gemcitabine **16** (3 - 300 nM) with DMSO (0.1 % v/v); or a combination of Pd^0 beads and prodrugs **24** – **26**, **33** - **36** (3 - 300 nM) with DMSO (0.1 % v/v). Untreated cells were incubated with Pd^0 beads and DMSO (0.1 % v/v), and DMSO (0.1 % v/v) alone. For 5-fluorouracil assays; wells were replaced with media containing prodrug **2** (30 - 3000 nM) with DMSO (0.1 % v/v); 5FU **1** (30 - 3000 nM) with DMSO (0.1 % v/v); or a combination of Pd^0 beads and prodrug (**2**) (30 - 3000 nM) with DMSO (0.1 % v/v). Untreated cells were incubated with Pd^0 beads and DMSO (0.1 % v/v), and DMSO (0.1 % v/v) alone. All cells were incubated with drugs for 5 days. PrestoBlue® cell viability reagent (10 % v/v) was added to each well

and the plate incubated for 1 hr. Fluorescence emission was detected and results normalized as described above.

7.2.5 Spontaneous Raman spectroscopy of drug, prodrug and cell pellet

For drug and prodrug Raman spectrum analysis, a spatula tip of dry powdered 5FU **1** or prodrug **2** was spread evenly across a Raman grade CaF_2 polished cover slip and mounted under the Raman spectrometer laser for signal acquisition. For cell pellet preparation, the adenocarcinomic human alveolar basal epithelial (A549) cell line was maintained in Dulbecco's Modified Eagle's Medium (DMEM, Sigma-Aldrich), supplemented with 2 mM L-glutamine and 10 % FBS (Thermo Fisher Scientific) at 37 °C in a humidified atmosphere containing 5 % CO_2. A549 cells were grown to confluence in a T75 flask, trypsinated and centrifuged into a cell pellet of ~ 1 mm in diameter. Supernatant was removed and the cell pellet bathed in **1** or **2** (1 mL of a 500 µM solution in 0.1 % DMSO) for 15 minutes. The cell pellet was snap frozen in liquid nitrogen, re-thawed to rt after 1 hr then gently pipetted across a Raman grade CaF_2 polished cover slip and mounted under the Raman spectrometer laser for signal acquisition. The spontaneous Raman spectra were acquired using a confocal Raman spectrometer (inVia Raman microscope, Renishaw) at rt. A 200 mW 532 nm laser excitation source was used to excite the sample through a 20 x objective, N.A. 0.75 objective (Leica Biosystems). The recorded spectral range for grating 1200 g mm^{-1} was 100 – 3500 cm^{-1}. The total data acquisition was performed during 10 s for drug and prodrug powder analysis, and 60 s for cell pellet analysis, both recorded at λ_{ex} = 532 nm without background correction using WiRE 4.1 software.

7.2.6 Spheroid Assay

A suspension of freshly trypsinated cells was dispensed as 10,000 cells in 50 µL aliquots into wells of a 96 Corning ULA® U-bottom plate at 4 °C. Pd^0 bead(s) in fresh media were dispensed into required wells in 50 µL aliquots. A solution of Matrigel® in cold media was made up and dispensed into the wells for a final concentration of 2 % in Matrigel® in 200 µL media. The Corning ULA® U-bottom plate was inserted into a pre-chilled 4 °C centrifuge and spun at 1000

G for 10 minutes. Cells were then incubated at 37 °C for 72 hr and viewed under microscope to confirm spheroid formation. Wells were replaced with media containing prodrug **43** 100 μM) with DMSO (0.1 % v/v) or doxorubicin (100 μM) with DMSO (0.1% v/v). Untreated cells were incubated with DMSO alone (0.1 % v/v). 2 μL of a 0.3 mM stock solution of DRAQ7™ live imaging apoptosis staining solution was added to each well, and the plate was incubated for 5 days. Microscopy at day 5 was carried out with an ImageXpress micro XLS widefield microscope (Molecular Devices) at 4 x magnification, imaged with transmitted light and a Cy5 far-red filter (excitation 628 +/- 40 nm, emission 692 +/- 40 nm). Images were taken as a Z-stack at multiple focal planes and processed into a single image using the manufacturer's maximum intensity projection routine. Transmitted light images and Cy5 images were merged using ImageJ.

7.2.7 Zebrafish Assay

All zebrafish work presented in this study has been performed in accordance with the UK legal requirements for the protection of animals used for experimental or other scientific research under the European Directive 2010/63/EU and the Animal (Scientific Procedures) Act 1986 amended in 2013. All experiments were performed under the Home Office Project License 70/8000 to EEP. Zebrafish welfare and husbandry were closely monitored by the MRC Human Genetics Unit Zebrafish Facility staff.

Zebrafish (AB line) were raised and maintained as previously described[303]. Embryos were generated by natural pair-wise mating and were kept and handled for all experiments in E3 medium (5 mM NaCl, 0.17 mM KCl, 0.33 mM $CaCl_2$, and 0.33 mM $MgSO_4$). Manually dechorionated embryos were incubated between 24 hpf and 120 hpf[304] in E3 medium containing either doxorubicin (Cambridge Biosciences) or prodrug **43** at the following concentrations (50 μM, 100 μM, 150 μM and 200 μM). Embryos were soaked in DMSO (0.1 %) and E3 media as a control. Embryos were kept in 6-well plates (15 embryos / well; 2 wells / condition) at 28.5 °C with dead embryos removed daily. Three experimental replicates were performed with n = 30 (15 x 2) embryos per condition and 2 replicates per condition. Pericardial edema and body surface was estimated using the area measurement tool in Fiji software.

Results were obtained by randomly taking > 10 embryos per condition, then determining cardiac/body ratios as previously described[273]. Statistical analyses were performed using Prism GraphPad5 software. Data were subjected to an ordinary one-way ANOVA test. All pictures (fluorescent images included) were taken at the same resolution and magnification using an AZ100 upright macroscope (Nikon) with a Plan Apochromat 2 x / 0.45 lens equipped with a Retiga Exi camera (Qimaging) camera. Images were analyzed and processed with Micro-Manager and Fiji software. Embryos were mounted laterally in 1.5 % Low Melting Point Agarose (Thermo Scientific) and kept in a 0.02 % w/v MS222 (Thermo scientific) solution in E3 medium and culled after imaging in an overdose of MS222 at the end of each experiment.

7.2.8 *In vivo* / *ex vivo* Mouse Assays

All murine experiments were approved by the Animal Welfare and Ethical Review Board at the University of Glasgow. The human prostate cancer cell line DU145 was purchased from ATCC, authenticated by LCG standards and grown in RPMI (Gibco) containing 10 % (v/v) serum supplement and 2 mM L-glutamine at a temperature of 37 C° with 5 % CO_2. Nude athymic mice were purchased from XimBio.

Intra-prostatic cancer cell implantation

Mice were anesthetized by intraperitoneal injection of 0.5 mg / 1 g body weight NembutalR, 3 µL / 1 g body weight of Ketamine/Xylazine/PBS mixture and subcutaneous Morphene was administered subcutaneously at the injection site. The mouse was then placed in an induction chamber with 2 % isoflurane / 98 % oxygen, and kept under anaesthesia through continuous nose cone flow during surgery. Mouse was positioned supine, and a midline incision provided access to the prostate gland. A 50 µL cell suspension containing 5 x 10^4 DU145 cells was injected into the prostate, and the round was appropriately closed with metal clips, before the mouse was transferred for recovering and monitoring.

Intra-tumoural cancer cell implantation

Mice identified as having produced tumours from initial cancer cell culture implantation were anaesthetized as above and positioned supine on a mounted platform within a Visual Sonics

Vevo 2100 Imaging Station. A solution of 2 mg 30 μm Pd^0 beads in 25 μL was suspended in sterile PBS and injected into the mouse prostate using an insulin syringe/needle. Sterile surgical jelly was applied to the injection site, and the needle was appropriately positioned into the plane of ultrasound observation in the prostate tumour. Injection was completed over 30 seconds, and was observed using the enhanced abdominal measurement package in the B-mode setting. Once the needle was removed, mice were transferred for recovery and monitoring.

Tumour resection

Mice were euthanized according to an IACUC approved method (CO_2 asphyxiation), and an abdominal incision provided access to the prostate. Prostate tumours were excised with scissors, photographed, sliced longitudinally using a rate brain slicer instrument into 1 mm sections and affixed to the bottom of a 24 well plate using 1 - 3 spots of tissue glue at the perimeter of each sample. Tumour slices were soaked in 2 mL of RPMI media containing 10 % (v/v) serum supplement and 2 mM L-glutamine, and 0.1 % (v/v) DMSO dissolving 100 uM of each treatment compound. Wells containing drug or prodrug were treated additionally with 2 μL of DAPI.

Fluorescent Imaging

Imaging was performed using the NIKON A1R confocal microscope. Excitation and Emission; The 403.1 nm laser was used to excite DAPI, laser power was set at 3 %, emission was detected at 450 nm with PMT voltage set at 83 V and offset at -3 V. The 488 nm laser was used to excite Rhodamine 110, laser power set at 6 %. Emission was detected with at 525 nm with PMT voltage set at 102 V and offset at -4 V. The 560.8 nm laser was used to excite the Doxorubicin drug/prodrug, laser power set at 3 %. Emission was detected at 595 nm with PMT voltage set at 112 V and offset at -9. In addition DIC images were captured simultaneously. Optics; A 20 x lens with a 0.75 numerical aperture was used and pinhole size was set at 65.13 μm.

Scanning system and acquisition; The microscope stage is enclosed in a perspex “cage” which is heated to 37 °C and CO_2 bubbled through water into the tissue enclosure to maintain tissue viability. The high resolution, non-resonant galvano scanner was used, with a scan size of 512 x 512 pixels at a speed of 1 frame/second and no line averaging. All images were take over a period of 63 hrs with a image taken every 3 hours from t = 0 giving 22 time-points for each position. For each well/condition at least two positions were imaged each time, most wells/conditions had three positions imaged however a few tissue sections were too small to allow for this. The positions were kept exact overtime by use of the perfect focus function of the NIKON A1R, which ensures the focus is maintained at each position overtime.

Standard vs. Xylene Free Fixation Method

Each tissue slice was processed conventionally (with xylene) or by the xylene-free method along with the daily routine material at the Department of Histology at the Beatson Institute Glasgow. The processing methods were those in use at the respective laboratories at the time of the experimentation, and found in detail in the reference included[305]. All paraffin blocks were then sectioned by one person in a working day using one microtome, with the embedding process illustrated. Automatic tissue processors utilized during this experiment were those in routine use at the the Beatson Laboratory Histology Department.

CHAPTER 8

Bibliography

1. Chalfie M, et al. *Green fluorescent protein as a marker for gene expression*. Science. 1994; 263(5148): 802-805.

2. Weissleder R, and Ntziachristos V. *Shedding light onto live molecular targets*. Nature Medicine. 2003; 9(1): 123-128.

3. Shimomura O, et al. *Extraction, Purification and Properties of Aequorin, a Bioluminescent Protein from the Luminous Hydromedusan, Aequorea*. Journal of Cellular and Comparative Physiology. 1962; 59(3): 223-239.

4. Prasher DC, et al. *Primary structure of the Aequorea victoria green-fluorescent protein*. Gene. 1992; 111(2): 229-233.

5. Shaner NC, et al. *Improved monomeric red, orange and yellow fluorescent proteins derived from Discosoma sp. red fluorescent protein*. Nature Biotechnology. 2004; 22(12): 1567-1572.

6. Francis MB, and Carrico IS. *New frontiers in protein bioconjugation*. Current Opinion in Chemical Biology. 2010; 14(6): 771-773.

7. Stephanopoulos N, and Francis MB. *Choosing an effective protein bioconjugation strategy.* Nature Chemical Biology. 2011; 7(12): 876-884.

8. Goodsell DS, et al. *The RCSB PDB "Molecule of the Month": Inspiring a Molecular View of Biology*. PLoS Biology. 2015; 13(5): 1-12.

9. Berman HM, et al. *The protein data bank*. Nucleic Acids Research. 2000; 28(1): 235-242.

10. Griffin BA, Adams SR, Tsien RY. *Specific covalent labeling of recombinant protein molecules inside live cells*. Science. 1998; 281: 269-272.

11. Hang HC, et al. *A metabolic labeling approach toward proteomic analysis of mucin-type O-linked glycosylation*. Proceedings of the National Academy of Sciences. 2003; 100(25): 14846-14851.

12. Rideout D. *Self-Assembling Cytotoxins.* Science. 1986; 233(4763): 561-563.

13. Saxon E, and Bertozzi C. *Cell Surface Engineering by a Modified Staudinger Reaction.* Science. 2000; 287(5460): 2007-2010.

14. Tornøe CW, et al. *Peptidotriazoles on solid phase: [1,2,3]-Triazoles by regiospecific copper(I)-catalyzed 1,3-dipolar cycloadditions of terminal alkynes to azides*. Journal of Organic Chemistry. 2002; 67(9): 3057-3064.

15. Rostovtsev VV., et al. *A stepwise huisgen cycloaddition process: Copper(I)-catalyzed regioselective "ligation" of azides and terminal alkynes*. Angewandte Chemie - International Edition. 2002; 41(14): 2596-2599.

16. McKay CS, and Finn MG. *Click Chemistry in Complex Mixtures: Bioorthogonal Bioconjugation*. Chemical Biology. 2014; 21(9): 1075-1101.

17. Yang M, et al. *Transition metal-mediated bioorthogonal protein chemistry in living cells.* Chemical Society Reviews. 2014; 43(18): 6511-6526.

18. Sletten EM, and Bertozzi CR. *Bioorthogonal Reactions.* Accounts of Chemical Research. 2011; 44(9): 666-676.

19. Blackman ML, et al. *The Tetrazine Ligation: Fast Bioconjugation based on Inverse- electron-demand Diels-Alder Reactivity*. Journal of the American Chemical Society. 130(41): 13518-13519.

20. Schmierer T, et al. *Femtosecond spectroscopy on the photochemistry of ortho-nitrotoluene.* Physical Chemistry Chemical Physics. 2010; 12(48): 15653-15664.

21. Pelliccioli AP, and Wirz J. *Photoremovable protecting groups: reaction mechanisms and applications.* Photochemical Photobiological Science. 2002; 1(7): 441-458.

22. Pillai VNR. *Photoremovable Protecting Groups in Organic Synthesis.* Synthesis. 1980; 1: 1-26.

23. Kaplan JH, et al. *Rapid photolytic release of adenosine 5'-triphosphate from a protected analog - utilization by Na-K pump of human red blood-cell ghosts*. Biochemistry. 1978; 17: 1929-1935.

24. Yamazoe S, et al. *Nitroreductase-activatable morpholino oligonucleotides for in vivo gene silencing.* ACS Chemical Biology. 2014; 9(9): 1985-1990.

25. Bae J, et al. *Nitroreductase-triggered activation of a novel caged fluorescent probe obtained from methylene blue.* Chemical Communications. 2015; 51(64): 12787-12790.

26. Thieriet N, et al. *Use of Alloc-amino acids in solid-phase peptide synthesis. Tandem deprotection-coupling reactions using neutral conditions.* Tetrahedron Letters. 1997; 38(41): 7275-7278.

27. Pal M, et al. *Palladium-catalyzed cleavage of O/N-propargyl protecting groups in aqueous media under a copper-free condition.* Organic Letters. 2003; 5(3): 349-352.

28. Isidro-Llobet A, et al. *Amino acid-protecting groups.* Chemical Reviews. 2009; 109(6): 2455-2504.

29. Kondo T, et al. *First ruthenium-catalyzed allylation of thiols enables the general synthesis of allylic sulfides*. Journal of the American Chemical Society. 1999; 121(37): 8657-8658.

30. Streu C, and Meggers E. *Ruthenium-induced allylcarbamate cleavage in living cells.* Angewandte Chemie - International Edition. 2006; 45(34): 5645-5648.

31. Völker T, et al. *Progress towards bioorthogonal catalysis with organometallic compounds.* Angewandte Chemie - International Edition. 2014; 53(39): 10536-10540.

32. Santra M, et al. *Fluorescent detection of palladium species with an O-propargylated fluorescein.* Chemical Communications. 2010; 46(22): 3964-3966.

33. Yusop RM, et al. *Palladium-mediated intracellular chemistry.* Nature Chemistry. 2011; 3(3): 239-243.

34. Weiss JT, et al. *Extracellular palladium-catalysed dealkylation of 5-fluoro-1-propargyl-uracil as a bioorthogonally activated prodrug approach.* Nature Communications. 2014; 5: 3277.

35. Jürgen S, et al. *1,2,4,5-Tetrazine: Synthesis and Reactivity in [4+2] Cycloadditions.* European Journal of Organic Chemistry. 1998: 2885-2896.

36. Versteegen RM, et al. *Click to release: Instantaneous doxorubicin elimination upon tetrazine ligation.* Angewandte Chemie - International Edition. 2013; 52: 14112-14116.

37. Matikonda SS, et al. *Bioorthogonal prodrug activation driven by a strain-promoted 1 , 3-dipolar cycloaddition.* Chemical Science. 2014; 1-7

38. Hanahan D, and Weinberg RA. *The hallmarks of cancer.* Cell. 2000; 100(1): 57-70.

39. Gilman A, and Philips FS. *The Biological Actions and Therapeutic Applications of the B-Chloroethyl Amines and Sulfides.* Science. 1946; 103(2675): 409-415.

40. Hurley LH. *DNA and its associated processes as targets for cancer therapy.* Nature Reviews Cancer. 2002; 2(3): 188-200.

41. Mills BA, and Roberts RW. *Cyclophosphamide-induced cardiomyopathy: A Report of Two Cases and Review of the English Literature*. Cancer. 1979; 43: 2223-2226.

42. Ayash LJ, et al. *Cyclophosphamide pharmacokinetics: Correlation with cardiac toxicity and tumor response.* Journal of Clinical Oncology. 1992; 10(6): 995-1000.

43. *Dihydrofolate Reductase Complexed with Methotrexate* - RCSB Protein Database. DOI: nar.oxfordjournals.org/content/28/1/235.abstract. Date Accessed: 14 May 2017

44. Rajagopalan PTR, et al. *Interaction of dihydrofolate reductase with methotrexate: ensemble and single-molecule kinetics.* Proceedings of the National Academic of Science. 2002; 99(21): 13481-13486.

45. Santi DV, and Carreras CW. *The Catalytic Mechanism and Structure of Thymidylate Synthase.* Annual Reviews in Biochemistry. 1995; 64: 721-762.

46. Goodsell DS. *The Molecular Perspective: Methotrexate.* The Oncologist. 1999; 4: 340-341.

47. May J *High incidence of methotrexate associated renal toxicity in patients with lymphoma: a retrospective analysis*. Leukaemia Lymphoma. 2014; 55(6): 1345-1349.

48. Perou CM, et al. *Molecular portraits of human breast tumours.* Nature. 2000; 406(6797): 747-752.

49. Alizadeh AA, et al. *Distinct types of diffuse large B-cell lymphoma identified by gene expression profiling*. Nature. 2000; 403(6769): 503-511.

50. Sorlie T, et al. *Gene expression patterns of breast carcinomas distinguish tumor subclasses with clinical implications.* Proceedings of the National Academy of Science. 2001; 98(19): 10869-10874.

51. Ramaswamy S, et al. *A molecular signature of metastasis in primary solid tumors.* Nature Genetics. 2003; 33(1): 49-54.

52. Wong S, and Witte ON. *The BCR-ABL Story: Bench to Bedside and Back.* Annual Reviews in Immunology. 2004; 22(1): 247-306.

53. Druker BJ, et al. *Efficacy and Safety of a Specific Inhibitor of the Bcr-Abl Tyrosine Kinase in Chronic Myeloid Leukemia.* New England Journal of Medicine. 2001; 344(14): 1031-1037.

54. Antarjian HAK, et al. *Hematologic and Cytogenetic Responses to Imatinib Mesylate in Chronic Myelogenous Leukemia.* New England Journal of Medicine. 2002; 346(9): 645-652.

55. Andrae J, et al. *Role of platelet-derived growth factors in physiology and medicine.* Genes and Development. 2008; 22: 1276-1312.

56. Lennartsson J, and Rönnstrand L. *Stem cell factor receptor/c-Kit: from basic science to clinical implications.* Physiological Reviews. 2012; 92(4): 1619-1649.

57. Kerkelä R, et al. *Cardiotoxicity of the cancer therapeutic agent imatinib mesylate*. Nature Medicine. 2006; 12(8): 908-916.

58. Elias J, et al. *Chronic myeloid leukemia: mechanisms of resistance and treatment.* Hematology Oncology Clinics of North America. 2011; 25(5): 981-995.

59. Mendelsohn J. *Blockade of receptors for growth factors: an anticancer therapy*. Clinical Cancer Research. 2000; 6(3): 747-753.

60. Ciardiello F, et al. *Antitumor Effect and Potentiation of Cytotoxic Drugs Activity in Human Cancer Cells by ZD-1839 (Iressa), an Epidermal Growth Factor Receptor-selective Tyrosine Kinase Inhibitor*. Clinical Cancer Research 2000; 6(May): 2053-2063.

61. Brabender J, et al. *Advances in Brief Epidermal Growth Factor Receptor and HER2-neu mRNA Expression in Non-Small Cell Lung Cancer Is Correlated with Survival.* Clinical Cancer Research. 2001; 7(July): 1850-1855.

62. Hirsch FR, et al. *Epidermal growth factor receptor in non-small-cell lung carcinomas: Correlation between gene copy number and protein expression and impact on prognosis.* Journal of Clinical Oncology. 2003; 21(20): 3798-3807.

63. Herbst RS, et al. *Gefitinib — a novel targeted approach to treating cancer.* Nature. 2004; 4(December): 956-965.

64. Prasad V, et al. *Precision oncology: Origins, optimism, and potential.* Lancet Oncology. 2016; 17(2): 81-86.

65. Le Tourneau C, et al. *Molecularly targeted therapy based on tumour molecular profiling versus conventional therapy for advanced cancer (SHIVA): a multicentre, open-label, proof-of-concept, randomised, controlled phase 2 trial.* Lancet Oncology. 2015; 16(13): 1324-1334.

66. Meric-Bernstam F, et al. *Feasibility of large-scale genomic testing to facilitate enrollment onto genomically matched clinical trials.* Journal of Clinical Oncology. 2015; 33(25): 2753-2762.

67. NCI. *Executive Summary : Interim Analysis of the NCI-MATCH Trial*. 2016. DOI: cancer.gov/nci-match Date Accessed 21 May 2017

68. Coley WB. *The Treatment of Inoperable Sarcoma by Bacterial Toxins (the Mixed Toxins of the Streptococcus erysipelas and the Bacillus prodigiosus)*. Proceedings of the Royal Society of Medicine. 1910; 3(Surg Sect): 1-48.

69. Alloatti A, et al. *Dendritic cell maturation and cross-presentation: timing matters!* Immunology Reviews. 2016; 272(1): 97-108.

70. Agrawal S, et al. *Biotin Deficiency Enhances the Inflammatory Response of Human Dendritic Cells.* American Journal of Physiology and Cell Physiology. 2016: 311; 386-391

71. Chen J, et al. *A novel vaccine for mantle cell lymphoma based on targeting cyclin D1 to dendritic cells via CD40.* Journal of Hematological Oncology. 2015; 8(1): 35.

72. Ramos CA, et al. *CD19-CAR Trials.* The Cancer Journal. 2014; 20(2): 112-118.

73. Klebanoff CA, et al. *Immunotherapy: Treatment of aggressive lymphomas with anti-CD19 CAR T cells.* Nature Reviews in Clinical Oncology. 2014; 11(12): 685-686.

74. Blankenstein T, et al. *The determinants of tumour immunogenicity.* Nature Reviews Cancer. 2012; 12(4): 307-313.

75. Lee DW, et al. *How I Treat: Current concepts in the diagnosis and management of cytokine release syndrome.* Blood. 2014; 124(2): 188-196.

76. Page DB, et al. *Immune modulation in cancer with antibodies.* Annual Reviews in Medicine. 2014; 65: 185-202.

77. Huttunen KM, and Raunio H, Rautio J. *Prodrugs — from Serendipity to Rational Design.* Pharmacological Reviews 2011; 63(3): 750-771.

78. Shinohara ET, et al. *The use of gene therapy in cancer research and treatment.* Technology in Cancer Research and Treatment. 2004; 3(5): 479-490.

79. Bagshawe KD, et al. *Antibody-directed enzyme prodrug therapy (ADEPT) for cancer.* Expert Opinions in Biological Therapy. 2004; 4(11): 1777-1789.

80. Zawilska JB, et al. *Prodrugs: A challenge for the drug development.* Pharmacological Reports. 2013; 65(1): 1-14.

81. Unciti-Broceta A, et al. *Synthesis of polystyrene microspheres and functionalization with Pd(0) nanoparticles to perform bioorthogonal organometallic chemistry in living cells.* Nature Protocols. 2012; 7(6): 1207-1218.

82. Guedea F. *Perspectives of brachytherapy: Patterns of care, new technologies, and "new biology."* Cancer/Radiothérapie. 2014; 18(5-6): 434-436.

83. Nesvacil N, et al. *Combining transrectal ultrasound and CT for image-guided adaptive brachytherapy of cervical cancer: Proof of concept.* Brachytherapy. 2016; 15(6): 839-844.

84. Hart, et al. *Chemotherapy wafers for high grade glioma.* Cochrane Database Systematic Reviews 2011. 2011; (3).

85. Fleming AB, and Saltzman WM. *Pharmacokinetics of the carmustine implant.* Clinical Pharmacokinetics. 2002; 41(6): 403-419.

86. Geiger EJ, et al. *Wound Healing Complications With Intraoperative Brachytherapy for Head and Neck Cancer.* Annals of Plastic Surgery. 2014; 73(4): 378-384.

87. Attenello FJ, et al. *Use of Gliadel (BCNU) wafer in the surgical treatment of malignant glioma: a 10-year institutional experience.* Annals of Surgical Oncology. 2008; 15(10): 2887-2893.

88. Weiss JT, et al. *N-alkynyl derivatives of 5-fluorouracil: susceptibility to palladium-mediated dealkylation and toxigenicity in cancer cell culture.* Frontiers in Chemistry. 2014; 2(July): 1-9.

89. Weiss JT, et al. *Development and bioorthogonal activation of palladium-labile prodrugs of gemcitabine.* Journal of Medicinal Chemistry. 2014; 57(12): 5395-5404.

90. Weiss JT, et al. *Palladium-Mediated Dealkylation of N-Propargyl-Floxuridine as a Bioorthogonal Oxygen-Independent Prodrug Strategy.* Scientific Reports. 2015; 5.

91. Rutman RJ, et al. *Studies in 2-acetylaminofluorine carcinogenesis III, the utilization of uracil-2-C-14 by preneoplastic liver and rat hepatoma.* Cancer Research. 1954; 14: 119.

92. Longley DB, et al. *5-Fluorouracil: Mechanisms of Action and Clinical Strategies.* Nature Reviews Cancer. 2003; 3(5): 330-338.

93. Heidelberger C, et al. *Fluorinated pyrimidines, a new class of tumour-inhibitory compounds.* Nature. 1957; 179(4561): 663-666.

94. Cascinu S, et al. A combination of gemcitabine and 5-fluorouracil in advanced pancreatic cancer. British Journal of Cancer. 1999; 80(10): 1595-1598.

95. Bamias A, and Pavlidis N. *Systemic Chemotherapy in Gastric Cancer: Where Do We Stand Today?* The Oncologist. 1998; 3(3): 171-177.

96. Ansfield FJ, et al. *A Ten-Year Study of 5-Fluorouracil in Disseminated Clinical Results and Survival Times in Breast Cancer*. Cancer Research. 1969; 29(May): 1062-1066.

97. Seiwert TY, et al. *The chemoradiation paradigm in head and neck cancer.* Nature Clinical Practice Oncology. 2007; 4(3): 156-171.

98. Labianca R, et al. *Efficacy of adjuvant fluorouracil and folinic acid in colon cancer. International Multicentre Pooled Analysis of Colon Cancer Trials (IMPACT) investigators.* Lancet. 1995; 345: 939-944.

99. Fluorouracil 25 mg/ml Injection - Summary of Product Characteristics (SPC) - (eMC). DOI: https://www.medicines.org.uk/emc/medicine/635. Date Accessed April 30, 2017.

100. Rougier P, et al. *5-fluorouracil (5-FU) continuous intravenous infusion compared with bolus administration. Final results of a randomised trial in metastatic colorectal cancer.* European Journal of Cancer. 1997; 33(11): 1789-1793.

101. Midena E, et al. *Treatment of conjunctival squamous cell carcinoma with topical 5-fluorouracil Treatment of conjunctival squamous cell carcinoma with topical 5-fluorouracil.* British Journal of Ophthalmology 2000; 84: 268-272.

102. Cunningham TJ, et al. *Randomized trial of calcipotriol combined with 5-fluorouracil for skin cancer precursor immunotherapy.* Journal of Clinical Investigation. 2017; 127(1): 106-116.

103. Wohlhueter RM, et al. *Facilitated transport of uracil and 5-fluorouracil, and permeation of orotic acid into cultured mammalian cells*. Journal of Cell Physiology. 1980; 104(3): 309-319.

104. Mukherjee KL, and Heidelberger C. *Studies on Fluorinated Pyrimidines.* Journal of Biological Chemistry. 1960; 235(2): 433-437.

105. Heggie GD, et al. *Clinical Pharmacokinetics of 5-Fluorouracil*. Clinical Pharmacokinetics. 1987; (47): 2203-2206.

106. Diasio R, and Harris B. Clinical Pharmacology of 5-Flurouracil. Clinical Pharmacokinetics 1989; 16: 215-237.

107. Dobritzsch D, et al. *Crystal structure of dihydropyrimidine dehydrogenase , a major determinant of the pharmacokinetics of the anti-cancer drug 5-fluorouracil*. The EMBO journal 2001; 20(4) 650-660.

108. Dobritzsch D, et al. *Crystal structure of the productive ternary complex of dihydropyrimidine dehydrogenase with NADPH and 5-iodouracil. Implications for mechanism of inhibition and electron transfer*. Journal of Biological Chemistry. 2002; 277(15): 13155-13166.

109. Podschun B, et al. *Acid base catalytic mechanism of the dihydropyrimidine dehydrogenase from pH studies.* Journal of Biological Chemistry. 1993; 268(5): 3407-3413.

110. NGL Viewer: *a web application for molecular visualization.* Nucleic Acids Research DOI: rcsb.org/pdb/ngl/ngl.do?pdbid=2NO0&bion Date Accessed (1 July 2017)

111. Malet-Martino M, et al. *The Prodrugs of 5-Fluorouracil.* Current Medicinal Chemistry - Anti-Cancer Agents. 2002; 2(44): 267-310.

112. Wittmann JG, et al. *Structures of the Human Orotidine-5'-Monophosphate Decarboxylase Support a Covalent Mechanism and Provide a Framework for Drug Design.* Structure. 2008; 16(1): 82-92.

113. Sommer H, and Santi DV. *Purification and amino acid analysis of an active site peptide from thymidylate synthetase containing covalently bound 5-fluoro-2'-deoxyuridylate and methylenetetrahydrofolate.* Biochemistry Biophysics Research Communications. 1974; 57(3): 689-695.

114. Santi DV, et al. *Mechanism of Interaction of Thymidylate Synthetase with 5-Fluorodeoxyuridylate.* Biochemistry. 1974; (3): 471-481.

115. Kufe DW, and Major PP. *5-Fluorouracil incorporation into human breast carcinoma RNA correlates with cytotoxicity.* Journal of Biological Chemistry. 1981; 256(19): 9802-9805.

116. Glazer RI, and Lloyd LS. *Association of Cell Lethality with Incorporation into Nuclear RNA in Human Cells in Culture of 5-Fluorouracil Colon Carcinoma.* Molecular Pharmacology. 1982; 21: 468-473.

117. Saif MW, et al. *Pharmacokinetically guided dose adjustment of 5-fluorouracil: A rational approach to improving therapeutic outcomes.* Journal of National Cancer Institute. 2009; 101(22): 1543-1552.

118. Pullarkat ST, et al. *Thymidylate synthase gene polymorphism determines response and toxicity of 5-FU chemotherapy.* Journal of Pharmacogenomics. 2001; 1: 65-70.

119. Jang YH, et al. *First Principles Calculation of pK a Values for 5-Substituted Uracils.* Journal of Physical Chemistry. 2001; 105(January): 274-280.

120. Malet-Martino M, and Martino R. *Clinical Studies of Three Oral Prodrugs of 5-Fluorouracil (Capecitabine, UFT, S-1): A Review.* The Oncologist. 2002; 7(4): 288-323.

121. Wenlock MC, et al. *A comparison of physiochemical property profiles of development and marketed oral drugs.* Journal of Medicinal Chemistry. 2003; 46(7): 1250-1256.

122. Vieth M, et al. *Characteristic Physical Properties and Structural Fragments of Marketed Oral Drugs.* Journal of Medicinal Chemistry. 2004; 47(1): 224-232.

123. Ludek OR, and Meier C. *New Convergent Synthesis of Carbocyclic Nucleoside Analogues.* Synthesis. 2003; 200475(13): 2101-2109.

124. Ludek OR, and Meier C. *Influence of the N3-protection group on N1- vs. O2-alkylation in the Mitsunobu reaction.* European Journal of Organic Chemistry. 2006; (4): 941-946.

125. Jessel S, et al. *Cyclopentane-nucleobase coupling in the synthesis of carbocyclic L-nucleosides: is a SN2-reaction an alternative to the Mitsunobu-reaction?* Nucleosides Nucleotides Nucleic Acids. 2007; 26(8-9) :1181-1184.

126. Quezada E, et al. *Synthesis of carbocyclic pyrimidine nucleosides using the Mitsunobu reaction: O2- vs. N1-alkylation.* Helvetica Chimica Acta. 2010; 93(2): 309-313.

127. Cho JH, et al. *Synthesis of Cyclopentanyl Carbocyclic 5‐Fluorocytosine ((−)-5- Fluorocarbodine) Using a Facially Selective Hydrogenation Approach*. The Journal of Organic Chemistry 2013; (78): 723-727.

128. Cruickshank KA, et al. *The benzoylation of uracil and thymine.* Tetrahedron Letters. 1984; 25(6): 681-684.

129. Caram L, et al. *Synthesis of 1- and 3-Arylcarbonyl Derivatives of 5-Fluorouracil.* Journal of Heterocyclic Chemistry. 1999; 36: 397-401.

130. Rubio-Ruiz B, et al. *Efficient Palladium-Triggered Release of Vorinostat from a Bioorthogonal Precursor.* Journal of Medicinal Chemistry. 2016; 59(21): 9974-9980.

131. Pérez-López AM, et al. Gold-Triggered Uncaging Chemistry in Living Systems. Angewandte Chemie International Edition. 2017: 1-6.

132. Alauddin MM. *Positron emission tomography (PET) imaging with 18F-based radiotracers.* American Journal of Nuclear Medicine and Molecular Imaging. 2012; 2(1): 55-76.

133. Zissen MH, et al. *18F-5-fluorouracil dynamic positron emission tomography/computed tomography shows decreased tracer activity after bevacizumab in colorectal metastases.* Nuclear Medicin Communications. 2011; 32: 343-347.

134. Wolf W, et al. *Tumor trapping of 5-fluorouracil: in vivo 19F NMR spectroscopic pharmacokinetics in tumor-bearing humans and rabbits.* Proceedings of the National Academy of Science. 1990; 87: 492-496.

135. Wolf W, et al. *Non-invasive 19F-NMRS of 5-fluorouracil in pharmacokinetics and pharmacodynamic studies.* NMR Biomedicine. 1998; 11: 360-369.

136. Zhang Y, et al. *Imaging with Raman spectroscopy.* Current Pharmaceutical Biotechnology. 2010; 11(6): 654-661.

137. Baranska-Schulz, H et al. *In situ simultaneous analysis of polyacetetylenes, catotenoids and polysaccharides in carrot roots.* Journal of Agricultural Food Chemistry. 2005; 53: 6565-6571.

138. Weeks T, et al. *Raman microscopy based on doubly-resonant four-wave mixing (DR-FWM).* Optics Express. 2009; 17(19): 17044-17051.

139. Yamakoshi H, et al. *Imaging of EdU, an alkyne-tagged cell proliferation probe, by Raman microscopy.* Journal of the American Chemical Society. 2011; 133(16): 6102-6105.

140. Yamakoshi H, et al. *Alkyne-tag Raman imaging for visualization of mobile small molecules in live cells.* Journal of the American Chemical Society. 2012; 134(51): 20681-20689.

141. Tipping WJ, et al. *Imaging drug uptake by bioorthogonal stimulated Raman scattering microscopy.* Chemical Science. 2017: 1-10.

142. Zhang G, et al. *Imaging the Prodrug-to-Drug Transformation of a 5-Fluorouracil Derivative in Skin by Confocal Raman Microscopy.* Journal of Investigative Dermatology. 2007; 127(5): 1205-1209.

143. Farquharson S, et al. *Surface-enhanced Raman spectral measurements of 5-fluorouracil in saliva.* Molecules. 2008; 13(10): 2608-2627.

144. Heidari-Torkabadi H, et al. *Following drug uptake and reactions inside escherichia coli cells by raman microspectroscopy.* Biochemistry. 2014; 53(25): 4113-4121.

145. Eli Lilly and Company. Gemzar (Gemcitabine) Prescribing Information. DOI: http://pi.lilly.com/us/gemzar.pdf. Date Accessed April 4, 2017.

146. Burris III HA, et al. *Improvements in Survival and Clinical Benefit With Gemcitabine as First-Line Therapy for Patients With Advanced Pancreas Cancer: A Randomized Trial*. Journal of clinicall Oncology 1997; 15(6): 2403-2413.

147. Sandler A, and Ettinger D. *Gemcitabine : Single-Agent and Combination Therapy in Non-Small Cell Lung Cancer.* The Oncologist 1999; 4: 241-251.

148. Lorusso A, et al. *Role of gemcitabine in ovarian cancer treatment.* Annals of Oncology. 2006; 17(Suppl. 5): 188-194.

149. Alberts SR, et al. *Gemcitabine and Doxetaxel for Hepatocellular Carcinoma: A Phase II North Central Cancer Treatment Group (NCCTG) Clinical Trial*. American Journal of Clinical Oncology. 2012; 35(5): 418-423.

150. Silvestris N, et al. *Role of gemcitabine in metastatic breast cancer patients: a short review.* The Breast. 2008; 17: 220-226.

151. Patra KC, and Hay N. *The pentose phosphate pathway and cancer.* Trends in Biochemical Science. 2014; 39(8): 347-354.

152. Galmarini CM, et al. *Nucleoside analogues and nucleobases in cancer treatment.* Lancet Oncology. 2002; 3(7): 415-424.

153. Jordheim LP, et al. *Advances in the development of nucleoside and nucleotide analogues for cancer and viral diseases.* Nature Reviews in Drug Discovery. 2013; 12(6): 447-464.

154. Liu P, et al. Fluorinated Nucleosides: Synthesis and Biological Implication. Journal of Fluorine Chemistry. 2009; 129(9): 743-766.

155. Mini E, et al. Cellular pharmacology of gemcitabine. Annals in Oncology. 2006; 17(Sup. 5): 7-12.

156. Alvarellosa ML, et al. *PharmGKB summary: gemcitabine pathway.* Pharmacogenetics Genomics. 2012; 24(11): 1.

157. Hazra S, et al. *Structural and kinetic characterization of human deoxycytidine kinase variants able to phosphorylate 5-substituted deoxycytidine and thymidine analogs*. Biochemistry. 2010; 49(31): 6784-6790.

158. Sabini E, et al. *Structure of human dCK suggests strategies to improve anticancer and antiviral therapy.* Nature Structural Biology. 2003; 10(7): 513-519.

159. Mini E, et al. Cellular pharmacology of gemcitabine. Annals in Oncology. 2006; 17(Suppl. 5): 7-12.

160. Ciccolini J, et al. *Integrating pharmacogenetics into gemcitabine dosing--time for a change?* Nature Reviews in Clinical Oncology. 2011; 8(7): 439-444.

161. Cancer Drug Information - Gemcitabine. National Cancer Institute. DOI: pdr.net/drug-summary/Gemcitabine-gemcitabine-3701. Date Accessed 4 June 2017

162. Damaraju VL, et al. *Nucleoside anticancer drugs: the role of nucleoside transporters in resistance to cancer chemotherapy.* Oncogene. 2003; 22(47): 7524-7536.

163. Gray JH, et al. *Functional and genetic diversity in the concentrative nucleoside transporter, CNT1, in human populations.* Molecular Pharmacology. 2004; 65(3): 512-519.

164. Mackey JR, et al. *Gemcitabine transport in xenopus oocytes expressing recombinant plasma membrane mammalian nucleoside transporters.* Journal of the National Cancer Institute. 1999; 91(21): 1876-1881.

165. Carmichael J, et al. *Phase II study of gemcitabine in patients with advanced pancreatic cancer.* British Journal of Cancer. 1996; 73(1): 101-105.

166. Gupta N, et al. *Gemcitabine-induced pulmonary toxicity: case report and review of the literature.* American Journal of Clinical Oncology. 2002; 25(1): 96-100.

167. Toschi L, et al. *Role of gemcitabine in cancer therapy.* Future Medicines. 2005; 1(1): 7-17.

168. Khan MF, et al. Gemcitabine-induced cardiomyopathy: a case report and review of the literature. Journal of Medicine Case Reports. 2014; 8(220).

169. Abbruzzese JL, et al. *A Phase-I Clinical, Plasma, and Cellular Pharmacology Study of Gemcitabine.* Journal of Clinical Oncology. 1991; 9(3): 491-498.

170. Wong A, et al. *Clinical pharmacology and pharmacogenetics of gemcitabine.* Drug Metabolism Reviews. 2009; 41(2): 77-88.

171. Ciccolini J, et al. *Cytidine deaminase residual activity in serum is a predictive marker of early severe toxicities in adults after gemcitabine-based chemotherapies.* Journal of Clinical Oncology. 2010; 28(1): 160-165.

172. Yoon K-A, et al. *Cytidine Deaminase as a Molecular Predictor of Gemcitabine Response in Patients with Biliary Tract Cancer.* Oncology. 2015; 89(6): 345-350.

173. Xu Y, et al. *Cathepsin B-sensitive cholesteryl hemisuccinate–gemcitabine prodrug nanoparticles: enhanced cellular uptake and intracellular drug controlled release.* RSC Advances. 2015; 5(9): 6985-6992.

174. Fang Y, et al. *Enhanced cellular uptake and intracellular drug controlled release of VESylated gemcitabine prodrug nanocapsules.* Colloids and Surfaces B: Biointerfaces. 2015; 128: 357-362.

175. Xu Y, et al. *Preparation of intravenous injection nanoformulation via co-assemble between cholesterylated gemcitabine and cholesterylated mPEG: enhanced cellular uptake and intracellular drug controlled release.* Journal of Microencapsulation. 2017; 34(2): 185-194.

176. Han H, et al. *The rational design of a gemcitabine prodrug with AIE-based intracellular light-up characteristics for selective suppression of pancreatic cancer cells.* Chemical Communications. 2015; 51: 17435-17438.

177. Carroll V, et al. *A boronate-caged [18F]FLT probe for hydrogen peroxide detection using positron emission tomography.* Journal of the American Chemical Society. 2014; 136(42): 14742-14745.

178. Bielski R, and Witczak Z. *Strategies for coupling molecular units if subsequent decoupling is required.* Chemical Reviews. 2013; 113(3): 2205-2243.

179. Ramesh R, *Highly selective deblocking of propargyl carbonates in the presence of propargyl carbamates with tetrathiomolybdate.* Journal of Organic Chemistry. 2005; 70(3): 837-840.

180. Amir RJ, et al. *Self-immolative dendrimers.* Angewandte Chemie - International Edition. 2003; 42(37): 4494-4499.

181. Avital-shmilovici M, and Shabat D. *Self-immolative dendrimers : A distinctive approach to molecular amplification.* RSC Soft Matter. 2010: 1073-1080.

182. Blencowe CA, et al. *Self-immolative linkers in polymeric delivery systems.* Polymeric Chemistry. 2011; 2(4): 773-790.

183. Grinda M, et al. *A self-immolative dendritic glucuronide prodrug of doxorubicin.* Medicinal Chemistry Communications. 2012; 3(1): 68.

184. Rambabu D, et al. *Pd/C-mediated depropargylation of propargyl ethers/amines in water.* Tetrahedron Letters. 2013; 54(9): 1169-1173.

185. Kaleta C, et al. *In Silico evidence for gluconeogenesis from fatty acids in humans*. PLoS Computational Biology. 2011; 7(7): 1-10.

186. Wakselman M. *1,4- And 1,6-Eliminations From Hydroxy And Amino-Substituted Benzyl Systems: Chemical And Biochemical Applications.* New Journal of Chemistry. 1983; 7: 439-447.

187. Greenwald RB, et al. *Drug delivery systems employing 1,4- or 1,6-elimination: poly(ethylene glycol) prodrugs of amine-containing compounds.* Journal of Medicinal Chemistry. 1999; 42(18): 3657-3667.

188. Thigpen JT. *Innovations in anthracyclin therapy: overview.* Community Oncology. 2005; 2(1): 3-7.

189. Arcamone F, et al. *Adriamycin (14-hydroxydaunomycin), a novel antitumor antibiotic.* Tetrahedron Letters. 1969; (13): 1007-1010.

190. Aubel-Sadron G, and Londos-Gagliardi D. *Daunorubicin and doxorubicin, anthracycline antibiotics, a physicochemical and biological review.* Biochimie. 1984; 66(5): 333-352.

191. Cancer Drug Information - Doxorubicin Hydrochloride. National Cancer Institute. DOI: http://www.cancer.gov/cancertopics/druginfo/doxorubicinhydrochloride. Date Accessed April 28, 2017.

192. Kiyomiya KI, et al. *Mechanism of specific nuclear transport of adriamycin: The mode of nuclear translocation of adriamycin-proteasome complex.* Cancer Research. 2001; 61(6): 2467-2471.

193. Skovsgaard T, and Nissen N. *Membrane transport of Anthracyclines.* Pharmaceutical Therapies. 1981; 18: 293-311.

194. Xu X, et al. *Molecular pharmacology of the interaction of anthracyclines with iron.* Molecular Pharmacology. 2005; 68(2): 261-271.

195. Nitiss J. *Targeting DNA topoisomerase II in cancer chemotherapy.* Nature Reviews Cancer. 2009; 9(5): 338-350.

196. Swift LP, et al. *Doxorubicin-DNA adducts induce a non-topoisomerase II-mediated form of cell death.* Cancer Research. 2006; 66(9): 4863-4871.

197. Dhalla NS, et al. *Role of oxidative stress in cardiovascular diseases.* Journal of Hypertension. 2000; 18(6): 655-673.

198. Kalivendi SV, et al. *Doxorubicin activates nuclear factor of activated T-lymphocytes and Fas ligand transcription: role of mitochondrial reactive oxygen species and calcium.* Journal of Biochemistry. 2005; 389(2): 527-539.

199. Tokarska-Schlattner M, et al. *New insights into doxorubicin-induced cardiotoxicity: the critical role of cellular energetics.* Journal of Molecular Cell Cardiology. 2006; 41(3): 389-405.

200. Octavia Y, et al. *Doxorubicin-induced cardiomyopathy: From molecular mechanisms to therapeutic strategies.* Journal of Molecular Cell Cardiology. 2012; 52(6): 1213-1225.

201. Dasdia T, et al. *Inhibiting Effect of the new cytotoxic antibiotic Daunomycin on nucleic acids and mitotix activity of HELA cells.* Journal of Cell Biology. 1962; 3: 545-550.

202. Forrest RA, et al. *Activation of DNA damage response pathways as a consequence of anthracycline-DNA adduct formation.* Biochemical Pharmacology. 2012; 83(12): 1602-1612.

203. Gewirtz DA. *A critical evaluation of the mechanisms of action proposed for the antitumor effects of the anthracycline antibiotics adriamycin and daunorubicin.* Biochemical Pharmacology. 1999; 57(7): 727-741.

204. Agudelo D, et al. *Intercalation of antitumor drug doxorubicin and its analogue by DNA duplex: Structural features and biological implications.* International Journal of Biological Macromolecules. 2014; 66: 144-150.

205. Pommier Y. *Drugging topoisomerases: Lessons and Challenges.* ACS Chemical Biology. 2013; 8(1): 82-95.

206. Chen SH, et al. *New mechanistic and functional insights into DNA topoisomerases.* Annual Review Biochemistry. 2013; 82: 139-170.

207. Zhang S, et al. *Identification of the molecular basis of doxorubicin-induced cardiotoxicity.* Nature Medicine. 2012; 18(11): 1639.

208. Coates A, et al. *On the receiving end - patient perception of the side-effects of cancer chemotherapy.* European Journal of Cancer Clinical Oncology. 1983; 19(2): 203-208.

209. Tacar O, et al. *Doxorubicin: An update on anticancer molecular action, toxicity and novel drug delivery systems.* Journal of Pharmaceutical Pharmacology. 2013; 65(2): 157-170.

210. Carvalho C, et al. *Doxorubicin: The Good, the Bad and the Ugly Effect.*Current Medicinal Chemistry 2009: 3267-3285.

211. Weiss RB. *The anthracyclines: Will we ever find a better doxorubicin?* Seminars in Oncology. 1992; 19(6): 670-686.

212. Lipshultz SE, et al. *Continuous Versus Bolus Infusion of Doxorubicin in Children With ALL: Long-term Cardiac Outcomes.* Pediatrics. 2012; 130(6): 1003-1011.

213. D. G. Streeter, et al. *Comparative cytotoxicities of various morpholinyl anthracyclines.* Cancer Chemotherapy Pharmacology. 1985; 14: 160-164.

214. Chatterjee K, et al. *Doxorubicin cardiomyopathy.* Cardiology. 2010; 115(2): 155-162.

215. Mcgovern P, et al. *Plasmin-Activated Prodrugs for Cancer Chemotherapy - Synthesis and Biological Activity of Peptidyl Derivatives of Doxorubicin.* Journal of Medicinal Chemistry. 1983; 5: 638-644.

216. Jacquesy J, et al. *Prodrugs of Anthracyclines for Use in Antibody-Directed Enzyme Prodrug Therapy.* Journal of Medicinal Chemistry. 1998; 2623(97): 3572-3581.

217. van Brakel R, et al. *A doxorubicin prodrug activated by the staudinger reaction.* Bioconjugation Chemistry. 2008; 19(3): 714-718.

218. Matikonda SS, et al. *Bioorthogonal prodrug activation driven by a strain-promoted 1,3-dipolar cycloaddition.* Chemical Science. 2014: 1-7.

219. Li J, et al. *Palladium-triggered deprotection chemistry for protein activation in living cells.* Nature Chemistry. 2014; 6(4): 352-361.

220. Coleman RS. *Chemoselective Cleavage of Benzyl Ethers, Esters, and Carbamates in the Presence of Other Easily Reducible Groups.* Synthesis. 1999; (S1): 1399-1400.

221. Suggs JW. Encyclopedia of Inorganic Chemistry - Palladium: Organometallic Chemistry. (King RB, Crabtree RH, Lukehart CM, Atwood DA, Scott RA, eds.). Chichester, UK: John Wiley & Sons, Ltd; 2006. doi:10.1002/0470862106.ia179.

222. Negishi E. Handbook of Organopalladium Chemistry for Organic Synthesis. (Negishi E, ed.). New York, USA: John Wiley & Sons, Inc.; 2002. doi:10.1002/0471212466.

223. Murakami M, and Matsuda T. *Metal-catalysed cleavage of carbon–carbon bonds.* Chemical Communications. 2011; 47(4): 1100-1105.

224. Chankeshwara SV, et al. *Palladium-mediated chemistry in living cells.* Current Opinion in Chemical Biology. 2014; 21: 128-135.

225. Li J, and Chen PR. *Development and application of bond cleavage reactions in bioorthogonal chemistry.* Nature Chemical Biology. 2016; 12(3): 129-137.

226. Toshima N. Metal Nanoparticles for Catalysis - Nanoscale Materials. (Luis M. Liz-Marzán PVK, ed.). Springer; 2003.

227. Cho JK, et al. *Captured and Cross-Linked Palladium Nanoparticles Captured and Cross-Linked Palladium Nanoparticles*. Journal of the American Society of Chemistry. 2006; 128(19): 6276-6277.

228. Chang J, et al. *Entangled palladium nanoparticles in resin plugs.* Chemical Communications. 2007; (August): 5031-5033.

229. Unciti-Broceta A, et al. *Synthesis of polystyrene microspheres and functionalization with Pd0 nanoparticles to perform bioorthogonal organometallic chemistry in living cells.* Nature Protocols. 2012; 7(6): 1207-1218.

230. Sarin VK, et al. *Quantitative monitoring of solid-phase peptide synthesis by the ninhydrin reaction.* Annals of Biochemistry. 1981; 117(1): 147-157.

231. Paul D, et al. *Phagocytosis dynamics depends on target shape.* Journal of Biophysics 2013; 105(5): 1143-1150.

232. Simon SI, and Schmid-Schonbein GW. B*iophysical aspects of microsphere engulfment.* Journal of Biophysics. 1988; 53(2): 163-173.

233. Champion J, et al. *Role of particle size in phagocytosis of polymeric microspheres.* Pharmaceutical Research. 2008; 25(8): 1815-1821.

234. Macarron R, et al. *Impact of high-throughput screening.* Nature. 2011; 10(March 2011): 188-195.

235. Pereira DA, and Williams JA. *Origin and evolution of high throughput screening.* British Journal of Pharmacology. 2007; 152(1): 53-61.

236. Mahmood TA, et al. *Adhesion-mediated signal transduction in human articular chondrocytes: The influence of biomaterial chemistry and tenascin-C.* Experimental Cellular Research. 2004; 301(2): 179-188.

237. Nath S, and Devi GR. *Three-dimensional culture systems in cancer research: Focus on tumor spheroid model.* Pharmacology Therapy. 2016; 163: 94-108.

238. Mbeunkui F, and Johann DJ. *Cancer and the tumor microenvironment: A review of an essential relationship.* Cancer Chemotherapy Pharmacology. 2009; 63(4): 571-582.

239. Quail DF, and Joyce JA. *Microenvironmental regulation of tumor progression and metastasis.* Nature Medicine. 2013; 19(11): 1423-1437.

240. Sun Y, et al. *Treatment-induced damage to the tumor microenvironment promotes prostate cancer therapy resistance through WNT16B.* Nature Medicine. 2012; 18(9): 1359-1368.

241. Blansfield JA, et al. *Combining agents that target the tumor microenvironment improves the efficacy of anticancer therapy.* Clinical Cancer Research. 2008; 14(1): 270-280.

242. Ma Y, et al. *Extreme low dose of 5-fluorouracil reverses MDR in cancer by sensitizing cancer associated fibroblasts and down-regulating Pgp.* PLoS One. 2017; 12(6): 1-11.

243. Okigami M, et al. *Intravital imaging of the effects of 5-fluorouracil on the murine liver microenvironment using 2-photon laser scanning microscopy.* Oncology Letters. 2016; 11(4): 2433-2439.

244. Shakibaei M, et al. *Curcumin potentiates antitumor activity of 5-fluorouracil in a 3D alginate tumor microenvironment of colorectal cancer.* BMC Cancer. 2015; 15: 250.

245. Liu Q, et al. *Chemotherapy and tumor microenvironment of pancreatic cancer.* Cancer Cell International Edition. 2017; 17(1): 68.

246. Hamada S, et al. *Novel therapeutic strategies targeting tumor-stromal interactions in pancreatic cancer.* Frontiers in Physiology. 2013; 4(November): 1-7.

247. Shah AN, et al. *Development and characterization of gemcitabine-resistant pancreatic tumor cells.* Annals of Surgical Oncology. 2007; 14(12): 3629-3637.

248. Elizabeth S. et al. *Imaging tumor-stroma interactions during chemotherapy reveals contributions of the microenvironment to resistance.* Cancer Cell. 2012; 76(October): 211-220.

249. Vinci M, et al. *Advances in establishment and analysis of three-dimensional tumor spheroid-based functional assays for target validation and drug evaluation.* BMC Biology. 2012; 10(1): 29.

250. Ma HL, et al. *Multicellular tumor spheroids as an in vivo-like tumor model for three-dimensional imaging of chemotherapeutic and nano material cellular penetration.* Molecular Imaging. 2012; 11(6): 487-498.

251. Freeman AE, and Hoffman RM. *In vivo-like growth of human tumors in vitro.* Proceedings of the National Academy of Science. 1986; 83(8): 2694-2698.

252. Hirschhaeuser F, et al. *Multicellular tumor spheroids: An underestimated tool is catching up again.* Journal of Biotechnology. 2010; 148(1): 3-15.

253. Friedrich J, et al. *Spheroid-based drug screen: considerations and practical approach*. Nature Protocols. 2009; 4(3): 309-324.

254. Lee JH, and Hur W. *Scaffold-free formation of a millimeter-scale multicellular spheroid with an internal cavity from magnetically levitated 3T3 cells that ingested iron oxide-containing microspheres.* Biotechnology Bioengineering. 2014; 111(5): 1038-1047.

255. Kim J Bin, et al. *Three-dimensional in vitro tissue culture models of breast cancer - a review*. Breast Cancer Research Treatment. 2004; 85: 281-291.

256. Mazzoleni G, et al. *Modelling tissues in 3D: The next future of pharmaco-toxicology and food research?* Genes Nutrition. 2009; 4(1): 13-22.

257. Kim JA, et al. *High-throughput generation of spheroids using magnetic nanoparticles for three-dimensional cell culture.* Biomaterials. 2013; 34(34): 8555-8563.

258. Niehoff A-C, et al. *A palladium label to monitor nanoparticle-assisted drug delivery of a photosensitizer into tumor spheroids by elemental bioimaging.* Metallomics. 2014; 6(1): 77-81.

259. Hornung A, et al. *Treatment efficiency of free and nanoparticle-loaded mitoxantrone for magnetic drug targeting in multicellular tumor spheroids.* Molecules. 2015; 20(10): 18016-18030.

260. Perche F, et al. *Accumulation and toxicity of antibody-targeted doxorubicin-loaded PEG-PE micelles in ovarian cancer cell spheroid model.* Journal of Controlled Release. 2012; 164(1): 95-102.

261. Perche F, and Torchilin VP. *Cancer cell spheroids as a model to evaluate chemotherapy protocols.* Cancer Biology Therapy. 2012; 13(12): 1205-1213.

262. Kane RC, et al. *Dexrazoxane (TotectTM): FDA Review and Approval for the Treatment of Accidental Extravasation Following Intravenous Anthracycline Chemotherapy.* The Oncologist. 2008; 13(17): 445-450.

263. Swain BSM, et al. *Cardioprotection With Dexrazoxane for Doxorubicin- Containing Therapy in Advanced Breast Cancer.* Journal of Clinical Oncology. 1997; 15(4): 1318-1332.

264. Tebbi CK, et al. *Dexrazoxane-associated risk for acute myeloid leukemia/myelodysplastic syndrome and other secondary malignancies in pediatric Hodgkin's disease.* Journal of Clinical Oncology. 2007; 25(5): 493-500.

265. European Medicines Agency: *EMA Recommends Restricting the Use of Dexrazoxane-Containing Medicines EMA/491205/2011*. Webpage: www.ema.europa.eu. Date Accessed 24 August 2017

266. Liu Y, et al. *Visnagin protects against doxorubicin-induced cardiomyopathy through modulation of mitochondrial malate dehydrogenase.* Science Translational Medicine. 2014; 6: 266-270.

267. Brown D, et al. *Advances in the Study of Heart Development and Disease Using Zebrafish*. Journal Cardiovascular Development and Discovery. 2016; 3(2): 13.

268. Kessler M, et al. Recent progress in the use of zebrafish for novel cardiac drug discovery. Expert Opinion in Drug Discovery. 2015; 10(11): 1231-1241.

269. Kitambi SS, et al. *Small molecule screening platform for assessment of cardiovascular toxicity on adult zebrafish heart.* BMC Physiology. 2012; 12(1): 3.

270. Stainier DY, et al. *Cardiovascular development in the zebrafish. I. Myocardial fate map and heart tube formation.* Development. 1993; 119(1): 31-40.

271. Moorman AFM, Christoffels VM. *Cardiac chamber formation: development, genes, and evolution.* Physiology Reviews. 2003; 83(4): 1223-1267.

272. Miura GI, Yelon D. *A Guide to Analysis of Cardiac Phenotypes in the Zebrafish Embryo*. Methods in Cell Biology. 2012: 161-180.

273. Zennaro C, et al. *Podocyte developmental defects caused by adriamycin in zebrafish embryos and larvae: A novel model of glomerular damage.* PLoS One. 2014; 9(5)

274. Hrushesky WJM, et al. *Circadian-shaped infusion of floxuridine for progressive metastatic renal cell carcinoma.* Journal of Clinical Oncology. 1990; 8(9): 1504-1513.

275. Muggia FM, et al. *Intraperitoneal 5-fluoro-2'-deoxyuridine with escalating doses of leucovorin: Pharmacology and clinical tolerance.* Investigational New Drugs. 1994: 12(3) 197-206.

276. Van Laar JAM, et al. *Comparison of 5-fluoro-2'-deoxyuridine with 5-fluorouracil and their role in the treatment of colorectal cancer.* European Journal of Cancer. 1998; 34(3): 296-306.

277. Peng Y, et al. *Discovery of an Orally Active and Liver-Targeted Prodrug of 5-Fluoro-2'-Deoxyuridine for the Treatment of Hepatocellular Carcinoma.* Journal of Medicinal Chemistry. 2016; 59(8): 3661-3670.

278. Tanabe K, et al. *One-electron reduction characteristics of N(3)-substituted 5-fluorodeoxyuridines synthesized as radiation-activated prodrugs.* Bioorganic Medicinal Chemistry. 2003; 11(21): 4551-4556.

279. Tanabe K, et al. *Hypoxia-selective activation of 5-fluorodeoxyuridine prodrug possessing indolequinone structure: Radiolytic reduction and cytotoxicity characteristics.* Bioorganic Medicinal Chemistry Letters. 2005; 15(9): 2321-2324.

280. Tanabe K, et al. *Reductive activation of 5-fluorodeoxyuridine prodrug possessing azide methyl group by hypoxic X-irradiation.* Bioorganic Medicinal Chemistry Letters. 2012; 22(4): 1682-1685.

281. Tanabe K, et al. *Synthesis and one-electron reduction characteristics of radiation-activated prodrugs possessing two 5-fluorodeoxyuridine units.* Bioorganic Medicinal Chemistry. 2012; 20(17): 5164-5168.

282. Eggener SE, et al. *Focal Therapy for Localized Prostate Cancer: A Critical Appraisal of Rationale and Modalities.* Journal of Urology. 2007; 178(6): 2260-2267.

283. Grills IS, et al. *High Dose Rate Brachytherapy as Prostate Cancer Monotherapy Reduces Toxicity Compared to Low Dose Rate Palladium Seeds.* Journal of Urology. 2004; 171(3): 1098-1104.

284. Yagoda A, and Petrylak D. *Cytotoxic chemotherapy for advanced hormone-resistant prostate cancer.* Cancer. 1993; 71(3S): 1098-1109.

285. Sella A, et al. *Phase II study of ketoconazole combined with weekly doxorubicin in patients with androgen-independent prostate cancer.* Journal of Clinical Oncology. 1994; 12(4): 683-688.

286. Frederiksen LJ, et al. *Hypoxia induced resistance to doxorubicin in prostate cancer cells is inhibited by low concentrations of glyceryl trinitrate.* Journal of Urology. 2003; 170(3): 1003-1007.

287. Undevia SD, et al. *Pharmacokinetic variability of anticancer agents.* Nature Reviews Cancer. 2005; 5(6): 447-458.

288. Allen TM. *Drug Delivery Systems: Entering the Mainstream.* Science. 2004; 303(5665): 1818-1822.

289. LaVan DA, et al. *Small-scale systems for in vivo drug delivery.* Nature Biotechnology. 2003; 21(10): 1184-1191.

290. Peer D, et al. *Nanocarriers as an emerging platform for cancer therapy.* Nature Nanotechnology. 2007; 2(12): 751-760.

291. Lu Y, et al. *Bioresponsive materials*. Nature Reviews Materials. 2016; 2(1): 16075.

292. L Zhang et al. *Nanoparticles in Medicine: Therapeutic Applications and Developments.* Nature Translational Medicine. 2008; 83(5): 761-769.

293. Freitas S, et al. *Microencapsulation by solvent extraction/evaporation: Reviewing the state of the art of microsphere preparation process technology.* Journal of Controlled Release. 2005; 102(2): 313-332.

294. Freiberg S, and Zhu XX. *Polymer microspheres for controlled drug release.* International Journal of Pharmaceuticals. 2004; 282(1-2): 1-18.

295. Avgoustakis K, et al. *PLGA-mPEG nanoparticles of cisplatin: In vitro nanoparticle degradation, in vitro drug release and in vivo drug residence in blood properties.* Journal of Controlled Release. 2002; 79(1-3): 123-135.

296. Chen W, and Lu DR. *Carboplatin-loaded PLGA microspheres for intracerebral injection: formulation and characterization.* Journal of Microencapsulation. 1999; 16(5): 551-563.

297. You J, et al. *Near-infrared light triggers release of paclitaxel from biodegradable microspheres: Photothermal effect and enhanced antitumor activity.* Small. 2010; 6(9): 1022-1031.

298. Menei P, et al. *Local and sustained delivery of 5-fluorouracil from biodegradable microspheres for the radiosensitization of glioblastoma: A pilot study.* Cancer. 1999; 86(2): 325-330.

299. Grinberg O, et al. *Sonochemically prepared BSA microspheres containing Gemcitabine, and their potential application in renal cancer therapeutics*. Acta Biomaterialia. 2009; 5(8): 3031-3037.

300. Kettenbach J, et al. *Drug-loaded microspheres for the treatment of liver cancer: Review of current results.* Cardiovascular and Interventional Radiology. 2008; 31(3): 468-476.

301. Song MJ, et al. *Comparative study between doxorubicin-eluting beads and conventional transarterial chemoembolization for treatment of hepatocellular carcinoma.* Journal of Hepatology. 2012; 57(6): 1244-1250.

302. Miller MA, et al. *Nano-palladium is a cellular catalyst for in vivo chemistry*. Nature Communications. 2017; 8(May): 15906.

303. Westerfield M, et al. *An on-line database for zebrafish development and genetics research.* Cell Developmental Biology. 1997; 8: 477-488.

304. Kimmel CB, et al. *Stages of embryonic development of the zebrafish.* Developmental Dynamics. 1995; 203(3): 253-310.

305 Falkeholm, et al. *Xylene Free Method for Histological Preparation: A Multicentre Evaluation*, Laboratory Investigation 2001 (81:9): 1213 - 1221.

Appendix

Patent:

Palladium Activated Prodrugs PCT/GB2017/051379. Priority Date: 29.04.2016. Inventors:

Belén Rubio-Ruiz, Thomas L. Bray, Ana M Pérez-López, Asier Unciti-Broceta.

BIOORTHOGONAL COMPOUNDS AND METHODS [SUMMARY EXCERPT]

Field of the Invention

The present invention relates to bioorthogonal deprotection methods, and to compounds for use in such methods, including prodrug forms of active agents that can be converted to the active agent *in situ* by palladium catalysis.

Background of the Invention

Bioorthogonal chemistry

As reported by Bertozzi, et al. in the early 2000's (Bertozzi, C. R. *et al. Science,* 2000, 287, 2007-2010 and Bertozzi, C.R. *et al. J. Am. Chem. Soc.* 2004, 126, 15046-15047), artificial synthetic chemistry can be conducted in a biological environment without adverse biological effects using highly chemospecific reactive partners. Such reactions which proceed in a biological environment without adverse biological consequences are now commonly referred to as being "bioorthogonal".

Initial bioorthogonal studies focussed on the development of labelling strategies based on the selective conjugation of two biologically-inert functional groups. This development has since enabled the real-time study of a wide range of biomolecules in their native environs (see, e.g. Bertozzi, C.R. *Ace Chem Res.* 2011, 44, 651-653).

Transition metal catalysed reactions

Transition metal catalysed reactions are an extremely powerful tool in organic synthesis as they provide chemospecific reaction profiles and facilitate a wide range of chemical transformations. From a bioorthogonal synthetic perspective, it is therefore desirable to develop bioorthogonal transition metal catalysed reactions that can perform efficiently in a biological environment to provide the biosynthetic chemist with more synthetic flexibility.

A large variety of transition metal catalysed reactions have been reported in the literature. However, there has been limited success in the application of such reactions in a biological environment. This is potentially due to a large number of reported reaction conditions being simply incompatible with a biological environment, e.g. requiring organic solvents and/or high temperatures, etc. For instance, the palladium-mediated cleavage of propargyl protecting groups from aryl amines requires biologically incompatible temperatures of at least 80 °C (see, e.g. Pal, M. *et ot., Org. Lett.* 2003, 5(3), 349-352).

Certain non-biological transition metal-catalysed reactions have however been shown to be promising candidates for use in bioorthogonal synthesis (e.g. Unciti-Broceta, A. *et al. Nature Protocols,* 2012, 7, 1207-1218 and Meggers, E. *et al. Chem Commun.* 2013, 49, 1581-1587). Such bioorthogonal organometallic (BOOM) reactions are biocompatible and involve chemospecific transformations undertaken usually by synthetic materials and mediated by a non-biotic metal source as described below.

In 2006, Meggers et al. described the application of a water-soluble ruthenium-based catalyst to carry out Allyl carbamate (Alloc) deprotection of bis-N,N'-allyloxycarbonyl rhodamine 110 inside human cells without adversely affecting cell viability (Meggers, E. et al., *Angew. Chem. Int. Ed.* 2006, 45, 5645-5648). The use of Pd^0-functionalized microspheres as a heterogeneous catalyst medium for promoting BOOM chemistry inside cells has also been reported (Bradley, M. *et al., Nat. Chem.* 2011, 3, 239-243 and Unciti-Broceta, A. *et al. Nature Protocols,* 2012, 7, 1207-1218). The palladium-functionalized microspheres were shown to be able to enter cells *in vitro* and catalyse Alloc deprotection and Suzuki-Miyaura cross-coupling in the cell cytoplasm without any observed cytotoxicity.

Biomedical applications

In biomedicine, bioorthogonal deprotection methods could be utilised to transform a bioorthogonal chemical into a bioactive material. Prodrugs, for example, are active agent precursors that are converted to the active agent following administration to a patient, typically by chemical rearrangement of the prodrug and/or by cleavage of a pro-moiety by natural biological metabolism. Typically, prodrugs are based on active agents that have been protected with a cleavable protecting group or pro-moiety. By providing an active agent precursor that produces the active agent within the body, compounds can be produced that exhibit improved pharmacokinetic properties compared to the active drug, such as greater oral bioavailability and sustained release profiles.

For safety and simplicity, it is desirable to provide prodrugs that do not exhibit biological activity themselves. The activity profile of the prodrug is then entirely dependent on the metabolic conversion of the prodrug to the active agent, providing a greater degree of predictability of biological activity *in vivo*.

Typically, prodrugs are converted to the respective active agents in the gut (for orally administered drugs), and/or by general cellular and/or plasma-based metabolic pathways. Conventional prodrugs are thus converted to the active agent in a non-bioselective manner,

leading to general systemic exposure of the body cells to the active agent, which may result in undesirable side effects.

It is therefore desirable from a toxicological perspective to be able to deliver active agents specifically to the relevant target/disease site, and to prevent the active agent acting on the rest of the body cells.

Accordingly, it is one object of the present invention to provide a method of delivering an active agent to a target site without substantially exposing the body cells outside of the target site to the active agent.

Article

Pérez-López AM, Rubio-Ruiz B, Sebastián V, Hamilton L, Adam C, Bray TL, Irusta S, Brennan PM, Lloyd-Jones GC, Sieger D, Santamaría J, Unciti-Broceta A, et al. *Gold-Triggered Uncaging Chemistry in Living Systems*. Angewandte Chemie - International Edition. 2017; 56(41): 12548 - 12552. DOI 10.1002/anie.201705609

A Journal of the Gesellschaft Deutscher Chemiker

Angewandte International Edition Chemie

GDCh

www.angewandte.org

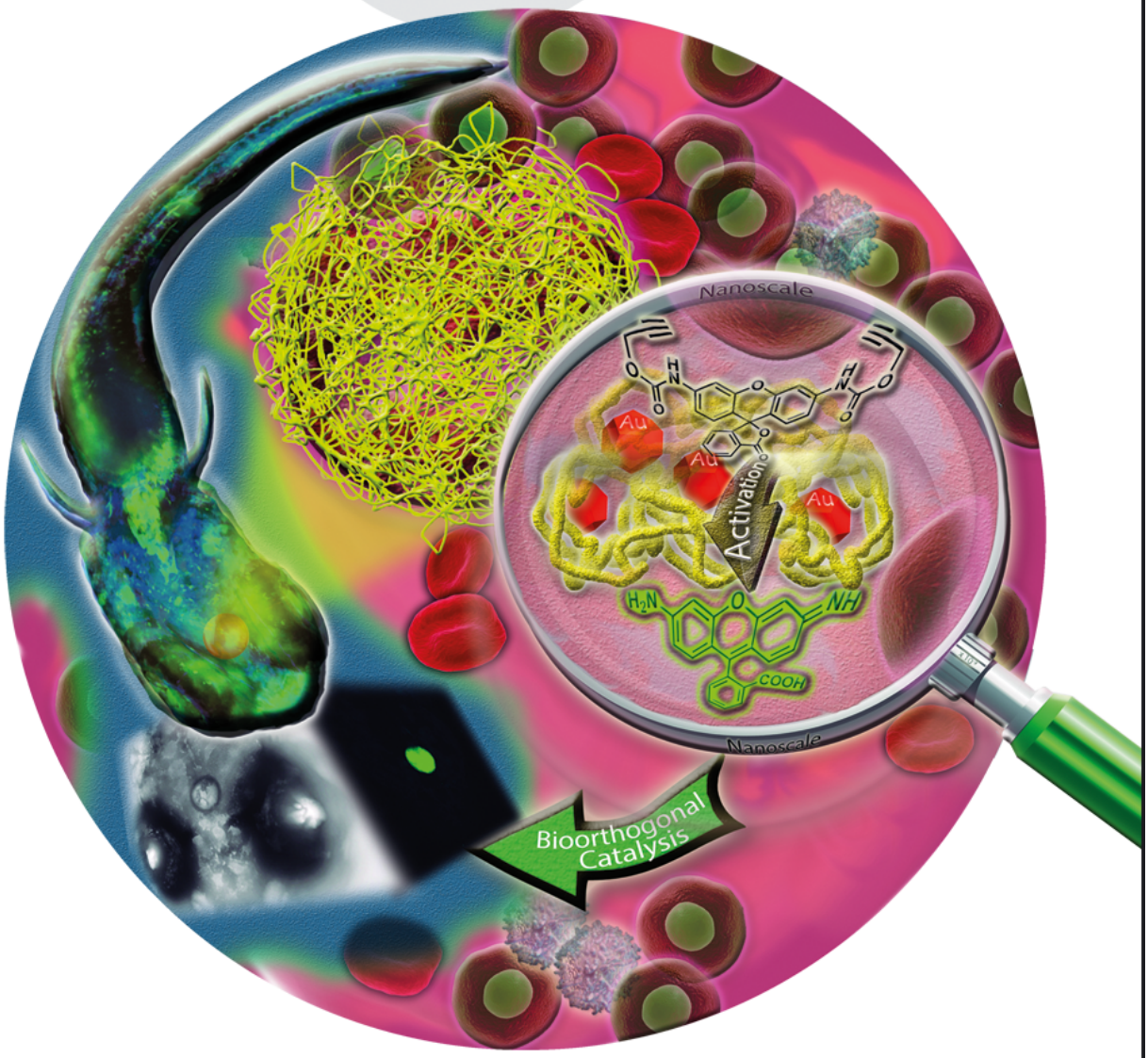

Bioorthogonal uncaging of a structurally diverse selection of cytotoxic precursors is achieved by heterogeneous gold catalysis, allowing safe activation of therapeutics by nonbiological chemical stimuli. In their Communication (DOI: 10.1002/anie.201705609), J. Santamaría and A. Unciti-Broceta et al. report gold-catalyzed bioorthogonal uncaging of clinically approved anticancer drugs in cancer cell culture, and the first intracranial activation of a bioorthogonal probe in a zebrafish.

150 Years GDCh

WILEY-VCH

Book chapter:

Rubio-Ruiz B, Bray TL, Pérez-López AM, *Masking Strategies for the Bioorthogonal Release of Anticancer Glycosides.* Z.J. Witczak and R. Bielski (eds.), Coupling and Decoupling of Diverse Molecular Units in Glycosciences (Springer) 2017.

Zbigniew J. Witczak · Roman Bielski
Editors

Coupling and Decoupling of Diverse Molecular Units in Glycosciences

Springer

Editors
Zbigniew J. Witczak
Pharmaceutical Sciences Department
Wilkes University
Wilkes-Barre, PA
USA

Roman Bielski
Pharmaceutical Sciences Department,
Nesbitt School of Pharmacy
Wilkes University
Wilkes-Barre, PA
USA

ISBN 978-3-319-65586-4 ISBN 978-3-319-65587-1 (eBook)
https://doi.org/10.1007/978-3-319-65587-1

Library of Congress Control Number: 2017948635

Printed on acid-free paper

This Springer imprint is published by Springer Nature
The registered company is Springer International Publishing AG
The registered company address is: Gewerbestrasse 11, 6330 Cham, Switzerland

Contents

Synthesis of N-Linked Glycopeptides Using Convergent Enzymatic Glycosylation Combined with SPPS 1
Renata Kowalczyk, Harveen Kaur, Antony J. Fairbanks and Margaret A. Brimble

Synthetic Antitumor Vaccines Through Coupling of Mucin Glycopeptide Antigens to Proteins 37
Markus Glaffig and Horst Kunz

Recent Advances in the Stereochemical Outcome of Multicomponent Reactions Involving Convertible Isocyanides 67
Krishnakant Patel and Peter R. Andreana

Glycoconjugate-Based Inhibitors of *Mycobacterium Tuberculosis* GlgE 91
Sri Kumar Veleti and Steven J. Sucheck

Selective Transformations of the Anomeric Centre in Water Using DMC and Derivatives 109
David Lim and Antony J. Fairbanks

[3, 3]-Sigmatropic Rearrangement as a Powerful Synthetic Tool on Skeletal Modification of Unsaturated Sugars 133
Gour Chand Daskhan, Malyasree Giri and Narayanaswamy Jayaraman

Recognition of Thiols in Coupling Reactions to Organic and Carbohydrate Acceptors 155
Zbigniew J. Witczak and Roman Bielski

Chemical Approaches Towards Neurodegenerative Disease Prevention: The Role of Coupling Sugars to Phenolic Biomolecular Entities 167
Catarina Dias, Ana M. Matos and Amélia P. Rauter

Probing for *Trypanosoma cruzi* Cell Surface Glycobiomarkers for the Diagnosis and Follow-Up of Chemotherapy of Chagas Disease 195
Nathaniel S. Schocker, Susana Portillo, Roger A. Ashmus, Carlos R.N. Brito, Igor E. Silva, Yanira Cordero Mendoza, Alexandre F. Marques, Erika Y. Monroy, Andrew Pardo, Luis Izquierdo, Montserrat Gállego, Joaquim Gascon, Igor C. Almeida and Katja Michael

Syntheses and Functions of Glycosaminoglycan Mimicking Polymers 213
Yoshiko Miura, Tomohiro Fukuda, Hirokazu Seto and Yu Hoshino

Methods for the High Resolution Analysis of Glycoconjugates 225
Christopher Gray and Sabine L. Flitsch

Masking Strategies for the Bioorthogonal Release of Anticancer Glycosides 269
Belén Rubio-Ruiz, Thomas L. Bray, Ana M. López-Pérez and Asier Unciti-Broceta

Example of Sacrificial Unit Using Two Different Click Reactions in Coupling and Decoupling (CAD) Chemistry 299
Roman Bielski, Zbigniew J. Witczak and Donald Mencer

Increased Efficacy of NKT Cell-Adjuvanted Peptide Vaccines Through Chemical Conjugation 309
Colin M. Hayman, Ian F. Hermans and Gavin F. Painter